Survivability of Wave Energy Converter and Mooring Coupled System using CFD

Edward Jack Ransley

A thesis submitted to the University of Plymouth in partial
fulfillment of the requirements for the degree of:

Doctor of Philosophy

School of Marine Science and Engineering

University of Plymouth

July 2015

Abstract

Survivability of Wave Energy Converter and Mooring Coupled System using CFD

Edward Jack Ransley

This thesis discusses the development of a Numerical Wave Tank (NWT) capable of describing the coupled behaviour of Wave Energy Converters (WECs) and their moorings under extreme wave loading. The NWT utilises the open-source Computational Fluid Dynamics (CFD) software OpenFOAM® to solve the fully nonlinear, incompressible, Reynolds-Averaged Navier-Stokes (RANS) equations for air and water using the Finite Volume Method (FVM) and a Volume of Fluid (VOF) treatment of the interface. A method for numerically generating extreme waves is devised, based on the dispersively-focused NewWave theory and using the additional toolbox waves2Foam. A parametric study of the required mesh resolution shows that steeper waves require finer grids for mesh independence.

Surface elevation results for wave-only cases closely match those from experiments, although an improved definition of the flow properties is required to generate very steep focused waves. Predictions of extreme wave run-up and pressure on the front of a fixed truncated cylinder compare well with physical measurements; the numerical solution successfully predicts the secondary loading cycle associated with the nonlinear ringing effect and shows a nonlinear relationship between incident crest height and horizontal load. With near perfect agreement during an extreme wave event, the reproduction of the six degree of freedom (6DOF) motion and load in the linearly-elastic mooring of a hemispherical-bottomed buoy significantly improves on similar studies from the literature.

Uniquely, this study compares simulations of two existing WEC designs with scale-model tank tests. For the Wavestar machine, a point-absorber constrained to pitch motion only, results show good agreement with physical measurements of pressure, force and float motion in regular waves, although the solution in the wake region requires improvement. Adding bespoke functionality, a point-absorber designed by Seabased AB, consisting of a moored float and Power Take-Off (PTO) with limited stroke length, translator and endstop, is modelled in large regular waves. This represents a level of complexity not previously attempted in CFD and the 6DOF float motion and load in the mooring compare well with experiments.

In conclusion, the computational tool developed here is capable of reliably predicting the behaviour of WEC systems during extreme wave events and, with some additional parameterisation, could be used to assess the survivability of WEC systems at full-scale before going to the expense of deployment at sea.

Acknowledgements

I would like to thank my supervisors: Professor Deborah Greaves, Dr Alison Raby and Dr Dave Simmonds, for their continued guidance, motivational messages and occasional sarcasm. It has been a pleasure working with you.

I would also like to acknowledge: Dr Joe Mellor for his ‘expert’ knowledge of ‘all-things-computer’, ~~Dr~~ Captain Martyn Hann for putting up with me being "annoying", Dr Colin "Jandal" Whittaker for not only listening but finding my constant stream of harebrained lunacy interesting and both Thomas Vyzikas and Scott Brown for numerous OpenFOAM® brain-melting sessions.

Finally, I'd like to thank my parents for not putting me down at 30, Dr Keri Collins for all those disapproving looks, Alastair Reynolds for making games-night a ‘challenge’ and both Peter Arber and Constantinos "Cos" Gitrowski for sharing the ‘Ultra-Gnarl’ with me.

This project has been funded by the Engineering and Physical Sciences Research Council (EPSRC) via the SuperGen UK Centre for Marine Energy Research (UKCMER) as part of the third phase in the consortium's programme of work (October 2011 - September 2016).

Edward Ransley

March 2015

Author's Declaration

At no time during the registration for the degree of Doctor of Philosophy has the author been registered for any other University award.

Work submitted for this research degree has not formed part of any other degree either at the University of Plymouth or at any other establishment.

An advanced doctoral training program supported by the SuperGen Marine UK Centre for Marine Energy Research was undertaken, which included workshops on tidal energy, wave energy, the marine environment, moorings and reliability.

Relevant scientific seminars and conferences were regularly attended at which work was often presented. As lead author, one paper has been accepted for publication in a refereed journal.

Signed: ____________________

Date: ____________________

Publications as lead author :

Ransley, E., Hann, M., Greaves, D., Raby, A. and Simmonds, D. (2013), 'Numerical and physical modelling of extreme waves at Wave Hub', *in* Conley, D.C., Masselink, G., Russell, P.E. and O'Hare, T.J. eds, *Journal of Coastal Research*, Special Issue 65, 1645-1650, ISSN 0749-0208.

Conference proceedings and poster presentations :

Göteman, M., Engström, J., Eriksson, M., Hann, M., **Ransley, E.**, Greaves, D., Leijon, M. (2015), 'Wave Loads on a Point-Absorbing Wave Energy Device in Extreme Wave', *in* Proceedings of the 25th International Offshore and Polar Engineering Conference, 21-26 June 2015, Kona, Hawaii Big Island, USA.

Ransley, E. (2014), 'Extreme Wave Impacts on a Mooring Buoy', Poster Presentation: SuperGen Marine Annual Assembly, 28 Nov. 2014, Edinburgh, UK.

Vyzikas, T., Greaves, D., Simmonds, D., **Ransley, E.**, Brown, S. (2013), 'Shape optimization of perforated caissons for wave energy harnessing', *in* Proc. of the 6th PanHellenic Conference of Marine Structures, 10-14 Nov. 2013, Athens, Greece.

Ransley, E. (2013), 'Extreme Wave Impacts on a Fixed Truncated Circular Cylinder', Poster Presentation: SuperGen Marine Annual Assembly, 27-28 Nov. 2013, Edinburgh, UK.

Vyzikas, T., **Ransley, E.**, Hann, M., Magagna, D., Greaves, D., Simmonds, D., Magar, V., Conley, D. (2013), 'Integrated Numerical Modelling System for Extreme Wave Events at the Wave Hub Site', *in* 'Proceedings of Institute of Civil Engineers (ICE) Coasts, Marine Structures and Breakwaters 2013: From Sea to Shore - Meeting the Challenges of the Sea', 18-20 September 2013, Edinburgh, UK.

Ransley, E., Hann, M., Greaves, D., Raby, A., Simmonds, D. (2013), 'Numerical and Physical Modelling of Extreme Wave Impacts on a Stationary Truncated Circular Cylinder', *in* Proceedings of the 10th European Wave and Tidal Energy Conference (EWTEC), 2-6 September 2013, Aalborg, Denmark.

Ransley, E. (2013), 'Numerical and physical modelling of extreme wave impacts on a fixed truncated circular cylinder', Poster Presentation: International Network for Offshore Renewable Energy Symposium, 12-18 May 2013, Pembrokeshire, UK.

Ransley, E. (2012), 'Validation tests of a wave generation toolbox for OpenFOAM CFD library', Poster Presentation: SuperGen Marine Annual Assembly, 29 October 2012, Plymouth, UK.

Word count for the main body of this thesis: 55,000

Contents

List of Figures

Abbreviations

6DOF Six Degrees Of Freedom.

ADV Acoustic Doppler Velocimeter.

AR Aspect Ratio.

BEM Boundary Element Method.

CAD Computer-Aided Design.

CDS Central Differencing Scheme.

CFD Computational Fluid Dynamics.

CFL Courant-Friedrichs-Lewy.

CICSAM Compressive Interface Capturing Scheme for Arbitrary Meshes.

CIP Constrained Interpolation Profile.

COAST Coastal, Ocean And Sediment Transport.

CoM Centre of Mass.

CV Control Volume.

DIC Diagonal Incomplete-Cholesky.

DILU Diagonal Incomplete-LU.

DNS Direct Numerical Simulation.

FDM Finite Difference Method.

FEM Finite Element Method.

FFT Fast Fourier Transform.

FPSO Floating Production Storage and Offloading.

FVM Finite Volume Method.

GAMG Geometric-Algebraic Multi-Grid.

GUI Graphical User Interface.

HPC High Powered Computing.

HRIC High Resolution Interface Capturing.

JONSWAP Joint North Sea Wave Observation Project.

KE Kinetic Energy.

LES Large Eddy Simulation.

LS Level Set.

MAC Marker And Cell.

MSE Mild Slope Equation.

MULES Multi-Dimensional Limiter for Explicit Solution.

MUSCL Monotonic Upstream-Centered Scheme for Conservation Laws.

NS Navier-Stokes.

NVA Normalised Variable Approach.

NVD Normalised Variable Diagram.

NWT Numerical Wave Tank.

O&G Oil and Gas.

PBiCG Preconditioned Bi-Conjugate Gradient.

PCG Preconditioned Conjugate Gradient.

PDE Partial Differential Equation.

PISO Pressure Implicit with Splitting of Operators.

PM Pierson-Moskowitz.

PTO Power Take-Off.

PWP Pelamis Wave Power.

RANS Reynolds-Averaged Navier-Stokes.

RBF Radial Basis Function.

RMS Root Mean Squared.

RNG Renormalised Group.

RZ Relaxation Zone.

SGS Sub-Grid-Scale.

SIMPLE Semi-Implicit for Pressure Link Equations.

SPH Smoothed Particle Hydrodynamics.

STL Stereo-Lithography.

SWL Still Water Level.

TLP Tension-Leg Platform.

TRL Technology Readiness Level.

TVD Total Variation Diminishing.

UDS Upwind Differencing Scheme.

UKCMER UK Centre for Marine Energy Research.

VOF Volume Of Fluid.

WEC Wave Energy Converter.

X-MED eXtreme loading of Marine Energy Devices due to waves, currents, flotsam and mammal impact.

Nomenclature

$\mathbf{A}$	Anchor position
$\mathbf{a}$	Acceleration of float (m s^{-2})
A	Area of control surface (m^{2})
a	Amplitude (m)
A_{cr}	Linear crest amplitude (m)
$\mathbf{a_{cm}}$	Inertia matrix (ms^{-2})
a_n	Amplitude of Fourier series coefficient n (m)
a_r	Acceleration of float in the direction of r (m s^{-2})
$\mathbf{B}$	Body forces (N)
B_i	Cartesian body force components (N)
C_α	Controls the intensity of the free surface compression
Co^0	Maximum local Courant number
$\mathrm{Co}_{\mathrm{max}}$	Prescribed maximum Courant number
Co	Courant number
Co_{P}	Courant number for a particular cell P
d	Water depth (m)
E	Wall roughness ($E = 9.8$ for smooth walls)
e	Internal energy (kg m^{2} s^{-2})
e	Spring extension from rest length (m)
f	Flux normal to cell face
f	Frequency (Hz)
F_ι	Mass flux across cell face ι
f_ι	Flux at centre of cell face ι

$\mathbf{F_N}$	Pressure force (normal to surface) (N)
$\mathbf{F_P}$	Viscous force (tangential to surface) (N)
f_p	Peak frequency (Hz)
$F_{restraint}$	Restraint force (N)
f_s	Sampling frequency (Hz)
$\mathbf{g}$	Vector acceleration due to gravity (0 0 -9.81 m s^{-2})
g	Acceleration due to gravity (9.81 m s^{-2})
H	Wave height (m)
h	Water depth (m)
H_s	Significant wave height (m)
$\mathbf{I}$	Inertia matrix (kg m^{-2})
i, j	Coordinate indices
K	Mean kinetic energy (J)
k	Turbulent kinetic energy (J)
k	Wave number (m^{-1})
$k(t)$	Instantaneous kinetic energy (J)
k_{es}	Endstop spring constant (N m^{-1})
k_n	Wave number of Fourier series coefficient n (m^{-1})
k_{spring}	Spring constant or stiffness (N m^{-1})
L	Charateristic length scale of a flow (m)
l_{es}	Endstop spring rest length (m)
m	Translator mass (kg)
m_0	Zeroth spectral moment
$\mathbf{n}$	Vector normal to control surface
N	Number of components

n	Fourier series coefficient
n_ι	Unit normal flux for cell face ι
n, s, e, w	Two-dimensional cell face labels
p	Pressure (Pa)
p	Static pressure ($\mathrm{kg\,m^{-1}\,s^{-2}}$)
p_0	Total pressure ($\mathrm{kg\,m^{-1}\,s^{-2}}$)
$p_{\rho gh}$	Modified mixture pressure ($\mathrm{kg\,m^{-1}\,s^{-2}}$)
p'	Pressure correction in SIMPLE algorithm
$\dot{q}_i$	Cartesian heat flux component ($\mathrm{W\,m^{-2}}$)
$\dot{\mathbf{q}}$	Heat flux vector ($\mathrm{W\,m^{-2}}$)
q	Arbitrary quantity being integrated in a volume-integral
q_P	Value of q at centre of cell P
Q_P	Arbitrary volume-integral solution for cell P
$\mathbf{R}$	Restraint attachment position
$\mathbf{r}$	Vector between $\mathbf{R}$ and $\mathbf{A}$ (m)
r	Magnitude of vector between $\mathbf{r}$ (m)
r_0	Magnitude of vector between $\mathbf{r}$ when the float is at rest (m)
Re	Reynolds number
Re_crit	Critical value of Re marking the onset of turbulence
S	Control surface
$S(f)$	Spectral density ($\mathrm{m^2s}$)
s_b	Distance between translator and floor at rest (m)
S_c	Solitary wave amplitude (m)
S_ϕ	Source term
$\mathbf{S}_\iota$	Outward-pointing face area vector ($\mathrm{m^2}$)

S_ι	Surface of cell face ι (m^2)
S'_{ij}	Mean of $s_{ij}(t)$ (s^{-1})
s'_{ij}	Fluctuating part of $s_{ij}(t)$ (s^{-1})
$s_{ij}(t)$	Rate of deformation of a fluid element in a turbulent flow (s^{-1})
$S_n(\omega)$	Spectral density of Fourier series coefficient n (m^{2}s)
S_{runup}	Maximum solitary wave run-up (m)
s_t	Distance between translator and endstop at rest (m)
S_u, S_p	Linearised source term coefficients
T	Wave period (s)
t	Time (s)
t_0	Initial time (s)
T_l	Local temperature (K)
t_n	Time $(n \times \delta t)$ after t_0 (s)
T_z	Zero up-crossing period (s)
$\bar{u}, \bar{v}$	Pseudo-velocities in SIMPLER algorithm
U	Charateristic velocity of a flow (m s^{-1})
u, v, w	Cartesian velocity components (m)
u_τ	Friction velocity (m s^{-1})
$u_{i,j}$	x component of velocity at a grid point with index (i,j) (m s^{-1})
u^+, ζ^+	Dimensionless groups used in turbulence modelling
$\mathbf{V}$	Vector velocity (m s^{-1})
V_x, V_y, V_z	Velocity components in x, y and z directions (m s^{-1}) (Wavestar case)
V	Volume (m^3)
V_P	Volume of cell P (m^3)
$\mathbf{V_r}$	Compression velocity - the vector of relative velocity between the two phases (m s^{-1})

$\mathbf{x}$	Position vector
x, y, z	Cartesian coordinates
x', y'	2D Cartesian coordinates in the frame of references of the Wavestar float
X_c	Linear displacement in Wavestar's hydraulic cylinder (m)
Y	Raw FFT output (m)
α	Average volume fraction for a CV
α_p	Under-relaxation of pressure correction in SIMPLE algorithm
α_{Ph}	Philips' constant
Γ	Diffusion coefficient
γ_R	Decay function in absorbing region
δ_{ij}	Kronecker delta ($\delta_{ij} = 1$ if $i = j$ and $\delta_{ij} = 0$ if $i \neq j$)
δl	Square-cell edge length (m)
δ_n	Stablising factor for nonuniform grids
$\Delta\omega_n$	Angular frequency increment of Fourier series coefficient n (rads^{-1})
δt	Time step (s)
δt^0	Previous time-step (s)
δt_{max}	Prescribed limit on the size of the time-step (s)
Δx	Distance between grid points in the x direction (m)
ε	The rate of dissipation of turbulent kinetic energy per unit mass (m^{2}s^{-3})
ζ	Coordinate distance normal to the wall (m)
ζ_{P}^{+}	Coordinate distance normal to the wall (m)
η_{cr}	Crest height (m)
ι	Individual cell face index
κ	Thermal conductivity (W m^{-1} K^{-1})
κ_{VK}	Von Karman's constant ($\kappa_{VK} = 0.41$)

λ	Wavelength (m)
λ_1, λ_2	Damping factors used to avoid time-step oscillations
λ_c	Curling factor - empirical value for the impact height of a breaking wave
λ_μ	Second viscosity coefficient (kg m^{-1} s^{-1})
μ	Molecular viscosity, or dynamic viscosity, (kg m^{-1} s^{-1})
μ_R	Relaxation coefficient in an RZ
μ_t	Eddy viscosity (kg m^{-1}s^{-1})
ν	Kinematic viscosity, μ/ρ, (m^{2}s^{-1})
ξ	Conservative face volume flux
ρ	Fluid density (kg m^{-3})
$\rho_\#$	Density of particular fluid phase (label #) (kg m^{-3})
τ_{ij}	Stress in the j-direction on a plane normal to the i-axis (N m^{-2})
τ_w	Local wall shear stress (N m^{-2})
$\bar{\phi}'$	Time-averaged version of ϕ'
Φ	Steady mean component of $\phi(t)$
ϕ	Arbitrary fluid property
$\tilde{\Phi}$	Density weighted version of Φ
$\phi'(t)$	Fluctuating component of $\phi(t)$ with zero mean value
ϕ_{computed}	Computed solution, in a RZ
ϕ_{target}	Target solution, in a RZ, prescribed by the boundary conditions
$\phi*$	Iteration value for variable ϕ in pressure-velocity coupling algorithm
$\phi***$	Correction value for variable ϕ in PISO algorithm
χ_R	Scaled x-coordinate in an RZ
ψ_B	Blending coefficient in OpenFOAM®'s Crank-Nicholson scheme
ω	Angular velocity (ms^{-1})

ω	Angular frequency (rads^{-1})
ω	Turbulence frequency (s^{-1})
ω_n	Angular frequency of Fourier series coefficient n (rads^{-1})
η	Surface elevation (m)
$\frac{\partial}{\partial t}$	Local derivative
$\frac{D}{Dt}$	Substantial derivative. The time rate of change following a moving fluid element
$\mathbf{V} \cdot \nabla$	Convective derivative

Chapter 1

Introduction

> *"The fuel in the earth will be exhausted in a thousand or more years, and its mineral wealth, but man will find substitutes for these in the winds, the waves, the sun's heat, and so forth"* - John Burroughs (1916)

The unequivocal warming of the climate system (IPCC 2007) and the steady rise in global energy demand, through population increase and economic growth in developing countries, are now major concerns for many of the world's governments. The ratification of the Kyoto protocol (1997) marked a step change in government attitudes towards CO_2-free energy sources. In many countries, the focus has now switched in favour of renewable energy sources to meet emissions targets, secure cost-effective energy supplies and prevent further anthropogenic interference with Earth's climate system (EU 2010). Until recently, in addition to onshore hydro-power, the search for economical, renewable and sustainable solutions to electricity production has been centred on wind, solar and biomass (Leijon et al. 2003).

Even though wave energy represents a renewable source with high power-density, relatively high utilisation factor and few negative impacts, extracting energy from ocean waves has been considered uneconomical due to a lack of good engineering solutions (Leijon et al. 2006; Henfridsson et al. 2007). It is clear, from the vast number of device concepts, that the wave energy industry is yet to reach maturity and converge on a single design like other renewable energy industries (*e.g.* wind or even tidal stream to some degree). If, however, economical and technical solutions were developed, the area would have a vast impact on the electricity production in the world (Leijon et al. 2003). Crucially, for countries with a significant resource (such as those in the North-East Atlantic), the emerging wave energy industry not only offers a secure and sustainable energy supply but the potential for lucrative economic development if a break-through were to be made.

One class of Wave Energy Converter (WEC), considered to have favourable characteristics by a number of developers, is the ‘point-absorber’ (Budar and Falnes 1975). These types of devices tend to be situated further offshore, where the wave energy is greatest, and typically consist of a float attached to the seabed via a mooring (Göteman et al. 2015; Engström et al. 2015). The relative motion between the float and mooring system is then used to convert wave energy into electricity via some Power Take-Off (PTO) arrangement. Although the performance of point-absorbers can be very poor without intelligent control strategies (due to practical limits on the size of the float) (Falcão 2010) their strength lies in their simplicity, making them cheaper and more resilient to the harsh conditions at sea.

Despite this, a history of international WEC and mooring failures demonstrates that considerable uncertainty exists around the prototype behaviour of fully coupled dynamic systems comprising WEC technologies and their moorings. For example, in 1995, Wavegen’s Osprey device suffered catastrophic structural damage when large waves broke open the giant ballast tanks during installation (Thorpe 1999); in 2007 the AquaBuOY 2.0, developed by Finavera Renewables, sank off the Oregon coast just before its planned removal date (Widman 2007); in 2009 Pelamis’ multi-million pound Aguacadora wave power project was scrapped after numerous technical problems off the Portuguese coast (Schwartz 2009); in 2010 the Oceanlinx device was ripped from its mooring during a huge swell 150 m off the West coast of Australia (Kraemer 2010); and early in 2014 a commercial-scale CETO 4 device was swept away by Cyclone Bejisa after the its mooring cable snapped (Parkinson 2014).

As the behaviour of these devices is dictated by a complex set of interactions between the structure, mooring systems and a large number of environmental factors (including wave, wind, current and bathymetry), predicting their response and standardising design criteria is extremely difficult. Research directly concerning WECs has focused primarily on optimising the response (Drew et al. 2009; Falcão 2010) and the majority of formal design guidance concentrates on the operational conditions of the device (The Carbon Trust 2005). However, this is not always the most critical factor, in a design context, as highlighted by the increasing number of device and mooring failures. Defined by the UK Energy Research Centre (2008) as *'the ability to survive predicted and surprise extremes in wind, wave and tidal current conditions, in any combination'*, *survivability* has now been identified as a key issue for the marine renewables industry, posing a significant challenge, requiring complementary development and underpinning research. Crucial to both the economic and environmental success of a WEC (EMEC 2009*a*), it is widely accepted that the current design procedures for the operational envelope must be complemented with a second level of design which considers the survival envelope (Haver and Anderson 2000; Faulkner 2000). Long-term reliability and failure rate estimates for WEC components have been attempted, but a lack of available data makes such analysis difficult (Thies et al. 2009). Whilst, short-term survivability assessments of complete WEC and mooring systems have yet to be completed with any rigor. Wave impact, green water and the episodic mooring loads experienced by WEC systems have received very little attention, with the exception of the conceptual criteria proposed by Pelamis Wave Power (PWP), who have been developing the Pelamis concept. PWP prioritise survival over power capture ensuring devices feature inherent load shedding and de-tuning capabilities in large waves (Yemm et al. 2000).

Many lessons can be learned from more established maritime activities and formal guidelines regularly refer to existing offshore design standards for mooring system analysis and environmental load assessment (The Carbon Trust 2005; Det Norske Veritas 2010). However, the wave energy industry is still in its infancy. Not only is it financially difficult to apply mature industry processes at this stage, but; there appears to be a preference, in the guidelines, to consider the advanced stages of a project, like installation, maintenance and decommissioning, whilst neglecting the crucial early development stages (The Carbon Trust 2005; EMEC 2009*a*). One of the main reasons for this is that the design of WECs will almost certainly be case specific, depending on conditions at a proposed deployment site, and a generic early-stage development strategy cannot be agreed upon. This is a difficult challenge to resolve but should be considered with urgent priority if the wave energy industry is to become economically viable (Cruz 2008). Research into wave loading on oil platforms (Morison et al. 1950), wind turbine foundations (Bredmose et al. 2006; Bredmose and Jacobsen 2010) and floating offshore structures like Floating Production Storage and Offloading (FPSO) units (Stansberg and Karlsen 2001; Faltinsen et al. 2002) provides a valuable insight into conditions at sea. However, unlike conventional offshore structures, WECs are designed to develop specific motions under wave loading. So, whilst a WEC's mooring system must constrain or withstand unwanted motions that may cause damage to the device, it must also be responsive to those motions which produce power. It is therefore unclear as to how much of the existing research is directly transferable to cases involving dynamically responsive WECs and essential that additional work is done to update the formal guidelines to reflect the differences between WECs and other offshore structures.

In terms of short-term survivability, it is the sometimes catastrophic impacts from abnormally large, 'freak' or 'rogue', waves which are of most concern to WEC developers. These 'extreme' waves, with amplitudes far exceeding the characteristic properties and operational conditions of a particular wave field, have received significant attention since 2000 after a few surprising offshore observations. There is now growing evidence that extreme waves will occur more frequently and cause more damage than previously predicted (Dysthe et al. 2009). However, current guidelines on the design and operation of wave energy converters fail to provide definitive guidance on how to prepare dynamic, coupled WEC and mooring systems for these discrete events (The Carbon Trust 2005; EMEC 2009*a*). Furthermore, there is still no consensus on the physical mechanism responsible for extreme waves or a standard definition for their shape or kinematics (Dysthe et al. 2009). As a consequence, these events have typically been reproduced via long-term, time domain simulations of extreme, irregular sea states restricting their analysis to physical experiments or numerical models with low CPU demand (EMEC 2009*b*). Historically the only deterministic representations of extreme waves have been produced using steep regular waves, saving time and improving the repeatability of tests, but there is now increasing evidence that this definition does not represent the true nature of large ocean waves and so alternatives have started to emerge (Tromans et al. 1991). Despite this, the specific wave group combinations responsible for the most severe loading conditions remain unclear and can, currently, only be found by testing a range of conditions (EMEC 2009*b*). Uncertainty over WEC survivability, caused by a lack of rigorous design guidelines, a poor understanding of device behaviour in extreme waves and ambiguity over the precise conditions responsible for the maximum load cases, represents an insurmountable risk to potential investors and contributes significantly to the industry's stagnation (UK Energy Research Centre 2008; SuperGen Marine 2011). If wave energy is to become an affordable part of the energy mix, potential design solutions require a greater understanding of the hydrodynamics and structural loading experienced during extreme events in order to mitigate the risk of device and mooring failure.

In order to promote the development of the wave energy industry, a number of parties have begun to suggest various 'roadmaps' outlining a proposed pathway for WECs from initial design concepts to commercialisation (UK Energy Research Centre 2008; Jeffery and Sedgwick 2011; Ruehl and Bull 2012). These stepwise development processes are typically related to Technology Readiness Levels (TRLs) (a commonly used metric to classify technologies based on development milestones), which provide a measure of the maturity of evolving technologies and are designed to ensure successful design optimisations, prototype deployments and, ultimately, full-scale commercial installations (Ruehl and Bull 2012). In the context of wave energy development, both physical and numerical modelling have become increasingly important in the assessment of a given concept before going to the expense of full-scale deployment at sea (Cruz 2008). It is widely accepted that this type of testing is crucial to assess wave loading, ensure devices behave as expected and mitigate against unexpected issues occurring throughout the project. A large test programme involving various levels of both physical and numerical modelling is, therefore, common for wave energy developers and this is reflected in TRLs 3, 4 and 5 (Ruehl and Bull 2012).

Physical modelling of wave structure interactions, using scale model WECs in a wave tank, has been widely used by developers to determine the frequency response of the device, assess its operational efficiency and optimise mooring systems. However, complicated experiments do not come without an associated cost in both terms of time and capital and scalability issues can make assessment of full-scale conditions difficult. Furthermore, data acquisition at the required resolution can be very difficult, or impossible, as some quantities (like the fluid velocity in the vicinity of a device) may be immeasurable without disturbing the flow itself or exponentially increasing the costs involved (Cruz 2008).

The continued increase in the performance-to-cost ratio of modern computers has meant that numerical models can now provide the quantitative description required for engineering analysis more cheaply and can simplify the processes of measurement and repeat testing (Cruz 2008). Furthermore, numerical experiments offer a means to interpret the fundamental phenomenological aspects of experimental conditions at full-scale that physical tests may not. As a result the ‘Review of model testing requirements for FPSO’s’ (BMT Fluid Mechanics Ltd 2001) (referred to in the ‘Guidelines on design and operation of wave energy converters’ (The Carbon Trust 2005) for issues related to wave structure model testing) states that optimisation of both the vessel and mooring system should typically now be performed on a computer, while physical model testing should be reserved for purposes of validation and design confirmation. This is supported by the TRLs which promote the use of linear frequency-domain models, like Morison’s load formula (Morison et al. 1950), and hydrodynamic inputs from potential flow solvers, like WAMIT (WAMIT Inc. 2015), to assess various concepts in TRL 3; recommend time-domain models, such as the commercial code ANSYS Aqwa (ANSYS, Inc. 2015) or mooring system design software Orcaflex (Orcina Ltd. 2015), to formulate a single, advance concept design in TRL 4, and; suggest fully nonlinear models for fluid-structure nonlinearities ‘if necessary’ and direct coupling between the various component models in TRL 5 (Ruehl and Bull 2012). Despite this, numerical simulations can be extremely time consuming without proper implementation and it is possible for a quantitatively incorrect solution to look reasonable. Without validation from physical tests, the consequences of accepting such a result may be severe (Ferziger and Perić 2002). Therefore, numerical models do not provide a substitute to physical experiments; the two form a pair of complementary development tools. However, in cases with highly nonlinear local effects (due to large variations in device geometry at the free surface) or strong nonlinear interactions between waves and structures, there is a lack of confidence in the predictive capability of numerical tools to provide extreme motions and loads on the hull, PTO, moorings and anchors. Furthermore, numerical tools capable of including all of the necessary physics for these cases tend to be extremely time-consuming. Survival tests are, therefore, considered to be a specialised experimental condition and physical tests are still preferred over numerical models when assessing the seaworthiness of a WEC (The Carbon Trust 2005; Ruehl and Bull 2012). Unfortunately, due to limitations on wave tank dimensions and a threshold on wave-maker capabilities, wave tank survival testing can typically only be performed at small scales (~1:50) when larger scales are highly recommended (Ruehl and Bull 2012; EMEC 2009*b*). Scale effects, therefore, result in a number of uncertainties surrounding extreme wave loading on full-scale WECs (Cruz 2008). If both the confidence in and the efficiency of fully nonlinear coupled numerical models could be increased, the design and survivability of full-scale WECs could be significantly enhanced.

Therefore, the aim of this project is to:

- develop a computational tool which can provide a reliable understanding of the behaviour of WEC systems under extreme wave loading.

To drive simulations of extreme waves, a fully nonlinear Computational Fluid Dynamics (CFD) approach has been used to model the free surface interaction with WEC hull forms. With an emphasis on moored point-absorber-type devices; a systematic, incremental development procedure has been implemented and validated against experimental data to assess the predictive capability of the tool at each stage of increasing complexity. The underlying objectives are to:

1. evaluate the existing numerical methods for wave-structure interaction problems and select an appropriate method for modelling extreme wave loading on moored WECs;
2. assess the relative importance and ease of implementation of elements involved in the development of a fully nonlinear Numerical Wave Tank (NWT);

3. assess the use of focused waves for the deterministic testing of WEC and mooring system survivability;
4. improve convergence between experimental measurement techniques and numerical modelling approaches and evaluate the ability of state-of-the-art NWT tools at increasing levels of complexity;
5. simulate entire, existing WEC systems including hull, mooring and PTO arrangement;
6. improve the understanding of the coupled behaviour of WECs and their moorings in extreme conditions and support guidance regarding the numerical modelling of WECs in cases involving extreme wave events;
7. identify the specific elements of present numerical techniques that require additional investigation and/or improvement.

In order to achieve these goals, an extensive program of research has been completed and documented in the following five chapters of this thesis. In Chapter 2 the many methods used to model numerically wave-structure interactions are briefly reviewed. Starting with an overview of the governing equations of fluid dynamics, the emphasis is placed on the conditions in which each technique and its corresponding simplifications are deemed appropriate. This process is crucial in identifying and selecting a preferred method with justification and introduces fundamental methodological elements referred to extensively throughout this work. The chosen method, CFD, is described in detail including a thorough discussion of the various options available for solving the equations and free surface behaviour required to meet the objectives of this work. Certain strategies and methods, involved in the solution process, are presented to provide a background knowledge of solution parameters discussed throughout this document. Based on an assessment of critical factors identified, the favoured software, OpenFOAM®, is then introduced and a brief description is given in terms of the elements discussed throughout the chapter.

In Chapter 3 the methodology for generic wave simulation in OpenFOAM® is described. The three stages of any CFD project (pre-processing, the solver and post-processing) are discussed and each element involved in the development of a so-called Numerical Wave Tank (NWT) is described. The various options, including the meshing parameters, boundary conditions, solution strategies and numerical schemes are discussed in the context of modelling extreme wave interactions with moored WECs. With the addition of some standard test cases for validation, Chapter 3 documents important information required to identify the parameters critical to achieving the specific needs of this project. The result is a basic methodology for the construction of a generalised NWT upon which specific additional elements can be added to accommodate the various applications considered in the subsequent chapters.

Chapter 4 outlines the threat posed by extreme waves and summarises the possible mechanisms responsible for their occurrence. This is followed by a discussion on essential water wave theory which culminates by introducing the notion of a ‘design wave’ to represent deterministic extreme wave events. In the remainder of the chapter, this concept is combined with the developments made earlier to demonstrate the ability of the NWT to reproduce physical experiments of extreme waves. The purpose of this is to ensure that this strategy and the numerical tool developed here is capable of reproducing the extreme environmental conditions required to assess the survivability of WEC and mooring systems. Only then can the additional complexity of a structure be introduced.

The main results from this work are collated and critically examined in Chapter 5. Here the NWT tool, developed in the preceding chapters, has been applied to a number of cases involving the interaction of extreme waves with various structures. In each of these applications, the results are compared with physical experiments and similar studies from the literature. Four cases are considered with the intention of presenting a step-wise increase in complexity from simple fixed structures to a fully-coupled WEC and mooring system. The motivation for this progression is to identify at which point, if any, the quality of the NWT tool begins to break down and where further improvements are required. In the first application, a fixed truncated circular cylinder is considered as a precursor to more complicated WEC structures with the advantage of having many similarities with more intensely studied offshore structures. The wave run-up and loading during an extreme event is measured and compared with both experimental results and those published in the literature. Following this, simulations of regular wave interactions with a 1:10 scale model of the Wavestar WEC are presented. These provide a range of results in the context of an existing wave energy device, where the motion is constrained to a single degree of freedom, thus providing the next step in the development of the NWT tool, allowing for freely moving structures to be modelled. Thirdly, a hemispherical-bottomed, cylindrical buoy with a linear spring mooring is simulated during an extreme wave event. In this application full Six Degrees Of Freedom (6DOF) motion and coupled mooring loads are compared with experimental measurements. This provides a test case at the very limit of state-of-the-art numerical modelling techniques. Finally, the Seabased wave energy generator is modelled at 1:20 scale including a single-point mooring and PTO system consisting of a damped, inline translator force, limited stroke length and end-stop spring. In doing so, the main goal of this project, to developing such a computational tool, has been achieved with the addition of functionality which is not currently available in the majority of alternative numerical models.

Lastly, in Chapter 6, the findings from this study are summarised and their implications on the survivability of moored WECs discussed along with a number of recommendations, potential improvements and proposed future work.

Chapter 2

Selecting an Appropriate Model

> *"If you want to model nature you must copy nature*
> *If you want to copy nature you must understand nature"* - Ib Arne Svendsen (2006).

Throughout history the behaviour of fluids has captivated philosophers and scientists alike. Not least of all, Leonardo Da Vinci who produced detailed descriptions of the movement of water, water waves and eddies, including the destructive force of water and the behaviour of floating bodies, long before the advent of modern hydrodynamics. Today, the science of fluid flow combines the sometimes spectacular flow visualisations of experimental studies, for which Da Vinci is famed, and the more fundamental, mathematical and theoretical description of fluid movement, to form a single discipline, ‘fluid mechanics’.

In most practical applications, fluids can be defined as substances in which the molecular structure does not resist external shear forces: even the slightest force causes a fluid particle to deform. The fluid is then regarded as a continuum described by macroscopic properties (e.g. velocity, pressure, density, temperature) which are average values over a suitable number of molecules. These properties must be known if one is to deduce the flow behaviour caused by external forces and determine relevant design factors for structures interacting with the fluid (Ferziger and Perić 2002).

Many phenomena affect fluid flow: temperature differences leading to heat transfer, density differences which give rise to buoyancy, differences in the concentration of solutes and phase changes, making the behaviour of fluids one of the most difficult subjects to replicate numerically (Anderson 1995). When simulating the complex flow structures in the vicinity of wave energy devices, it is vital we understand the strengths and limitations of the model used. This requires an understanding of the basic theory, the equations and the effect of features within those equations if one is to have any confidence in the results generated.

Therefore, in this chapter the governing equations of fluid dynamics are presented in their various forms. This is to introduce the various flow variables and the crucial terms, requiring special solution strategies, at a fundamental level. Following this, a summary of common simplifications to these equations and the scenarios in which they are deemed appropriate is given. This highlights the breadth of fluid mechanics applications and provides an assessment of available models allowing for a justified choice of equations for this project. Finally, the various options available for solving the chosen equations are discussed, so that basic methodological decisions can be made with support from the literature.

2.1 The Governing Equations of Fluid Dynamics

In many cases, numerical simulation can provide a valuable insight into the processes behind fluid flow phenomena and generate crucial data needed for informed design parameters. The purpose of fluid dynamics is to form a mathematical description of what is happening in nature. The physical characteristics of any fluid flow are governed by three fundamental principles which make up the conservation laws of physics:

1. The conservation of mass (or the continuity equation);
2. Newton's second law of motion, $F = ma$ (or the conservation of momentum); and
3. The conservation of energy (or the third law of thermodynamics).

These three principles can each be expressed in terms of basic mathematical equations which describe the behaviour of fluids in terms of flow properties such as velocity, pressure and density. These 'governing equations' are the physical foundations on which all fluid dynamics is based. In their most general form, the governing equations are made up of a set of integral or partial differential equations (Anderson 1995). Understanding the physical meaning and significance of these equations, and each of the terms in them, is crucial in analysing the results obtained by solving them.

2.1.1 Forms of the governing equations and the continuity equation

The governing equations appear in a number of different forms depending on the visualisation used when applying the fundamental physical principles listed above. Each form is subtly different, for example, the integral form allows for the presence of shock waves whereas the differential form assumes the flow properties are continuous. The combination of these different forms and a particular solver algorithm can mean the difference between success and instability in the solution (Anderson 1995).

In order to examine the different forms of the governing equations we will discuss the four possible flow models used to visualise a moving fluid, in the context of the first physical principle - the conservation of mass. This will result in the four different forms of the same equation (the continuity equation). However, this approach is not limited to the continuity equation, it can be used for both the momentum and energy equations as well.

Finite control volume fixed in space

Two of the flow models consider a closed volume within a finite region of the flow defining a Control Volume (CV), V, and a control surface, S. This allows us to limit our attention to the fluid flow inside and across the boundary of this finite region only.

In the first model this control volume is fixed in space with the fluid flowing through it (Figure 2.1). Then by applying the physical principle of mass conservation we know that the mass flow out of the control volume through the control surface must equal the time rate of decrease in mass inside the control volume. This leads to the following equation

$$\frac{\partial}{\partial t}\iiint\limits_{V} \rho \mathrm{d}V + \iint\limits_{S} \rho \mathbf{V}\cdot \mathrm{d}\mathbf{S} = 0 \tag{2.1}$$

where ρ is the fluid density, $\mathbf{V}$ is the vector velocity field and $\mathrm{d}\mathbf{S}$ is the normal component of the control surface, S. This is the continuity equation in integral form and in conservation (or divergence) form. The integral form comes directly from considering a finite control volume whereas the conservation aspect comes from considering the CV to be fixed in space.

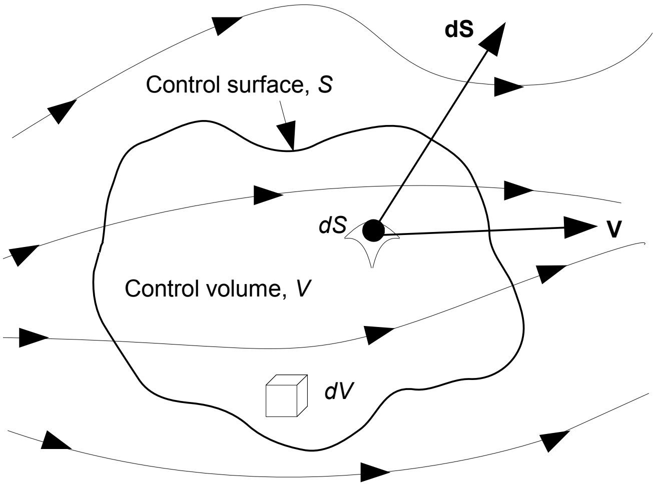

Figure 2.1: Finite control volume (CV) fixed in space with the fluid moving through it (Anderson 1995).

Finite control volume moving with the fluid

Alternatively the CV can be modelled to move with the fluid such that the same fluid particles are always inside. In this scenario the mass contained is fixed but the shape and volume of the CV can change. This model leads to the following equation

$$\frac{D}{Dt}\iiint_V \rho \mathrm{d}V = 0 \tag{2.2}$$

where $\frac{D}{Dt}$ is the *substantial derivative* which gives the time rate of change following a moving fluid element and is the sum of the local derivative, $\frac{\partial}{\partial t}$, and the convective derivative, $\mathbf{V}\cdot\nabla$. This is another form of the continuity equation in integral form (as we are still considering a finite CV) but now it is in non-conservation form due to the CV being in motion.

Infinitesimally small fluid element fixed in space

Alternatively, the fluid can be modelled by considering an infinitesimally small fluid element with differential volume, $\mathrm{d}V$, instead of a finite control volume (Figure 2.2). By fixing the fluid element in space (Figure 2.2a) the following equation is obtained when considering the conservation of mass

$$\frac{\partial \rho}{\partial t} + \nabla \cdot (\rho \mathbf{V}) = 0 \tag{2.3}$$

This is the continuity equation in conservation form (as the element is stationary) but this time the equation is in Partial Differential Equation (PDE) form as we have only considered an infinitesimally small element of the fluid.

Infinitesimally small fluid element moving with the fluid

Finally we can allow the infinitesimal fluid element to move along a streamline with velocity vector, $\mathbf{V}$, equal to the flow velocity at each point (Figure 2.2b). This flow model gives

$$\frac{D\rho}{Dt} + \rho \nabla \cdot \mathbf{V} = 0 \tag{2.4}$$

which is the continuity equation in PDE form and non-conservation form.

All of these equations are different forms of the same equation - the continuity equation, and can be shown to be equivalent through mathematical transformation. For a full derivation of these equations and the manipulation required to show them to be equivalent see Anderson (1995).

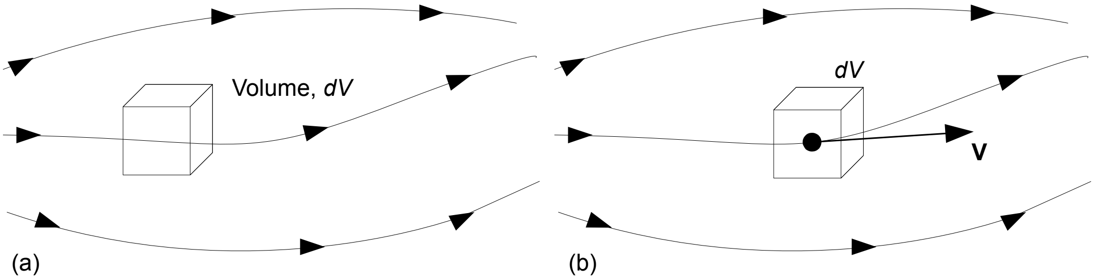

Figure 2.2: Infinitesimal fluid element: (a) fixed in space with the fluid flowing through it; (b) moving along a streamline with with velocity, **V**, equal to the local velocity (Anderson 1995).

2.1.2 The momentum equation

The second physical principle from which the governing equations are derived, is the conservation of momentum (or Newton's second law of motion), whereby the rate of change of momentum of a fluid particle is equal to the sum of the forces acting on it ($\mathbf{F} = m\mathbf{a}$). This is a vector relation which (when working in the Cartesian frame of reference) can be split into three scalar relations along the x, y and z axes generating the three equations known as the Navier-Stokes (NS) equations.

There are two sources of force in fluid dynamics:

1. *body forces* which act directly or "at a distance" on the volumetric mass of the fluid (e.g. gravity); and
2. *surface forces* which are imposed by the fluid outside an element and act directly on its surface. Surface forces can be due to:
    (a) the pressure distribution surrounding the element; or
    (b) the shear and normal stress distribution due to friction.

The x, y and z components of the momentum equation (or the Navier-Stokes equations) in PDE and conservation form are

$$\frac{\partial(\rho u)}{\partial t} + \nabla \cdot (\rho u \mathbf{V}) = \frac{\partial p}{\partial x} + \frac{\partial \tau_{xx}}{\partial x} + \frac{\partial \tau_{yx}}{\partial y} + \frac{\partial \tau_{zx}}{\partial z} + \rho B_x \tag{2.5}$$

$$\frac{\partial(\rho v)}{\partial t} + \nabla \cdot (\rho v \mathbf{V}) = \frac{\partial p}{\partial y} + \frac{\partial \tau_{xy}}{\partial x} + \frac{\partial \tau_{yy}}{\partial y} + \frac{\partial \tau_{zy}}{\partial z} + \rho B_y \tag{2.6}$$

$$\frac{\partial(\rho w)}{\partial t} + \nabla \cdot (\rho w \mathbf{V}) = \frac{\partial p}{\partial z} + \frac{\partial \tau_{xz}}{\partial x} + \frac{\partial \tau_{yz}}{\partial y} + \frac{\partial \tau_{zz}}{\partial z} + \rho B_z \tag{2.7}$$

where τ_{ij} is the stress in the j-direction on a plane normal to the i-axis, p is the pressure, u, v, and w, are the velocity components in the x, y and z directions respectively and B_i are the body force components. For a full derivation of these equations see Anderson (1995).

In the majority of offshore and coastal fluid dynamics problems, the fluid is assumed to be isotropic and Newtonian meaning the shear stress in the fluid is proportional to rate of strain (i.e. the velocity gradients). Stokes obtained the following relationships for Newtonian fluids known as the *constitutive equations*

$$\begin{aligned} \tau_{xx} &= \lambda_\mu(\nabla\cdot\mathbf{V}) + 2\mu\frac{\partial u}{\partial x} \qquad \tau_{yy} = \lambda_\mu(\nabla\cdot\mathbf{V}) + 2\mu\frac{\partial v}{\partial y} \qquad \tau_{zz} = \lambda_\mu(\nabla\cdot\mathbf{V}) + 2\mu\frac{\partial w}{\partial z} \\ \tau_{xy} &= \tau_{yx} = \mu\left(\frac{\partial u}{\partial y} + \frac{\partial v}{\partial x}\right) \quad \tau_{yz} = \tau_{zy} = \mu\left(\frac{\partial v}{\partial z} + \frac{\partial w}{\partial y}\right) \quad \tau_{zx} = \tau_{xz} = \mu\left(\frac{\partial w}{\partial x} + \frac{\partial u}{\partial z}\right) \end{aligned} \tag{2.8}$$

where the two constants are the molecular viscosity coefficient (or dynamic viscosity), μ, which relates stresses to linear deformations and the second viscosity coefficient, λ_μ, which relates stresses to volumetric deformation (Anderson 1995). Very little is known about the second viscosity coefficient, λ_μ, because, in practice, its effect is small. For liquids, which are incompressible, $\nabla\cdot\mathbf{V} = 0$ and the viscous stresses reduce to the dynamic viscosity times twice the local rate of linear deformation (Versteeg and Malalasekera 2007). The momentum equations for a Newtonian, viscous flow, in conservation form, are then

$$\begin{aligned} &\frac{\partial(\rho u)}{\partial t} + \frac{\partial(\rho u^2)}{\partial x} + \frac{\partial(\rho uv)}{\partial y} + \frac{\partial(\rho uw)}{\partial z} \\ &\quad = -\frac{\partial p}{\partial x} + \frac{\partial}{\partial x}\left(\lambda_\mu\nabla\cdot\mathbf{V} + 2\mu\frac{\partial u}{\partial x}\right) + \frac{\partial}{\partial y}\left[\mu\left(\frac{\partial v}{\partial x} + \frac{\partial u}{\partial y}\right)\right] \\ &\qquad + \frac{\partial}{\partial z}\left[\mu\left(\frac{\partial w}{\partial y} + \frac{\partial v}{\partial z}\right)\right] + \rho B_x \end{aligned} \tag{2.9}$$

$$\begin{aligned} &\frac{\partial(\rho v)}{\partial t} + \frac{\partial(\rho uv)}{\partial x} + \frac{\partial(\rho v^2)}{\partial y} + \frac{\partial(\rho vw)}{\partial z} \\ &\quad = -\frac{\partial p}{\partial y} + \frac{\partial}{\partial y}\left(\lambda_\mu\nabla\cdot\mathbf{V} + 2\mu\frac{\partial v}{\partial y}\right) + \frac{\partial}{\partial x}\left[\mu\left(\frac{\partial v}{\partial x} + \frac{\partial u}{\partial y}\right)\right] \\ &\qquad + \frac{\partial}{\partial z}\left[\mu\left(\frac{\partial w}{\partial y} + \frac{\partial v}{\partial z}\right)\right] + \rho B_y \end{aligned} \tag{2.10}$$

$$
\begin{aligned}
\frac{\partial(\rho w)}{\partial t}+\frac{\partial(\rho u w)}{\partial x}+\frac{\partial(\rho v w)}{\partial y}+\frac{\partial(\rho w^2)}{\partial z}
&= -\frac{\partial p}{\partial z}+\frac{\partial}{\partial z}\left(\lambda_\mu \nabla\cdot\mathbf{V}+2\mu\frac{\partial w}{\partial z}\right)+\frac{\partial}{\partial x}\left[\mu\left(\frac{\partial u}{\partial z}+\frac{\partial w}{\partial x}\right)\right]\\
&\quad+\frac{\partial}{\partial y}\left[\mu\left(\frac{\partial w}{\partial y}+\frac{\partial v}{\partial z}\right)\right]+\rho B_z
\end{aligned}
\tag{2.11}
$$

2.1.3 The energy equation

The final, fundamental physical principle needed to generate the complete set of governing equations for fluid flow is the conservation of energy (or the first law of thermodynamics). This law states that the rate of change of energy inside a fluid element is equal to the net flux of heat entering the element (through volumetric heating or heat transfer due to temperature gradients) plus the rate of work done on the element due to body and surface forces.

The energy inside the fluid element can be expressed in terms of a number of different energy forms (*e.g.* that associated with random molecular motion - the internal energy, e, or; with translational motion - the Kinetic Energy (KE)). The PDE and conservation form of the energy equation (written in terms of the total energy , $e+\frac{|\mathbf{V}|^2}{2}$) is then

$$
\begin{aligned}
&\frac{\partial}{\partial t}\left[\rho\left(e+\frac{|\mathbf{V}|^2}{2}\right)\right]+\nabla\cdot\left[\rho\left(e+\frac{|\mathbf{V}|^2}{2}\right)\mathbf{V}\right]\\
&\quad=\rho\dot{\mathbf{q}}+\frac{\partial}{\partial x}\left(\kappa\frac{\partial T_l}{\partial x}\right)+\frac{\partial}{\partial y}\left(\kappa\frac{\partial T_l}{\partial y}\right)+\frac{\partial}{\partial z}\left(\kappa\frac{\partial T_l}{\partial z}\right)-\frac{\partial(up)}{\partial y}-\frac{\partial(vp)}{\partial y}\\
&\quad-\frac{\partial(wp)}{\partial z}+\frac{\partial(u\tau_{xx})}{\partial x}+\frac{\partial(u\tau_{yx})}{\partial y}+\frac{\partial(u\tau_{zx})}{\partial z}+\frac{\partial(v\tau_{xy})}{\partial x}+\frac{\partial(v\tau_{yy})}{\partial y}\\
&\quad+\frac{\partial(v\tau_{zy})}{\partial z}+\frac{\partial(w\tau_{xz})}{\partial x}+\frac{\partial(w\tau_{yz})}{\partial y}+\frac{\partial(w\tau_{zz})}{\partial z}+\rho\mathbf{B}\cdot\mathbf{V}
\end{aligned}
\tag{2.12}
$$

where $\dot{\mathbf{q}}(\dot{q}_x,\dot{q}_y,\dot{q}_z)$ is the heat flux vector and by Fourier's Law of heat conduction relates the heat flux to the local temperature gradient using the thermal conductivity, κ, giving:

$$
q_x=-\kappa\frac{\partial T_l}{\partial x}\quad q_y=-\kappa\frac{\partial T_l}{\partial y}\quad q_z=-\kappa\frac{\partial T_l}{\partial z}\quad\text{or}\quad \mathbf{q}=-\kappa\nabla T_l \tag{2.13}
$$

Once again, for a full derivation of the energy equation see Anderson (1995).

2.1.4 The "complete" Navier-Stokes equations

In the previous sections, we have introduced the equations on which all of theoretical and computational fluid dynamics is based. The continuity equation, momentum equation and energy equation form a coupled system of nonlinear PDEs collectively known as the 'complete Navier-Stokes Equations' expanding the name to refer to the complete system of governing equations. These equations apply to a viscous flow including the dissipative transport phenomena of friction and thermal conduction. Mass diffusion, which arises due to gradients in concentration of different chemical species, has not been included here. Furthermore, effects due to surface tension, resulting from the interface between fluids, have not been included as they are assumed to be negligible at the wave periods and water depths considered in this work (Hughes 1993).

The NS equations, stated above, share a number of commonalities. Typically, it is convenient to rewrite these equations in the form of a generalised transport equation for an arbitrary scalar fluid property, ϕ, which could be, for example, a velocity component, the temperature or the concentration of a transported substance etc. The generalised transport equation, in PDE and conservation form, is then

$$\frac{\partial(\rho\phi)}{\partial t} + \nabla\cdot(\rho\phi\mathbf{V}) = \nabla\cdot(\Gamma\nabla\phi) + S_\phi, \tag{2.14}$$

where Γ is the diffusion coefficient and S_ϕ is the source term which contains all of the terms which are not shared between the equations. The first term in Equation 2.14 is called the *transient term* and describes the rate of change in the amount of ϕ in the fluid element. The second term is the *convective term* which signifies the net rate of decrease of ϕ due to convection. The first term on the right hand side of Equation 2.14 is the *diffusive term* which represents the net rate of increase in ϕ due to diffusion and the final term, the *source term*, describes the rate of increase in ϕ due to sources inside the fluid element (Versteeg and Malalasekera 2007).

Alternatively, when integrating over a CV and by applying Gauss's divergence theorem, Equation 2.14 becomes

$$\frac{\partial}{\partial t}\left(\int_{CV} \rho\phi dV\right) + \int_{A} \mathbf{n}\cdot(\rho\phi\mathbf{V})dA = \int_{A} \mathbf{n}\cdot(\Gamma\nabla\phi)dA + \int_{CV} S_{\phi}dV, \tag{2.15}$$

which is the generalised transport equation in conservation and integral form, where $\mathbf{n}$ is the vector normal to the surface element dA (Versteeg and Malalasekera 2007).

This set of nonlinear integral or partial differential equations form the basis upon which all numerical methods, for the calculation of unknown flow properties, are built. However, these equations have yet to be solved in their entirety and so the purpose of these numerical methods is to generate a meaningful output by applying acceptable simplifications to the equations. What constitutes ‘acceptable’ in terms of a simplification depends entirely on the scenario in which the model is being run.

2.2 Simplifications of the Governing Equations

The system of equations introduced in the previous section is more complex than it appears. In general, it is very difficult to solve due to the nonlinear nature of the convective term in the momentum equations, $\nabla\cdot(\rho\phi\mathbf{V})$, which describes the time-independent, ‘convective’ acceleration of the fluid with respect to position, *i.e.* the transport of velocity by itself. It is widely accepted that the generalised NS equations describe the flow of a Newtonian fluid accurately (Ferziger and Perić 2002). However, existing mathematical tools have only been able to solve these equations analytically for a small number of cases, with limited practical relevance. Various attempts have been made to discretise the NS equations into a set of algebraic equations, which can be solved numerically using a computer, and modern CFD codes (discussed further in Section 2.3) have become increasingly sophisticated. Furthermore, there now exist Direct Numerical Simulation (DNS) solvers capable of solving the full NS equations numerically, without simplification, provided that all temporal and spatial scales of turbulence are resolved within the discretisation. Despite these advances, the numerical modelling of complex geometries and flow configurations has become common practice in engineering science and the demand on computational and human resources to interpret them has increased considerably. Therefore, the use of simplified equations is still justified by the significant reduction in computing effort required to solve them.

Additional equations can be generated by making appropriate assumptions and some terms, considered to be unimportant, can be neglected. This simplification inevitably introduces an associated error, and, in most cases, even the simplified equations cannot be solved analytically (Ferziger and Perić 2002). Furthermore, "no model/equation is more accurate than the underlying assumptions or approximations" (Svendsen 2006) and so, the responsible application of these equations requires great care to monitor the physical implications of any approximations that are made.

In many applications, including the flow of liquids (whose compressibility is negligible), the fluid density can be assumed constant. Such flows are called *incompressible* flows and there is no linkage between the mass and momentum equations and the energy equation. If the flow is *isothermal*, *i.e.* constant temperature, the viscosity is also constant. Then the problem can often be solved by considering conservation of mass and momentum only, with the addition of some pressure-velocity coupling strategy (discussed further in 2.3.2).

In fluid flow far from solid surfaces, the dissipative effects of viscosity, mass diffusion and thermal conductivity are typically ignored. This is known as *inviscid* flow and the NS equations reduce to the *Euler equations* which are often used to study compressible flows at high *Mach numbers*. The Euler equations can be obtained from the complete NS equations in Section 2.1 by simply dropping the friction and thermal conductivity terms. Equation 2.14 then becomes

$$\frac{\partial(\rho\phi)}{\partial t}+\nabla\cdot(\rho\phi\mathbf{V})=S_{\phi}. \tag{2.16}$$

Despite this significant simplification, the Euler equations still cannot be solved analytically.

Potential flow models, one of the simplest and most widely used models, assume inviscid flow with the additional constraint that the flow is *irrotational*, *i.e.* there is no vorticity and the curl of the flow is equal to zero. Potential flows can then be described by the *scalar Laplace equation*, the solutions to which are harmonic functions, or potential functions, described by their singularities and boundary conditions (such as Dirichlet boundary conditions or Neumann boundary conditions). These functions are extremely useful in fluid dynamics, allowing the three-component velocity vector field to reduce to a single-component scalar function, the *velocity potential*, the gradient of which returns the velocity vector. For incompressible flow, the continuity equation then becomes *Laplace's equation*

$$\nabla^2 \phi = 0, \tag{2.17}$$

and the momentum equations can be integrated to give the *Bernoulli equation*, the solution of which can be found analytically once the velocity potential is known (Ferziger and Perić 2002). Potential flow models are used frequently in coastal and ocean engineering, however, due to the assumptions made, these models are not capable of describing breaking waves or wave-structure interactions where viscosity and turbulence become important.

When the horizontal length scale is much greater than the vertical length scale, *i.e.* the vertical velocity of the fluid is small, the incompressible NS equations can be depth-integrated to give the *shallow water equations*. This process, however, means that shallow water equation models cannot describe any parameter that varies with height and so the frequency dispersion of waves, *i.e.* the dependence of a wave's phase speed on its wavelength, is not accounted for. This limitation typically restricts these models to large scales like oceanic modelling and the simulation of Coriolis forces in the atmosphere (Holthuijsen 2007).

For water waves which propagate over bathymetry, when the effects of diffraction and refraction are important, the *Mild Slope Equation* (MSE) can be derived from potential flow theory using linear wave theory. The MSE is regularly used in coastal engineering to simulate the evolution of wave-fields near coasts and harbours. However, it is not capable of describing nonlinear effects like wave-current interaction or energy dissipation due to viscosity directly. Modified versions of the MSE have been developed to include the effects of more complex phenomena, but these methods are still typically reserved for kilometre-scale wave models (Lin 2008).

For flows, accompanied by heat transfer, where the density variation is not too large, one can treat the density as only variable in the gravitational term. This is the *Boussinesq approximation* for buoyancy-driven flow. In terms of water waves, the ‘Boussinesq approximation’ is also used to describe a process by which the vertical coordinate is removed from the flow equations whilst retaining some influence from the flow structure vertically beneath water waves. This allows for the inclusion of frequency dispersion and so Boussinesq-type equations are widely used in coastal engineering to describe the behaviour of water waves in shallow seas and harbours. However, being depth-averaged these models do not resolve the turbulence distribution or allow for the evaluation of the forces on structures due to overturning (Jacobsen et al. 2012).

When the flow is dominated by viscous, pressure and body forces, *i.e.* at low flow speeds, high viscosity or very small length scales, when the *Reynolds number* (Re) is small, it is said to be *creeping flow* and the convective term in the NS equations can be neglected. For constant fluid properties, the momentum equations become the *linear Stokes equations*.

When there is a dominant flow direction and the geometry varies only gradually, the flow is mostly influenced by upstream events. The flow is then called a *boundary layer flow* and the NS equations can be simplified to give the *boundary layer equations*.

For many more complex flows including turbulence, combustion and multiphase flow, semi-empirical models are regularly used to represent these phenomena as an exact mathematical description is difficult to describe, let alone solve.

When the flow is dominated by inertial forces, *i.e.*, at high Reynolds numbers, it is characterised by chaotic eddies, vortices and other instabilities, collectively known as *turbulence*. Due to the unfeasibly fine meshes required for Direct Numerical Simulation of all the different mixing-length scales, a popular simplification to the NS equations, when considering turbulent flow, is ‘Reynolds decomposition’. This yields the Reynolds-Averaged Navier-Stokes (RANS) equations which allow the effect of turbulence to be included in flow models by taking time averages of the velocity terms in the NS equations. Reynolds decomposition defines each flow variable, ϕ, as $\phi(t) = \Phi + \phi'(t)$, where Φ is the steady mean component and $\phi'(t)$ is a fluctuating component with zero mean value. The generalised time-averaged transport equation is then,

$$\frac{\partial(\bar{\rho}\tilde{\Phi})}{\partial t}+\nabla\cdot(\bar{\rho}\tilde{\Phi}\tilde{\mathbf{V}})=\nabla\cdot(\Gamma_{\Phi}\nabla\tilde{\Phi})+\left[-\frac{\partial(\overline{\rho u'\phi'})}{\partial x}-\frac{\partial(\overline{\rho v'\phi'})}{\partial y}-\frac{\partial(\overline{\rho w'\phi'})}{\partial z}\right]+S_{\Phi}, \quad (2.18)$$

where an overbar symbolises the time-average of the variable and a tilde indicates a density-weighted variable (Versteeg and Malalasekera 2007). For incompressible fluids, the density is constant and we get

$$\frac{\partial\Phi}{\partial t}+\nabla\cdot(\Phi\mathbf{V})=\frac{1}{\rho}\nabla\cdot(\Gamma_{\Phi}\nabla\Phi)+\left[-\frac{\partial(\overline{u'\phi'})}{\partial x}-\frac{\partial(\overline{v'\phi'})}{\partial y}-\frac{\partial(\overline{w'\phi'})}{\partial z}\right]+S_{\Phi}, \quad (2.19)$$

which is the generalised form of the RANS equations for incompressible flow. By comparing Equation 2.19 with Equation 2.14, it can be seen that time-averaging has introduced a set of additional unknowns $\overline{u'\phi'}$, $\overline{v'\phi'}$ and $\overline{w'\phi'}$. When considering the momentum equations (*i.e.*, $\phi'=u',v'$ or w') these unknowns represent additional turbulent stresses called the *Reynolds stresses*. Turbulence modelling, to predict the value of these terms and close the RANS equations, is typically accomplished empirically or through detailed time-dependent simulations, alleviating the need for high resolution DNS and greatly improving the computational efficiency of simulations.

An alternative to the RANS equations is Large Eddy Simulation (LES), which applies a model to the smallest scales of the flow field allowing the larger, more problem-dependent, scales to be resolved fully within the time-dependent simulation. Rather than time-averaging the equations, LES applies a spatial filter function and a cut-off width to separate large eddies from smaller eddies. This process leads to a set of governing equations containing filtered flow variables and additional Sub-Grid-Scale (SGS) stress terms which must be described using a SGS model in a similar way to RANS turbulence modelling. LES is generally more computationally expensive than RANS, but produces more accurate results due to the explicit calculation of the larger turbulent structures.

In this project turbulent cases are considered using Reynolds decomposition only. Turbulence modelling and various closure equations are discussed further in Section 3.1.6.

2.3 Computational Fluid Dynamics (CFD)

Computational fluid dynamics (CFD) is the analysis of fluid systems by means of computer-based simulation. In general, a number of terms in the governing equations, such as derivatives, cannot be solved using computer algebra. For these terms a numeric approximation is found using an algorithm or an assigned numerical scheme. In a CFD analysis the integrals or partial derivatives in the governing equations are replaced with discretised algebraic forms which can be solved numerically to find the flow field variables at discrete points in space and time. CFD complements pure theory and pure experiment by offering a third approach to help interpret and understand fluid flow behaviour. CFD attempts to replicate, or predict, real fluid flow in a virtual environment and is becoming a strong and valuable design tool in the development of offshore structures.

Most CFD codes contain three main elements:

1. the *pre-processor*, which includes the input of problem parameters, the definitions of fluid properties and the description of the computational domain geometry, grid generation and boundary conditions;

2. the *solver*, which takes the appropriate mathematical model and uses one of a number of discretisation techniques to solve for the flow field values; and

3. the *post-processor*, which then offers various data visualisation tools and outputs.

Within each element, numerous schemes have been developed to improve the quality and efficiency of CFD simulations but the end product remains a collection of numbers and it is the responsibility of the user to be aware of the assumptions made during the process. The non-trivial goal of a convergent solution comes with experience and a full consideration of the stability and accuracy of the numerical method used. Only through comparison with experimental or theoretical work can the validity of CFD solutions be assured.

2.3.1 Discretisation methods

Once a suitable mathematical model for the target application, *i.e.* incompressible, inviscid, turbulent, 3D or 2D etc., has been chosen, the next important component of the numerical solution is the choice of discretisation method. As mentioned above, CFD relies on the approximation of continuous functions in the governing equations (integral or Partial Differential Equation) by a system of discrete algebraic forms. These equations can then be solved computationally using either an iterative method or a fully coupled solver (Ferziger and Perić 2002; Westphalen 2010). For CFD applications the governing equations are typically discretised in both time and space. In this section we will be considering spatial discretisation only. Temporal discretisation will be described in Section 3.2.1. There are many approaches to discretise the equations, the most common of which are briefly discussed below. Each method produces the same solution provided the resolution is sufficiently fine, but some methods are better suited to particular classes of problems than others. The ultimate goal of any scheme is to achieve the desired accuracy whilst minimising the computational effort required.

Typically, the most complex methods (used to study the most complex flow behaviour) are mesh techniques, such as the finite difference (FDM), finite volume (FVM) and finite element (FEM) methods, which use a grid of nodes and cells to spatially subdivide the domain. Here the discrete algebraic forms are then expressed strictly in terms of the flow variables at two or more discrete grid points.

More recent developments include meshless, Lagrangian methods such as Smoothed Particle Hydrodynamics (SPH) where the coordinate system moves with the fluid particles (Monaghan 2005). These methods exhibit a number of advantages over mesh-based methods including: the ability to handle very large deformations, commonly seen in high energy phenomena like explosions, and; keeping a record of the time history of material particles, which is especially useful in bio- and nano- engineering. However, these methods have shown stability and accuracy problems requiring further development (Liu and Liu 2010) and their performance when turbulent flow is present or when dealing with complex boundary conditions is questionable (Qiu 2008). Furthermore, SPH remains computationally expensive in 3D and the statistical approach of kernal estimation gives no clear relationship between the particle properties and the governing equations of fluid dynamics discussed above (Liu and Liu 2010). Therefore, despite the advantages, these methods will not be considered further here.

The *Finite Difference Method* (FDM) was one of the first methods developed to solve PDEs. Starting with the governing equations in partial differential and conservation form, the differential terms are replaced by a truncated Taylor series expansion or polynomial fitting to the first or second order in terms of nodal values at each grid point. The result is a single algebraic equation at each node with the flow field variable at that location and a specific number of neighbouring locations as unknowns. For example, consider the two-dimensional structured grid in Figure 2.3, if $u_{i,j}$ is the x component of velocity at a grid point P, with index (i,j), then $u_{i+1,j}$ (the x-velocity at $(i+1,j)$) can be given as the Taylor series expansion

$$u_{i+1,j} = u_{i,j} + \left(\frac{\partial u}{\partial x}\right)_{i,j} \Delta x + \left(\frac{\partial^2 u}{\partial x^2}\right)_{i,j} \frac{(\Delta x)^2}{2} + + \left(\frac{\partial^3 u}{\partial x^3}\right)_{i,j} \frac{(\Delta x)^3}{6} + \cdots \tag{2.20}$$

Solving Equation 2.20 for $(\partial u/\partial x)_{i,j}$ gives

$$\left(\frac{\partial u}{\partial x}\right)_{i,j} = \frac{u_{i+1,j} - u_{i,j}}{\Delta x} - \left(\frac{\partial^2 u}{\partial x^2}\right)_{i,j} \frac{\Delta x}{2} - \left(\frac{\partial^3 u}{\partial x^3}\right)_{i,j} \frac{(\Delta x)^2}{6} + \cdots \tag{2.21}$$

The first term on the right-hand-side gives the finite-difference representation, or quotient, of $(\partial u/\partial x)_{i,j}$ while the remaining terms constitute the *truncation error*. In this case the finite-difference quotient is said to be *first-order accurate* as the lowest order term in the truncation error includes Δx to the first order. Furthermore, because the Taylor expansion in Equation 2.20 is for the grid point to the right of point (i,j), the finite-difference quotient in this case is known as a *forward difference*. If, alternatively, Equation 2.20 considered $u_{i-1,j}$ the finite-difference would be a *backward difference*. This is also first-order accurate. Typically, higher-order accuracy is desired, but, these representations, like the *central difference* quotient which is second-order accurate, require more grid points and so greater computing

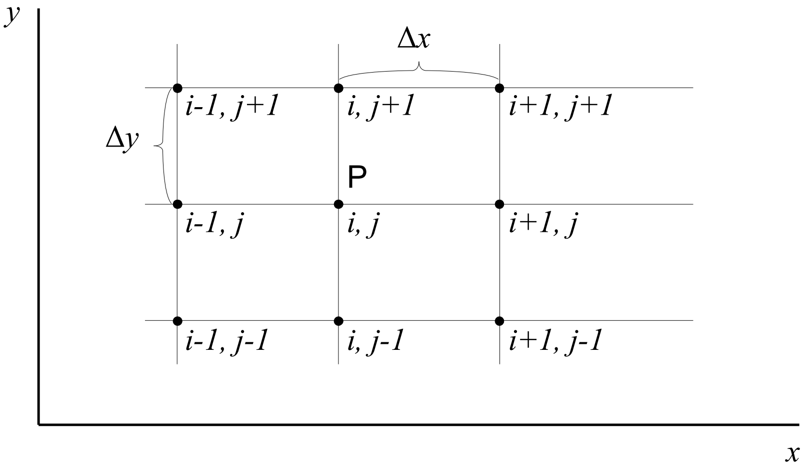

Figure 2.3: Two-dimensional uniform structured grid (reproduced from Anderson (1995)).

effort. However, often an improved accuracy can be obtained using a higher-order scheme with a reduced number of total grid points (Anderson 1995). For a more thorough description of the various differencing schemes, polynomial fitting and a treatment of second derivatives see Ferziger and Perić (2002) or Anderson (1995).

The advantage of the FDM is that it is conceptually simple, easily programmed and effective on structured (or regular) grids, the simplest type of grid structure. The disadvantage of the FDM is that conservation is not enforced and the method is typically restricted to simple geometries (Ferziger and Perić 2002).

In the *Finite Volume Method* (FVM) the numerical grid defines the boundaries of a finite number of contiguous Control Volumes (CVs), rather than the computational nodes (as in the FDM). In the most common example, where the flow variables are 'co-located' at computational nodes, the nodes can be placed either: at the centre of these CVs (Figure 2.4a); or such that the faces of the CVs lie midway between the nodes (Figure 2.4b). The mean over the CV is given to a higher accuracy by the nodal values in the first approach but the derivatives at CV faces can be given more accurate when using the second approach. Alternatives to this 'cell-centred' approach include: vertex-centred (Khalil and Wesseling 1992) and face-centred methods, but these will not be considered further here. Furthermore,

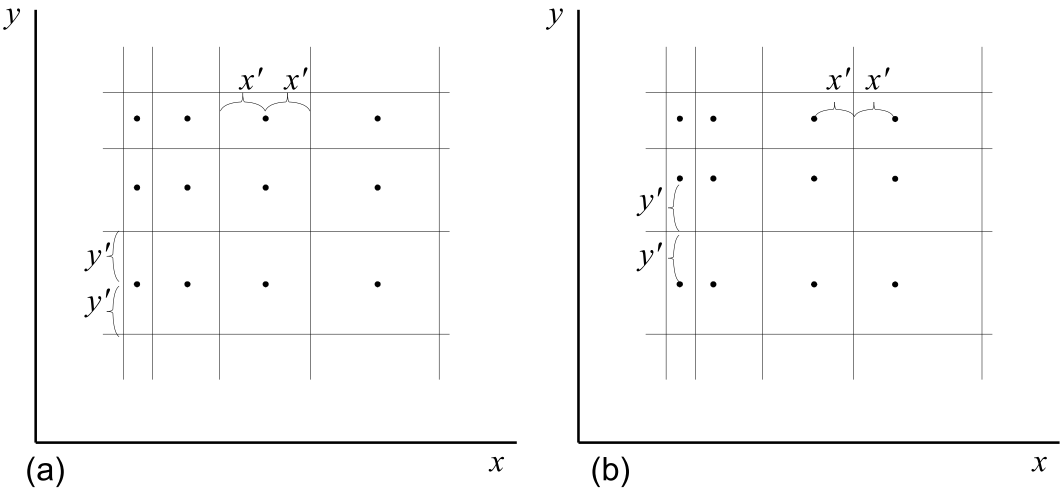

Figure 2.4: Examples of two-dimensional structured finite volume grids with: (a) nodes at CV centres; and, (b) CV faces midway between nodes (Ferziger and Perić 2002).

staggered grid arrangements (Ferziger and Perić 2002), requiring slightly more memory, have been proposed instead of co-located arrangements in order to remedy the so called "checker-board" effect which can result in converged, but unphysical, solutions to the pressure field (Patankar 1980). This is particularly problematic when strong pressure-velocity coupling or a complex grid is needed. However, the higher-order pressure velocity coupling method of Rhie and Chow (1983) has been used to resolve this issue on co-located grid arrangements. Therefore, for the remainder of this work we will consider the first cell-centred variant of the co-located grid method only.

Starting from the integral form of the governing equations, in conservation form and having applied Gauss's divergence theorem (see Equation 2.15), the FVM integrates over each CV resulting in the *exact* conservation of relevant properties at each cell centre. This is one of the most compelling features of the FVM and makes it ideal for cases involving discontinuities such as those seen between phases in multiphase flows. In the first stage of the discretisation process, the integrals are approximated, by suitable quadrature formulae, which consist of a set of algebraic statements for each CV based on the evaluation of the integrand at one of more locations on the cell surface. Interpolation is then used to express

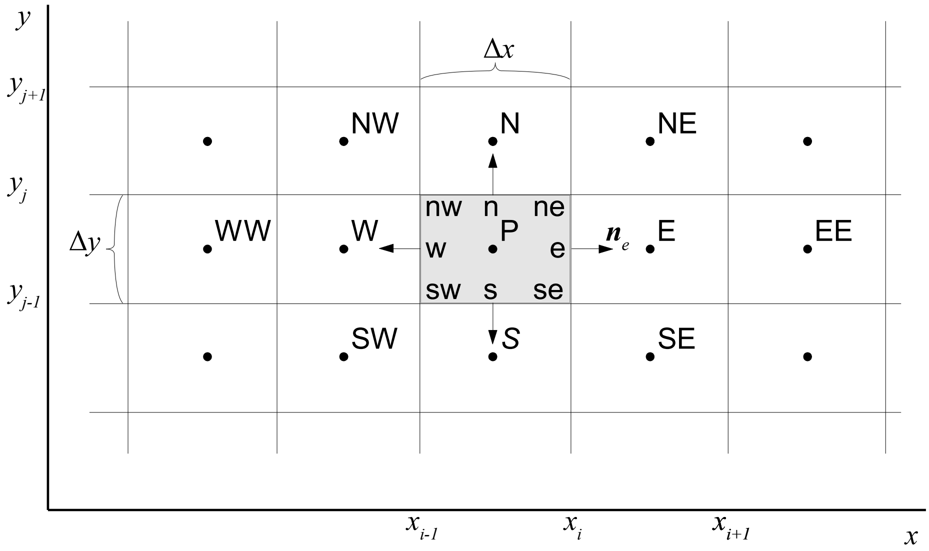

Figure 2.5: Notation for a typical 2D Cartesian CV (reproduced from Ferziger and Perić (2002)).

the flow variables at the surfaces of the CVs in terms of nodal values. For example, if we consider a typical 2D Cartesian CV with central node, P (Figure 2.5), the net flux across its boundary is equal to the sum of the integrals across each of its faces (e, w, n and s)

$$\int_S f dS = \sum_{\iota} \int_{S_\iota} f dS, \tag{2.22}$$

where ι indicates the individual faces and f denotes the flux (either convective ($\mathbf{n} \cdot (\rho\phi\mathbf{V})$) or diffusive ($\mathbf{n} \cdot (\Gamma\nabla\phi)$) normal to that face. Then, by considering the right-hand face, e only, the mass flux F_e can be given by

$$F_\mathrm{e} = \int_{S_\mathrm{e}} f dS = \bar{f}_\mathrm{e} S_\mathrm{e} \approx f_\mathrm{e} S_\mathrm{e}, \tag{2.23}$$

which is the *midpoint* (or *linear*) approximation of the integral and is second-order accurate, provided f_e is known, *i.e.* this is a one-point quadrature method. Here $\bar{f}_\mathrm{e}$ denotes the mean value over the face to which f_e is itself an approximation. It is common to call this Gaussian integration, due to the previous use of Gauss's theorem, but this can lead to confusion (as explained below). Higher-order approximations are possible but these typically require multiple-point quadrature methods, e.g., the fourth-order *Simpson's rule*, which states

$$F_{\mathrm{e}} = \int\limits_{S_{\mathrm{e}}} f dS \approx \frac{S_{\mathrm{e}}}{6}(f_{\mathrm{ne}} + 4f_{\mathrm{e}} + f_{\mathrm{se}}). \tag{2.24}$$

Here, the flux must be known at the cell corners (ne and se) as well as the face centre (e). Since the value of f is only known at the cell centres (nodal points), these values must be found in the second stage of discretisation using interpolation (Ferziger and Perić 2002). The use of multiple-point methods inevitably increases the computational cost of the solution and, in general, this increases exponentially with dimension. It is therefore favourable to use a quadrature method that can ensure suitable accuracy whilst minimising the integrand evaluations required.

Gaussian quadrature, or Gaussian integration is a popular method in FVM applications which can include an arbitrary number of integration points, *abscissas*, which are the precise roots of a set of orthogonal polynomials (Moroney 2006). The n-point Gaussian quadrature approximation over the interval [a,b] is then

$$\int\limits_{a}^{b} w(x) f(x) dx \approx \sum_{i=1}^{n} w_i f(x_i), \tag{2.25}$$

where w_i are weights from the *weighting function*, $w(x)$, and, along with the abscissas x_i, are given values so that Equation 2.25 is exact for polynomials of order $2n$. There are various forms of Gaussian quadrature utilising various polynomials. The weighting and abscissas for some common variations are readily available. For 1-point Gaussian quadrature, $n = 1, x_1 = 0$ and $w_1 = 1$ returning the midpoint rule hence the confusion.

The volume integrals in the transport equation are tackled in much the same way. The most simple approximation to the volume integral is

$$Q_{\mathrm{P}} = \int\limits_{V_P} q dV = \bar{q} V_P \approx q_{\mathrm{P}} V_P, \tag{2.26}$$

where q_P is the value of q at the centre of the CV. In this case no interpolation is required and, in general, this approximation is second-order accurate. For higher-order accuracy the value of q is required at locations other than the cell centre and so, as with the surface integrals, interpolation is required to express these values in terms of the known nodal values (Ferziger and Perić 2002). As an example, the second-order accurate, ‘semi-discretised’ version of the general transport equation (Equation 2.15), assuming a linear variation of ϕ in space, is then

$$\frac{\partial(\rho\phi_P V_P)}{\partial t} + \sum_{\iota} \mathbf{S}_{\iota} \cdot (\rho\mathbf{V})_{\iota}\phi_{\iota} = \sum_{\iota} (\rho\Gamma_{\phi})_{\iota}\mathbf{S}_{\iota} \cdot (\nabla\phi)_{\iota} + S_u V_P + S_p V_P \phi_P \tag{2.27}$$

where $\mathbf{S}_{\iota}$ is the outward-pointing face area vector and the source term has been linearised so that $S_{\phi} = S_u + S_p\phi$.

Interpolation is typically achieved using an analog to the differencing approximation used in the FDM and again a number of different schemes, with varying orders of accuracy exist. However, when considering arbitrarily unstructured meshes, interpolation schemes requiring values other than those from the nearest neighbouring CVs are considered impractical due to the associated information storage required to compute them (Jasak 1996). It is, at this time, important to consider the physical meaning of *boundedness* in the convective term. If the numerical method were to produce values of a dependent variable outside the bounds of physical meaning (*i.e.* a negative turbulent kinetic energy) it would have catastrophic impacts (negative viscosity in this case) on the solution algorithm. One of the most common interpolation schemes is the first-order *Upwind Differencing Scheme* (UDS) which is analogous to selectively using either forward- or backward-differencing depending on the flow direction. Although the UDS is the only truly bounded approximation, it is inherently inaccurate introducing a large diffusive error without an impractically refined grid (Jasak 1996). Linear interpolation, which is analogous to the *Central Differencing Scheme* (CDS) is of second-order (consistent with the overall method accuracy) and provides an effective compromise between accuracy and simplicity (Ferziger and Perić 2002). However, intense research has stemmed from the inherently unstable combination of the CDS and explicit time-integration in convection-dominated problems. This has resulted in a range of alternative schemes including combined spatial and temporal discretisation schemes (MacCormack 1969, 1982) and alternatives to the second-order CDS (Beam and Warming 1976, 1978). Unfortunately, the combined schemes result in an unacceptable dependence of the solution on the time-step and the Beam and Warming (1976; 1978) schemes require artificial diffusion to improve boundedness, which reduces the accuracy of the schemes (Jasak 1996). A number of possible solutions have been proposed to achieve a compromise between accuracy and boundedness (Jasak 1996). Some of these will be discussed further in Section 2.3.4 when considering the discretisation of the scalar phase fraction transport equation in the Volume Of Fluid (VOF) method. For a more thorough description of interpolation in the FVM, see Ferziger and Perić (2002) or Versteeg and Malalasekera (2007).The specific schemes used in this project will be discussed further in Section 3.2.1.

The FVM concept is conservative by construction and all approximated terms have physical meaning making it simpler to understand and more popular than some of the other methods. Furthermore the FVM can accommodate any grid structure and CVs can be any general polyhedra provided they do not overlap and each face is shared with only one neighbouring CV. This makes the FVM suitable for use with complex geometries and allows for local grid refinement without disturbing the entire mesh. As a consequence, this formulation is widely used in commercial CFD packages such as PHOENICS, FLUENT and STAR-CCM+. The disadvantages of the FVM are that, compared with the FDM, with higher than second order in 3D, it is significantly more difficult and computationally demanding, requiring three stages of approximation - interpolation, differentiation and integration (Ferziger and Perić 2002).

The *Finite Element Method* (FEM) shares many similarities with the FVM in that the domain is again subdivided into discrete volumes or finite elements. The main difference between the two methods is that, in the FEM, a shape function (a simple piecewise function describing local variations of unknown flow variables) for each element is substituted into versions of the governing equations which have been multiplied by a weighting function before being integrated over the domain. The main advantage of this method is its ability to cope with arbitrary geometries and grid refinements. However, as with any method based on unstructured grids, the main issue is finding an efficient solution method to deal with the complicated data structure produced (Ferziger and Perić 2002).

Some other methods also exist. The hybrid control-volume-based finite element method (CV-FEM) is another mesh-based method which takes the shape function descriptions of variables from the FEM and applies them to control volumes formed between the centres of each element like in the FVM (Ferziger and Perić 2002). CFX, developed by Ansys, Inc., is an example of commercial software which uses the CV-FEM (Westphalen 2010). Furthermore, as an extension to the empirical approaches of Morison et al. (1950) and Keulegan and Carpenter (1958) to solve wave-induced forces on structures, the Boundary Element Method (BEM), or panel method, is commonly used in marine hydrodynamics and attempts to fit boundary values, from specific boundary conditions, into the integral form of the governing equations. Typically BEMs employ the simplifications of potential flow theory, *i.e.* inviscid and irrotational flow, and are usually restricted to single phase flows. Consequently, BEMs are often more efficient than the other methods listed above, but the basic method is generally limited to linear problems and is incapable of resolving overturning waves and green water on structures (when viscosity and two phase flow cannot be neglected). Higher-order BEMs are under development and have been shown to be able to compute results for large, complex structures and multi-body interactions efficiently (Newman and Lee 2002). However, in cases with moving structures, direct coupling between wave-induced forces and body motion is typically not possible, restricting BEMs to applications involving only small displacements. Lastly, there also exist spectral schemes where the solution is expanded into a series of orthonormal functions and the governing equations given in terms of the expansion coefficients. This is known as a *frequency domain* analysis and, although generally very fast to converge, these methods are typically restricted to linear theory (relying on the linear concept of superposition) and simple geometries and, crucially, they are unable to resolve the shape of waves as they evolve in time (Naulin and Nielsen 2003). The frequency domain BEM model WAMIT (WAMIT Inc. 2015) is a popular choice among developers for analysis of operational applications such as the response of a WEC to wave excitation. However, it is widely accepted that these types of model are not appropriate when modelling extremely nonlinear wave-structure interactions (Jacobsen et al. 2012).

This project is concerned with the episodic event of an extreme wave impact on a single WEC, the nonlinear coupling between the WEC, PTO and mooring system and the implications this has on the survivability of the device. In order to simulate this behaviour accurately, a fully nonlinear, time-domain solution capable of including the effects of highly nonlinear wave-structure interactions and coupled dynamic motion is required. Therefore, in order to solve a suitably unabridged version of the full NS equations, on an unstructured grid (allowing for complex geometries and moving bodies), one of either the FVM or the FEM techniques must be used and those methods which are widely considered inappropriate for nonlinear interactions at the device scale have been rejected.

2.3.2 Pressure coupling for incompressible solvers

As mentioned earlier, when considering the flow of liquids, a justifiable simplification to the NS equations is to assume incompressibility, allowing the density to remain constant. In this case, the pressure (which is not normally known beforehand) cannot be calculated from the equation of state, using the temperature and density correlation, as it is no longer linked to the density, but instead, represents an additional constraint on the velocities. Therefore, incompressible solvers in CFD require some method to couple the pressure to the other flow variables (usually the velocity).

There have been a number of iterative solution strategies proposed to couple the pressure in NS solvers. The most familiar of which is SIMPLE (Semi-Implicit for Pressure Link Equations) which uses a ‘guess-and-correct’ method for the pressure, based on the velocity field, and a staggered grid arrangement designed to remedy the ‘checker-board’ problem associated with oscillatory pressure fields (Harlow and Welch 1965; Patankar and Spalding 1972; Muzaferija and Perić 1999). Figure 2.6a shows a basic schematic representation of the 2D SIMPLE algorithm; for a thorough explanation see Versteeg and Malalasekera (2007).

Various prediction-correction algorithms have since been proposed to improve the convergence and, hence, the computational efficiency of SIMPLE. SIMPLEC (SIMPLE-Consistent)

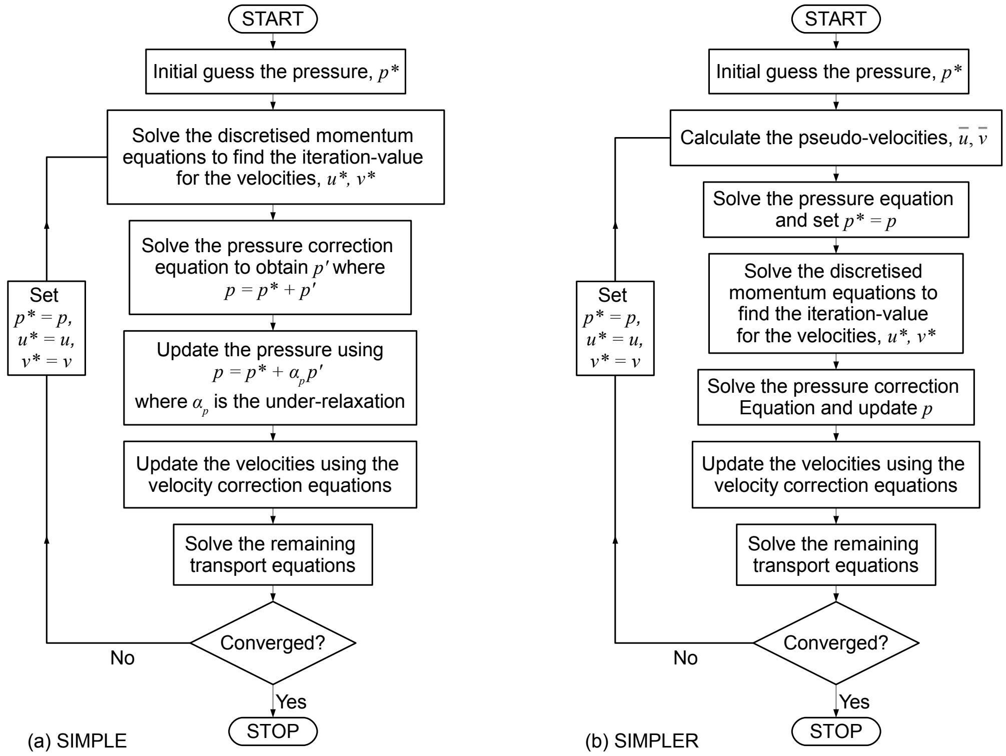

(a) SIMPLE

(b) SIMPLER

Figure 2.6: Basic schematic representations of (a) the 2D SIMPLE algorithm; and (b) the 2D SIMPLER algorithm (Jang et al. 1986; Versteeg and Malalasekera 2007).

takes the same steps as SIMPLE but rearranges the momentum equations so that the velocity-correction equations omit less significant terms than in SIMPLE (Van Doormaal and Raithby 1984). The basic algorithm is the same as Figure 2.6a but the under-relaxation factor, α_p, equals one for the SIMPLEC algorithm. SIMPLER (SIMPLE Revised) has a separate, more effective pressure equation which, although more computationally demanding, converges almost twice as fast as SIMPLE (Patankar 1980; Versteeg and Malalasekera 2007). A basic schematic of the SIMPLER algorithm is shown in Figure 2.6b. Issa (1986) developed a pressure-velocity calculation method, PISO (Pressure Implicit with Splitting of Operators) that has been adapted for iterative strategies and resembles SIMPLE with an additional corrector step. A schematic representation of the PISO algorithm is shown in Figure 2.7. For a detailed description of these algorithms and the equations involved see Versteeg and Malalasekera (2007).

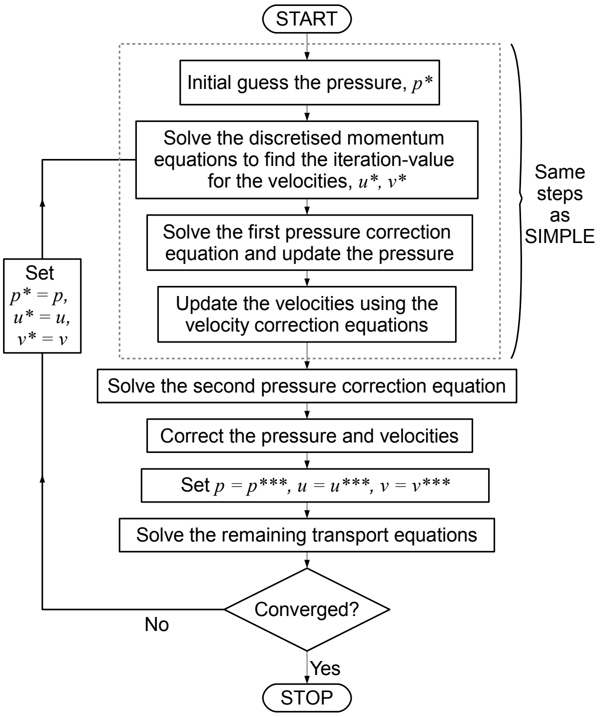

Figure 2.7: Basic schematic representations of the 2D PISO algorithm (Jang et al. 1986; Versteeg and Malalasekera 2007).

Comparisons between these algorithms have shown their performance to be case-specific. PISO can be more efficient in cases where the momentum and scalar variables are not strongly linked or in situations involving interaction between a turbulence model and the momentum equations. However no advantage over SIMPLER and SIMPLEC is documented in strongly coupled cases (Jang et al. 1986; Versteeg and Malalasekera 2007).

2.3.3 Initial and boundary conditions

Once the appropriate set of governing equations have been selected, and discretised, the conservation laws for the fluid flow in the interior of the domain are dealt with for all times after $t = t_0$. However, in order to close the equations, the domain boundaries need to be included. These must be calculated at every timestep, using prescribed boundary data in order to avoid introducing additional unknowns. Furthermore, the initial fields of all variables must be known and must satisfy all of the equations.

Each physical boundary, *i.e.* walls, inlet, outlet etc, is given a set of numerical boundary conditions upon each variable being calculated. There are two basic numerical boundary conditions, the surface integrals corresponding to the cell faces on the domain boundary can be described by either variable values, known as Dirichlet (or fixed value) conditions, or, their gradients normal to the boundary, known as Neumann conditions (Muzaferija and Perić 1999). For a thorough description of these conditions and their implementation see Ferziger and Perić (2002). The specific boundary conditions used in this project, and the generation method for the initial conditions, are described in greater detail in 3.1.3.

2.3.4 Free surface modelling techniques

The fully nonlinear, time-domain method used must be able to accommodate a highly distorted, multivalued free surface and cope with topological changes like wave breaking and recombination in 3D. Accurate simulation of a moving fluid interface, particularly one which is highly distorted, is extremely challenging in CFD. The position of the interface must be calculated as part of the solution as it is not known in advance of any given time-step (Greaves 2004). As is typical in these types of multiphase simulations, the fluids are assumed to be immiscible. The few strategies appropriate for free surface modelling can then be divided into two categories:

1. *Surface tracking schemes* including nonlinear potential flow methods; and
2. *Surface capturing schemes* including NS solvers like the volume of fluid (VOF) and level set (LS) methods (Gao et al. 2007).

Surface tracking methods

Surface (or interface) tracking schemes typically solve for the flow in the fluid region only making features like trapped gas bubbles in liquids unachievable. The free surface is modelled as a moving boundary containing the fluid domain. The instantaneous position of the boundary is defined by applying a kinetic boundary condition. This allows for the location of the free surface to be calculated precisely and for simple cases these methods are very accurate, however, these mesh-based methods require constant repositioning of the grid points introducing numerical errors and a low stability (Gao et al. 2007). Furthermore, surface tracking methods do not perform well when there are high levels of surface distortion, like wave breaking, as they cannot accommodate a multivalued interface and grid skewness becomes a problem without very complex mesh manipulations which themselves can cause additional numerical dissipation (Muzaferija and Perić 1997). Computation of multiphase flow is possible, but a coupled solution in two separate domains, with a common moving boundary for the free surface, is required (Muzaferija and Perić 1999). Therefore these methods are typically developed using nonlinear potential flow theory where the effects of air entrainment, viscosity and turbulence are usually ignored.

There are three main surface tracking techniques:

1. *Front tracking methods* use a separate unstructured grid and a piecewise polynomial fit to represent the free surface with massless markers evenly distributed along the surface. These are then advected with the flow field as part of the solution (Greaves 2004). These methods have an inherent weakness as, depending on the surface curvature, the markers become bunched or stretched as the simulation progresses and need to be redistributed or renumbered regularly. Therefore, the computational effort required increases disproportionately with the dimension and the level of surface curvature, and the treatment of interrupted or merging interfaces is limited (Daly 1969).

2. *Moving mesh methods*, such as the boundary integral approach, allow the grid to deform to track the free surface, reconstructing the mesh with every timestep. They have been shown to be efficient and successfully simulate free surface waves up until the point of breaking keeping the interface sharply defined. However, moving mesh methods are limited by the maximum deformation of the mesh and, typically, they only model one fluid. Problems are encountered when the interface overturns during wave breaking and these methods struggle to cope with the associated entrainment of air and spray from break up (Demirdžić and Perić 1990; Muzaferija and Perić 1997; Zwart et al. 1999; Greaves 2004).

3. *Particle tracking methods*, like Smoothed Particle Hydrodynamics (SPH), are very powerful, eliminating the need for a mesh and have been gaining popularity recently (Stansby et al. 2008), but as mentioned earlier these methods will not be considered further here.

Surface capturing methods

In surface (or interface) capturing schemes computation is performed on a fixed grid that extends over a region occupied by both fluids. This, in contrast to moving mesh methods, allows the initial grid quality to be retained throughout. A marker function, which describes the fluid properties at a particular location, is then used to identify the position of the interface, where a discontinuity in the density field exists. This eliminates the need for specialised free surface tracking. In these methods the full Navier-Stokes equations can be solved with an additional transport equation, for the particular marker function, solved at each time step to reconstruct the free surface. These methods are more robust than surface tracking methods and can include viscous effects, but capturing and reconstructing the interface is complicated, prone to numerical diffusion when evolving the volume fraction field and comes at a high CPU cost (Gao et al. 2007).

There are a number of different surface capturing methods, each distinguishable by the individual marker function used. For example, in the *Marker And Cell* (MAC) method marker particles are utilised (Harlow and Welch 1965), in the *Volume Of Fluid* (VOF) method a volume fraction field is used (Hirt and Nichols 1981) and in the *Level Set* (LS) method the interface is located via the zero contour of a distance function. The MAC method has been shown to deal with complex flow phenomena, however, the CPU cost and storage requirements, particularly in three dimensions, are excessive (Hirt and Nichols 1981). Both the VOF and LS methods are known as front-capturing methods and have been shown to be capable of simulating large scale deformations of the free surface including wave breaking and merging (Hirt and Nichols 1981; Greaves 2004; Rhee et al. 2005; Zhang et al. 2009). As these two techniques appear to be the most suitable for this project further detail is given below.

Volume of fluid (VOF) methods include an additional non-dimensional indicator function, α, which moves with the fluid and represents the averaged volume fraction for each CV. α ranges from zero in an 'empty' (or full of another fluid) cell to one in a 'full' cell; cells in which $0 < \alpha < 1$ therefore contain the interface. Two immiscible fluids are then effectively considered as one, with the physical properties, in the interface region, coming from a weighted average based on the volume fraction, α. For example, the density

$$\rho = \rho_1 \alpha + \rho_2 (1 - \alpha), \tag{2.28}$$

where ρ_1 and ρ_2 represent the densities of the two fluids. This reduces the storage requirements considerably in comparison to the MAC method. However, the position of the interface is not known precisely and has to be calculated using the additional transport equation,

$$\frac{\partial \alpha}{\partial t} + \nabla \cdot (\mathbf{V} \alpha) = 0, \tag{2.29}$$

which represents the PDE equivalent to the evolution of marker particles (Hirt and Nichols 1981). Typically these methods consist of two parts:

1. *a VOF transport algorithm* which uses the velocity field to determine the volume fraction values at each new time step; and
2. *an interface reconstruction algorithm* which approximates the position of the interface from the volume fraction field.

As mentioned previously, the critical issue with these methods is the discretisation of the convective term in Equation 2.29. Careful treatment of the α flux across cell faces is required to ensure a sharp interface is preserved and sufficient boundedness is achieved. High-order accuracy is difficult due to low-order discretisation schemes tending to smear the interface and produce artificial mixing between the fluids, making interface properties, like curvature, difficult to calculate accurately. Also, early compression schemes have been found to lead to stepping of the interface whilst, second- and higher-order schemes tend to produce over- and under-shoots (unboundedness) of the volume fraction, violating mass conservation (Dawish and Moukalled 2006). Furthermore, for cells containing the interface, it is not clear as to what extent each phase contributes to the velocity of the effective fluid and so definition of the free surface velocity can be misleading.

The general VOF transport method, termed the *donor-acceptor flux approximation*, approximates the interface as horizontal and vertical lines within each CV. In cells containing the interface, a combination of pure upwind and downwind fluxing is used to calculate the flux where the downwinding is 'controlled' to limit the amount of fluid available to the donor cell guaranteeing overall boundedness. It is normally accredited to Hirt and Nichols (1981) and is robust, conservative, flexible and widely used. Geometric interface reconstruction methods were employed to improve the overall method. Examples include Simple Line Interface Calculation (SLIC) (Noh and Woodward 1976) based on the under-recognised KRAKEN method (DeBar 1974); Piecewise Linear Interface Calculation (PLIC) (Greaves 2004); and Parabolic Reconstruction Of Surface Tension (PROST) (Renardy and Renardy 2002). The software SURFER is based on the PLIC method but uses a directional-split algorithm to reduce the volume error (Lafaurie et al. 1994). Simple geometric reconstruction schemes have been shown to produce spurious oscillations in wave profiles and instabilities in regions of separated flow as well as a high sensitivity to the mesh quality (Rhee et al. 2005). More advanced methods, using splines or least-squares procedures, have been developed giving good approximations of the interface shape and fluxes across CV faces. However these methods are typically restricted to simple geometries and structured grids and the computational effort required to reconstruct the interface is substantial (Wacławczyk and Koronowicz 2008). More recent methods avoid a geometrical representation of the interface and attempt to solve the aforementioned issues with the convective term by developing improved discretisation schemes. The majority of recent VOF methods aim to balance the stability of upwind fluxing and the interface sharpening of compressive, downwind schemes by employing some switching or blending strategy based on either the angle between the flow direction and the grid (Dawish and Moukalled 2006), or the ratio between advection and diffusion (*Péclet number*) (Jasak 1996). Despite the improvements in accuracy, the amount of blending required between convective schemes to preserve boundedness is not known beforehand and it varies from face to face making the specification of the ‘blending factor’ in these methods difficult. Further attempts to find accurate and bounded differencing schemes have employed ‘flux-limiting’ resulting in a collection of methods known as Flux Corrected Transport (FCT) schemes (or ‘shock-capturing schemes’) (Boris and Book 1973; van Leer 1973) and eventually nonlinear Total Variation Diminishing (TVD) differencing schemes where the discretisation method is a function of the local shape of the solution. These methods guarantee boundedness and can achieve good accuracy but smooth profiles can become distorted and in general these methods are too diffusive (Jasak 1996). Consequently the Normalised Variable Approach (NVA) was introduced by Leonard (1988) which considers each cell individually. Many schemes have developed from the Normalised Variable Diagram (NVD) including the High Resolution Interface Capturing (HRIC) differencing scheme of Muzaferija and Perić (1999) and the Compressive Interface Capturing Scheme for Arbitrary Meshes (CICSAM) of Ubbink (1997) which employs a blending of modified upwind and downwind schemes based on the volume fraction, the interface position and the *Courant number*, (Co). The Courant number for a cell P, $\mathrm{Co_P}$, links the flow velocity and cell size to the timestep, δt, like so

$$\mathrm{Co_P} = \sum_k \mathrm{max}\left\{ \frac{-F_k \delta t}{V_\mathrm{P}}, 0 \right\} \tag{2.30}$$

where, again, F_k is the mass flux across face k, δt is the timestep and V_P is the cell volume (Ubbink 1997). A similar HRIC method has been shown to perform well in cases involving spilling breaking waves and free surface wave flow around structures (Rhee et al. 2005), but these methods do not guarantee convergence (Jasak 1996) and, because their compression characteristics are dependent on the time step, a short time step is required to capture the interface sharply. Greaves (2004) added high resolution adaptive hierarchical remeshing with Ubbink’s VOF transport algorithm, CICSAM, combining the advantages of both interface tracking and capturing schemes to achieve a sharp interface with a reduced CPU cost. Commercial software STAR CCM+® uses the CICSAM scheme for surface reconstruction (Westphalen 2010). Dawish and Moukalled (2006) showed that both the HRIC and CICSAM schemes deteriorate in performance, becoming increasingly diffusive, with increasing Co. They went on to show that their new scheme, STACS (Switching Technique for Advection and Capturing of Surfaces), had superior performance over the other schemes. Barth and Jespersen (1989) developed a high-order differencing scheme basing the convection of the volume fraction on the maximum and minimum values in the surrounding cells making it independent of the timestep or Co. This scheme is used in the commercial software package CFX®, developed by ANSYS Inc., but can cause significant numerical diffusion at low blending factors (Westphalen 2010).

Frustratingly, although improvements have been made, these methods also increase the computational demand through increased algorithmic complexity, finer grids and smaller time steps (Greaves 2004). The issue, of *'which differencing scheme to use?'*, remains a compromise between stability, accuracy and efficiency.

A more detailed description of the VOF method used in this project is given in Section 2.3.6.

The level set (LS) method contains a signed difference function (the level set function), which is negative in one fluid and positive in the other, used to describe the shortest normal distance from the interface to a static grid system. The interface is then represented by the zero level set or zero contour of the distance function. The evolution of this function is normally governed by a standard advection equation (the level set equation). Highly complex three-dimensional boundaries can be dealt with easily (Zhang et al. 2009). The main difficulties inherent in the LS method are keeping the interface thickness finite and conserving mass.

The discretisation of the level set equation can lead to numerical diffusion and mass loss and requires high order advection schemes. Furthermore, in regions of high surface curvature additional mass conservation issues may arise (Zhang et al. 2009).

Many attempts have been made to improve the LS approach but, in the majority of cases, the simplicity of the original LS method is lost. Sussman et al. (1994) managed to improve, but not eliminate, the mass conservation issues using a redistancing procedure. Zhang et al. (2009) were able to achieve excellent mass conservation by adding a global mass correction to the redistancing procedure. The particle level set method allows for massless particles around the interface adding an extra constraint resulting in very good mass conservation. Other methods combine the strong mass conservation of the VOF method with the interface capturing ability of the LS method to make coupled LS/VOF methods which utilise the advantages of both front capturing methods (Zhang et al. 2009).

2.3.5 Solution Strategies

As mentioned in Section 2.3.1, the discretisation of the governing equations returns a system of algebraic equations, which can be either linear or nonlinear depending on the PDEs (or integral equations) used. Linear systems can be solved very accurately using *direct* methods such as Gauss Elimination, LU Decomposition or Tri-diagonal Matrix Algorithm (TDMA) which give the solution within a finite number of operations. However, the CPU cost of these methods is relatively high, particularly for large systems and, typically, the error associated with the discretisation of the equations is far greater than that for the arithmetic. Therefore, we can justify the use of more efficient methods with accuracies closer to that of the discretisation scheme used (Ferziger and Perić 2002).

Iterative methods

Iterative solution methods, which are the only option for nonlinear problems, are commonly used in CFD for sparse linear systems as a more economical alternative to direct methods. In these methods the solution is ‘guessed’ and then systematically improved using the corresponding equation until some ‘tolerance’ is met. However, these methods only guarantee convergence when the matrix resulting from the system of equations is diagonally equal. This is akin to the issue of boundedness, discussed earlier, where upwind differencing is the only bounded differencing scheme, for the convective term, and thus the only scheme which creates a diagonally equal matrix. Based on the nature of the equations being solved (*i.e.* symmetric or asymmetric systems; linear or nonlinear equations; orthogonal or non-orthogonal meshes), various methods to increase the diagonal dominance of the system, and hence the convergence and boundedness of the solver, have been proposed. Typically only the treatment of the source term (particularly the linear part) and the temporal derivative actually enhance the diagonal dominance of the matrix (Jasak 1996). For a detailed description of many of the methods available see Ferziger and Perić (2002). Further information on the solution methods available and those used in this work can be found in Section 3.2.3.

Solving coupled equations

The governing equations of fluid dynamics, the NS equations, are nonlinear and 'coupled', meaning the main variable of each equation can also be found in some, or all, of the other equations. Due to the complexity of nonlinear equation solvers and the associated CPU cost, the nonlinear convective term is typically linearised in steady-state solutions. In transient solutions, either the nonlinear terms are iterated over to retain fully nonlinear resolution at the expense of drastically increasing the CPU cost, or the nonlinear effects are 'lagged'. If the time-step is sufficiently small the effect of this lag is negligible (Jasak 1996). These systems can then be solved using a variety of methods: by considering all equations as part of the same single system and solving for all variables simultaneously; or by treating the ancillary variables as known and iterating over the equations sequentially until a solution is met; or by using a mixture of the two. *Simultaneous methods*, which generally use iterative solution techniques to reduce CPU cost, are typically preferred when the equations in question are linear and tightly coupled. When the equations are more complex and nonlinear, like those governing viscous flow, simultaneous solution techniques become too complex and expensive (Jasak 1996). Either nonlinear terms, like the convective terms in the momentum equations, must be linearised or a *sequential, or segregated, method* should be used. These methods solve each of the equations in turn, treating the dominant variable as the only unknown, replacing the other variables with the best available values. This process is then repeated until all equations are satisfied using an algorithm such as PISO or SIMPLE to establish the inter-equation coupling. Iterative solvers are used to solve each equation as it is considered inefficient to produce an accurate result initially (due to the coupled nature of the equations). The iterations performed on the individual equations are known as *inner iterations*, whereas, the cycles over the complete set of equations are called *outer iterations*. Optimising the ratio of inner to outer iterations is complicated. Furthermore, the change in a variable's value, between outer iterations, needs to be limited to improve convergence and avoid instabilities. This is called *under-relaxation*. Typically the number of iterations is selected empirically as the precise behaviour is case specific and difficult to predict (Ferziger and Perić 2002).

Stopping criteria

As an exact solution is never produced, with iterative solvers, some *stopping criteria* has to be defined. A common method is to stop the iteration once the difference between two successive iterates is less than some pre-defined tolerance. However, in general a small difference does not necessarily mean a small error and so some sort of normalisation is required. Unfortunately this can become complex and typically requires a number of extensions and approximations. As a compromise, many CFD codes stop the iterations when the *residual*, a factor quantifying the degree to which a solution fails to satisfy the equations exactly, has reduced to a suitable fraction of its original size (normally three or four orders of magnitude) (Ferziger and Perić 2002).

2.3.6 Open-source Field Operation And Manipulation (OpenFOAM®)

Based on the aims of the project (*i.e.* simulation of extreme wave loading on dynamically moored WECs) and the considerations discussed throughout this chapter, the Open-source Field Operation And Manipulation (OpenFOAM®) CFD Toolbox, developed by OpenCFD Ltd, has been selected as the most appropriate platform on which to run the necessary simulations.

OpenFOAM® has an extensive user community, including academic and commercial organisations, covering most active areas in engineering and science. The collection of C++ libraries are designed using the object orientated philosophy and contain a large range of features including a multiphase flow solver, `interFoam`, which solves the RANS equations for two incompressible, isothermal, immiscible fluids using a VOF-based interface capturing scheme similar to that of Ubbink (1997). Utilising the two-fluid Eulerian model, where the phase fraction equations for each fluid are solved separately, the interface-capturing method, developed by H. G. Weller (as cited by Rusche (2002)), does not use a compressive differencing scheme, like those mentioned above. Instead an *artificial compression term* is added to the volume fraction equation (third term in Equation 2.31) in order to provide a sharper interface resolution. Assuming the contributions of each phase to the free surface velocity are proportional to the phase fraction, the transport equation for α becomes

$$\frac{\partial \alpha}{\partial t} + \nabla \cdot (\mathbf{V}\alpha) + \nabla \cdot (\mathbf{V_r}\alpha(1-\alpha)) = 0 \tag{2.31}$$

where $\mathbf{V_r}$ is the 'compression velocity' representing the vector of relative velocity between the two phases. The compression term represents an additional convective term which is only active within the region containing the interface. Discretisation of this term is based on the compression velocity at the cell faces,

$$V_{r,\iota} = n_\iota \,\mathrm{min}\left[C_\alpha \frac{|\xi|}{|\mathbf{S}_\iota|}, \mathrm{max}\left(\frac{|\xi|}{|\mathbf{S}_\iota|}\right)\right], \tag{2.32}$$

where ξ is the conservative face volume flux, from the pressure-velocity algorithm; and, C_α controls the intensity of the interface compression when the two phases have comparable velocities. n_ι is the unit normal flux, which is determined from the phase fraction gradient,

$$n_\iota = \frac{(\nabla\alpha)_\iota}{|(\nabla\alpha)_\iota + \delta_n|} \cdot \mathbf{S}_\iota, \tag{2.33}$$

where δ_n represents a stablising factor for nonuniform grids. This method achieves a higher interface resolution compared to the general VOF approach without the need for a specialised scheme like CICSAM (Jasak 1996). The boundedness of the volume fraction equation is then achieved via a specially designed solver called Multi-Dimensional Limiter for Explicit Solution (MULES) (Rusche 2002; Higuera et al. 2013).

A segregated, iterative technique is used to solve separate matrix equations, constructed using the FVM applied to an unstructured grid, where the solution variables are co-located at the cell centres. The pressure-velocity coupling is achieved using adapted versions of either the PISO or SIMPLE algorithms which incorporate the phase fraction equation to derive a new pressure equation (OpenCFD 2014).

Also included in the standard release of OpenFOAM® are tools covering most aspects of pre- and post-processing (such as meshing and data visualisation) as well as a range of dynamic mesh functionality including internal boundary motion (essential for simulating floating objects). Furthermore, almost all features run in parallel as standard, so users can take advantage of all the computation resources at their disposal (OpenCFD 2014).

Being open-source, OpenFOAM® is free and allows users the freedom to extend and customise the existing functionality. This could be crucial in this research as the rapidly evolving wave energy industry has the potential to introduce new concepts yet to be implemented in commercial CFD software where standard releases are typically based on well established activities. Furthermore, there is no restriction due to licensing on the parallelisation of the code, which is common among commercial codes. Due to the complexity of the scenario under consideration in this project, one of the more computationally demanding methods is required and so any restriction on the computing power could render the work unfeasible within reasonable time constraints.

OpenFOAM®, therefore, appears to make provision for all the necessary requirements of this project and has been shown to perform well in cases including breaking waves (Jacobsen et al. 2012) and nonlinear wave-structure interactions (Bredmose et al. 2006; Bredmose and Jacobsen 2010). In the following chapter the specific methodological elements required to produce a NWT in OpenFOAM®, and examine the behaviour of WECs in extreme waves, are discussed. Various parametric decisions are then made to form a basic methodology which can be applied to the various applications in later chapters.

Chapter 3

Developing a Numerical Wave Tank

"Essentially, all models are wrong, but some are useful" - George E. P. Box (1987)

With the ever increasing human exploitation of the ocean environment, and deployment of technologies therein, numerical modelling of wave motion and wave-structure interaction has become an extremely useful tool for offshore industries. As discussed in the previous chapter, CFD involves solution of the governing equations of fluid dynamics on a spatially discretised version of the domain of interest. In wave modelling, the geometry of the computational domain can take many forms but is typically a function of the scale under investigation. For large scale oceanic and regional models, investigating wave interaction with coasts and coastal structures or assessing the wave resource at a potential site, the computational domain is usually two-dimensional and bounded by the topography of the research area. Far-field boundaries are then typically made up of straight or curved edges depending on the type of mesh used (Figure 3.1). At smaller scales, such as those under investigation here, the interest is placed more on the interior processes in the vicinity of a central structure. In these cases, the computational domain typically constitutes a three-dimensional, cuboidal or cylindrical subvolume of the research area with artificial, planar boundaries on all sides (Figure 3.2). As the validation for these small scale models typically comes from experiment, the domain frequently resembles that of a physical wave tank. Hence, these formulations are commonly described as Numerical Wave Tanks (NWTs) (Tanizawa 2000). Furthermore, in order to improve simulation efficiency, the width of the domain is typically made as narrow as possible whilst making sure not to adversely affecting the flow being simulated. Then, for cases where permitted *i.e.* those where only

Figure 3.1: An example of an unstructured mesh used for regional-scale wave modelling with topological boundaries and straight far-field boundaries (Greenwood 2014)

unidirectional waves and currents are modelled, simulations are commonly performed in two dimensions. By analogy, this could then be described as a ‘numerical wave flume’.

Despite the advantages of numerical modelling, however, many of the challenges involved are analogous to those encountered in physical experiments. Although the methods employed to tackle them may differ, both numerical and physical experiments involving waves and wave-structure interactions have two main challenges:

1. wave generation - how can one produce the desired wave form in the tank/domain so that its propagation and interaction with any structure might be studied? and,
2. wave absorption - how might one reduce the effect of wave reflection from the tank/domain boundaries so that the experiment better represents the unconfined nature of reality?

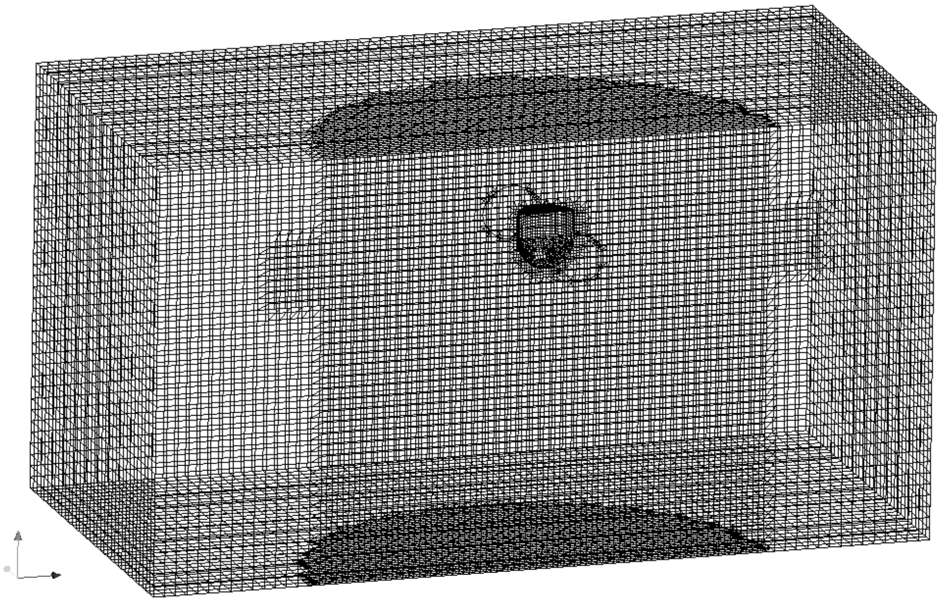

Figure 3.2: An example of an unstructured mesh used for device-scale CFD simulations, showing artificial planar boundaries and a central structure

For CFD codes, such as OpenFOAM®, the proposed solution to these issues is decided upon during the first of three stages: *pre-processing*, which includes a definition of the fluid properties; a description of the domain geometry and its spatial discretisation; and an implementation of a set of flow conditions on the boundaries. In physical experiments, it is rare that the tank architecture is considered as a variable and a thorough description of the fluid properties is typically omitted as it is considered to be unnecessary when using ‘real’ fluids. However, in the ‘real world’ one does not have the luxury of constraining variables to fixed values or removing the effects of unwanted physical processes such as phase changes or temperature fluctuations and a thorough error analysis is required if the experiment is to be reproducible (a prerequisite of good scientific practice). As mentioned earlier, by carefully selecting the appropriate governing equations to be solved, unwanted physical processes can be avoided in CFD models. These equations are chosen along with the corresponding discretisation methods and control strategies in the second stage of the CFD code, *the solver*. This stage does not have a clear analogue in physical experiments as the behaviour of the physical fluid is perfectly resolved at all length scales and no simplifications have to be made. The ‘solution’ in a physical experiment is then realised in real time simply by using a real fluid. Numerical models, on the other hand, require careful consideration of the various solution strategies and schemes used, to ensure an accurate result is found.

The analogy returns in the third stage of CFD codes - *post-processing*, which includes the data acquisition, output and visualisation of the results. A key difference in CFD is that data is available everywhere in the domain. Although considered an advantage over physical modelling, the extensive data sets produced by CFD simulations can quickly become overwhelmingly cumbersome especially on high resolution meshes. It is, therefore, still in the user’s interest to be selective about the data retained during the ‘experiment’. This is analogous to placing probes in physical experiments which record a subset of the output at a specific point of interest. Once the data has been recorded the analysis is essentially the same in both cases and data visualisation is typically the final step in the process.

In the following sections, the elements involved in these three stages (pre-processing, solver and post-processing) are discussed in more detail. As will become clear, there exist a vast number of possible options at each stage and so priority has been placed on those areas which are likely to have the most impact on the final solution. The general issues encountered during the development process and the approaches used to remedy them are discussed. As a result, a generalised NWT for simulation of extreme wave impacts on WECs is devised within the OpenFOAM® environment. Specific, case-dependent additions to this formulation are then described alongside the various applications in Chapter 5.

3.1 Pre-processing

The pre-processing stage involves the set up of a fluid flow problem, specification of the fluid properties and decisions regarding the configuration of the computational domain, including the spatial discretisation (mesh) and boundary conditions. In OpenFOAM®, the parameters describing these decisions are amassed in a series of *dictionaries* (text documents) which are read from a specific directory structure, by a number of *utilities* (computer applications), in order to transform the inputs into a form that is suitable for the solver stage.

3.1.1 Fluid properties

The fluid properties are specified in the `transportProperties` dictionary. Here one can state the density and viscosity of the various fluids as well as the type of fluid being modelled. As mentioned at the end of Chapter 2, OpenFOAM® contains a multiphase solver for incompressible, isothermal, immiscible fluids called `interFoam`. This (or an adaptation of this) will be the solver used throughout this work and so, in keeping with these simplifications, an incompressible, isotropic Newtonian fluid will be assumed for the two phases; air and water. In that case, the dynamic (or shear) viscosity, μ, is a scalar constant relating the strain rate to the viscous stress in the fluid and the kinematic viscosity, ν is the ratio of μ to the density of the fluid, ρ.

Unless stated otherwise, the densities of the air and water phases have been taken to equal 1.2 kg m^{-3} and 1000 kg m^{-3} respectively. The kinematic viscosity, ν, has then been taken to equal 1.36$\times 10^{-5}$ m^{2}s^{-1} for air and 1$\times 10^{-6}$ m^{2}s^{-1} for water. These properties are based on standard temperature and pressure values *i.e.* those at 20 $^{\circ}C$ and 1.013$\times 10^5$ Pa (Massey and Ward-Smith 1998).

3.1.2 Meshing (spatial discretisation)

From the discussion in Chapter 2, it is clear that the solution accuracy is highly sensitive to the spatial discretisation of the governing equations. Consequently a vast amount of time spent on CFD projects is dedicated to defining the domain geometry and generating the computational mesh. Most commercial software has a Graphical User Interface (GUI) and built-in mesh generator or the facilities to import data from third-party software in order to maximise the productivity of the user (Ferziger and Perić 2002). Although OpenFOAM® has no GUI, a number of mesh generation utilities are supplied with the standard release and it is possible to import geometries from external Computer-Aided Design (CAD) software or meshing tools (OpenCFD 2014). The most common of these will be critically examined in the following sections along with a discussion on the development process and issues encountered while attempting to create generic meshing procedures for a NWT in OpenFOAM®.

It is of great importance in high-quality CFD work, that the mesh be carefully designed to control the magnitude and distribution of the error associated with discretisation. Theoretically, one can reduce this discretisation error to an arbitrarily small value by successively refining the mesh, but this has the adverse effect of increasing the computation time and memory requirements (Versteeg and Malalasekera 2007). Unstructured (non-uniform meshes) are commonly used to try and optimise the accuracy to execution time of CFD codes. Typically this involves defining finer areas in the mesh where large variations in the flow variables occur, while allowing regions where there is relatively little change, to be coarser. Adaptive meshing methods, which automatically refine (or coarsen) the mesh depending on the flow variations (Greaves 2004), have begun to emerge but these techniques require a significant amount of development and it remains the responsibility of the user to design a mesh which will achieve the desired level of accuracy at the least cost (Ferziger and Perić 2002).

Good mesh design and optimal solution speed comes with experience and extensive use of the code in question. There is no *bona fide* method for estimating the error associated with a poor mesh design. A background knowledge of the fluid dynamics of the problem and experience simulating similar cases is extremely useful. However, the only way to remove the errors associated with excessive grid coarseness is to perform a mesh dependency (or mesh convergence) study. This process is an essential part of good CFD practice, it involves repeated simulation on successively refined meshes until there is no change in the solution from further refinement. The solution is then said to be ‘mesh independent’ (Versteeg and Malalasekera 2007). Mesh dependency studies are, however, time consuming and when irregular meshes are being used it is not always clear as to which regions of the mesh require further refinement (in these cases it would be inefficient to refine the mesh equally in all areas when performing a mesh convergence study). Currently, there does not appear to be any definitive guidance on good meshing practice in cases involving NWTs. Therefore, in the following subsection, a series of mesh dependency studies based on standard test cases have been carried out. The purpose of these is to ascertain which mesh attributes have the biggest impact on the solution so that generalised decisions on mesh generation can be made in the context of NWTs. It is hoped that this process will aid in the informed design of future meshes and provide increased confidence in their quality, saving time and improving simulation efficiency. Ultimately, case specific parameterisation of mesh attributes, such as resolution and cell shape, would streamline the generation of converged meshes and help to inform guidelines for good meshing practices in NWT simulations.

Mesh dependency studies

As mentioned above, OpenFOAM® contains a number of mesh generation utilities. The most basic of these is `blockMesh` which creates parametric meshes allowing for cell grading and curved edges. The principle behind this utility is to subdivide the domain into one or more three-dimensional, hexahedral *blocks*. These blocks are defined by a set of *vertices*; the *edges* connecting them, which can be straight lines, arcs or splines; and, the *faces* bounding them. The boundary of the computational domain is then defined as the bounding box containing the blocks and is divided into *patches* (regions) described by the block faces coinciding with the boundary. `blockMesh` is a relatively simple meshing tool typically only used to create structured meshes with some grading, or refinement, in specified directions (OpenCFD 2014).

The meshes used in these mesh dependency studies are all two dimensional structured meshes with uniform resolution across the entire domain. For this, `blockMesh` is sufficient. Selective mesh refinement and unstructured grids will be discussed later in the chapter and more advanced meshing will be explained when introducing structures into the domain.

Solitary wave case. The classic case of a solitary wave run-up on a vertical wall forms the basis of the initial mesh dependency study. Figure 3.3 shows the computational domain, which has been constructed to mimic that used in a number of previous works (e.g. Zhang et al. (2009)), with a two-dimensional channel size of $20h \times 2h$, where h is the still water depth. The boundary conditions for the bottom and right-hand walls state that the fluid has zero velocity on the boundary (no-slip) and the atmosphere uses the `pressureInletOutletVelocity` patch which will be discussed further in Section 3.1.3. S_c and S_{runup} represent the amplitude of the solitary wave in the centre of the NWT and the max-

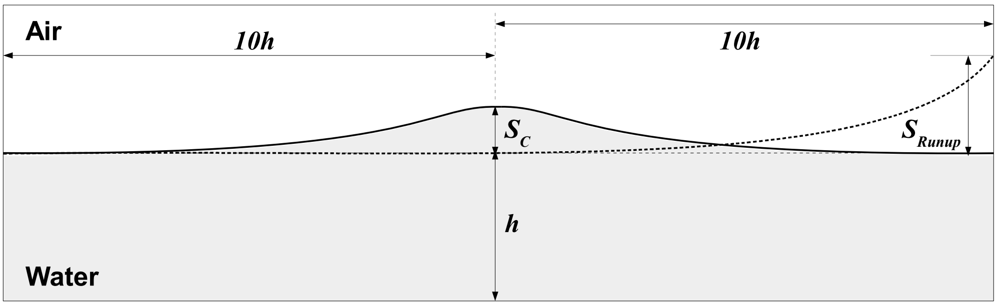

Figure 3.3: Schematic of the computational domain used in the simulation of a solitary wave run-up on a vertical wall.

imum run-up on the right-hand wall boundary, respectively. For this case, the water and air have kinematic viscosities of $1\times10^{-6}\,\mathrm{m^2s^{-1}}$ and $1.8\times10^{-5}\,\mathrm{m^2s^{-1}}$ respectively, to match those used by Zhang et al. (2009). The RANS equations are solved without a turbulence model, *i.e.* laminar flow is assumed throughout. The method of wave generation will not be described here as a full discussion of this will be given in Chapter 4. For the solution procedure, all terms are approximated using 1-point Gauss quadrature and linear interpolation is used as default with the exception of the divergences $\nabla\cdot(\mathbf{V}\alpha)$ and $\nabla\cdot(\mathbf{V_r}\alpha)$, from the phase fraction transport equation (2.31), for which the TVD scheme Monotonic Upstream-Centered Scheme for Conservation Laws (MUSCL) (van Leer 1976) and OpenFOAM®'s `interfaceCompression` scheme (described in Section 2.3.6) have been used respectively. Further information regarding the various numerical schemes used throughout the course of this project can be found in Section 3.2.1. A conservative value of 1 is used for the compression term, C_α.

Initially, the maximum run-up, which was deemed to be the critical result, was recorded using a water depth $h=$1 m. A 1 m air layer was used, on regular square-celled meshes with between 1000 and 182,250 cells. The execution time was also recorded so that a compromise between computational effort and solution convergence could be discussed.

As mentioned earlier, in order to reduce the computational time, whilst maintaining the solution accuracy, the mesh is typically allowed coarser regions where the flow variables are not

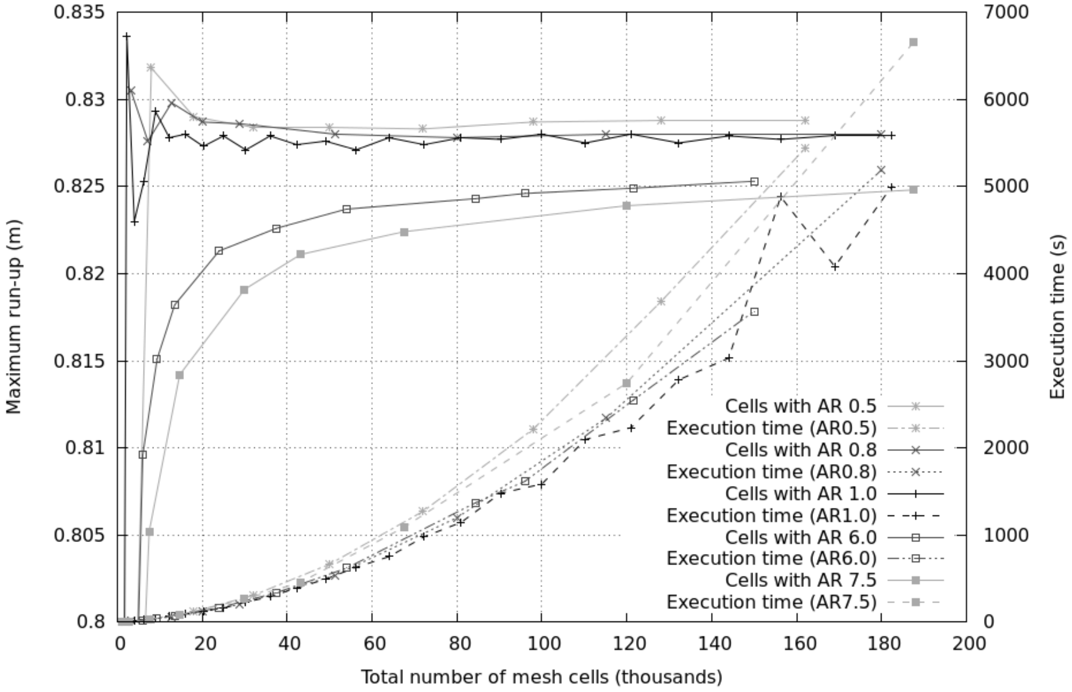

Figure 3.4: Maximum run-up and execution time for a 0.4 m high solitary wave in a 1 m deep tank (h =1 m) vs. the total number of cells in the computational mesh for five different cell aspect ratios.

changing as rapidly. On a structured, regular, two-dimensional mesh made of quadrilaterals, this leads to cells with an elongated character (Bredmose and Jacobsen 2010). This in turn leads to a directional bias on the discretisation error and could affect the convergence of the solution, depending on the gradients present in flow variables. In Zhang et al. (2009) the grid is extensively stretched in the direction of wave propagation resulting in cells with an Aspect Ratio (AR) of 7.5, where AR is defined as the cell width over its height. In order to evaluate the effect cell shape has on the mesh convergence, further simulations were undertaken for meshes with cell ARs of 0.5, 0.8, 6.0 and 7.5.

Figure 3.4 shows the maximum run-up of a solitary wave (S_c =0.4h) against the number of cells used (*i.e.* the mesh resolution) for the 5 different shaped grid cells (AR 7.5 represents the cell shaped used by Zhang et al. (2009)). Also plotted are the execution times for each four second simulation using a single Intel® Xeon® processor E5430 @ 2.66 GHz running on Ubuntu 10.04 (lucid) Linux kernel 2.6.32-44-generic.

By first examining the execution times for each of the simulations (dotted lines), the same behaviour can be seen regardless of cell AR; the execution time increases exponentially with the number of cells. This highlights the need to limit the number of cells in order to ensure practical time scales for simulations, particularly as this issue is likely to be compounded with the addition of a third dimension. Another observation is that, the further the AR is from 1 (square cells) the quicker the execution time increases with grid resolution.

In terms of maximum run-up, it can be seen that each of the simulations tends to a stable value of between 0.825 m and 0.828 m as the number of mesh cells increases. This shows convergence (mesh independence). At very low cell numbers none of the simulations have converged leading to spurious results for the maximum run-up. As the simulations begin to converge, simulations where AR$<$1 tend to overestimate the maximum run-up whereas for AR$>$1 the maximum run-up is underestimated. For square grid cells (AR$=$1) convergence is reached with the lowest mesh resolution, with some oscillation about the converged value at intermediate cell numbers. For AR$<$1 convergence follows soon after the square cell simulations but for AR$>$1 convergence has still not been reached (even with five times the number of cells).

This pattern, however, may be dependent on the orientation of the interface. In this test the maximum run-up, which coincides with the moment the interface is at its most vertical, is taken to be the key result. Cells orientated such that the grid is refined in the direction normal to the surface are likely to resolve the interface more accurately. Therefore cells with AR$<$1 will resolve the maximum run-up better, but will not perform well at times leading up to this, when the interface is horizontal. In this case, it appears the dynamics of the run-up are the critical factor as cells with AR$<$1 perform much better than those with AR$>$1. However, these results are generated using the largest solitary wave considered ($S_c =$0.4 m). Smaller waves with less run-up may be simulated better by high AR cells as the surface is closer to horizontal. Nevertheless, square cells perform equally well whatever the orientation of the surface and this compromise has proven to be superior in terms of both required mesh resolution and execution time.

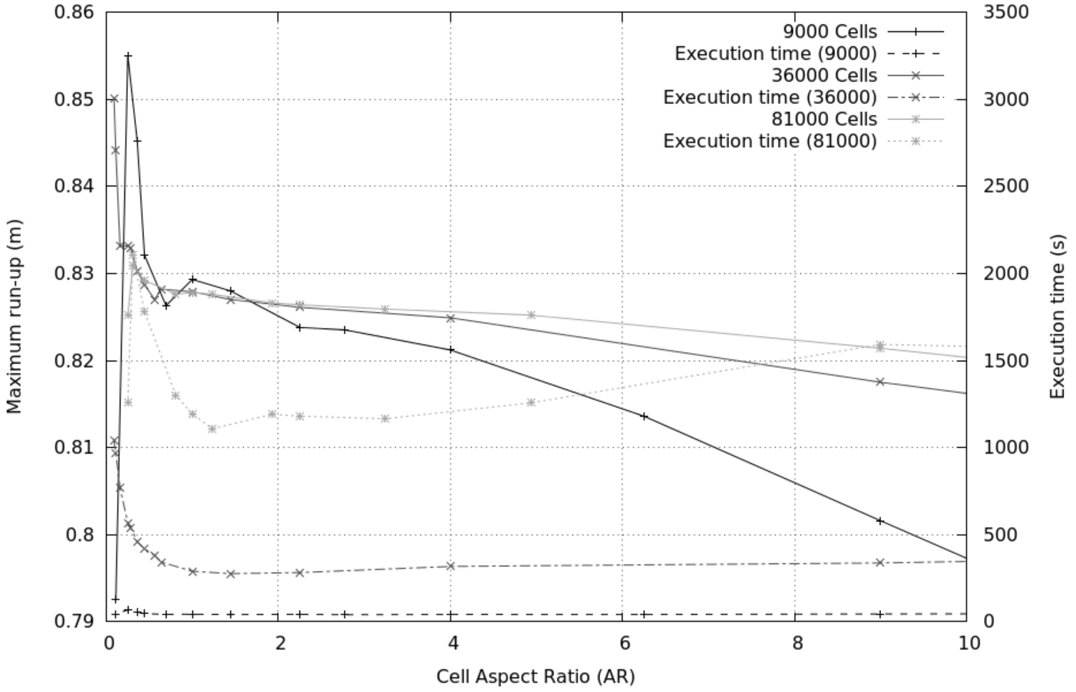

Figure 3.5: Maximum run-up and execution time for a 0.4 m high solitary wave vs. the AR of cells in the computational mesh for three meshes with a fixed number of cells.

Figure 3.5 further examines the effect cell AR has on the maximum run-up ($S_c =$0.4 m). This time the number of cells is fixed for three meshes of different refinements and the AR of the cells is altered. The execution time is again recorded using the same hardware as before.

From Figure 3.4 we know that the solution has converged for the 81,000 square cell case suggesting the true maximum run-up is 0.8275 m. From Figure 3.5, we can see that square cells (AR=1) perform best on all three meshes and again high AR cells underestimate the maximum run-up while low AR cells overestimate. As expected from Figure 3.4 the discrepancy is increased as the number of cells is reduced. Furthermore, square cell simulations are again shown to have the shortest execution time.

These initial trials confirm that, for simple quadrilateral meshes, square grid cells perform best. In general, square cells are quicker to reach a converged solution and eliminate any directional bias in the mesh resolution. It seems reasonable to extend this finding to three-dimensions making cubic cells the most desirable in hexahedra-based meshes.

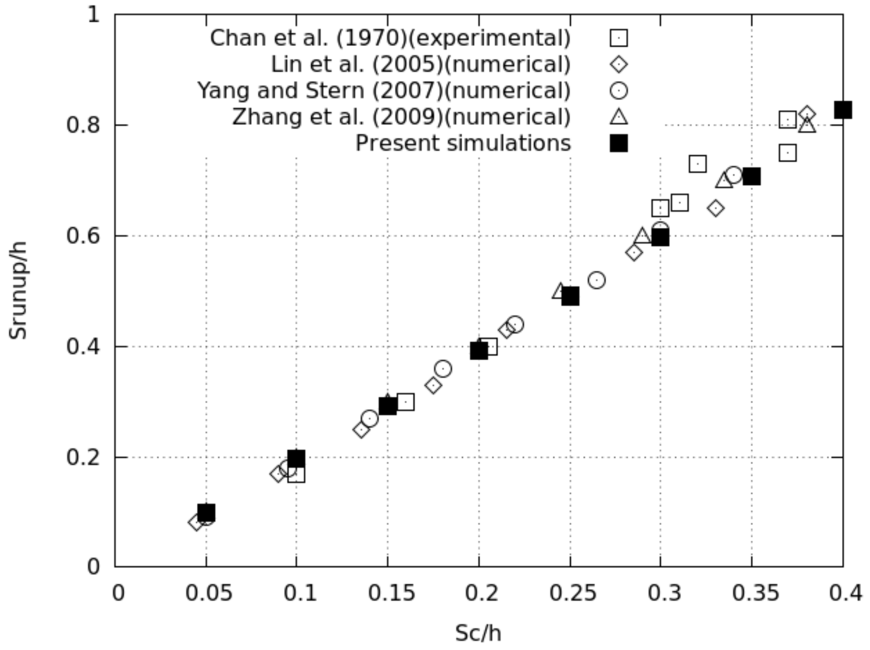

Figure 3.6: Comparison between results in the literature and the present work (using 36,000 square grid cells) for run-up, S_{runup}, of a solitary wave with height S_c on a fixed vertical wall.

Furthermore, 36,000 square cells appear to be sufficient to reach a converged solution; in this case, however, this resolution is probably excessive in regions where the flow is slow moving. These findings have been applied in a series of simulations comparing the maximum wave run-up on the right-hand wall with the incident wave height. The results are shown in Figure 3.6 along with the numerical results from Zhang et al. (2009), Lin et al. (2005) and Yang and Stern (2007) and the experimental data from Chan and Street (1970). As in the work by Zhang et al. (2009), the agreement between the numerical and experimental results is very good for $S_c/h < 0.3$. Above this the experimental data shows some scatter but, in general, the agreement between the current work and the results in the literature is very good.

Periodic wave case. Having found square cells to have favourable characteristics, the second mesh dependency study aims to parametrise the required grid resolution, based on some case-specific measurement. It is hoped that this test will enable the mesh to be specified in future simulations with some confidence that results are already near mesh

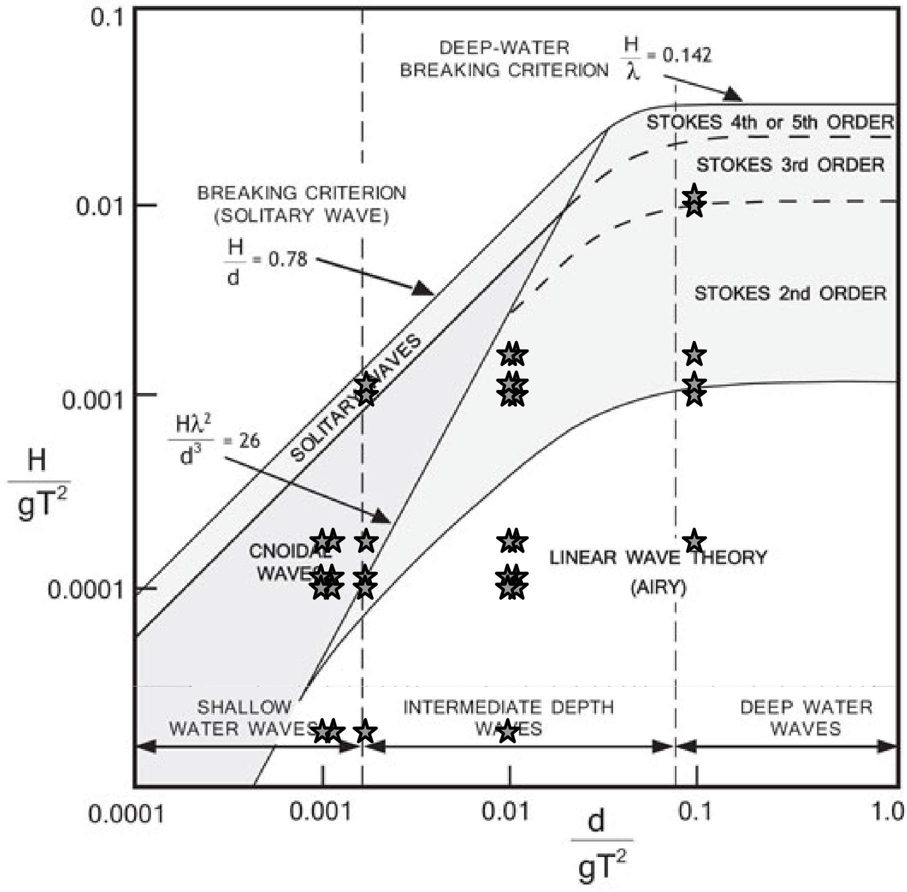

Figure 3.7: Wave characteristics used in mesh dependency study (marked with stars) and the ranges within which various wave theories are suitable (adapted from U.S. Army Corps of Engineers (2006))

independent. For this, the wave steepness, (H/λ), has been selected as the defining feature in NWT simulations. Thus a relationship between the cell size required to meet the desired accuracy and the wave steepness is sought.

To find this relationship, a set of periodic wave cases, covering a range of wave regimes (*i.e.* linear, second order; deep water, shallow water etc.), were simulated using a two-dimensional NWT with the same boundary conditions as those used in the solitary wave case above. The same solution strategy as before was used and C_α was again set to a conservative value of 1. Figure 3.7 shows the wave cases considered on the classic chart first produced by Le Méhauté (1976). Here, d is the water depth, T the wave period, H

the wave height, λ the wavelength and g is the acceleration due to gravity. A full discussion of this diagram can be found in the Coastal Engineering Manual (U.S. Army Corps of Engineers 2006). Further detail on essential wave theory will be given in Section 4.3.

In order to keep the wave steepness (defined as H/λ) as the only variable across the experiments and remove the influence of wave reflections and numerical losses, the simulations were constructed with the following parametrisations:

1. The water depth, d, was fixed at 2 m for all tests.
2. The height of the air phase was fixed at 1.5 m.
3. Each NWT was 10 wavelengths long.
4. A Relaxation Zone (RZ) with a length sufficient to absorb 99% of the wave (see Jacobsen et al. (2012)) was added to the end of the domain.
5. The initial mesh had a square-cell edge length of $\delta l = \frac{1}{10}\sqrt{\lambda H^2}$.
6. Simulations were run for a duration of 15 wave periods.
7. Full domain results were recorded every $1/4$ period.
8. Time series of the surface elevation were recorded at every integer wavelength from the wave maker.

The waves were generated using the stream function wave theory, supplied with additional toolbox `waves2Foam` (Jacobsen et al. 2012). This offers a solution to the exact nonlinear equations, assuming waves of constant form, using a truncated Fourier expansion (Svendsen 2006). First developed by Dean (1965) and since improved by Rienecker and Fenton (1981), this allows for the generation of a periodic wave to tenth order (in this case), according to a specified amplitude, period and water depth. In theory the wave should then propagate without a change in shape and so this is also assumed to be the target solution at each of the downstream locations. Simulations were run, starting with the initial mesh resolution described above, and then repeated with increasingly refined (or unrefined) meshes until convergence was found. The two-dimensional meshes were refined using the quadtree method (Greaves 2004) where cells are split in half in both dimensions, maintaining square mesh cells but with half the edge length. Convergence was believed to have been met when the simulation result had a Root Mean Squared (RMS) difference of less than $H/100$ when compared to the stream function theory. This value was hoped to be an adequate solution without a significant dependency on the choice of solution strategy. The required cell size, for an RMS of exactly $H/100$, was then interpolated, using an exponential fit, from the results of unconverged and converged meshes in each case.

The results from this study are plotted in Figure 3.8. It was found that once convergence had been achieved the required grid resolution was not a function of distance from the wave maker, *i.e.* the same grid resolution is required for convergence regardless of propagation distance. This supports the idea that once convergence has been achieved the effects of numerical diffusion, which typically increase with propagation distance, are negligible. Therefore, as there was some scatter in the required grid resolution found, an average was taken from the results at 2, 3 and 4 wavelengths distance from the wave maker in each case. Furthermore, the results in Figure 3.8 have been separated by depth regime (marker shape) and nonlinearity (colour) based on the chart in Figure 3.7. Solitary waves and the two types of cnoidal waves are coloured black. Unfilled markers represent the tests where the convergent resolution has been interpolated from unconverged solutions only since a solution with an RMS below $H/100$ was not found in the tests performed. Confidence in these results is therefore greatly reduced. It is believed that other variants in the solution strategy, such as the discretisation schemes and interface compression, are responsible for the lack of convergence in these cases as opposed to the mesh resolution and so the trend may not increase as rapidly as shown in Figure 3.8.

However, as expected, the number of cells required over the height of the wave increases with the wave steepness. Kleefsman (2005) also showed the required mesh resolution to be highly dependent on wavelength. In order to resolve the wave correctly, shorter waves require a much finer mesh than longer waves. Furthermore, shallow water waves appear to

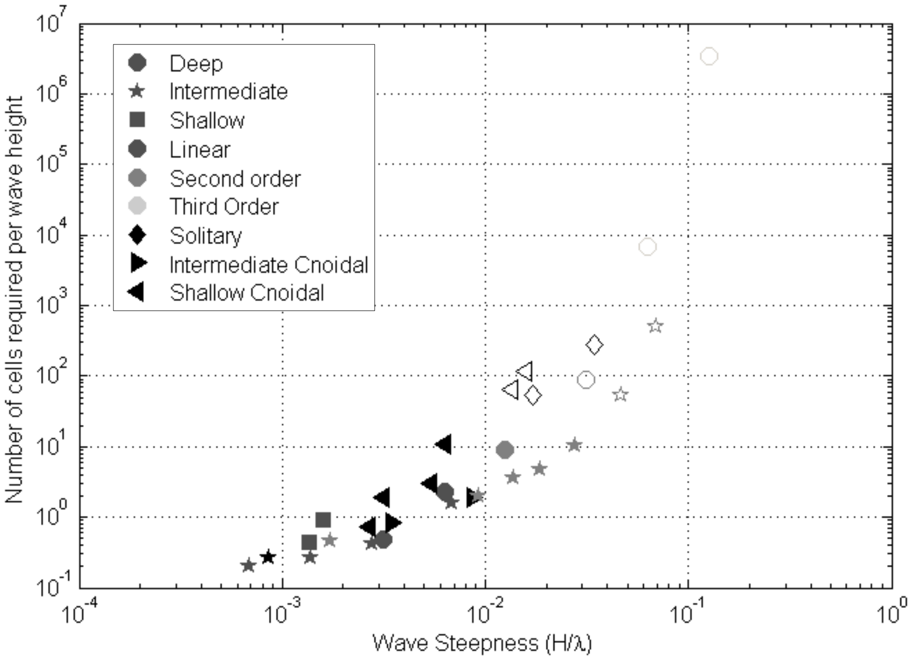

Figure 3.8: Results from a mesh dependency study showing the required number of cells over the wave height against the wave steepness, for a range of wave regimes and a RMS tolerance of $H/100$.

require a higher grid resolution than other waves, but deep water waves do not necessarily require a lower resolution than intermediate waves. Interestingly, some of the least steep waves ($H/\lambda < 4\times10^{-3}$) require less than 1 cell over the wave height to achieve convergence. In this project, however, the smaller waves simulated have a steepness of around 0.05 meaning the mesh resolution required, for a 1% tolerance, is between 10 and 100 cells over the wave height. For steeper waves the required mesh resolution would be far too high without reducing the tolerance or resolving the issue with non-convergent solutions.

Figure 3.9 shows the result of relaxing the convergence criteria to 2 % of the wave height. As can be seen this greatly reduces the required number of cells over the wave height. With this tolerance, waves with a steepness of 0.1 can be simulated with as little as 10 cells per wave height. Furthermore, for an RMS error of $H/50$, a converged solution has been found for all but the steepest two cases alleviating the uncertainty surrounding the unconverged steeper wave cases when applying a 1 % tolerance (open markers in Figure 3.8).

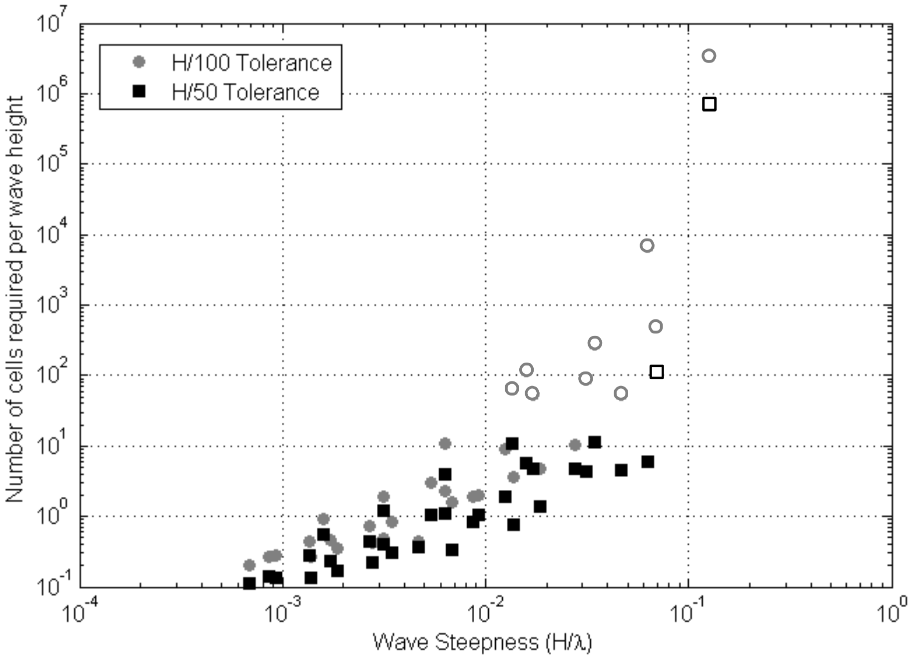

Figure 3.9: Required number of mesh cells vs. wave steepness, for RMS tolerances of $H/100$ (grey circles) and $H/50$ (black squares). Open markers correspond to interpolated results from unconverged cases.

Figure 3.10 shows the solution for the deep water wave, with $d/gT^2 = 0.1$, $H/gT^2 = 0.01$ and steepness 0.0628, when the value of C_α is set to 1 (as before), 2 (enhanced compression) and 0 (which represents no compression of the interface). It is immediately obvious why the convergence criteria was not being originally met for cases of steep waves; the surface elevation at the wave crests is distorted for some reason. It is believed that the surface compression does not cope well when the interface exhibits a high curvature as this issue is compounded when $C_\alpha = 2$ and resolved when the compression is removed ($C_\alpha = 0$). However without the interface compression, the solution in this case, although without distortion, has not converged to within 1 % of the target either. There are, however, only 14 cells over the wave height and so further refinement may improve the uncompressed case when it did not in the case of $C_\alpha = 1$. Unfortunately, it is expected that less steep waves, without the distortion issue, would also require an increased mesh resolution when C_α is set to zero. It is likely that the optimal arrangement will consist of a compromise between mesh resolution

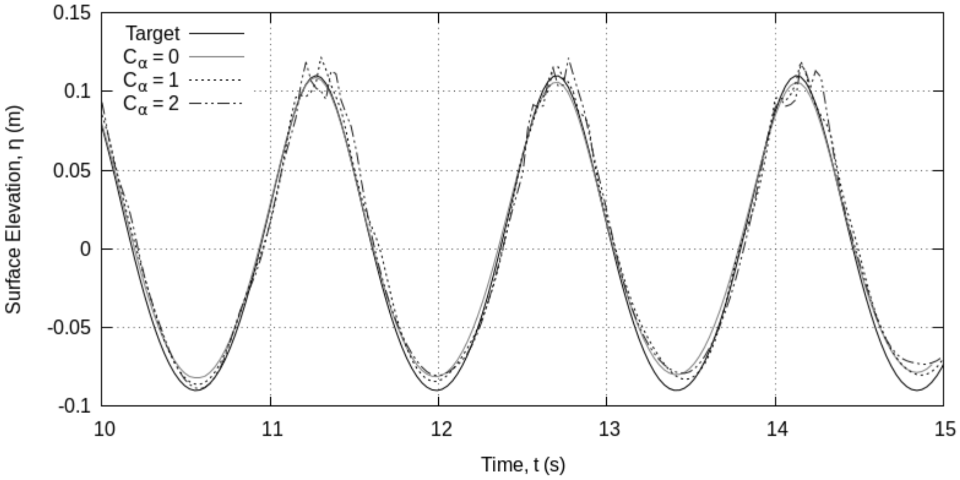

Figure 3.10: A comparison of unconverged surface elevation results for a wave with a steepness of 0.0628 and surface compression values of C_α =0, 1 and 2.

and surface compression and the relative importance of the two will depend on the wave steepness, *i.e.* as the steepness increases the mesh resolution must increase while the surface compression, C_α, will likely need to be reduced. Parametrisation of this relationship will be revisited in future work.

In summary, for regular waves, with steepness's in the range 0.01$< H/\lambda <$0.1, a mesh resolution corresponding to 10 mesh cells over the wave height is sufficient for a 2 % RMS error in the free surface time series (when using a surface compression, $C_\alpha = 1$). For improved accuracy the mesh resolution must be increased but it is also likely that the surface compression must be relaxed or removed altogether. For waves with steepness's below 0.01 a mesh resolution corresponding to only 1 mesh cell over the wave height is adequate for a 1 % RMS error when C_α=1. However, if the surface compression were to be relaxed it is likely that a greater mesh resolution would be required to retain the same accuracy at these steepness's. Throughout the remainder of this work C_α has been set to 1. Therefore waves with steepness's below 0.01 are considered to have been resolved to within an RMS error of 1 % provided the mesh resolution is greater than 1 cell over the wave height and waves with steepness's of 0.01$< H/\lambda <$0.1 are considered to have been resolved to within a 2 % RMS error provided the mesh resolution is greater than 10 cells over the wave height.

Selective mesh refinement

It is clear from the results presented above that the mesh resolution required to study extreme waves will be at the top end of that used in free surface simulations, even before a structure is introduced. However, this resolution is not required in all areas of the domain. In these cases it is even more important to reduce the total number of mesh cells by allowing the mesh to remain coarse in regions where the flow variable gradients are small. Otherwise it is likely that the execution time for the simulation will quickly become intolerable.

From the previous discussion on the VOF method and a basic theory of water waves we know that the highest gradients (particularly in the volume fraction field, α) will be at the interface between the two phases. Therefore, it is common in simulations of these types, to refine the region containing the interface, allowing the rest of the mesh to remain relatively coarse (Bredmose and Jacobsen 2010; Cao et al. 2011). OpenFOAM® does provide dynamic refinement/unrefinement of the mesh about a fluid interface (OpenCFD 2014), but this functionality cannot be used in addition to the mesh motion solver, required for rigid body motion (see Section 3.1.2), and so will not be considered further in this work. A parametric convergence study of selectively refined meshes is planned as further work.

Meshing around structures

Up until now, we have only considered what is effectively an unoccupied wave tank. For the applications in Chapter 5, and ultimately to reach the objectives of this project, a structure has to be incorporated into the computational domain. Essentially this involves removing the portion of the mesh occupied by the structure and creating a set of additional boundaries requiring specific conditions to be satisfied. The boundary conditions on the structure are case specific and will be discussed alongside the applications in Chapter 5. Furthermore, the focus is typically on the fluid behaviour in the vicinity of the structure and so mesh refinement is normally required in this region to resolve the complex flow structures present (Bredmose and Jacobsen 2010; Chen, Zang, Hillis, Morgan and Plummer 2014). In this section, the methods used to add a structure and refine the mesh appropriately are outlined and the issues faced as a consequence of these additions discussed.

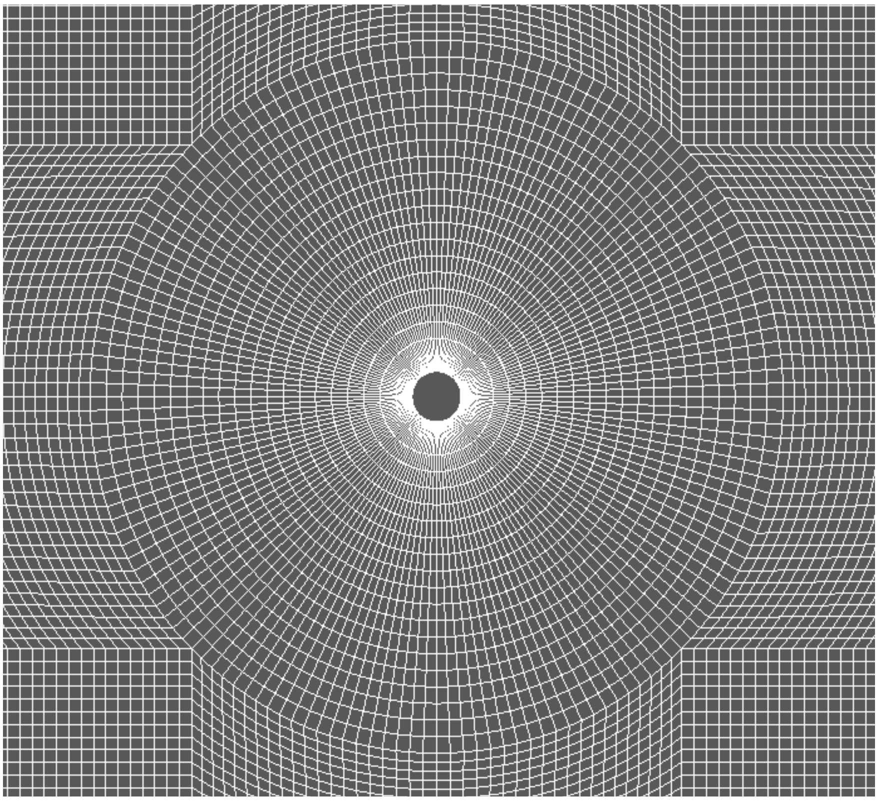

Figure 3.11: An example of the mesh in the vicinity of a truncated circular cylinder when using `blockMesh` to generate the mesh.

`blockMesh` can be used to include simple structures, such as a truncated cylinder, but even then the definition of the blocks required to achieve the desired refinement is tortuous. Figure 3.11 shows part of the mesh for such a cylinder case, generated using `blockMesh`. The complete mesh was made up of 49 separate blocks, 100 vertices, numerous curved edges and various grading vectors, all defined in an extremely complicated dictionary file. Figure 3.12 shows the resulting solution for the free surface surrounding the cylinder during a wave run-up simulation. The jagged nature of the free surface solution, on the edge of the cylinder, is of great concern. It is believed that this is due to a poorly designed mesh in the region close to the cylinder. Due to the way the mesh refinement is generated, when using `blockMesh`, the cells near the cylinder surface have very high ARs. As discussed earlier, high AR cells cause issues with the convergence of the solution and may be responsible for anomalous free surface behaviour on the cylinder surface. There is evidence of this issue

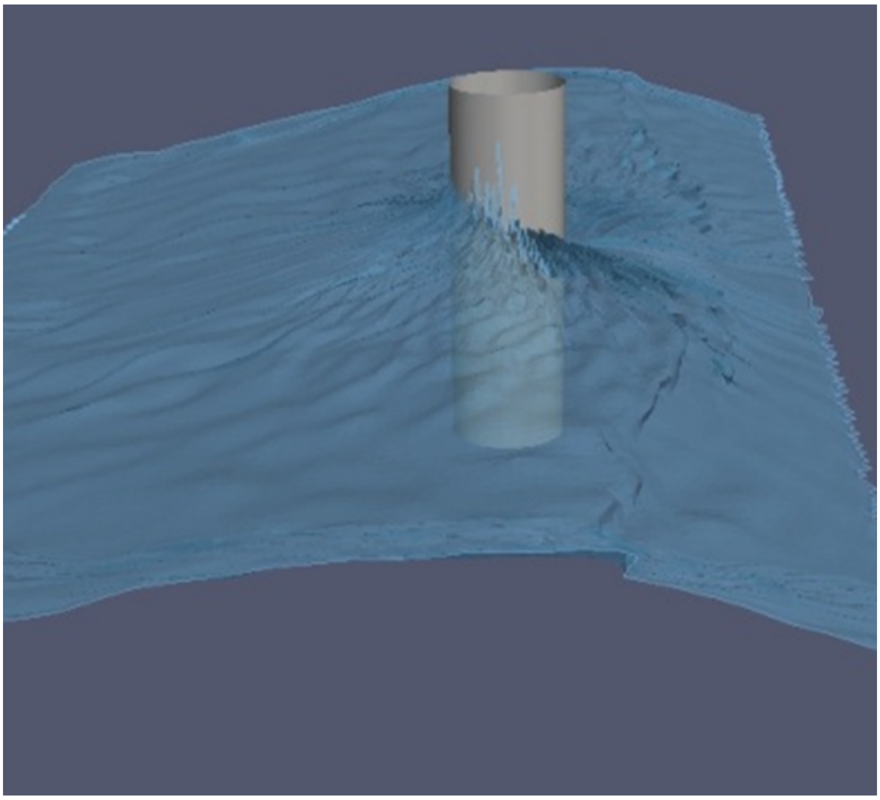

Figure 3.12: The resultant free surface solution around a truncated circular cylinder when the mesh has been generated using `blockMesh`.

in other work using a similar meshing method (Bredmose and Jacobsen 2010) but there are also examples where this does not appear to be a problem (Cao et al. 2011; Chen, Zang, Hillis, Morgan and Plummer 2014). However, due to the complexity involved when including even geometrically simple structures and the limited mesh refinement capabilities in `blockMesh`, an alternative, more powerful meshing tool is required.

Also included in the standard release of OpenFOAM® is a meshing utility called `snappyHexMesh` which can be used to generate three-dimensional meshes automatically from complex CAD surface geometries in Stereo-Lithography (STL) format. `snappyHexMesh` therefore allows for structures with relatively complicated geometries which could not be reasonably constructed using `blockMesh`. These meshes consist of hexahedra and split-hexahedra, and allow for very flexible mesh refinement and robust surface treatment by iteratively refining a starting mesh toward a pre-defined final mesh quality (OpenCFD 2014).

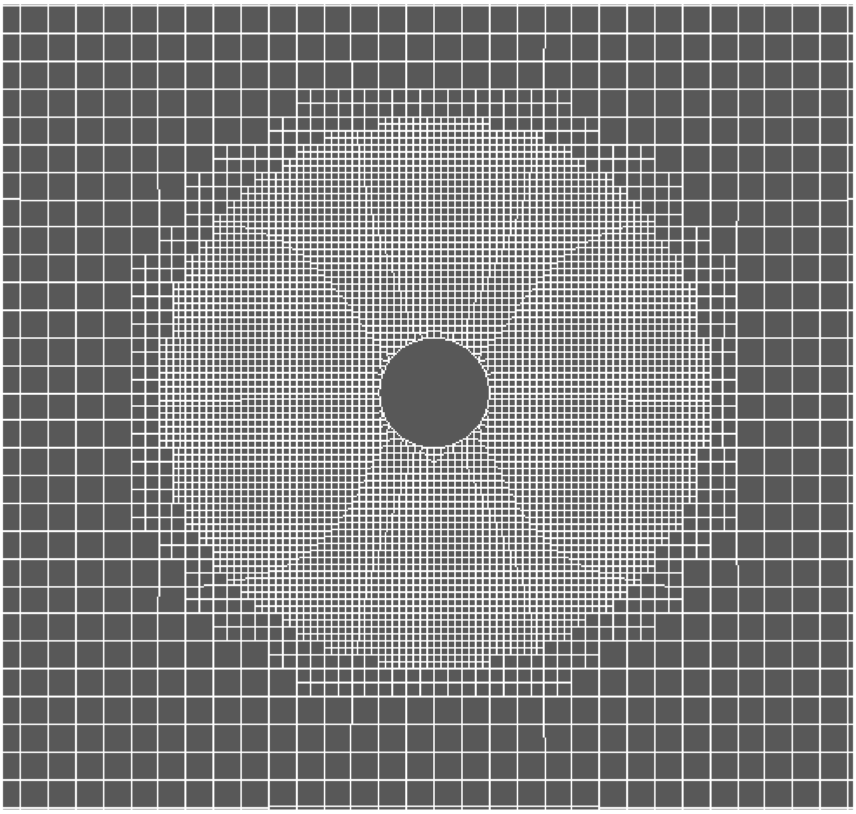

Figure 3.13: An example of the mesh in the vicinity of a truncated circular cylinder when using `snappyHexMesh` to generate the mesh.

Another advantage of `snappyHexMesh` over `blockMesh` is that it uses an octree (the 3D version of quadtree (Greaves 2004)) formulation for refining the mesh. Therefore, cubic cells remain cubic and refinement does not produce a directional bias, thus improving the CPU efficiency and convergence characteristics as discussed above.

Figure 3.13 shows the mesh for the same truncated circular cylinder as above when using `snappyHexMesh`. The quadtree (octree in 3D) refinement can be seen clearly. The resulting free surface solution can be seen in Figure 3.14. Clearly, the mesh generated using `snappyHexMesh` produces a superior result. The free surface is much smoother and the irregularities observed, when using `blockMesh`, are no longer present.

For even more complicated meshes and structures, there are a number of external meshing tools that are compatible with OpenFOAM®, including both open-source tools like Gmsh

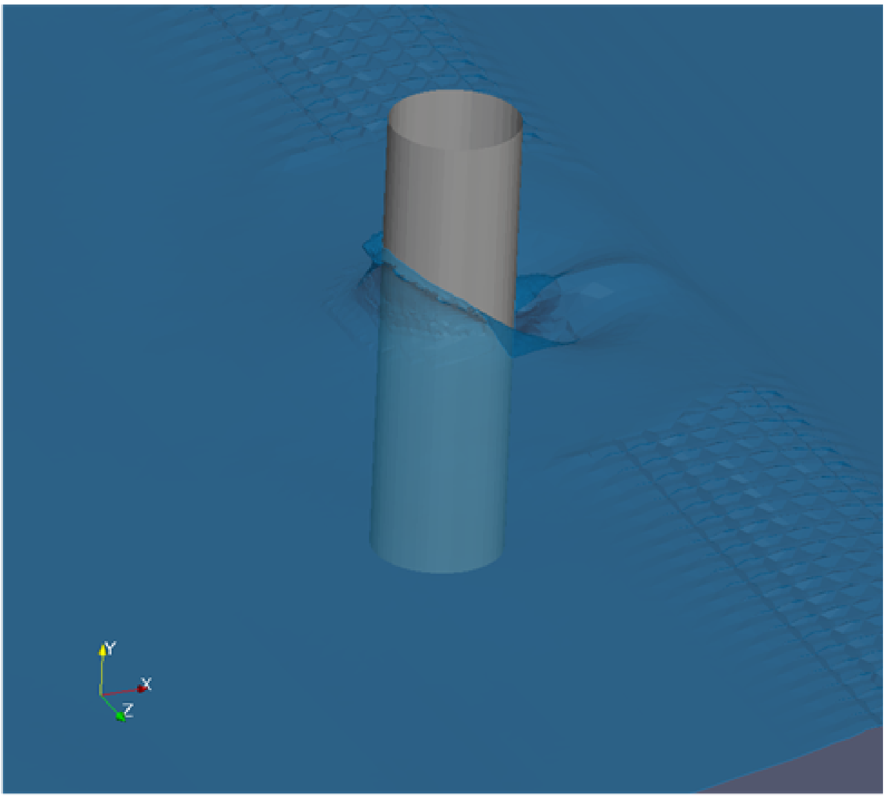

Figure 3.14: The resultant free surface solution around a truncated circular cylinder when the mesh has been generated using `snappyHexMesh`.

and commercial meshing software like Pointwise®. It is also possible to import meshes from other CFD codes. However, for the purpose of this project, `snappyHexmesh` has been deemed sufficient and will be used as the primary meshing tool throughout. Assessment of alternative meshing methods will remain a task for future projects.

One issue that has been encountered, when introducing a structure into the computation domain, is that unexpected air flow can be generated where the mesh has been altered. As can be seen in Figure 3.15, the presence of the structure causes an acceleration of the air phase in the vicinity of the interface, driving it parallel to the structures edge, drawing-in air from across the top of the interface and circulating it around. These anomalous velocities in the air phase can become very high as the simulation progresses (particularly when a laminar model is used) and in a number of cases the solution has become unstable as a result. It has been noted that, for co-located variable arrangements, large normal velocities

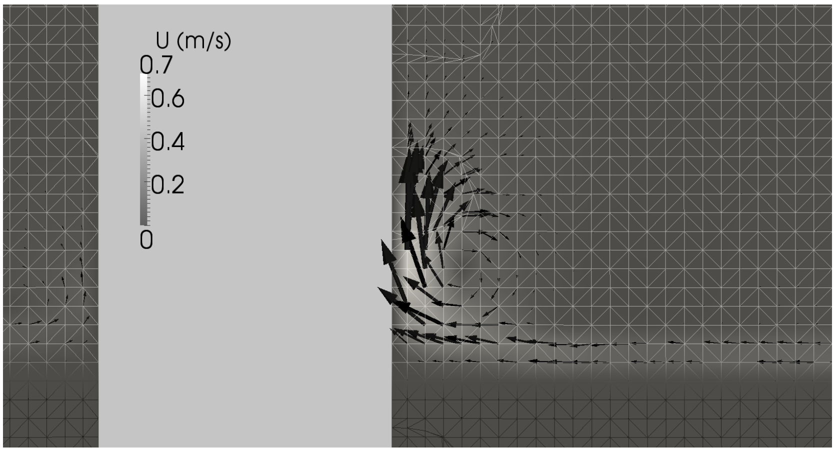

Figure 3.15: Abnormal air velocities caused by the addition of a structure. The air phase corresponds to the region where the mesh is coloured white, whilst the water phase has a black mesh. The glyph length is scaled with the magnitude of the velocity, U which is also shown by the colour scale.

can occur when steep pressure gradients exist in the vicinity of the boundary. Refining the mesh locally, often resulting in prismatic layers near bodies in the flow, can help to alleviate this issue (Ferziger and Perić 2002). `snappyHexMesh` allows for the addition of these ‘layers’ and a brief investigation shows a decrease in the anomalous air flow around structures when layers are used. However, a similar phenomenon has been observed when the mesh containing the interface is not uniform or when the mesh cells are misaligned with the interface. When layers are used, an otherwise uniform mesh can become distorted elsewhere in the domain, causing greater abnormal air flow problems than were present without the layers. The consequences of these observations are of great concern as the free surface is rarely aligned with the mesh when modelling waves and a uniform mesh at the interface is extremely restrictive when incorporating surface-piercing structures into the domain. Furthermore, as will be discussed later, by allowing the structures to move during the simulation, the mesh is continually warped causing further, time-dependent misalignment of cells at the interface. It is possible that these issues are an inherent problem with the VOF method and that, due to the treatment of the interface, momentum transfer between the two phases cannot be avoided. It is believed that this is particularly evident in cases where the densities vary greatly between the two fluids. The surface compression strategy and the value of the compression term may help to resolve these issues but until now only refinement of the mesh has been shown to improve the situation. So for the remainder of this project, layers will not be used and the mesh containing the free surface will be uniform and significantly more refined than the rest of the domain. Resolution of the issue of anomalous air flow generation will be revisited in future work.

Dynamic meshing and the rigid body solver

In order to simulate the fully coupled case of wave and floating body interaction, the boundary corresponding to the structure must be allowed to move relative to the rest of the domain. Furthermore the body's motion is unknown and forms part of the solution itself. OpenFOAM® supports a range of dynamic mesh functionality for solid body and internal mesh motion including *mesh deformation*, in which boundary motion is accommodated by simply moving mesh points, and various *topological changes*, which alter the number and connectivity of points at each time step (Jasak 2009). For cases in this project involving solid body motion, OpenFOAM® version 2.3.0 has been used throughout. This version includes a specialised motion solver which calculates the pressure and viscous forces, $\mathbf{F_N}$ and $\mathbf{F_T}$, on a given surface, S, by summing contributions from cell faces on that surface.

$$\mathbf{F_N} = \sum^{S} \mathbf{n} A p \tag{3.1}$$

$$\mathbf{F_T} = \sum^{S} \mathbf{n} A \cdot \left(-\frac{(\mu + \mu_t)}{\rho} \operatorname{dev}\left[\left(\Delta \mathbf{V} + \Delta \mathbf{V}^T \right) \right] \right) \tag{3.2}$$

where $\mathbf{n}$ is the unit vector normal to the cell face, A is the cell face area, μ_t is the *eddy viscosity* and 'dev' is the *deviatoric component* giving the total stress minus the mean stress. The solver then solves the 6DOF equations of motion for a rigid body boundary,

$$\mathbf{F_T} + \mathbf{F_N} + \mathbf{F_{restraints}} = m\mathbf{a_{cm}} \qquad \mathbf{M_T} + \mathbf{M_N} + \mathbf{M_{restraints}} = \mathbf{I} \cdot \dot{\omega} + \omega \times (\mathbf{I} \cdot \omega) \tag{3.3}$$

where $\mathbf{F_{restraints}}$ and $\mathbf{M_{restraints}}$ are the force and torque applied by any restraints, such as moorings, m is the body's mass and $\mathbf{I}$ its inertia matrix and $\mathbf{a_{cm}}$ and ω are the acceleration of the centre of mass and the angular velocity respectively.

A symplectic splitting technique is used to retain the structure and time-reversal symmetry of the rigid body motion when integrated. This helps to reduce the nonphysical dynamic behaviour observed in more traditional quaternion methods whilst improving the efficiency and stability of the simulations (Dullweber et al. 1997). The calculated motion then provides a boundary condition for the dynamic mesh solver which also controls internal mesh motion. Based on mesh motion using Radial Basis Functions (RBFs), the internal mesh cells are repositioned using spherical linear interpolation and the distance from the body (Bos 2009). A cosine profile is included in the distancing function to maintain the grid quality close to the body. This allows the mesh to deform in response to flow forces and is believed to be an improvement on previous versions in which the mesh quality could be easily degraded by rotating bodies causing shearing of mesh cells (OpenCFD 2014). In the case of a floating body, OpenFOAM® has been shown to accommodate large deformations without a significant loss of mesh quality provided the body does not capsize (Jasak 2009). However, despite the improvements made, mesh motion in OpenFOAM® still requires careful consideration. As the solid body moves, the grid points are continually repositioned, inevitably resulting in a loss of the original grid quality, particularly when large movements are observed; mesh cells can become highly deformed and their alignment altered radically if the parameters controlling the dynamic mesh solver are overlooked. It is essential that the mesh remains geometrically valid *i.e.* cell volumes and face areas must remain positive, cell and face convexness must be preserved and the mesh non-orthogonality must remain reasonable (Jasak 2009; Jasak and Tuković 2010). An example of unacceptable mesh deformation can be seen in Figure 3.16. As discussed earlier, highly deformed mesh cells can have a range of impacts on the numerical solution. Furthermore, the process of repositioning the grid points requires additional computational effort and additional mesh-induced discretisation errors are introduced when flow variable values are mapped between meshes (Jasak and Tuković 2010). It is therefore the responsibility of the user to ensure that the mesh quality, in cases with moving bodies, is not so degraded as to impact significantly on the solution while maintaining the accuracy and computational efficiency of the simulation. Specific use of this functionality will be discussed further in Chapter 5.

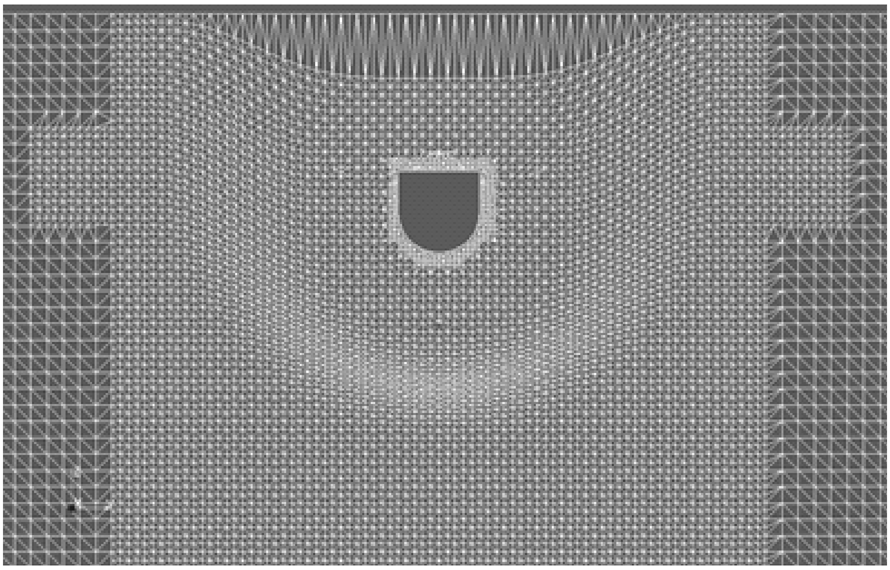

Figure 3.16: An example of unacceptable mesh deformation caused by a moving body and poorly specified dynamic mesh properties.

Dynamic mesh handling, for the purpose of rigid body motion solvers, remains a highly active development area and a number of alternatives exist to alleviate the issues observed in the adaptive meshing (or mesh deforming) method of OpenFOAM®. In cases with extreme changes in shape, where mesh deformation alone is not sufficient, a strategy of applying some modification to the mesh topology, connectivity or resolution is required, *i.e.* a sliding mesh interface or addition/removal of cells/cell layers (Jasak and Tuković 2010). One example, is the Cartesian cut cell method which is used in the commercial software ComFLOW®. In this method the body is 'cut' out of a background Cartesian mesh at each time step (Yang et al. 1997). This method can reduce the computational cost, remove any restrictions on body motion and eliminate the problems caused by mesh distortion. However, it is thought to produce less realistic behaviour compared with adaptive meshing methods (Higuera et al. 2013). Another example, employed in commercial software STAR CCM+, is the overset mesh, which consists of an additional fixed mesh, attached to the moving body, which moves relative to a background mesh (Schreck et al. 2012). This method removes the issues caused by cell deformation allowing for larger movements, but requires special treatment to transfer flow variables between the two meshes. Another option is tetrahedral edge swapping which has been shown to automatically handle surface breakup and separation of viscoelastic droplets post impact (Mooney et al. 2010). As this functionality is not currently available in OpenFOAM® it will not be consider further here. However, improving the dynamic meshing method and assessing alternatives have been identified as a key elements in any future work concerning wave interaction with floating objects.

3.1.3 Boundary conditions and initial fields

As mentioned in the previous chapter, each of the domain boundaries requires a set of ‘boundary conditions’ to specify the boundary data for each of the flow variables present. The generalised NWT consists of 6 boundaries: top, bottom, inlet - where the wave maker is, outlet - opposite the wave maker, front and back.

Although the domain in OpenFOAM® simulations is essentially always three dimensional, for cases with unidirectional waves and no structure, the calculations can be limited to two dimensions by specifying the `empty` boundary condition on those boundaries normal to the third dimension (front and back). Then no solution is required on these boundaries.

For the three dimensional cases in this project, the front, back, bottom and outlet boundaries are treated as walls with a `zeroGradient` condition on the phase fraction, α, and a `fixedValue` of zero (no slip) condition on the velocity, $\mathbf{V}$. Due to the single-pressure treatment of the two-phase, VOF method, the momentum equation at a wall would require a different pressure gradient for each phase if the densities are different. This is impossible in a single-pressure system and so, in incompressible multiphase solvers, the pressure is modified to simplify the pressure boundary condition on walls and remove steep gradients due to hydrostatic effects (Rusche 2002). The modified mixture pressure used in OpenFOAM® is then

$$p_{\rho gh} = p - \rho_1 \mathbf{g} \cdot \mathbf{x} \tag{3.4}$$

which is the *static pressure*, p, minus the *hydraulic pressure*, ρgh, where $\mathbf{x}$ is the position vector, $\mathbf{g}$ is the vector acceleration due to gravity and ρ_1 is the density of the denser fluid (Rusche 2002). The $p_{\rho gh}$ gradient on these boundaries has then been set to a derived value such that the flux on the boundary is equal to that specified by the velocity boundary condition (`fixedFluxPressure`) (OpenCFD 2014).

On the top boundary a generic outflow condition is applied to the phase fraction which applies a zero-gradient condition for positive flux (out of the domain) and a user-defined value (of zero in this case) for negative flux (`inletOutlet`). This means water is allowed to leave the domain through the top boundary but it cannot enter. The `pressureInletOutletVelocity` condition is used for the velocity on the top boundary. This applies a zero-gradient condition for positive flux and derives a value from the normal component of the internal cell value for negative flux. A `totalPressure` boundary condition has been applied to the pressure on the top boundary. This ensures that the total pressure, $p_0 = p + \frac{1}{2}\rho|\mathbf{V}|^2$, is fixed (OpenCFD 2014).

The boundary conditions on the inlet require a more detailed discussion as these are what drive the flow of waves in a NWT (analogous to the wave maker in physical experiments). The various methods of wave generation are outlined below; a full description of the method used in this project can be found in Chapter 4. Turbulence quantities and their treatment at domain boundaries will be discussed alongside specific turbulence models in Section 3.1.6.

In order to finally close the equations and ready the simulation for initiation, the flow variable values at time $= t_0$ need to be specified. As the applications in this project are based on physical experiments, the initial conditions correspond to still water with a specific depth. The velocity in both the air and water phases is set to zero and the pressure is derived from hydrostatic theory (*i.e.* $\rho g h$). The phase fraction, α, equals 1 in 'wet' cells completely below the Still Water Level (SWL) and 0 in 'dry' cells completely above. For cells containing the interface the phase fraction is specified as the proportion of their volume which is below the SWL. This is important as other methods, in an attempt to improve efficiency, only allow for fully wet or dry cells when setting the initial field values (and when specifying the inlet boundary condition) (Higuera et al. 2013). Without a greatly refined mesh this has been seen to cause persistent discrepancies and spurious oscillations at the free surface and so the specification of partially wet cells is deemed essential (Jacobsen et al. 2012).

3.1.4 Wave Generation

As mentioned in the previous section the inlet boundary requires special treatment in order to make provision for the generation of waves. A number of authors have proposed a variety of methods for wave generation in NWTs. These include numerical representations of physical wave makers using mesh motion (Zhao and Hu 2012), specification of boundary fluxes via mathematical expressions based on specific wave theories (Jacobsen et al. 2012) and adaption of the governing equations to include addition wave-making source terms (Lin and Liu 1999). In this section, the most common methods of wave generation in NWTs will be discussed, including an assessment of their pros and cons. Finally, the method to be used in this project will be selected. Further information on the specific wave generation in this project will then be provided in Chapter 4.

Numerical wave paddle (physical wave generation)

Continuing the analogy with physical wave tanks, the first option for wave generation in a NWT is to create a ‘numerical wave paddle’ (Zhao and Hu 2012), *i.e.* give the inlet wall-type boundary conditions and a prescribed motion based on wave maker theory (Dean and Dalrymple 1991; Schäffer 1996). There are two common types of wave maker, in physical experiments, piston-type and flap-type (see Figure 3.17). However, more specific and theoretically more efficient wave makers have been proposed that, although often restricted by practical limitations in reality, could be implemented in NWTs without issue (Fochesato et al. 2007). The advantage of this method is that the numerical simulation resembles a physical experiment more closely than any other method. The only input parameter is the wave maker displacement which is usually known. However, the mesh motion required is likely to increase the CPU demand and would inevitably degrade the mesh quality in mesh morphing methods. Furthermore, the solution would be forced to include the complex flow structures in the vicinity of the wave maker which would further increase the execution time and likely introduce additional inaccuracies. For these reasons, a more efficient alternative is sought and this method will not be considered further.

As a compromise, some authors have taken the idea of a numerical wave maker and instead

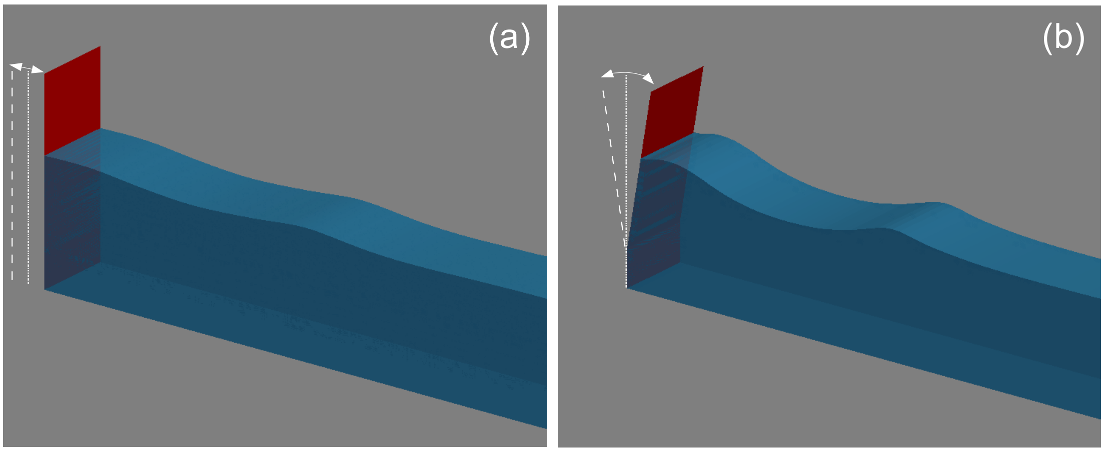

Figure 3.17: Numerical representation of physical wave makers; (a) piston-type and (b) flap-type.

of prescribing the motion of the boundary they have prescribed the fluid velocity, surface elevation and pressure on a fixed boundary as if it were being accelerated by a wave maker (Higuera et al. 2013). This reduces the complexity of having a moving mesh but makes the input data more complicated as some foreknowledge of the run-up on the paddle's face and the pressure distribution is required. Furthermore this method assumes the stroke length (*i.e.* the change in position) of the wave maker is small, and therefore can be neglected. This may not be the case when generating large waves.

Expression-based boundary conditions (artificial wave generation)

Similarly to the method of Higuera et al. (2013), a number of authors have used boundary conditions based on expressions involving the flow field variables to generate waves. Some have chosen to eliminate the wave maker aspect completely and attempt to create the waves on the boundary, as if they had been generated some distance before hand. Although the standard release of OpenFOAM® 2.3.0 does not support wave generation, a number of implementations of this type have been developed for OpenFOAM® and distributed independently in the form of additional toolboxes: `groovyBC`, part of `swak4Foam`, allows boundary conditions to be defined as arbitrary, non-uniform expressions for the flow variables (Gschaider 2014); `waves2Foam` is a toolbox which allows for the generation of waves using a set of generic wave theories (Jacobsen et al. 2012); and `IHFOAM` allows similar wave generation to `waves2Foam` (Higuera et al. 2013). These methods do not need a dynamic mesh and allow for a greatly reduced domain size (and CPU effort) compared with physical experiments by avoiding the complex flow structures that can occur close to the wave maker. The main drawback of these methods is that, the precise wave properties (surface elevation, velocity and pressure) on the inlet boundary need to be known. Various wave theories can be used but typically these represent an additional approximation to the true values at the boundary, particularly when complex incident waves are desired or when trying to reproduce physical experiments. Furthermore, discrepancies between the flow variable values specified on the boundary and those calculated just inside the fully nonlinear domain, due to the use of simplified wave theories or the unanticipated return of reflected waves, can lead to instabilities and ultimately divergence of the solution. Furtherstill, it has been shown that, in long simulations, these methods can lead to an increase in the energy of the system and a rise in the water level as a result of excess mass in the incident wave crests (Torres-Freyermuth et al. 2010; Jacobsen et al. 2012; Higuera et al. 2013). Despite these issues, an expression-based wave generation method will be used throughout this project. A more detailed discussion on the implementation of the selected method and wave theories used in this project can be found in Section 4.3. Comparison with other methods is beyond the scope of this project.

Other methods

Other methods of wave generation exist, include purely numerical, mass and momentum, source term methods which add extra terms into the governing equations to generate waves (Lin and Liu 1999; Hafsia et al. 2009). These methods also do not require a moving mesh but they show no significant advantage over expression-based boundary conditions and so will not be considered further in this project.

3.1.5 Wave Absorption

Another important element in the development of a NWT is wave absorption. As in physical wave tanks, the spatial constraints on the size of the domain make reflected waves, rebounding from the domain boundaries, of considerable concern to NWT users. This is compounded in NWTs as efficient numerical simulations typically rely on minimising the sample area to reduce the number of grid points, which subsequently moves the boundaries closer to the region of interest. As the goal is to reproduce the essentially unconstrained situation in the field, unwanted interference caused by reflected waves must be removed.

More often than not and exclusively in this project, experiments involve unidirectional waves travelling from one end of a long narrow tank to the other and so of greatest concern are those reflected waves returning from the end wall of the tank. In cases with a structure, scattered waves which are subsequently reflected from the side walls are also a problem and will be discussed further in Chapter 5. Nevertheless, an effective way of removing the effect of reflected waves is a vital part of any NWT.

There exists a wide variety of methods employed to dissipate or absorb the waves reaching domain boundaries and therefore remove any unwanted reflections in the NWT. The majority of these methods fall under the classification of ‘passive’ wave absorbers, however, ‘active’ wave absorbers have recently begun to emerge (Higuera et al. 2013).

Passive wave absorption

Passive wave absorption methods come is many different forms. Firstly, it is possible to design a ‘beach’ in a NWT, much like those seen in physical wave tanks, which is shaped in such a way that the waves are made to break, dissipating their energy. This is a reasonably effective way of removing wave energy and any shaped beach is easily implemented in a NWT. However, simulating breaking waves is one of the most computationally expensive phenomena to model numerically and so this method is less efficient than many of the alternatives. Furthermore long waves, which typically do not break, are still reflected.

In NWTs, one has the opportunity to take advantage of a number of unphysical, passive wave absorption methods. As mentioned earlier, poor mesh design can lead to discretisation errors in the solution. Although this effect, called *numerical diffusion*, needs to be limited in the area of interest, it can be utilised to artificially remove wave energy in NWTs. By allowing the mesh cells to increase in volume towards the end of the NWT the discretisation error increases and the flow variables, like velocity, are diffused (reduced). Alternatively, the difference schemes used to discretise the equations can be altered towards the end of the NWT to take advantage of naturally diffusive methods, like upwinding. This has the effect of removing wave energy without the need to simulate wave breaking and can be much more computationally efficient. However, these methods are pretty crude, uncontrolled and likely to be inefficient so more sophisticated methods have evolved.

A more systematic passive method of wave absorption involves altering the fluid behaviour in a region of the NWT known as a *sponge layer*. Typically, within sponge layers an additional forcing term is added to the governing equations which increases the energy dissipation due to internal friction within the fluid. Sponge layers are, in many ways, analogous to the addition of a porous medium for wave absorption in physical experiments. For cases in which internal reflections could interfere with the wave maker, this concept has also been used to introduce a prescribed disturbance, such as wave generation, by means of a *forcing sponge* (Bodony 2006). Sponge layers are widely used in NWTs solving the RANS equations (Lin and Liu 1999; Lara et al. 2006, 2008) but the required length of absorption zone depends on the wavelength and can become excessively large, drastically increasing the CPU cost. A further incarnation of the sponge layer, dubbed *Relaxation Zones* (RZs), can be employed by multiplying the computed values in the absorbing region by a decay function, γ_R. For the general case (*i.e.* including absorption on wave generation boundaries) a generic flow variable, ϕ is 'relaxed' as so,

$$\phi = \gamma_R \phi_{\text{computed}} + (1 - \gamma_R)\phi_{\text{target}}, \tag{3.5}$$

where ϕ_{target} is the target solution prescribed by the boundary conditions (*i.e.* wave generation or pure absorption) and the decay function,

$$\gamma_R(\chi_R) = 1 - \frac{\exp\left(\chi_R^{\mu_R}\right) - 1}{\exp(1) - 1} \quad \text{for} \quad \chi_R \in [0;1], \tag{3.6}$$

where χ_R is the scaled x-coordinate, which increases linearly from 0 at the start of the RZ to 1 at the end, and $\mu_R = 3.5$ is the relaxation coefficient (Fuhrman et al. 2006; Jacobsen et al. 2012). This method of wave absorption is available for OpenFOAM® via the addition toolbox `waves2Foam` (Jacobsen et al. 2012). Jacobsen et al. (2012) quantify the performance of a purely absorbing RZ for periodic shallow water waves and different length RZs. They found the absorption to be especially good for RZs with a length equal or greater than the wavelength. However, for larger amplitude waves the reflection increases for a given wavelength and for the steepest shallow water wave considered in Section 3.1.2, a 99 % absorption would require a RZ of at least six times the wavelength. The required length of the RZ is the main weakness of this method resulting in greatly increased domain sizes and consequently greater CPU demand (Higuera et al. 2013). Furthermore, the performance of the RZ has yet to be quantified for deep water waves. Alternative decay functions have been proposed for the Relaxation Zone including a free polynomial weighting; a third order polynomial weighting, specifically designed for RZs simultaneously generating and absorbing waves (Engsig-Karup 2006), and; additional temporal correction based on the local Courant number (Seng et al. 2012; Jacobsen 2014). However, the performance of these additional weighting functions has not be quantified and so they will not be considered further here. It has been reported that the use of numerical damping zones like RZs can produce unbounded increases in the mean water level and instability in VOF simulations (Mendez et al. 2001). Nevertheless, the RZ method will be used throughout the project, with the original exponential decay function. Comparison with alternative methods will remain a task for future studies.

Active wave absorption

Active absorption has been implemented in state-of-the-art physical wave makers and involves a feedback loop between the force experienced by a wave maker and that predicted in the absence of any unwanted wave energy (reflections). The wave maker then adjusts its motion to remove any unwanted waves whilst continuing to generate the target wave. A similar idea has recently been implemented in a NWT, allowing for wave absorption by adjusting the velocities on the boundary according to the specified target. This method prevents reflections without increasing the size of the domain, while retaining the boundedness of the water level and the stability of the solution (Higuera et al. 2013). Despite the apparent advantages of the active absorption method its performance, from the available documentation, remains unclear and so it will not be considered further here.

3.1.6 Turbulence Modelling

Another decision that must be made in the pre-processing stage is whether or not turbulence needs to be included in the model. All flows become *turbulent* (*i.e.* chaotic and random with continuous changes in pressure and velocity) when the *Reynolds number* (Re) exceeds a critical value, Re_{crit}. For fluid flows with Reynolds numbers greater than this value some strategy for including the effects of turbulence is required.

The Reynolds number is given by,

$$Re = \frac{UL}{\nu}, \tag{3.7}$$

where U and L are velocity and length scales characteristic of the flow and ν is the *kinematic viscosity*. In the context of a NWT it is unclear as to when turbulence must be included in the simulation. It is well known that when waves break turbulence becomes important (Jacobsen et al. 2012; Brown et al. 2014) and so one might expected turbulence to play a crucial role during the interaction of an extreme wave with a WEC.

As mentioned in Section 2.2, a number of methods exist to include the effects of turbulence, without resolving the entire range of scales present in turbulent flow. Reynolds decomposition is one of the most popular methods used in engineering based CFD and will be the only method considered here, despite producing less information than some of the more complex methods. This technique yields the Reynolds-Averaged Navier-Stokes (RANS) equations (Equation 2.19), via time-averaging, producing an additional set of unknowns called the Reynolds stresses. In order to calculate these additional terms, *turbulence modelling* is used (Ferziger and Perić 2002; Versteeg and Malalasekera 2007).

There have been many different turbulence models developed for the RANS equations and OpenFOAM® is distributed with many of the most common ones. In cases, such as recirculating flow, where convection and diffusion have significant impact on the turbulence, the simplest turbulence models are not feasible (Versteeg and Malalasekera 2007). Instead statements which consider the dynamics of the turbulence are used. However, some of the more complex models increase the computational demand excessively and have been considered impractical here. For the purpose of this project only a few widely used and well established models will be considered. The most common of these is the k-ε model which considers the processes affecting the energy in the turbulence, the *turbulent kinetic energy*, k. In turbulent flows the instantaneous kinetic energy,

$$k(t) = K + k, \tag{3.8}$$

where K is the mean kinetic energy. Two further governing equations, for the mean flow kinetic energy and the turbulent kinetic energy, can then be constructed from the RANS equations (Equation 2.19) (see Versteeg and Malalasekera (2007) for a derivation).

An important quantity when studying the dynamics of turbulence is then *the rate of dissipation of turbulent kinetic energy per unit mass*,

$$\varepsilon = 2\nu\overline{s'_{ij} \cdot s'_{ij}}, \tag{3.9}$$

where s'_{ij} is the fluctuating part of the rate of deformation of a fluid element in a turbulent flow and the overbar again refers to a time-averaged quantity. It is possible to devise an exact transport equation for ε but the number of unknowns and unmeasurable terms are excessive. This has led to the development of the *standard* k-ε *model* which contains the following transport equations for k and ε (Versteeg and Malalasekera 2007):

$$\frac{\partial(\rho k)}{\partial t} + \nabla \cdot (\rho k \mathbf{V}) = \nabla \cdot \left[\frac{\mu_t}{\sigma_k}\nabla k\right] + 2\mu_t S_{ij} \cdot S_{ij} - \rho\varepsilon, \tag{3.10}$$

$$\frac{\partial(\rho \varepsilon)}{\partial t} + \nabla \cdot (\rho \varepsilon \mathbf{V}) = \nabla \cdot \left[\frac{\mu_t}{\sigma_\varepsilon}\nabla \varepsilon\right] + C_{1\varepsilon}\frac{\varepsilon}{k}2\mu_t S_{ij} \cdot S_{ij} - C_{2\varepsilon}\rho\frac{\varepsilon^2}{k}, \tag{3.11}$$

where S_{ij} is the mean component of the rate of deformation of a fluid element and

$$\mu_t = \rho C_\mu \frac{k^2}{\varepsilon} \tag{3.12}$$

is the *eddy viscosity*. The values of the five constants have been found empirically through extensive experimental work:

$$C_\mu = 0.09 \quad \sigma_k = 1.00 \quad \sigma_\varepsilon = 1.30 \quad C_{1\varepsilon} = 1.44 \quad C_{2\varepsilon} = 1.92 \tag{3.13}$$

(Versteeg and Malalasekera 2007). In the standard k-ε model the Reynolds stresses are then found using the Boussinesq relationship:

$$-\rho \overline{u_i' u_j'} = \mu_t \left(\frac{\partial V_i}{\partial x_j} + \frac{\partial V_j}{\partial x_i} \right) - \frac{2}{3}\rho k \delta_{ij} = 2\mu_t S_{ij} - \frac{2}{3}\rho k \delta_{ij} \tag{3.14}$$

where δ_{ij} is the *Kronecker delta* ($\delta_{ij} = 1$ if $i = j$ and $\delta_{ij} = 0$ if $i \neq j$). Along with the definition of the eddy viscosity (Equation 3.12) this assumes that turbulence only depends on the local flow conditions. In more realistic models, the Reynolds stress is also a function of the rate of change of mean strain. This assumption of isotropic turbulence results in poor performance in cases with transitional turbulence or adverse pressure gradients and has led to development of the Renormalised Group (RNG) and nonlinear k-ε models (Versteeg and Malalasekera 2007; Brown et al. 2014).

On the walls of the domain, the boundary conditions for k and ε require special treatment and the approach is dependent on Re. At high Re, the standard k-ε model uses the *log-law* behaviour of the turbulent region close to a smooth wall to develop a set of *wall functions* for the mean velocity, k and ε (Versteeg and Malalasekera 2007). These are based on the local wall shear stress, τ_w, through the *friction velocity*, $u_\tau = \sqrt{\tau_w/\rho}$:

$$u^+ = \frac{U}{u_\tau} = \frac{1}{\kappa_{VK}} \ln(E\zeta_{\mathrm{P}}^+) \quad k = \frac{u_\tau^2}{\sqrt{C_\mu}} \quad \varepsilon = \frac{u_\tau^3}{\kappa_{VK}\zeta} \tag{3.15}$$

where $\kappa_{VK} = 0.41$ is Von Karman’s constant, $E = 9.8$ is the wall roughness for smooth walls,

ζ is the coordinate distance normal to the wall and $30 < \zeta_{\mathrm{P}}^{+} = \rho u_\tau \zeta_P / \mu < 500$ describes the region in which the log-law holds. At low Re, the log-law does not hold and these functions cannot be used without modification (Versteeg and Malalasekera 2007).

The k-ε model has been used to simulate breaking waves and produces good results up until the point of breaking when it tends to over-estimate the eddy viscosity, leading to increased mixing and a reduction in surface elevation. Furthermore, k-ε models generally predict wave breaking to occur earlier than seen in experiments and underestimate the undertows (Zhao et al. 2004).

An alternative to the k-ε model is the k-ω model proposed by Wilcox (as cited in Versteeg and Malalasekera (2007)) in which the *turbulence frequency*, $\omega = \varepsilon / k$, is the second variable. The k-ω model does not require wall functions and has been shown to perform better than the standard k-ε model in cases with adverse pressure gradients (Brown et al. 2014). Furthermore, the k-ω model has also been used to simulate breaking waves (Jacobsen et al. 2012) but does not appear to be an improvement on the k-ε model in that case (Zhao et al. 2004). Even within Reynolds decomposition, there are many more models and turbulence modelling as a whole remains a highly active research area. Some specific models have started to be developed for waves (Zhao et al. 2004) but a full assessment of the available turbulence models is outside the remit of this project. In this project only the k-ε and RNG k-ε models have been considered. For more information on turbulence closure models see Versteeg and Malalasekera (2007).

3.2 Solver

Once pre-processing is complete, the next stage in the process is the solver. As discussed in Chapter 2, there are a considerable number of options available for the governing equations, the discretisation method, the pressure-velocity coupling, the integration and differencing schemes, the stopping criteria, the solver tolerance, etc. and it is beyond the scope of this project to consider them all in detail. To reiterate, the `interFoam` solver, which solves the RANS equations for two immiscible, incompressible fluids using a finite volume discretisation, the PISO algorithm for the pressure-velocity coupling and a VOF treatment of the interface, will be used exclusively throughout this project. In this section only the numerical schemes and solver options used in this particular project will be considered fully. The pros and cons of alternative options will remain as future work.

3.2.1 Numerical schemes

In OpenFOAM® the user has an unrestricted choice of schemes for dealing with derivatives and interpolations. The set of terms, requiring a specified numerical scheme, are subdivided within the `fvSchemes` dictionary (OpenCFD 2014). In the context of NWTs, information regarding the appropriate use of each numerical scheme and the qualities of various options is scarce. Typically, this information is not documented in NWT literature and so decisions regarding the selection of specific schemes can only be based on their use in generic cases. As mentioned above, critical assessment of the full range of numerical schemes will not be given here. Instead, what follows is a summary of the schemes used in the project and is intended purely for completeness and reproducibility.

Throughout this project, 1-point Gaussian integration (the midpoint rule), labelled as '`Gauss`' is used as default without exception. This requires interpolation of the values at face centres from those at the cell centres. The interpolation schemes used for each of the various terms are outlined below.

For the *gradient terms*, linear interpolation is deemed to be effective (OpenFOAM Foundation 2012) and is used throughout. For the *divergence terms*, *e.g.* $\nabla \cdot (\rho \mathbf{V}\mathbf{V})$, there are many more options. Typically second-order, unbounded, linear interpolation is used. However, when boundedness is a requirement, a number of first/second order, bounded, TVD schemes, such as the van Leer limiter or the MUSCL limiter, have been used. The Laplacian schemes, *e.g.* $\nabla \cdot (\nu \nabla \mathbf{V})$, require an interpolation scheme for the diffusion coefficient, ν in this case, as well as a surface normal gradient scheme (`snGradScheme`), for $\nabla \mathbf{V}$ in this case. Linear interpolation is used unremittingly and the unbounded, second-order, conservative `snGradScheme`, `corrected` is applied as standard.

Up until now we have only discussed the spatial discretisation of the governing equations. However, in transient solutions (*i.e.* those which are changing with time) the equations must also be discretised in the fourth dimension: *time*. Fundamentally, the solution, ϕ, at some short time, δt, after the initial time, t_0, needs to be found. Then, the solution at time, $t_1 = t_0 + \delta t$ can be taken as the new initial value and the solution advanced, or 'marched', in 'time-steps'. The simplest methods are based on

$$\int_{t_n}^{t_{n+1}} \frac{d\phi}{dt} dt = \phi(t_{n+1}) - \phi(t_n) = \int_{t_n}^{t_{n+1}} f(t, \phi(t)) dt \tag{3.16}$$

where the integral on the right hand side is not known and so must be found using some approximation. Common methods include: the *explicit* or *forward Euler* method, which approximates the right hand integral as the value of the integrand at the initial time, t_n; the *implicit* or *backward Euler* method which approximates the integral as the value at the final time, t_{n+1}; the *midpoint rule* which uses the midpoint of the interval, $t_{n+\frac{1}{2}}$, and; the *trapezoid rule*, which is the basis for the popular Crank-Nicholson method and uses a straight line interpolation between the initial and final points. For these 'two-level' methods, which only require values of the unknown at two times, the highest possible accuracy is second-order. The solutions are good if Δt is small but at larger time-steps these methods are 'unconditionally stable', producing bounded solutions provided $\partial f(t, \phi)/\partial \phi < 0$. However, at very larger time-steps, the first-order, implicit Euler method still produces a smooth result whereas the second-order, trapezoid rule can produce oscillating results. Therefore, when solving nonlinear equations the implicit Euler method tends to behave well, while the trapezoid method can be unstable (Ferziger and Perić 2002). Higher order methods, such as multi-point and Runge-Kutta methods, are possible and have been implemented into NWT simulations (Tanizawa 2000), but these require information at more points increasing the memory requirements and the CPU demand on the simulation (Ferziger and Perić 2002). Only two-level methods will be considered in this project, for more information on these, and more complicated, methods see Ferziger and Perić (2002). Furthermore, for the purpose of this project, we shall limit the options to either: the first-order implicit Euler or the second-order, Crank-Nicholson methods. The implicit Euler Scheme is robust and efficient, and is an appropriate choice for slow-varying flows (Dawish and Moukalled 2006). However, this method is known to suffer from numerical diffusion and when the time evolution of the free surface is important higher order methods, such as Crank-Nicholson, should be used (Muzaferija and Perić 1999). OpenFOAM® offers the Crank-Nicholson scheme with an off-centering coefficient, ψ_B, which blends the scheme from pure Crank-Nicholson, when $\psi_B = 1$, to pure Euler, when $\psi_B = 0$. This can be used to improve the overall stability in cases where pure Crank-Nicholson is unstable (OpenFOAM Foundation 2012).

For more information on the various numerical schemes available refer to the OpenFOAM user guide (OpenFOAM Foundation 2012).

3.2.2 Time and input/output control

The `controlDict` dictionary acts as a case control (or steering) file, stating a range of parameters, used to create the database upon which the inputs/outputs of the solver are based. Here the start and stop times, the write interval and the format of the written data must be defined. However, the most important part of the `controlDict` is the specification of the time-step, δt, which defines the amount of time by which the solution is advanced during each iteration of the solver.

In the general case, to ensure temporal accuracy and numerical stability (Anderson 1995), the Courant-Friedrichs-Lewy (CFL) condition must be satisfied,

$$\text{Co} = \frac{\delta t |\mathbf{V}|}{\delta x} < 1 \tag{3.17}$$

where Co is the *Courant number* for a particular cell, δt is the time-step over which the solution is progressed, $|\mathbf{V}|$ is the magnitude of the velocity through that cell and δx is the convected distance across the cell in the direction of that velocity (Ferziger and Perić 2002).

Time-step control is considered to be important in cases with a free surface as the algorithm is thought to be more sensitive to Co than standard flow calculations. For these cases Co should not exceed 0.5 (OpenCFD 2014). However, the flow velocity, $|\mathbf{V}|$, typically varies throughout the domain and so δt normally has to be chosen based on the worst case scenario (highest velocity, smallest cell) with the maximum local Courant number, Co^0. For simple cases, with predictable velocities, a fixed time-step can be used to satisfy the CFL condition but in more complex cases this is not possible. For these cases, OpenFOAM® contains an `adjustableTimeStep` function which automatically adjusts the time-step so that it satisfies the CFL condition where the maximum Courant number, $\mathrm{Co}_{\mathrm{max}}$, for the phase fields, `maxAlphaCo` and other fields, `maxCo`, can be specified separately. Then the new time step

$$\delta t^n = \min\left\{ \frac{\mathrm{Co}_{\mathrm{max}}}{\mathrm{Co}^0}\delta t^0,\ \left(1+\lambda_t \frac{\mathrm{Co}_{\mathrm{max}}}{\mathrm{Co}^0}\right)\delta t^0,\ \lambda_2\delta t^0,\ \delta t_{\mathrm{max}} \right\}, \tag{3.18}$$

where δt^0 is the previous time-step and δt_{max} is the prescribed limit on the size of the time-step. λ_1 and λ_2 are damping factors used to avoid time-step oscillations and possible instabilities (Berberović et al. 2009). Berberović et al. (2009) suggested $\mathrm{Co}_{\mathrm{max}}$ should not exceed 0.2 and set $\lambda_1 = 0.1$ and $\lambda_2 = 1.2$.

For the convergence tests in Section 3.1.2 the `adjustableTimeStep` function was used with `maxAlphaCo` = `maxCo` = 0.5 and a `maxDeltaT` of 1 s. In order to analyse the effect of various length time-steps, however, a time-step dependency test was performed on the solitary wave run-up case (described on page 57). Three uniform, square-celled meshes of different resolution, were used and the length of the time-step was fixed throughout each simulation. Figure 3.18 shows the maximum run-up against the time-step, `DeltaT`, for the three meshes as well as the results when using the `adjustableTimeStep` function (the average `DeltaT` is used for plotting purposes). Finally the maximum Courant number for each simulation is also plotted.

It can be seen that the maximum Co increases linearly with `DeltaT` and the rate of increase is proportional to the number of grid cells used. This is to be expected, as the spatial length scales are reduced, the temporal length scales must also be reduced to maintain the same Co. This confirms that in order to reduce the Co number and satisfy the CFL condition either an increase in the cell size or a decrease in time-step can be applied. Increasing the cell size is undesirable, however, as this would reduce the resolution of the output and increase the truncation error and numerical diffusion in the simulation.

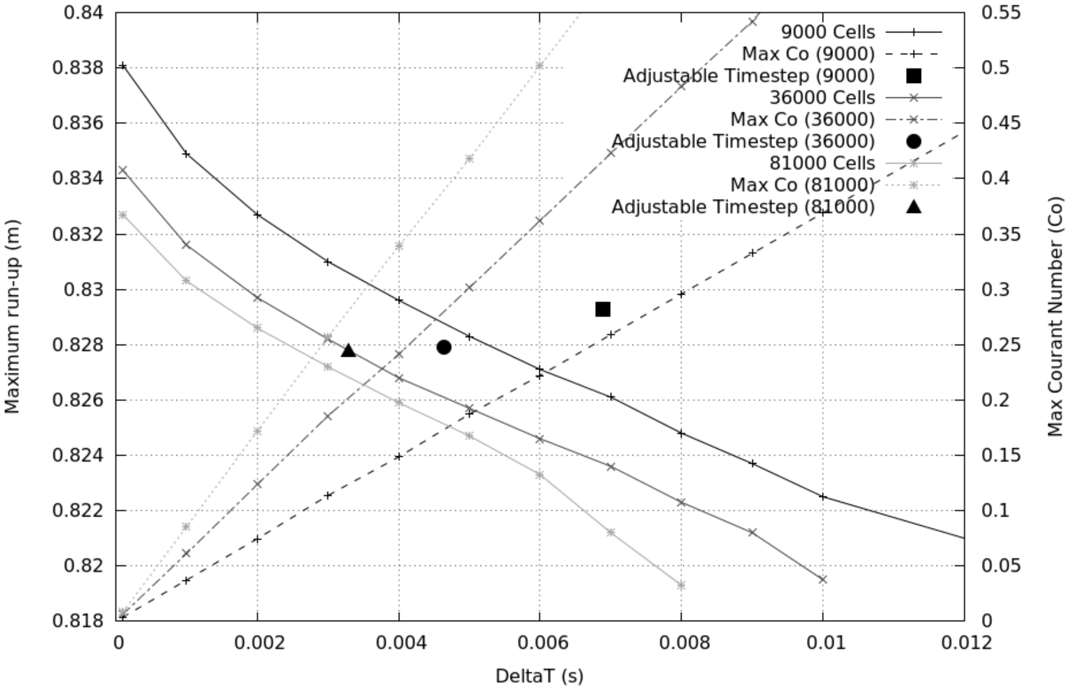

Figure 3.18: Maximum run-up of a 0.4 m high solitary wave on a fixed wall, for three different square celled meshes of different resolution, plotted against the fixed time step `DeltaT`. Also plotted are the maximum run-up against the average time-step for simulations using the `adjustableTimeStep` function and the maximum Courant number obtained for simulations with fixed time-step `DeltaT`.

Initially it was thought that the time-step dependency test would show a similar pattern to the mesh dependency test where the solution would converge on a stable value for the maximum run-up as the time-step was reduced. This is indeed the case when using the `adjustableTimeStep` but the data for maximum run-up against a fixed `DeltaT` shows a more unexpected relationship: there is no convergence; as the time-step is reduced to very low values the solution is actually divergent. This is a potentially serious issue as it suggests instability in the solution. It is likely that there is some error associated with the choice of discretisation schemes or the solver strategy which is compounded when the time-step is reduced making the accumulated error significant. Without identifying the source of this divergence, the only way to avoid unacceptable errors is to ensure that the time-step is only reduced when strictly necessary (to satisfy the CFL condition) and able to increase at times when the flow behaviour allows, *i.e.* by using the `adjustableTimeStep` function.

Therefore, throughout this project the `adjustableTimeStep` function will always be active. A more thorough assessment of the issues with divergence at low time-steps will be left as further work. Furthermore, both `maxAlphaCo` and `maxCo` will be set to 0.25 as standard and the effect of varying these values will be identified in future studies.

3.2.3 Solution control

In OpenFOAM®, the equation solvers, tolerances and algorithms are specified in the `fvSolution` dictionary (OpenFOAM Foundation 2012). Each discretised equation is allocated a particular solver requiring a specific set of parameters. There exists a number of solvers and a full description of these is again outside the scope of this project. Furthermore, as with the numerical schemes, the specific solvers used are rarely documented in NWT literature and the qualities of each can only be inferred from abstract mathematical concepts relating to the treatment of similar classes of equations. Therefore, and only for completeness, a brief summary of the specific solvers used and the parameters set in each case will follow below.

Typically, to solve the equations for the pressure either a generalised *Geometric-Algebraic Multi-Grid* (GAMG) solver or a *Preconditioned Conjugate Gradient* (PCG) solver with a GAMG preconditioner is used. The equations for the velocity and the phase fraction are solved using either the `smoothSolver` option, which is a solver using a smoother, or a *Preconditioned Bi-Conjugate Gradient* (PBiCG) solver with a *Diagonal Incomplete-LU* (DILU) preconditioner. The solvers iterate over a succession of solutions in order to reduce the residual in the equation being solved. After each iteration, the residual is calculated and the solver is stopped if either the residual is less than the prescribed *tolerance*, the ratio of the current to the initial residual is less than the prescribed *relative tolerance* (`relTol`) or the maximum number of iterations has been reached. In this project the `relTol` is set to zero in order to ensure the solution has converged to the tolerance at each time-step (OpenFOAM Foundation 2012). The tolerances and maximum number of iterations used in each solver throughout this project have be set to 1×10^{-8} and 100 respectively.

The `smoothSolver` option and the GAMG solver both require a *smoother*. The `smooth-`

`Solver` is used exclusively with the reliable *Gauss-Seidel* smoother while; the GAMG solver is used with the *Diagonal Incomplete-Cholesky* (DIC) smoother, which offers better convergence for bad matrices. When GAMG is used as a preconditioner, additional post-smoothing of the DIC smoother using Gauss-Seidel can be beneficial (OpenFOAM Foundation 2012). For more information on the available solvers, preconditioners and smoothers refer to the OpenFOAM® user guide (OpenFOAM Foundation 2012).

As well as the solver-types, the `fvSolution` dictionary controls the under-relaxation of the computation, which can be used to improve the stability of the calculation. The user can specify the under-relaxation factor for any particular field where a value of 1 represents no relaxation and a value of 0 represents no change in the solution between iterations. As standard, no under-relaxation has been applied to the general NWT in this project.

Finally, the pressure-velocity coupling algorithm is also specified in the `fvSolution`. As mentioned earlier, OpenFOAM® offers a choice between the PISO and SIMPLE algorithms. Whereas SIMPLE only makes one correction, the number of corrections in PISO can be specified. In this work the PISO algorithm has been used without exception and the number of correctors has been set at 2.

3.3 Post-processing

The final stage in any CFD simulation is the extraction and graphical representation of the results - post-processing. One of the advantages of numerical, over experimental, simulations is the large data sets produced, however, the volume of data created can quickly become overwhelming. The disc space required in a typical 3D NWT simulation can easily exceed several hundred gigabytes (Westphalen 2010). It is therefore wise to have a planned methodology for the data sampling and a predetermined idea of the required output just like when designing a physical experiment. Consequently, there are a range of decisions to be made regarding the spatial and temporal resolution of output variables and a number of further approximations, used to display the desired results, must be considered. Frequently referred to techniques for post-processing in this project are discussed further below.

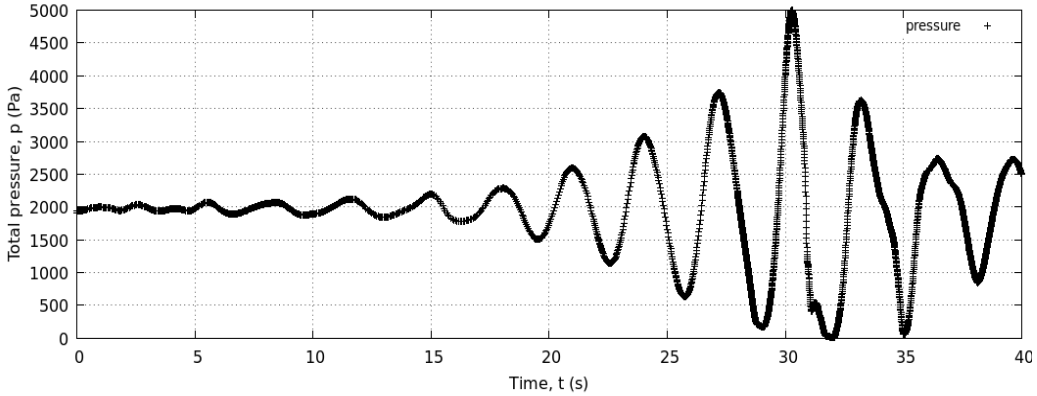

Figure 3.19: A point measurement example of pressure on the surface of a cylinder recorded at every time-step during a focused wave impact.

3.3.1 Point measurements (probes)

For the most part, we are interested in how the particular flow variables (*e.g.* pressure, velocity *etc.*) evolve in space and time. It is, however, unreasonable to retain the data for all variables, at all grid nodes, at all time-steps. Furthermore, it is common for numerical results to be compared with those from physical experiments which generally consist of only a few specific measurements. Therefore, the full domain results are typically written out with a greatly reduced and uniform temporal resolution for purposes of animation and 2D or 3D flow visualisation. For greater temporal resolution, point measurements (analogous to physical probe measurements from, for example, pressure transducers) can be obtained at every time-step (or after a specified number of time-steps) to give a time series (*e.g.* Figure 3.19). However, it is not always the case that the desired point coincides with a grid node and therefore the value at that position must be interpolated from those known values around it. This requires interpolation. There are a number of `interpolationSchemes` available in OpenFOAM®, but in this project a linear weighted interpolation is used throughout. It is hoped that the mesh resolution is sufficiently fine that the interpolation errors due to sampling will be negligible.

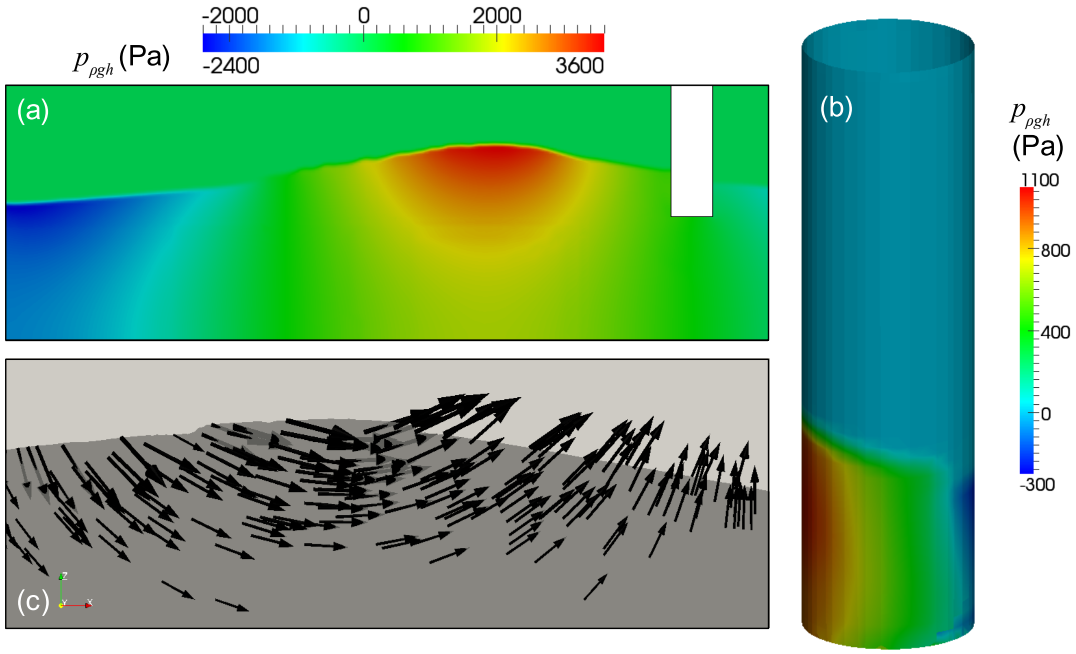

Figure 3.20: Examples of 2D snapshots (spatial representations of flow variables at a distinct moment in time) from a NWT simulation. (a) pressure results on a 2D planar slice through the computational domain. (b) pressure on the surface of a cylinder. (c) velocity vectors on a 2D planar slice through the domain.

3.3.2 2D snapshots

One of the key strengths of numerical, over physical, models is the spacial resolution of the data produced during the 'experiment'. Essentially, the value of each of the flow variables is recorded everywhere in the computational domain without causing any disturbance to the flow, by adding an excessive number of physical probes or by seeding the fluid with particles. Measurements over short distances (profiles) are possible (*e.g.* velocity measurements using an Acoustic Doppler Velocimeter (ADV)) but typically the quality of the results diminishes as one moves away from the focus point of the device (*i.e.* as the beam correlation reduces). High resolution spatial measurements are possible in physical wave tanks but typically require very expensive equipment and can lead to health and safety risks (*i.e.* when using high powered lasers). When using a NWT, all of these issues can be avoided.

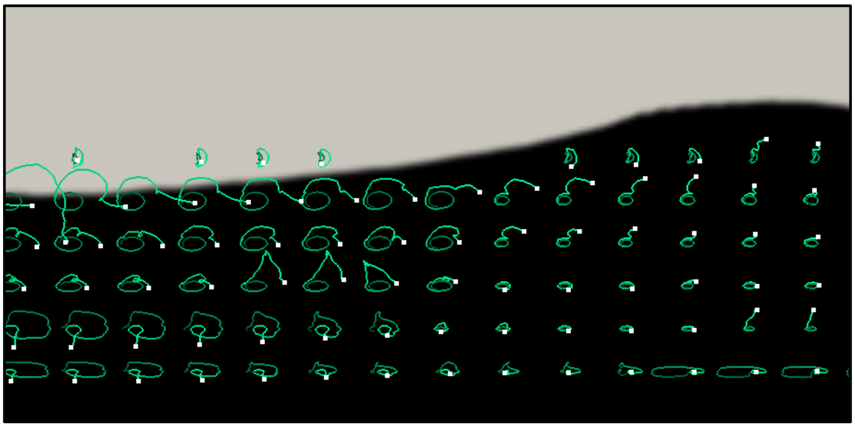

Figure 3.21: An example of flow visualisation using particle tracking in a NWT. Here the particle age is represented by the track colour and the final position of the particle is given as a white point.

When trying to visualise how particular flow variables change with position, it is common to display the results for multiple locations simultaneously at a specific instant (snapshot) in time. In 3D cases the data is usually displayed: on a plane representing a slice through the domain (Figure 3.20a), or on the surface of the structure under investigation (Figure 3.20b) which can then be projected onto a plane to improve accessibility. In these cases, a colour scale can then be used to display the value of the flow variable at high resolution over a 2D portion of the domain (using interpolation between the calculated values at the cell centres). The images in Figure 3.20 are produced using the post-processing tool, ParaView and linear interpolation between the grid points. ParaView is an open-source, visualisation application that is distributed with, and supported by, OpenFOAM®.

In addition to scalar flow variables, vector quantities such as the velocity can be displayed in the form of glyphs (arrows) which represent a snapshot of both their direction and magnitude on a 2D planar section of the domain (Figure 3.20c). For comparison between flow variables over a range of spatial extents these methods can then be combined to form a single plot containing a vast amount of information about multiple flow variables simultaneously.

3.3.3 Flow visualisation

More complicated representations are required to display the evolution of a flow variable in both space and time simultaneously. Obviously a series of snapshots arranged in chronological order or an animation would achieve this, but, in many cases, these representations fail to show the crucial features and make analysis of the data more challenging. A common technique for visualising the evolution of the velocity structure of a flow, over a wider spatial extent, is *particle tracking*. By 'seeding' the flow with massless 'particles' the velocity structure over a certain time-span (particle age) can be inferred from the paths traced out by these particles (see Figure 3.21).

3.3.4 Derived measurements

Of particular interest, in this and any project concerning waves, is the position and evolution of the interface, or surface elevation, η, at specific locations. This quantity is not a direct output of the simulation solver and has to be derived from the volume fraction field , α. This is achieved using the native `waves2Foam` utility `surfaceElevation` which integrates α along a vertical line analogous to experimental 'wave gauges' (Jacobsen 2014). Another parameter of interest, that is not directly calculated during the simulation, is the force on a structure. OpenFOAM® has a utility that calculates the forces and moments, at every time-step, by integrating the pressure over the given patches (surfaces) (OpenCFD 2014). Both of these derived measurements will be referred to extensively in the following chapters alongside specific NWT applications.

3.4 Summary - Generalised NWT Decisions

Throughout this chapter the three stages of a CFD project (pre-processing, the solver and post-processing) have been introduced. The various elements within these stages, deemed crucial to the development of a NWT, have been discussed. Based on the findings in the literature and from a variety of preliminary studies, a series of decisions have been made to design a generalised NWT methodology. It is hoped that this will provide a solid basis for further development towards more complex applications involving extreme waves and

WECs. Additions to the generalised NWT are described alongside the specific applications in Chapter 5. In this section the various decisions made throughout this chapter have be summarised. For a concise list of the elements involved in the generalised NWT and the values used as standard throughout this project refer to Appendix A.

3.4.1 Pre-processing decisions

The fluid properties used in this work will be based on standard temperature and pressure values at 20 $^{\circ}C$ and 1.013$\times10^5$ Pa (Massey and Ward-Smith 1998). The densities of air and water used will be 1.2 kg m^{-3} and 1000 kg m^{-3} respectively, while their kinematic viscosities will be 1.36$\times10^{-5}$ m^{2}s^{-1} and 1$\times10^{-6}$ m^{2}s^{-1} respectively.

The meshes will be constructed from square mesh cells (cubes in 3D) and have a resolution, at the free surface, of at least ten mesh cells over the wave height for waves with steepness (H/λ) between 0.01 and 0.1 (in order to achieve a 2 % RMS error). For waves with steepness's below 0.01 the mesh resolution will be decreased to only 1 cell over the wave height (producing an RMS error below 1 %). `snappyHexMesh` will be used, without layers, to include structures in the domain. At the free surface the meshes will be uniform and significantly refined, compared to the rest of the mesh. A quadtree refinement strategy (octree in 3D) will be used to achieve localised refinement of the mesh.

The flow conditions on the front, back, bottom and outlet boundaries will consist of wall-type boundary conditions: α will have a zero gradient condition; the velocity will have a fixed value condition of zero (no slip), and; the mixture pressure, $p_{\rho gh}$, will have a derived gradient condition based on the velocity. On the top boundary: α will have a zero gradient condition for positive flux (out of the domain) and a fixed value condition of zero for negative flux; the velocity will have a zero gradient condition for positive flux and a derived value based on an internal cell value for negative flux; the pressure will be derived based on a fixed total pressure.

The initial field values will be based on still water at the specified depth: the initial velocity of both the air and water phases will be set to zero; the pressure will be based on hydrostatic theory (ρgh), and; α will equal 1 in fully submerged cells, 0 in completely dry cells and the ratio of the submerged volume to the total cell volume in partially submerged cells.

Wave generation on the inlet boundary will be achieved using an expression-based boundary condition, while wave absorption will be achieved using the passive Relaxation Zone (RZ) formulation with an exponential decay function as the weighting factor (both part of the `waves2Foam` toolbox (Jacobsen et al. 2012; Jacobsen 2014)).

For cases where necessary, the effect of turbulence will be included using Reynolds decomposition and either the standard $k-\varepsilon$ or the Renormalised Group (RNG) $k-\varepsilon$ models.

3.4.2 Solver decisions

The equations solved within the NWT will be the Reynolds-Averaged Navier-Stokes (RANS) equations for two immiscible, incompressible fluids based on the Finite Volume Method (FVM) of discretisation and the Volume Of Fluid (VOF) treatment of the interface. The pressure-velocity coupling will be achieved using the Pressure Implicit with Splitting of Operators (PISO) algorithm with two correctors.

Single-point Gaussian quadrature will be used exclusively as the integration method. The gradient terms in the equations will be dealt with using second-order, unbounded, linear interpolation as will the majority of the divergence terms. However, when boundedness is a requirement, a number of first/second order, bounded, TVD schemes, such as the van Leer limiter or the MUSCL limiter, will be used. Linear interpolation will be used for the diffusion coefficient in the Laplacian terms while the surface normal gradient scheme used will be the second-order unbounded `corrected` method.

The temporal discretisation will be achieved using a blend between the second-order Crank-Nicholson and the first-order implicit Euler schemes where the blending coefficient will depend on the stability requirements of the specific simulation.

The time-step will be controlled using the `adjustableTimeStep` function based on the Courant-Friedrichs-Lewy (CFL) condition. `maxAlphaCo` and `maxCo` will both be set to 0.25 and the maximum time-step will be 1 s.

A number of different solver types will be used: For the pressure equations either a Geometric-

Algebraic Multi-Grid (GAMG) solver with a Diagonal Incomplete-Cholesky (DIC) smoother or a Preconditioned Conjugate Gradient (PCG) solver with a GAMG preconditioner and either a DIC or Gauss-Seidel smoother will be used; for the velocity and phase fraction equations either the `smoothSolver` with a Gauss-Seidel smoother or a Preconditioned Bi-Conjugate Gradient (PBiCG) solver with a Diagonal Incomplete-LU (DILU) predonditioner will be used. The relative tolerance of the solution residual in each of the equations will be set to zero. The tolerances and maximum number of iterations in each case will be 1×10^{-8} and 100 respectively. No under-relaxation will be applied.

3.4.3 Post-processing decisions

Full domain results will be recorded at regular intervals (typically every one hundredth of the total simulation time). For greater temporal resolution, point measurements will be recorded at every time-step using linear interpolation, from known values, if their position does not coincide with a grid point. Surface elevation measurements will be recorded at specific locations by integrating the phase fraction over a vertical line typically consisting of 1000 points. In cases involving structures, force and moment measurements will be derived by integrating the pressure over the surface of the body in question.

Having developed a generalised NWT methodology its performance will now be assessed, first by considering a number of extreme wave cases in Chapter 4 and then by studying extreme wave-structure interactions in Chapter 5.

Chapter 4

Extreme Waves

> *"Horrific, monstrous. You feel as if the end of the world has come"* - Capt. Dai Davies (Smit Marine South Africa) describing his experience of freak waves (Horizon 2002).

Extreme waves (also known as ‘rogue’ or ‘freak’ waves) have received much attention in recent years due to their unexpected, frightening and life-threatening impacts on a number of oil platforms and their associated damage to cargo ships and other vessels (Rosenthal and Lehner 2008). It is clear that the design of safe and economical offshore structures is reliant on knowledge of the extreme wave environment and the associated wave-structure interactions. However, despite intensive study, the limited number of real-life observations of these apparently random phenomena, has resulted in some debate over the definition of an ‘extreme’ and a clear consensus on the physical origins of extreme waves remains elusive (Toffoli and Bitner-Gregerson 2011). The difficultly in reaching an agreed definition of an extreme wave arises from their unpredictable nature and the variety of shapes and sizes that occur. It is suspected that these waves, which seem to appear from nowhere, exist for a very short time and then disappear, are a result of the focusing of waves with different frequencies coupled with strong nonlinear interactions between the waves (Svendsen 2006).

Extreme waves can have up to ten times the average wave energy (Dysthe et al. 2009) and are typically very steep and highly-nonlinear, characterised by a highly distorted free surface and asymmetric shape. Captain Mallory (1974) described a deep trough, or ‘hole in the sea’, before a crest with a steeper leading face. An operational approach is to define a wave as ‘extreme’ when its height is greater than a certain threshold for the sea state. One generally accepted criterion is that the wave height, H, must be greater than twice the significant wave height, H_s. Another definition is that the crest height above the still water level, η_{cr}, must exceed $1.25H_s$ (Dysthe et al. 2009).

A large body of work has focused on the frequency of occurrence of these waves (White and Fornberg 1998; Toffoli and Bitner-Gregerson 2011; Massel 2013) but this will not be considered here. It is widely accepted that these events pose a threat to offshore structures and so, in this work, emphasis is placed on the definition of a single wave event, for the purpose of numerical modelling and episodic survival studies at the device scale.

4.1 Observations

Enormous waves have been reported by mariners for centuries but until recently these tales have been dismissed as folklore (Massel 2013). It was not until incidents like the destruction of Norwegian tanker *Wilstar*’s bow (Figure 4.1) or the structural damage to oil and gas platforms (Jonathon and Taylor 1997; Haver 2004; Santo et al. 2013) that engineers realised the very real threat extreme waves pose to offshore structures and vessels.

The majority of reliable field observations of extreme waves have been from offshore oil platforms. Only here have there been sufficiently long-term, quality-checked data sets collected to record these unpredictable events. A number of notable records confirm the existence of these extreme waves and emphasize the importance of their consideration in the design of offshore structures.

One example is the data from the Frigg oil field in the northern North Sea (depth 100 m). This data set contains 79 or 74 extreme waves depending on the criteria used to define them ($H > 2H_s$ or $\eta_{cr} > 1.25H_s$ respectively). This suggests both definitions have a similar probability of exceedence. The Frigg data contained 1.6 million waves with an extreme wave probability of occurrence similar to that predicted by state-of-the-art wave statistics (Dysthe et al. 2009).

In contrast, the data recorded on the 17th of November 1984 at the Gorm field in the central

Figure 4.1 has been removed due to Copyright restrictions.

Figure 4.1: Structural damage caused by a rogue wave to the Norwegian tanker, The Wilstar, in 1974. Image Credit: H. Gunther and W. Rosenthal

North Sea (depth 40 m) displays a population of abnormal waves which cannot plausibly be explained by current wave statistics. Twenty-four waves with $H/H_s > 2$ were recorded, the most extreme of which had a ratio of 2.94. However, it should be noted that the significant wave height was only 2-4 m for the most extreme waves (Dysthe et al. 2009).

Finally, and referred to extensively in the literature, is the *Draupner wave*, or *New Year wave*, which occurred on the 1st of January 1995 (Haver 2004; Walker et al. 2005; Adcock et al. 2011). Despite having a wave height below the 100-year return wave for the site in the North Sea, the 26 m wave was indeed astonishing within a sea state characterised by a significant wave height of approximately 12 m (Hagen 2002; Walker et al. 2005; Dysthe et al. 2009). Furthermore, satellite images of the 100×100 km site showed a number of extreme events on that day (Rosenthal and Lehner 2008).

For a comprehensive summary of freak wave observations see Massel (2013).

4.2 Proposed physical mechanisms

From the Gorm data in particular, it would appear that these extreme wave incidents cannot simply be assumed to be rare events within the standard statistical models. Could there be some exceptional physical conditions, not contained within these models, which explain the existence of extreme waves?

It is well known that unexpected, large waves can form through refraction in coastal waters or areas with strong currents (White and Fornberg 1998; Rosenthal and Lehner 2008) but there is some debate over how extreme waves are produced in the deep ocean. Some of the most common mechanisms proposed, in order to explain the existence of extreme waves, are as follows:

1. *Superposition* is typical of the standard linear model (see Section 4.3) and extreme waves have been recorded in standard irregular seas where several waves sum together in phase. However, it is statistically improbable that this mechanism is responsible for the frequent occurrence of extreme waves (Adcock et al. 2011).

2. *Spatial focusing* is caused by refraction of waves by bathymetry or currents and can lead to crest alignment or trapping of waves and caustic reflections (White and Fornberg 1998). But, this does not explain the occurrence of extreme waves in deep water or far from strong opposing currents;

3. *Dispersive focusing* is another linear effect, similar to superposition, taking into account the frequency dependence of wave celerity (Equation 4.3). A chirped wave packet can be formed by adding waves of different frequencies in such a way that they combine constructively (or ‘focus’) at a specific point in space and time. Chirped wave trains can exhibit strong focusing even if a random wave field is also present. However there is some controversy over whether or not these contrived wave forms are the likely cause of real extreme waves as no physical processes have been identified that are capable of producing the required phase and directional requirements (Dysthe et al. 2009);

4. *Nonlinear focusing* has also been proposed including the application of the nonlinear Schrödinger (NLS) equation (from quantum physics) and the modulation instability of a regular unidirectional wave train known as the Benjamin-Feir instability (Clauss 2010). It has been shown experimentally that during the development of this instability there is a distinct increase in the number of extreme waves (Dysthe et al. 2009). Furthermore, results using the Modified Nonlinear Schrödinger equation, which assumes small steepness and a narrow spectrum, have been shown to agree well with tank tests and fully nonlinear 3D simulations (Dysthe et al. 2009). However, although the concept is physically and mathematically robust, it remains unclear as to whether or not the phenomenon can be practically responsible for extreme waves in realistic ocean conditions, particularly as a finite water depth and directional spreading reduce this effect considerably (Adcock et al. 2011).

5. Finally, it has been proposed that extreme waves, including the Draupner wave, may be the result of a 'crossing sea' in which two wave-groups cross from different directions. Adcock et al. (2011) show that a crossing sea can describe the abnormal 'set-up' of the Draupner wave if the directional spread of the two wave-groups is sufficient and if their mean directions differ by at least 90°. Furthermore, it was shown that waves as steep as the Draupner wave were possible in a crossing sea whereas wave breaking would occur in unidirectional seas. However, despite convincing evidence, Adcock et al. (2011) made a number of assumptions when recreating the wave and could not be sure of the directionality of the sea state during the Draupner event.

It is possible that all of these processes are capable of creating an extreme wave, however, for any particular incident, the mechanism is likely to depend upon the environment in which it occurs, *i.e.* water depth, current strength, wave direction *etc*. A generalised mechanism therefore remains elusive and a consensus on the practical reproduction of these waves, for the purpose of model simulations, has not been reached. Furthermore, there has yet to be any work considering which of these mechanisms might produce the most threatening, and therefore most important (in terms of survival design), extreme waves at a site.

4.3 Modelling an extreme wave

The controlled generation of waves for the purpose of experimentation, either physical or numerical, requires the specification of some driving mechanism (wave paddle motion or inlet boundary condition) typically based on a theoretical description of the desired wave shape and kinematics. As mentioned in Section 3.1.4, there are a number of wave generation methods possible in NWTs. In the method that will be used here, `waves2Foam`, an expression-based, inlet boundary condition is applied, allowing for wave generation based on a set of generic wave theories. These theories specify the time evolution of the surface elevation, η, and hence the volume fraction, α, as well as the vector velocity, $\mathbf{V}$, at each point on the inlet boundary (Jacobsen et al. 2012). The mixture pressure, $p_{\rho gh}$, on the inlet is then given a zero gradient boundary condition.

Water wave theory has been the subject of research for over 300 years. During the early twentieth century, the linear theory of wave motion was developed to a high level of sophistication to describe the many diverse occurrences of waves in nature. The classic theory deals with situations in which a range of suitable simplifications allow the governing equations to reduce to a set of linear partial differential equations, typically *the wave equation* or *Laplace's equation*, and some linear boundary conditions. The free surface elevation for a single, regular wave 'component' is then given by

$$\eta(x,t) = a\cos(kx - \omega t), \tag{4.1}$$

where a is the wave amplitude; k is the wavenumber, which is related to the wavelength, λ, by $k = 2\pi/\lambda$, and; ω is the angular frequency, which is related to the period, T, and the frequency, f, by $\omega = 2\pi/T = 2\pi f$. The corresponding velocity potential, the gradient of which gives the velocity, is then given by

$$\Phi = \frac{\omega}{k} a \frac{\cosh(k(z+h))}{\sinh(kh)} \sin(kx - \omega t). \tag{4.2}$$

ω and k are not independent, they are linked through the *dispersion relation*

$$\omega^2 = gk\tanh(kh), \tag{4.3}$$

which describes the relationship between the wavelength and the wave speed as a function of ω, k and the water depth, h.

The nature of linear theory means a linear sum of solutions is itself a solution. This allows the irregular surface elevation observed in reality to be described as the superposition of single, regular wave solutions and the use of analysis techniques like Fourier- and integral-transforms (Craik 1985).

Fourier transforms are used extensively, in ocean engineering, allowing time series signals to be displayed in the *frequency domain*. This process transforms a function, such as the surface elevation recorded at sea, into a set of discrete, complex amplitudes, a_n, known as Fourier series coefficients. These coefficients represent the amplitudes of the individual, periodic wave components (Equation 4.1) present in a linear description of the free surface so that any free surface can be represented as

$$\eta(x,t) = \sum_{n=0}^{N} a_n \cos(k_n x - \omega_n t). \tag{4.4}$$

The velocity potential is then given as

$$\Phi = \sum_{n=0}^{N} \frac{\omega_n}{k_n} a_n \frac{\cosh(k_n(z+h))}{\sinh(k_n h)} \sin(k_n x - \omega_n t). \tag{4.5}$$

This concept allows a particular surface elevation to be described by its *frequency spectrum* which gives a measure of the energy present as a function of the frequency and has distinctive properties depending on the scenario in question. As an example, a number of idealised spectra exist, and are used regularly in offshore engineering, to describe realistic sea states. The Pierson-Moskowitz (PM) spectrum (Equation 4.6, Figure 4.2a) is one of the simplest standard spectra and is used to describe a ‘fully developed sea’, *i.e.* one in which

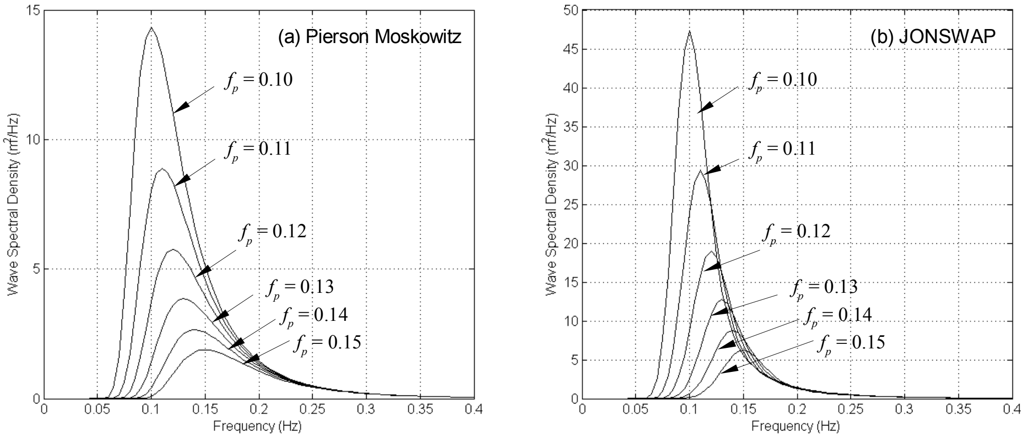

Figure 4.2: Examples of the Pierson-Moskowitz (a) and JONSWAP (b) spectra for a range of peak frequencies, f_p. $\alpha_P = 8.1 \times 10^{-3}$.

the wind has blown long enough and over a great enough distance (fetch) for the waves to have reached their maximum size for that wind strength. The spectral energy density, $S(f)$, for the PM spectrum is then given by

$$S(f) = \alpha_{Ph} g^2 (2\pi)^{-4} f^{-5} \exp\left(-\frac{5}{4}\left(\frac{f_p}{f}\right)^4\right) \tag{4.6}$$

where α_{Ph} is Philips' constant and f_p is the peak frequency (Pierson and Moskowitz 1964).

Alternatively, Hasselmann et al. (1973) adapted the PM spectrum, for seas with a 'limited fetch', in order to improve the fit with measurements taken as part of the Joint North Sea Wave Observation Project (JONSWAP). The JONSWAP spectrum (Figure 4.2b) is then given by

$$S(f) = \alpha_P g^2 (2\pi)^{-4} f^{-5} \exp\left(-\frac{5}{4}\left(\frac{f_p}{f}\right)^4\right) \gamma^{\exp\left(\frac{-(f-f_p)^2}{2\sigma^2 f_p}\right)} \tag{4.7}$$

where $\gamma = 3.3$ and

$$\sigma = \begin{cases} 0.07, & \text{if } f < f_p \\ 0.09, & \text{if } f \geq f_p \end{cases}$$

(Hasselmann et al. 1973).

Since the governing equations and boundary conditions of fluid mechanics are never strictly linear, these approximations are restricted to small displacements about a known equilibrium or steady state. The size of the displacements permitted varies with circumstances, for example, for gravity waves in deep water the wave-slope need only be very small compared with unity ($ka << 1$); but in shallow water or shear flows the requirements are much stricter (Dingemans 1997). Despite linear theory providing useful results, even up to the limit of applicability (Dean and Dalrymple 1991), greater displacements require the use of far more complicated nonlinear wave theories.

When the wave slope is sufficiently large, terms including higher powers of the amplitude cannot be ignored and we must consider the nonlinear effects of real wave motions. Such an analysis can be used to gauge the conditions under which nonlinear terms are negligible as well as uncover some of the important and remarkable phenomena qualitatively unaccounted for by linear theory (such as solitons, resonant interactions, side-band instability and wave-breaking) (Lighthill 1978). Nonlinear systems do not satisfy the superposition principle, the variables being solved cannot be written as a linear combination of independent components. Nonlinearities manifest themselves as an exchange of energy between different frequencies and so techniques like Fourier transforms are no longer appropriate (Dingemans 1997). Therefore, nonlinear wave simulations require a time domain model.

In the most general case, water waves propagate in multiple directions, interacting nonlinearly, in the presence of shear currents, over water of non-uniform density and a deformable, permeable bathymetry. An analytical solution to this problem is impossible. Despite this, significant progress into the field of weakly-nonlinear wave propagation has been made, most notably by Stokes (Fenton 1990).

By making a number of approximations which effectively transform the problem into a two-dimensional, irrotational, incompressible, inviscid flow, an analytical solution can be found which corresponds to a steadily-propagating, single, periodic wave train, which does not change form. This ‘steady wave’ solution is considered to be a convenient model for the more general case but, being a regular wave solution, does not describe the irregular nature of real sea states. There are two main steady wave theories: Stokes theory which is only suitable for wavelengths which are short relative to the water depth, and Cnoidal theory which applies when wavelengths are long compared to the water depth (Fenton 1990).

Stokes theory is commonly used to describe nonlinear wave problems in offshore engineering. It relies on applying a 'perturbation' method, known as *Stokes expansion*, to the Taylor series expansion of the surface elevation (Dean and Dalrymple 1991). Up to fifth order Stokes wave theories are commonly used but in general any order theory could be devised in this way. However, the details of the expansion for higher order theories would be extremely onerous. For that reason alternative wave theories have been devised that can be developed iteratively on a computer (Dean and Dalrymple 1991). Of note is the *stream function wave theory* (used for the mesh dependency work in 3.1.2) which solves the exact governing equations and their boundary conditions by expanding the so called 'stream function', ψ, and surface elevation into Fourier series (Svendsen 2006). The result is the solution to a horizontally symmetrical, periodic wave of constant form.

In coastal waters the approach, developed by Boussinesq (1872) and by Korteweg and De Vries (1985), which leads to the constant-form Cnoidal wave theory, can also be applied to unsteady wave solutions. This 'Boussinesq wave theory' is the basis of many of the most sophisticated and successful wave models used today (Svendsen 2006).

4.3.1 Design waves

As mentioned earlier, the majority of research directly concerning WECs has focused primarily on optimising the response of the device. Typically a 'design spectrum', similar to the PM and JONSWAP spectra, is used to describe the wave conditions for a particular site. Developers then design their device to achieve maximum energy output based on the results of a parametric study over the range of frequencies present in this spectrum. Commercial efficiency requires that this process be relatively fast and so linear methods in either the frequency- or time-domain are common (Pizer et al. 2005; Retzler et al. 2003). Although essential for understanding the operational efficiency of devices, these methods cannot describe the survivability of WECs as they either neglect the shape of the waves completely (frequency-domain) or assume only linear wave-structure interactions (time-domain) (Westphalen 2010). The modeling of wave events such as freak waves requires what is known as a phase-resolving approach (Massel 2013).

It is widely accepted that present design procedures for the operational envelope need to be complimented by a second level of design which takes into account the extreme wave spectral parameters and survivability envelope (Clauss 2010). Despite the random nature of the ocean surface, historically, experiments and simulations have been performed using large, deterministic, regular waves, such as 5th order Stokes waves. These are typically based on the most probable, highest wave expected from a three hour sea state with a return period of 100 years (or some other extrapolation of the data based on an acceptable life-time for the device) (Tromans et al. 1991). Haver and Anderson (2000) define extreme waves as those which are not represented by the Rayleigh model, a linear model which under-estimates the maximum crest heights, suggesting that higher order processes are significant in reality. They suggest that in addition to the 100 year design wave (Ultimate Limit State), design procedures should include waves with an Accidental Limit State of 10,000 years. Faulkner (2000) also recommends the consideration of wave impact loads from extreme sea states in addition to the standard operational conditions. He suggests a survival design wave height, $H_d > 2.5H_s$ based on observations of freak waves.

In general, however, extreme waves are sporadic events embedded within a random sea state making their prediction and reproduction difficult. As a fully nonlinear theoretical model of an extreme wave does not exist, a more realistic alternative to the periodic representation is to simulate the complete, random time history, including the entire spectral and directional properties, of the three hour interval. This is typically performed at scale in a laboratory basin (Massel 2013). A probabilistic idea of the structural response can then be found by repeating this simulation many times with statistically similar sea states (Tromans et al. 1991). However, a stochastic analysis of this type is insufficient to capture the local characteristics needed to derive appropriate design criteria and random time domain simulations for extremes are unfeasibly time consuming (Rozario et al. 1993; Clauss 2010).

Finally, the idea of an extreme wave allows for the notion of a single event with a specific shape, and crest height, η_{cr}, over a single associated period. Then a convenient ‘design-wave’ can be constructed to examine the peak surface elevations and loads due to extreme events in a reproducible, deterministic way. In offshore engineering a design-wave known as ‘NewWave’ is referred to extensively and has become the industry standard for modelling extreme wave interactions with offshore structures (Walker et al. 2005; Bateman et al. 2012; Santo et al. 2013). NewWave relies on the dispersive nature of water waves to produce an extreme wave event at a specific point in space and time by combining smaller, sinusoidal components of different frequencies. Retaining the broad-banded nature of extreme ocean waves, the linear NewWave has a shape based on the average extreme in a linear, random, Gaussian sea and is proportional to the auto-correlation function (the Fourier transform of the sea state power spectrum in question) (Walker et al. 2005). By discretising this definition into a finite number of sinusoidal components, N, and limiting ourselves to uni-directional seas, a linear, crest-focused wave group then has the surface elevation

$$\eta(x,t) = \sum_{n=0}^{N} a_n \cos(k_n(x - x_f) - \omega_n(t - t_f)), \tag{4.8}$$

where x_f and t_f are the target position and target time respectively. For a linear NewWave the individual component amplitudes are given by

$$a_n = \frac{A_{cr} S_n(\omega)\Delta\omega_n}{\sum_n S_n(\omega)\Delta\omega_n}, \tag{4.9}$$

where $S_n(\omega)$ is the energy spectrum, $\Delta\omega_n$ is the frequency increment and A_{cr} is the linear crest amplitude given by

$$A_{cr} = \sqrt{2m_0 \ln(N)} \tag{4.10}$$

where m_0 is the zeroth moment of the spectrum. Equation 4.10 then ensures a NewWave model of the largest wave in N waves. It is generally accepted that a three hour sea state has approximately 1000 waves and so $N = 1000$ (Hunt-Raby et al. 2011).

NewWave has been shown to model the underlying linear part of large ocean waves in both deep and intermediate water well (Taylor and Williams 2004; Jonathon and Taylor 1997). It has been shown to outperform traditional 5th order Stokes wave methods when predicting the forces on offshore space-frame structures (Rozario et al. 1993). However, there still exists some concern over the use of NewWave in shallow water as dispersion has less effect and nonlinearities become significantly more important. Higher-order corrections to the NewWave definition have been proposed (Walker et al. 2005) and the subject remains a source of ongoing research. Despite this and due to limitations with the physical wave maker software used to generate the validation waves, a linear NewWave approximation will be used to describe the incident extreme wave. Any nonlinearities present at the position of the wave maker will be ignored. Furthermore, only unidirectional waves will be considered in this project. It is believed that, even with these simplifications, the use of a NewWave profile in this work provides a more probable version of an extreme wave compared to those used in similar applications which tend to use either 5th order Stokes waves or focused waves based on generic ocean spectra (*e.g.* PM or JONSWAP) (Bredmose and Jacobsen 2010; Chen, Zang, Hillis, Morgan and Plummer 2014). In order to limit the effect of this linearised input signal it can be argued that the position and time of the extreme event should be such that the maximum crest amplitude (and so contribution of nonlinearities) at the wave maker is minimised. Bateman et al. (2012) discuss how this leads to unfeasibly long simulations but provided the second-order corrections are within 4 % a relatively short simulation is sufficient to allow the nonlinearities to form after generation. It is therefore believed that, positioning the target location sufficiently far from the wave maker allows suitable time and distance for nonlinearities to form and thus produce a realistic, fully-nonlinear, extreme wave result. Further-still, it has been shown that global loads calculated using NewWave with second-order corrections are the same as those derived using the equivalent linear NewWave (Rozario et al. 1993). Therefore, it is hoped that this simplification will not reduce the applicability of the results produced here when compared to realistic extreme ocean waves.

4.4 Implementation and validation

As the aim of this project is to provide a *reliable* understanding of the behaviour of WEC systems, the applications investigated here are all designed to reproduce a scaled physical experiment. This provides a measure of the validity of the NWT developed by allowing comparisons between the numerical results and those produced in a controlled environment using a real fluid. Only then can this tool be used to explore cases beyond the capabilities of physical experiments, such as those at full scale, with any confidence in the results.

All of the experiments used for validation purposes in this project have been performed in the Ocean Basin at Plymouth University's Coastal, Ocean And Sediment Transport (COAST) laboratory. Any uncertainties in the experimental measurements have been identified and considered alongside the corresponding numerical results when a discrepancy has been observed. For cases involving extreme waves, unidirectional NewWaves are physically generated by 24 flap-type wave paddles at one end of the 32 m long and 15.5 m wide wave tank. The depth is 4 m at the wave paddles (which have a hinge depth of 2 m) and decreases linearly to a depth which can be varied between 0 and 3 m. As a result there is a depth change between the paddles and the test area with a steepness which is a function of the test depth used. There is a parabolic absorbing beach at the far end of the basin, opposite the wave makers (Figure 4.3).

In order to produce a NewWave profile at a wave gauge located at a point of interest some distance from the wave makers, 243 wave components with frequencies uniformly spaced between 0 and 2 Hz are generated using NewWave theory within the paddle control software. Typically the measured surface elevation at the point of interest does not match the desired NewWave profile; it is common for there to be significant horizontal asymmetry. This is likely due to the presence of nonlinear interactions in the wave propagation up until this point which are not accounted for in the paddle software. One method to resolve this issue is to linearly deconstruct the measured time series, using a Fast Fourier Transform (FFT), and adjust the phases of the wave components so that they arrive 'in-phase' at the point of interest - *focused*. This can be done by 'trial-and-error' until a sufficiently sym-

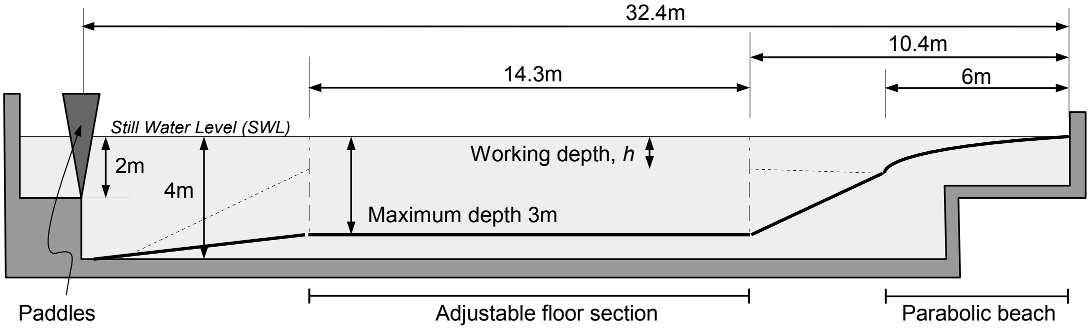

Figure 4.3: Schematic diagram of the COAST laboratory Ocean Basin

metrical measurement is recorded (Hunt 2003). Unfortunately this does not guarantee the precise NewWave is produced and leaves a number of unanswered questions regarding the kinematics of the wave at the target location.

As an initial validation case, the 100 year extreme wave at the Wave Hub, with a crest height at full-scale of 13.4 m, was reproduced at 1:50 scale (Ransley et al. 2013*a*). The Wave Hub is a designated test area for pre-commercial wave energy devices located 16 km off the north coast of Cornwall, UK (Wave Hub Ltd. 2015). In this case, a Weibull fit was used to approximate the frequency spectrum for the 1 in 100 year sea state at the site. Then a NewWave, based on a scaled version of the JONSWAP spectrum with an H_s of 14.4 m and a T_z of 14.1 s, was produced experimentally. In order to ensure symmetry at the target location, the trial-and-error phase adjustment was used on 243 wave components, ranging between 0.1 Hz and 2 Hz (Ransley et al. 2013*a*). To allow for such a large wave, the experiment was performed at a scale of 1:50. As a consequence the depth could not be scaled correctly to the Wave Hub site (50 m). This is because it is believed that undesirable hydrodynamic effects would arise from the dramatic change in water depth between the deep section in front of the wave makers (4 m) and the correctly positioned raisable floor (at 1 m) (Figure 4.3). Instead, the depth, h, of the raisable section was set to 2.8 m.

A two-dimensional NWT, based on the discussion in the previous chapters, was constructed. The experimental waves were reproduced numerically by applying the same NewWave definition for the surface elevation (and thus the phase fraction) on the inlet boundary, as that used in the experiment. The velocities on the inlet boundary where then assumed to equal the sum of the linear velocities of each of the discrete wave components present in the NewWave definition. The depth in the NWT was a constant 2.8 m, the air phase was given a height of 1 m and the domain was made 35 m long. A 5 m Relaxation Zone (RZ) was installed on the wall opposite the inlet boundary. A uniform, square-celled mesh was used with a cell size of 0.0074 m $\times$ 0.0074 m. This resolution allowed for approximately 68 cells over the wave height which, based on the mesh convergence study in Section 3.1.2, should be sufficient to be within an RMS error of 1 % (based on a steepness of 0.048). The steepness in this case has been calculated as the maximum crest-to-trough height (0.47 m) over the wavelength of the peak frequency (9.707 m). Interestingly at this high steepness one would expect to see the same distortions to the wave crest as those seen for steep regular waves. However, there are no distortions which suggests that this definition of the wave steepness does not correspond to the same steepness in regular waves *i.e.* it over-estimates. An alternative categorisation based on the maximum free surface curvature may be a more appropriate way to parameterise the mesh resolution in the NWT as this is likely to be the most critical property and can be applied to both irregular and regular waves. However, this concept will be revisited in future studies and the definition of steepness used above will be used throughout this project for purposes of mesh design.

The generic decisions described in Chapter 3 were applied to the 2D NWT and the RANS equations were solved without a turbulence model *i.e.* laminar flow was assumed. One-point Gauss quadrature was used for the integration and linear interpolation was used for all terms except the divergence terms in the phase fraction transport equation. For these the MUSCL scheme and OpenFOAM®'s `interfaceCompression` scheme were used. C_α was set to 1.

The surface elevation recorded at the target location, in both the physical and numerical simulations, can be seen in Figure 4.4. The numerical simulation has been reasonably successful, particularly considering the distance over which the wave has travelled from the wave maker (20.82 m) and the significant differences in wave generation method. However,

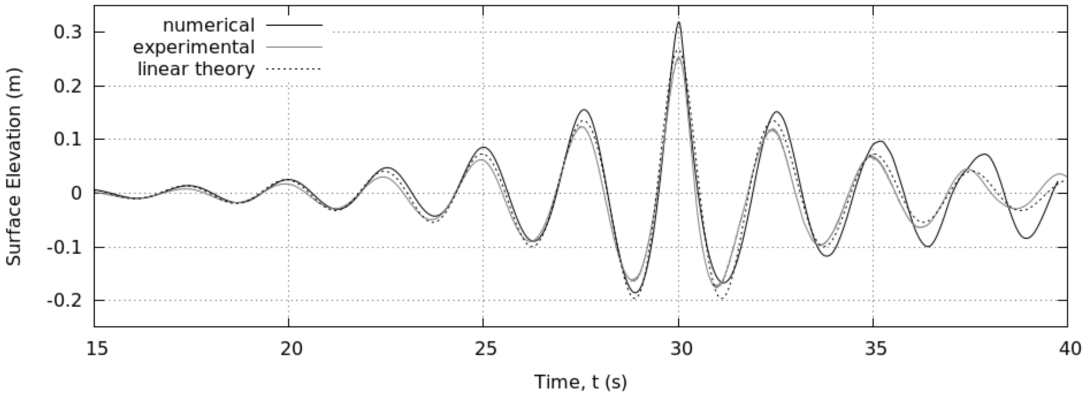

Figure 4.4: Comparison between the free surface elevations measured at the target location in the initial extreme wave validation case. Numerical (black), physical experiment (grey) and linear theory (dotted).

there is some loss of symmetry about the main crest and significant differences afterwards. It is believed the variance after the main crest is due to the different methods of wave absorption used. The efficiency of absorption in the NWT is known to be a function of the wavelength and the RZ length (Jacobsen et al. 2012) whereas the efficiency of the physical beach is a nonlinear relationship depending on the wave frequency and the amplitude (Dr Keri Collins, personal communication, January 23, 2015). The 5 m RZ in the NWT is less than half the length of the wave component with the most energy and so less than 95% absorption can be expected (Jacobsen et al. 2012). However, noticeable reflections were also observed in the physical experiments shortly after the main crest passes. Reflection analysis of the physical beach suggests that there will have been between a 5 and 10 % reflection of the dominant frequencies present in this case (Dr Keri Collins, personal communication, January 23, 2015). It is unlikely that the precise absorption of the physical beach can be reproduced in the RZ and so reducing the effect of reflected waves is crucial when validating the NWT. This highlights another advantage of using a focused wave over a regular wave; the compact wave packet ensures the extreme event occurs before reflected waves have had time to disturb the fluid in the test area. In addition to the discrepancy after the main peak, the numerical solution has overestimated all of the crests, increasing with severity with the crest height (the main crest height in the numerical case is 21.1 %

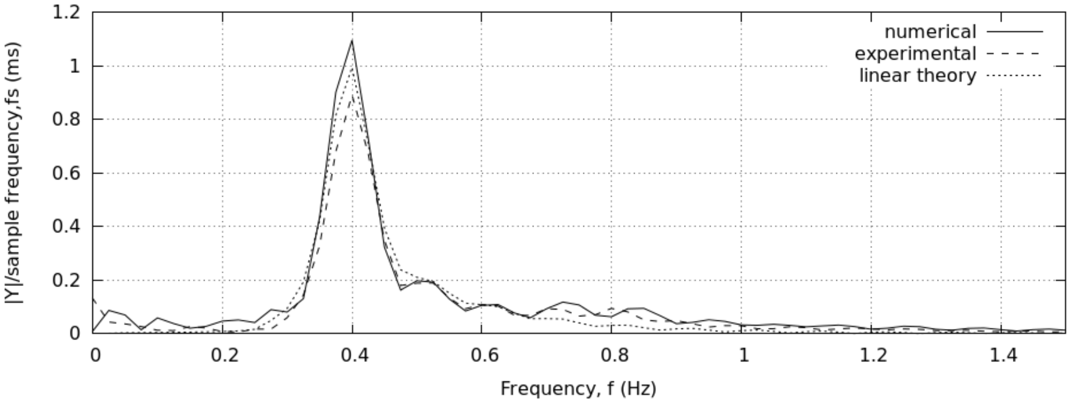

Figure 4.5: Frequency domain analysis of the time series at the target location, as well as that predicted by linear theory, in the initial extreme wave validation case. Y is the raw FFT output and $f_s = 128$ Hz.

higher than that in the experiment). This is unexpected as typically one might expect a poor numerical solution to have lower peaks due to excessive numerical diffusion or a failing to capture the full nonlinearity of the situation.

As a check, Figure 4.5 shows a frequency domain analysis of the results at the target location. Clearly, the numerical solution over-predicts the energy at the peak frequency, 0.4 Hz, showing an increase compared to linear theory whereas the physical result shows a decrease. This is consistent with the over-estimation in crest amplitudes in Figure 4.4. As seen in the experiment, a decrease in the energy at the peak frequency, compared to linear theory, is expected as nonlinear effects cause energy exchanges between frequencies. Despite the over-estimation at the peak frequency, the numerical solution shows similar increases in energy at low frequencies and at the second harmonic of the peak, 0.8 Hz, as those seen in the experiment. This gives some confidence that the nonlinearities are being correctly captured by the model, but, the over-estimation at the peak frequency remains unresolved. It is possible that accumulated reflected waves could cause an increase in the energy at the peak frequency, but, it is also possible that the observed discrepancies are a result of uncertainties regarding the behaviour of the synthesiser software (which controls the physical wave makers) or because of the depth change in front of the paddles or unexpected vorticity close to the paddles or possibly a combination of all of these.

In an attempt to remove the complexities of the fluid flow in the vicinity of the wave paddles, improve the computational efficiency of simulations and eliminate any error in the predictions made by the wave maker software, the method used from now on employs an additional wave gauge situated 8 m from the wave maker. This then serves as the numerical input data for the simulation. It is hoped that any effect due to the wave generation or the depth change near the wave maker will have occurred by the time the wave reaches this forward wave gauge, from where a constant depth can be assumed. The drawback of this method is that only the surface-elevation is recorded at the forward position. The velocity is also needed to fully define the inlet boundary conditions. Therefore, the time series recorded at the forward wave gauge is reduced into linear wave components using an FFT. The velocity is then approximated as the linear sum of velocities arising from the linear velocity potential (Equation 4.2) for each component.

In order to test this new methodology, the 100 year wave simulated above has been rerun, at a scale of 1:30, using the forward wave gauge method for the inlet boundary conditions and with the depth correctly scaled to the Wave Hub site. The 2D computational domain was 25 m long and 1.73 m deep with a 13 m long RZ installed at the end opposite the inlet boundary. The mesh resolution, in the region containing the free surface, was 36 cells over the maximum wave height (~0.6 m). Based on the work in Section 3.1.2, this was deemed sufficient to ensure mesh independence with an RMS error within 2 %. In order to improve the simulation efficiency, the rest of the domain was allowed to be two levels of refinement less with 3 layers of cells between refinement levels (Figure 4.6). A mesh dependency study shows no noticeable difference in the surface elevation at the target location when using this mesh instead of a uniform mesh, *i.e.* the simulation is still mesh independent. Furthermore, no difference is observed when the CFL condition (Equation 3.17) is relaxed to have `maxCo` and `maxAlphaCo` equal to 0.5 instead of 0.25. Therefore the former has been used in this case. Apart from this, the generic NWT tool developed in Chapter 3 has been used with the same integration, interpolation and solution strategies as before.

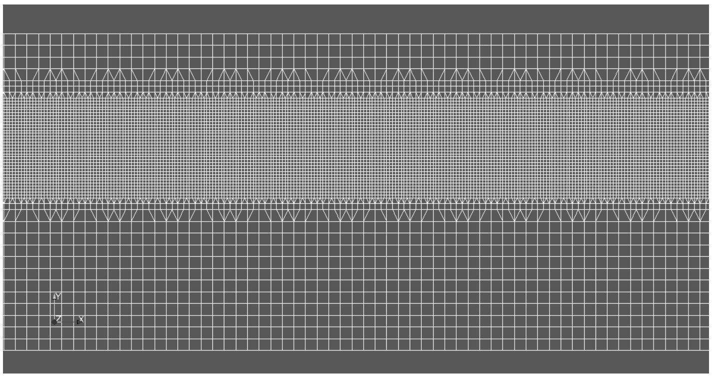

Figure 4.6: Side on view of the mesh used in the second extreme wave validation case showing two levels of quadtree refinement at the free surface.

The resultant free surface elevation at the target location, compared with that from the experiment, is shown in Figure 4.7. The main crest in the numerical simulation is certainly better than that in the initial validation case, however, there are a number of additional discrepancies present. The troughs are noticeably shallower in the numerical result and the surface elevation has an unusual form after the main crest, which no longer resembles reflections. Throughout this project, it has been noticed that the numerical wave can become unstable on the trailing edge of the main crest resulting in behaviour similar to localised wave breaking. The current (and probable) explanation for this is that the forward wave gauge was too close to the top of the sloping part of the basin floor for such a large wave in that water depth. This is likely to have caused the surface elevation measured there to be distorted and the linear approximation of the velocities at the inlet boundary to be a poor approximation to those present in the physical experiment. Consequently, the fluid in the numerical domain has to compensate for the poorly defined inlet boundary conditions and instabilities form when the discrepancy is too large, *i.e.* when the main crest is generated. These then persist as a disturbance to the free surface and hence at all times after the main crest the surface elevation is distorted. Figure 4.8 shows a series of snapshots of the entire free surface at a number of times after the generation of the main crest in the wave packet. It can be seen that, although the preceding crest is smoothly generated, there is an issue when producing the larger main crest which causes disturbances to the free surface in the wake of this peak.

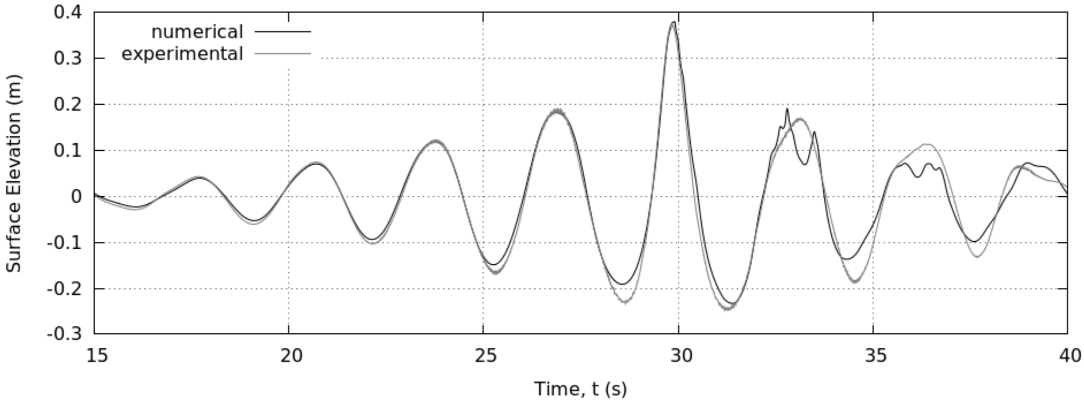

Figure 4.7: Comparison between the numerical result for the second extreme wave validation case (black), the free surface elevation measured at the target location in the corresponding physical experiment (grey) and the surface elevation predicted by linear theory (dotted)

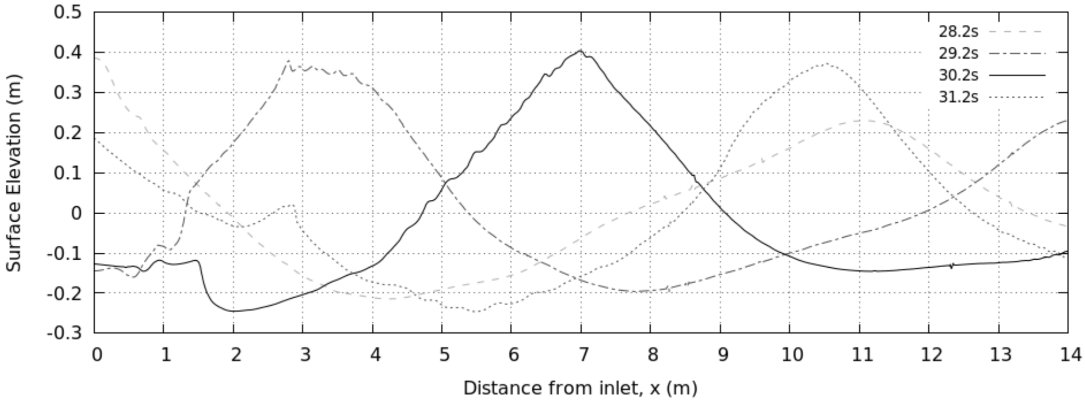

Figure 4.8: Free surface snapshots from the second extreme wave validation case showing an issue when generating the main crest and disturbances to the free surface as a consequence.

As in the previous case, the time series at the target location has been transformed into the frequency domain and plotted in Figure 4.9. Also plotted is the frequency spectrum derived from the surface elevation at the forward wave gauge/numerical inlet boundary. It can be seen that there has only been very subtle exchanges of energy between frequencies during the propagation from the inlet and target locations (a distance of 7 m in this case) and that the NWT has done a reasonably good job of capturing these. Although the numerical solution predicts a reduction in energy at the peak frequency, whereas the experimental predicts an increase, this could be explained by the localised wave 'breaking' in the

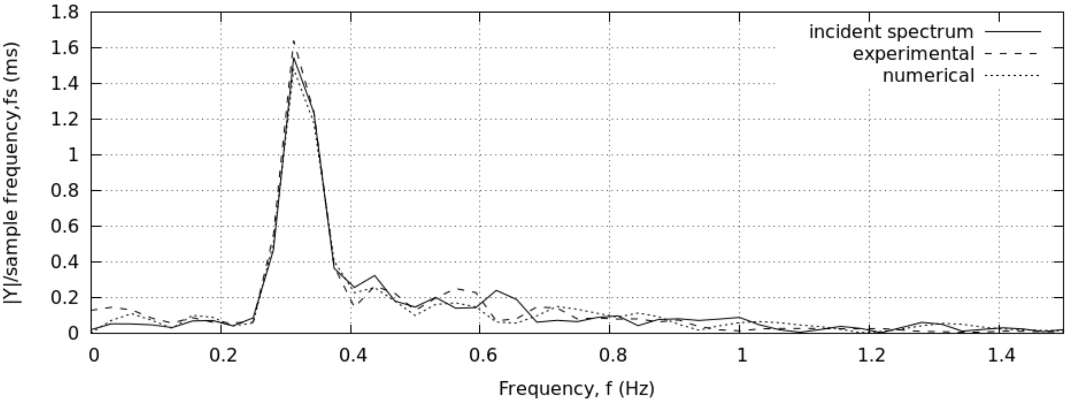

Figure 4.9: Frequency domain analysis of the time series at the target location, as well as that at the inlet position (incident spectrum), in the second extreme wave validation case. Y is the raw FFT output and $f_s = 128$ Hz.

numerical simulation which would tend to dissipate energy. Despite this, both the experimental and numerical agree on an increase in energy at lower frequencies and a shifting of the peaks at higher frequencies (most noticeably at approximately 0.6 Hz). Again, this provides confidence that the NWT is capable of capturing the nonlinear effects of extreme wave propagation and that the new forward wave gauge method removes some of the uncertainties near the wave maker. However, the inlet boundary condition still needs further consideration to resolve the free surface disturbances on the wake of large wave crests.

In a final wave-only validation case, a NewWave based on field measurements during a storm at the Wave Hub site in 2012, was reproduced at 1:20 scale. The site and the conditions are described in more detail by Vyzikas et al. (2013). The wave in this example was much smaller than the 100 year event used in the previous two cases. This meant a greater scale was possible and consequently the basin floor could be positioned deeper in the experiment (at 2.5 m), reducing the severity of the depth change in front of the paddles. It was hoped that this case, with a less extreme wave and a reduced depth change, would provide a test for the NWT without the inlet issues discussed above.

A two-dimensional NWT was constructed and the experimental waves were reproduced numerically using the forward wave gauge method described above. The numerical domain was 23 m in length with an 8 m RZ on the outlet. The water depth was 2.5 m and 0.5 m was

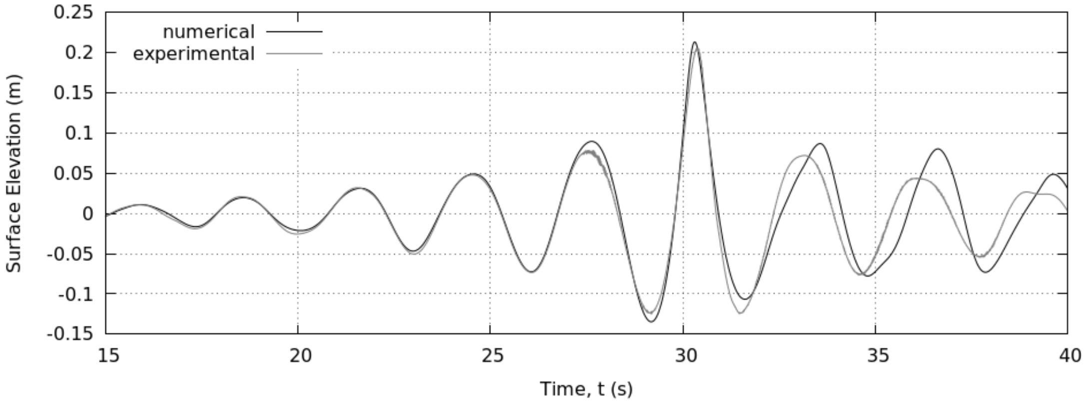

Figure 4.10: Comparison between the numerical result for the third extreme wave validation case (black) and free surface elevation measured at the target location in the corresponding physical experiment (grey)

allowed for the air phase. The modestly sized wave had a scaled maximum crest to trough height of 0.35 m and so the region from $z = -0.2$ m to $z = 0.3$ m had a square-celled mesh resolution of 0.02 m × 0.02 m giving 17.5 cells over the full wave height (sufficient for mesh independence with at most a 2 % RMS error tolerance). As in the previous case, the rest of the mesh was allowed to be more coarsely resolved (one level of refinement less than that at the free surface in this case). Again, `maxCo` and `maxAlphaCo` were relaxed to 0.5. The same integration, interpolation and solution strategies as in the previous case were maintained and the same boundary conditions were implemented.

The resulting surface elevation at the target location, compared with the measured time series, can be seen in Figure 4.10. Clearly the numerical simulation has reproduced the physical results up until 27 s and the height and shape of the main crest extremely well. There is still some discrepancy either side of the main crest and the comparison is again poor after the main crest has passed. However, the free surface disturbances observed in the previous case are no longer present. It is believed that this is because, in this case (with a less extreme wave and gentler depth change), the linear superposition of waves used by the forward wave gauge method provides an accurate prediction of the flow properties at that position. The differences after the main crest have been accredited to a disparity in the reflections between the physical and numerical cases. The 8 m RZ is certainly not long

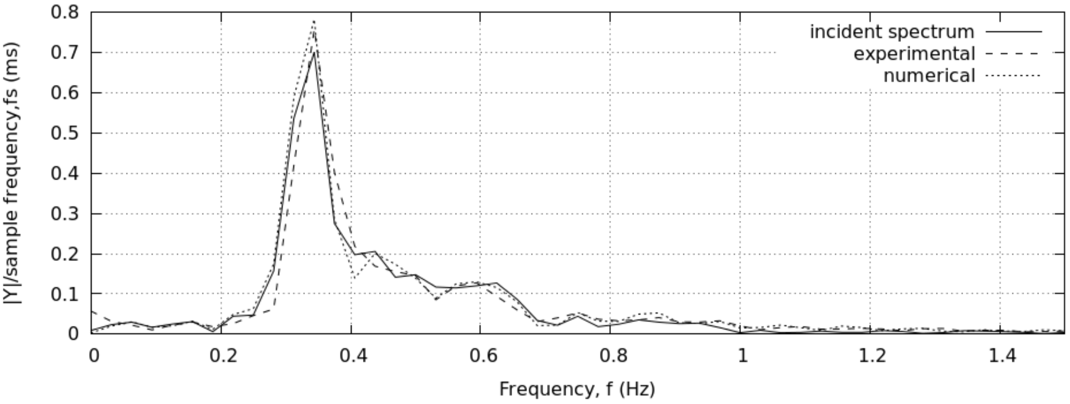

Figure 4.11: Frequency domain analysis of the time series at the target location, as well as that at the inlet position (incident spectrum), in the third extreme wave validation case. Y is the raw FFT output and $f_s = 128$ Hz.

enough to absorb the incident wave completely but again there were noticeable reflections present in the physical experiment also.

Once again, the time series' at the target location (and that at the inlet position) have been transformed into the frequency domain and are plotted in Figure 4.11. In this case, the evolution of the spectrum, between the inlet and the target location, is even more subtle (possibly because the wave is less extreme and therefore the nonlinear interactions are less pronounced). One difference is an increase in energy at the main frequency which can be observed in both the experimental and numerical cases. This suggests that, if it was not for the wave 'breaking' in the previous case, the numerical result there would have also shown an increase in energy at the main frequency to match that in the physical result. Another observation is that, the main peak in the experimental spectrum is slightly shifted to higher frequencies, compared to the numerical spectrum, which could explain the differences in the free surface histories in Figure 4.10. However, there is currently no explanation for this shift in energy to higher frequencies.

However, these results provide confidence in the ability of the NWT to reproduce physical experiments of extreme waves. However, a couple of improvements may be possible. Firstly, reflections appear to be an issue. A longer RZ would help to reduce the reflected waves in the NWT at the expense of an increased execution time. However, there is no guarantee that this would improve the comparison with the physical results as there are also considerable reflections present in the experiment. Secondly, the forward wave gauge method for specifying the numerical inlet boundary conditions appears to be sensitive to both the depth change near the wave paddles *i.e.* the test depth, and the nonlinearity of the wave being generated. Reducing the depth change in the physical basin (by having a deeper test area) or by moving the forward wave gauge further from the wave makers may help to remedy the first of these. However, an improved definition of the flow properties at the forward wave gauge position is likely to be the only way to address the second of these.

Chapter 5

Applications

> *[Why people buy quarter-inch drill bits.] "They don't want quarter-inch bits. They want quarter-inch holes"* - Leo McGinneva as quoted in Levitt (1983).

In this chapter, the NWT tool developed in this project has been used to simulate the interaction of waves with structures of increasing complexity. A progressive development process has been employed, beginning with validation of the NWT for a simplified generic WEC-type structure and ending with a full model of an existing moored wave energy device. In the first application, extreme wave interactions with a fixed truncated circular cylinder are studied. Next, progressing to moving structures, the Wavestar machine, which is an existing point absorber-type WEC able to move in only one degree of freedom (pitch), is simulated in regular waves. Thirdly, full 6DOF motion is considered; a floating buoy with a linear spring mooring is simulated under extreme wave loading. Finally, the Swedish, Seabased wave energy generator is modelled including 6DOF, single point mooring and PTO with limited stroke length. In each of these applications, additions to the generic NWT designed in the previous chapters are discussed in detail. Each of the numerical results are compared with those from an equivalent physical validation experiment and with similar studies in the literature. A number of variables are considered during these comparisons including surface elevation measurements, pressures and forces on structure surfaces, position of moving bodies and mooring line tensions. Some further analysis, beyond these comparisons, is performed but the main goal is to ensure the NWT tool is capable of describing the behaviour of WEC and mooring coupled systems under extreme wave loading. Only then can this work be applied to the survivability of WECs with any confidence.

5.1 Fixed truncated circular cylinder

Cylinders form the key structural components of many offshore structures and are also often assumed to be a good approximation to many more complicated geometries. For example, bottom-mounted, surface-piercing cylinders have been used to support causeways and piers as well as more recent developments like offshore wind turbines. Truncated cylinders, beyond simple marker buoys, are used for buoyancy in a range of floating structures including semi-submersibles, spar buoys and Tension-Leg Platforms (TLPs) as well as floating offshore wind applications (Kim et al. 1997). Furthermore, the elements of space-frame structures, sub-sea umbilicals, risers and flowlines all tend to be cylinders. As a result, there is a vast amount of research concerning the interaction of water waves with cylinders, ranging from analytical solutions which take advantage of the simple geometry to fully nonlinear work concerning the fundamentals of more complicated flow structures. It is for this reason that a surface-piecing truncated circular cylinder has been chosen as the initial validation case; not only is there a considerable amount of existing literature with which to compare results, but it can be argued that a number of point-absorber-type WEC concepts closely resemble this simplified geometry. In order, to limit the rate of change of complexity, the cylinder was fixed and the waves remained unidirectional in this investigation. Moving structures have been considered in subsequent applications.

5.1.1 Background - Modelling interactions between waves and cylinders

The interest in wave-structure interaction accelerated markedly with the exploration and production of offshore energy sources like Oil and Gas (O&G). Initially, for offshore O&G structures, the engineering focus was concentrated on the forces exerted by waves on the cylindrical support structures of the platforms (piles). In 1950 Morison et al. (1950) published their influential work on the force exerted by surface waves on piles. The result was the Morison equation which, based on linear regular wave kinematics and a horizontal bottom, predicts the force on a cylindrical pile using a set of empirical coefficients to represent any asymmetric velocity variations. In the so-called ‘Morison regime’ the diameter of the cylinder is assumed to be ‘small’, *i.e.* the cylinder is treated as being invisible to the waves.

Modified versions of the Morison equation, including the effects of turbulence and vortexes, are still widely used in applications involving the interaction of non-breaking waves with offshore structures, but these typically do not incorporate important diffraction effects (Rozario et al. 1993; Kim et al. 1997). Furthermore, empirical methods cannot be valid for all flow regimes and scaling results can be problematic. It was not until much later that nonlinear, interface-resolving models were developed and the hydrodynamics, run-up, and surface elevation in the vicinity of 'large' structures (the 'diffraction regime') investigated in detail. These nonlinear models were motivated by unexpected damage to offshore structures (Cao et al. 2011) and the observation that, despite preventative design of offshore installations (like TLPs) to limit their response to waves, some loads and motions still take place at the natural frequencies of the structure (Ferrant et al. 1999). In the context of moored WECs, however, these effects are likely to be even more important as the device itself is typically designed to exploit the resonance effects at the natural frequencies. Furthermore, radiation from freely floating WECs is an important factor in the design of wave energy installations and can only be described by considering the diffraction regime. Kriebel (1992) calculated the run-up of a second-order Stokes wave on a large-diameter bottom-mounted cylinder using potential flow theory and a second-order diffraction code. He compared his results against experiments in regular nonlinear waves and found that both first and second-order theory greatly under-estimate the maximum run-up on the front of the cylinder. Similarly, on the rear of the cylinder results show that significant nonlinear diffraction effects are present particularly as the wave steepness increases. Ferrant et al. (1999) found the same result while comparing a semi-analytical, frequency-domain diffraction approach, at first and second order, with a fully nonlinear time-domain BEM model. It is clear that linear diffraction theory is inadequate and, even before the onset of wave breaking, nonlinear effects are critical in wave-structure interaction problems. Furthermore, assumptions applied by potential flow models, that the structure is 'large' and therefore flow separation does not occur, may be inaccurate when considering smaller WEC designs. As a result, a wide range of fully nonlinear time-domain CFD programs have also been employed in similar investigations (Cao et al. 2011).

In recent years, the impact of breaking waves on cylindrical structures has become an area of intense research and is likely to be important when considering the survivability of offshore structures due to the additional short-lived impulsive force coming from a breaker front, or tongue. Typically the force from breaking wave impacts has been calculated as the sum of a quasi-static component, derived using the Morison equation, and a dynamic component involving an empirical measure of the impact area known as the curling factor, λ_c (Irschik et al. 2004; Wienke and Oumeraci 2005). More recently, fully nonlinear CFD models of breaking wave impacts on cylinders have been published and compared with estimates from the Morison equation. These have shown that the simpler Morison-type approach is capable of predicting the general trends during inertia dominated cases but not extreme wave loading (Bredmose et al. 2006; Bredmose and Jacobsen 2010). Despite this, breaking wave impacts will not be considered in this work as crucial phenomena such as fluid aeration and entrapment of air pockets are not accounted for in the incompressible solver used here. Nevertheless, the evidence in the literature suggests that considerable nonlinear effects, crucial for the assessment of survivability, occur during the interaction of steep waves with fixed cylinders and that simpler numerical models do not reproduce these accurately.

5.1.2 Additions to the general NWT - Fixed structures

In keeping with the gradual development of the NWT, only a couple of changes have been made to the methodology used in the wave-only cases.

1. Firstly, the computational domain has been extended to three dimensions in order to include the cylinder geometry. It is common to take advantage of the symmetry of such cases by allowing the domain to incorporate only half the volume with a specialised boundary condition along the symmetry plane (Bredmose and Jacobsen 2010). However, due to the possibility of asymmetric flow phenomena, like vortex shedding, in this study the structures are located in the centre of the domain, at the expense of increased CPU demand, and the front and back boundaries have been given no-slip, wall-type boundary conditions the same as the bottom boundary.

2. Secondly, as mentioned in Chapter 3, the addition of a structure requires the use of the meshing utility `snappyHexMesh` and the specification of additional boundary conditions on the structure's surface.

When considering unidirectional, long-crested waves, the extension to three dimensions, although not trivial in terms of execution time, is simple. The only concern is the possibility of a directional bias in the mesh, analogous to that observed in the convergence study with high aspect ratio mesh cells (Section 3.1.2). As a precaution therefore, the background mesh in all 3D cases will be constructed out of cubic cells and any possible advantage gained from a directional bias in the mesh resolution will be ignored due to the implications on the convergence of the solution.

The addition or, more accurately, removal of a structure from the computational domain is much more involved. `snappyhexMesh` offers a wide variety of options and quality control measures to ensure the mesh quality is not degraded significantly by the addition of complex boundary geometries. In this project only a few crucial elements have been considered. An investigation into the full suite of parameters available in `snappyHexMesh` remains a task for future studies. For the work presented in this thesis, any unmentioned parameters have been assigned their default value.

As mentioned in Section 3.1.2, `snappyHexMesh` can incorporate structures into the mesh from CAD surface geometries in STL format and allow for regional refinement using the quadtree (octree in 3D) formulation and an iterative procedure which ensures a pre-defined final mesh quality. In this case the computational domain was made 25 m long and 6 m wide. The water depth was again 1.73 m in order to represent the Wave Hub site at 1:30 scale (as in the second wave-only case in Section 4.4). The air phase was given a height of 1 m. The background mesh cell side length was 0.1 m. The region containing the free surface was then refined twice with a minimum of three cells between levels. This gave a cell side length of 0.025 m at the free surface. In addition to this, a cylindrical region with a radius of 1 m, stretching the full height of the domain and sharing an axis with the cylinder, was also refined to level 2. The mesh near the boundary of the cylinder was not refined

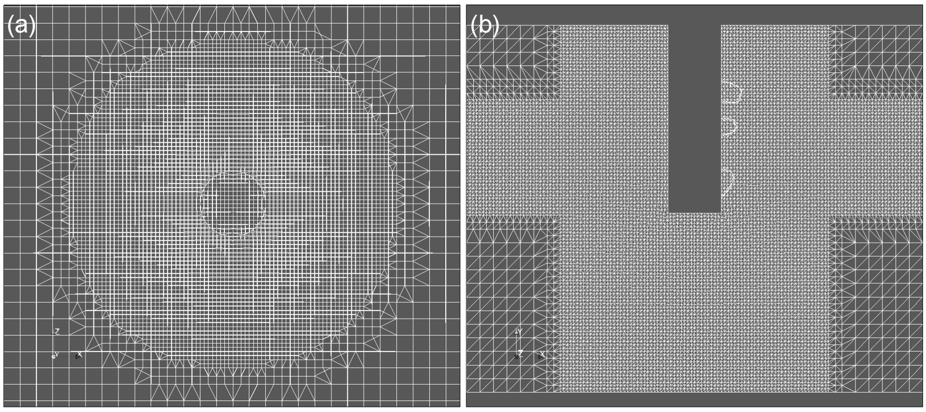

Figure 5.1: Part of the mesh used in the fixed cylinder cases: (a) plan view, (b) cross-section of region containing the cylinder.

any further and layers were not used. It was hoped that having a uniform mesh across the entire free surface would reduce the anomalous air flow discussed in Section 3.1.2. Figure 5.1 shows the mesh in the vicinity of the cylinder. As in the second wave-only case, a 13 m relaxation zone was applied to the end of the NWT. A 1 m relaxation zone was positioned on the inlet to absorb any reflections from the cylinder which was given no-slip wall-type boundary conditions the same as the front, back and bottom of the domain.

5.1.3 Validation experiment - Extreme wave interaction with a fixed cylinder

To assess the ability of the NWT tool to simulate extreme wave loading on stationary structures, a series of validation cases were designed in which a fixed, vertical, truncated cylinder was subjected to focused waves. In terms of survivability, maximum experienced loads are highly important. However, there is a lack of knowledge regarding the precise conditions in which these occur (particularly for dynamic systems, see Hann et al. (2015)). Therefore, a set of experiments were performed to ascertain both the pressure and run-up on the front of the cylinder as a function of the target position of an extreme wave. Four physical experiments were conducted using the same 100-year wave at the Wave Hub site as that used in the second wave-only cases in Section 4.4. The target position of the wave was the only variable in each case. The cylinder has a diameter of 0.4 m and a draft of 0.4 m and the target positions for the wave, relative to the cylinder axis, were -2.4 m, -1.2 m, 0 m and 1.2 m

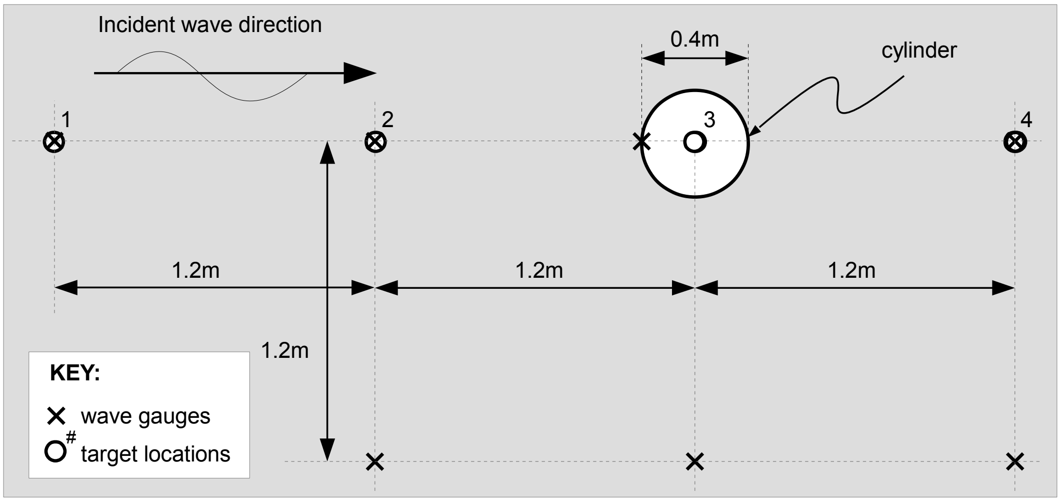

Figure 5.2: Schematic of the experimental set-up in the fixed cylinder case showing the wave gauge positions and wave target locations (1-4) relative to the cylinder.

in the direction of wave propagation. An array of wave gauges was used to measure a representation of the surface elevation and the run-up on the cylinder (Figure 5.2). A pressure transducer was located on the front of the cylinder at the SWL (Ransley et al. 2013*b*).

As an initial step, the waves were produced in the absence of the cylinder using the phase adjustment method, described in Chapter 4, to achieve a symmetrical 'focus' at each of the target locations. Furthermore, in these wave-only cases, an additional wave gauge was located 8.2 m upstream of where the cylinder centre would be in order to record the numerical input data. The resulting time series' at the target locations in these wave-only cases, from both the experimental and numerical tests, can be seen in Figure 5.3.

Clearly there is some variation in the success of the numerical simulation to reproduce the experimental results. Unsurprisingly, as the same wave and water depth has been used, all four of the numerical results plotted in Figure 5.3 show similar free surface distortions after the main crest to those seen in the second extreme wave case in Section 4.4. Plot 1 in Figure 5.3, corresponding to the target location closest to the wave paddles, is the same as the second extreme wave case in the previous chapter and shows the best comparison with the experiment. Then as the target location is shifted further away from the paddles (Plots 2

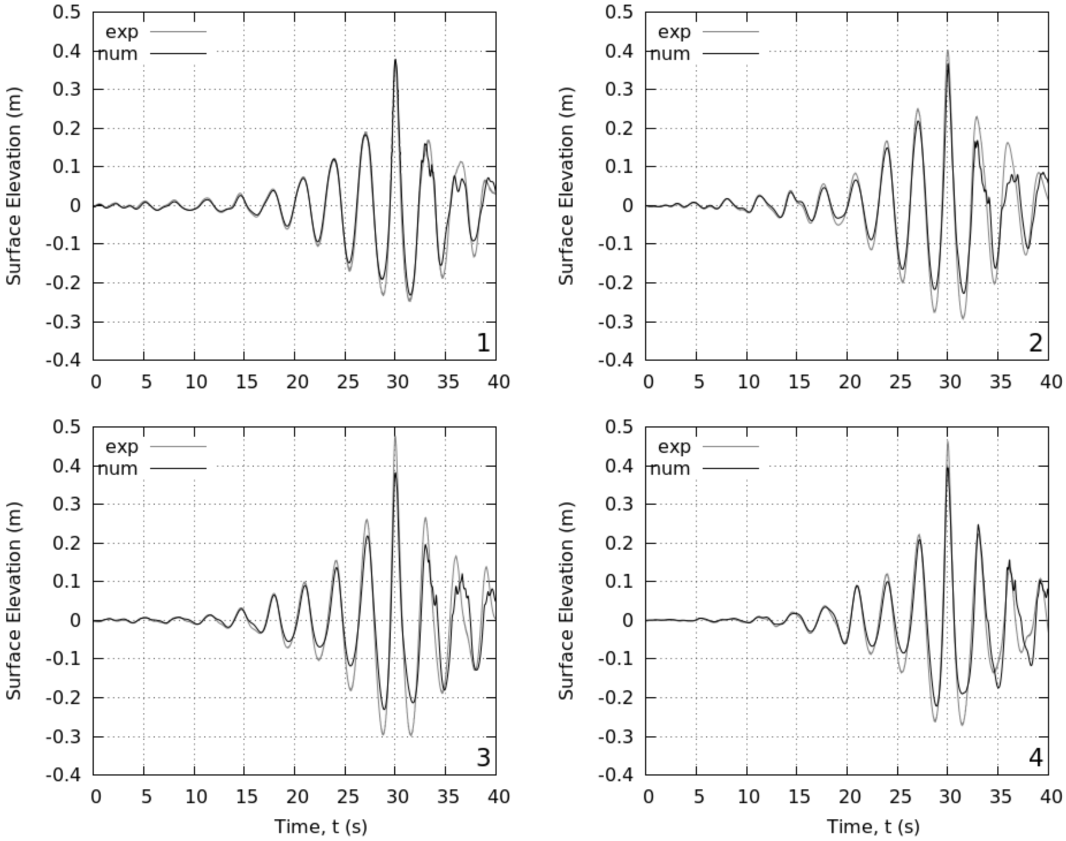

Figure 5.3: Surface elevation time histories at the four target locations in Figure 5.2. Numerical (black); physical (grey).

and 3 in Figure 5.3) the numerical result gets progressively worse, failing to reproduce either the amplitude of the crests or the deep troughs observed in the physical experiment. Finally, in Plot 4 there is a slight improvement but the main crest is still greatly underestimated, as are the depths of the troughs either side of it. Furthermore, the experimental results themselves show some variation at the four target locations. This can be seen better in Figure 5.4a. In order to draw comparisons between the results, a requirement of this study was for the waveform to be the same at each of the target locations. As clearly shown in Figure 5.4a this is not the case. There is a large variation in both the crest heights and trough depths at the different target locations. The trend is for the crest heights to increase with distance from the wave paddles, which is possibly due to greater nonlinear interaction effects built up over the increased propagation distance. However, the results also suggest

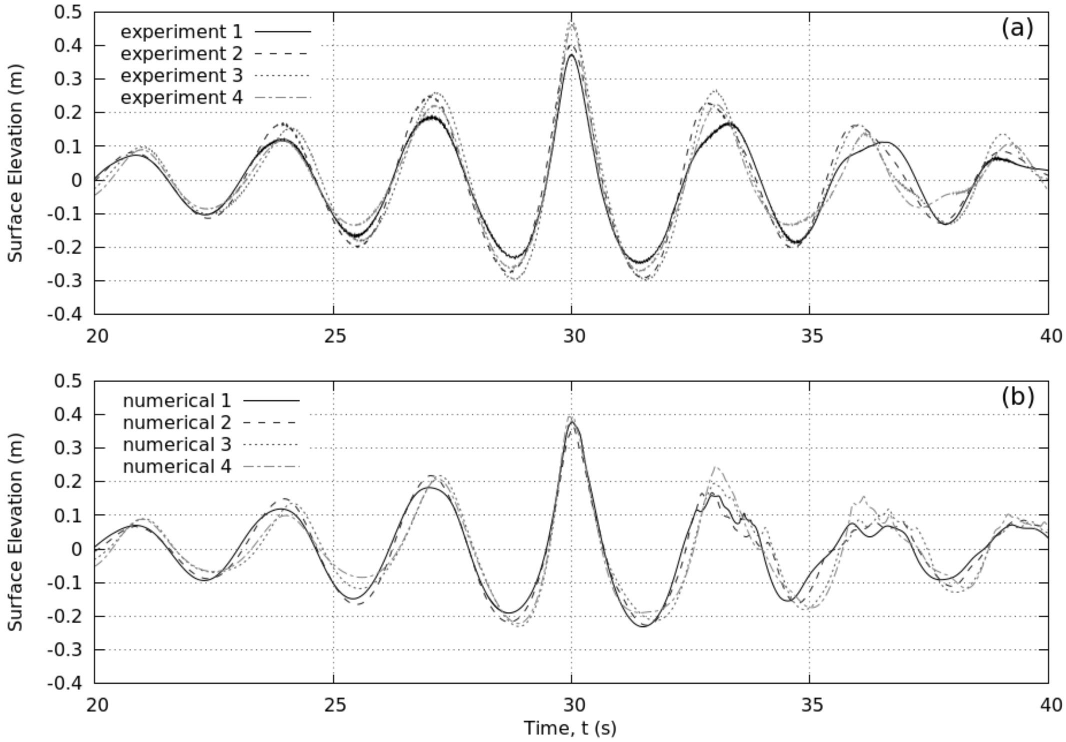

Figure 5.4: Surface elevation time histories at the four target locations in Figure 5.2. (a) physical; (b) numerical.

that the troughs become deeper at greater distance which is the opposite of that expected from the previous argument. Unfortunately, due to their size, the waves generated here may have been affected by automatic reductions made by the paddle control software. These reductions are likely to be a function of the target location; for dispersively focused waves, more distant targets require lower amplitudes to be generated at the wave maker, and hence lower paddle motions, allowing less of a reduction and an improved result at the target location (Bateman et al. 2012). An alternative explanation is that there is some variation in the ability of the paddle control software to account for the slope in the basin floor in front of the paddles (Figure 4.3). However, this should not affect the quality of the numerical solution which, using the forward wave gauge method, takes its input from the measured surface elevation. Despite this, the quality of the numerical solution appears to degrade as the target location is moved further from the inlet. Interestingly, there is far less variation in the numerical solutions (Figure 5.4b), compared to the physical results (Figure 5.4a), at each of the target locations. This suggests that whatever causes the differences in the physical experiments has not been accounted for numerically. Unfortunately, as mentioned in Section 4.4, the forward wave gauge may have been too close to the top of the ramp in the basin floor and so the linear decomposition of the surface elevation at this point may be a poor representation of the true fluid kinematics. Again, this is believed to be the reason for the free surface distortions observed after the main crests in Figures 5.3 and 5.4b. It is possible that these distortions gradually reduce the quality of the numerical results as the propagation length increases. However, this does not explain the slight improvement seen in the fourth case. An alternative suggestion is that the quality of the numerical results is proportional to the height of the main crest being generated. This idea fits the observed data and reinforces the idea that the quality of the inlet boundary and hence the resulting wave form is dependent on the nonlinearity of the incident wave.

The physical experiments were repeated 3 times in each case. The run-up and pressure measurements, compared with corresponding numerical solutions, are shown in Figures 5.5 and 5.6 respectively. The repeatability of the experiments is unquestionable. Only one of the physical results from each case has been plotted in Figure 5.5 as the measurements from repeat tests were near identical. In Figure 5.6, all three of the pressure results are shown in each case but there is no noticeable difference between them. Furthermore, each of the cases display the same phenomena: The run-up shares a very similar time series to that of the wave-only case but with increased amplitude and an additional small peak immediately after the main crest; the pressure has a series of peaks which coincide with the peaks in run-up whilst troughs appear as zero pressure due to the transducer drying. There is a consistent anomaly at the beginning of each of the pressure records which has been attributed to ‘thermal shock’ (the effect of temperature changes on the transducer electronics). Once the transducer is fully submerged, *i.e.* when the first waves arrive, this effect is resolved and the anomaly is removed. Finally, some of the early smaller pressure peaks predicted by the numerical simulation, in Figure 5.6, are not observed in the physical data. This is because the 1 bar (100 kPa) pressure transducer is operating at the limit of its sensitivity in this case and the measurement is at the same level as the noise in the signal.

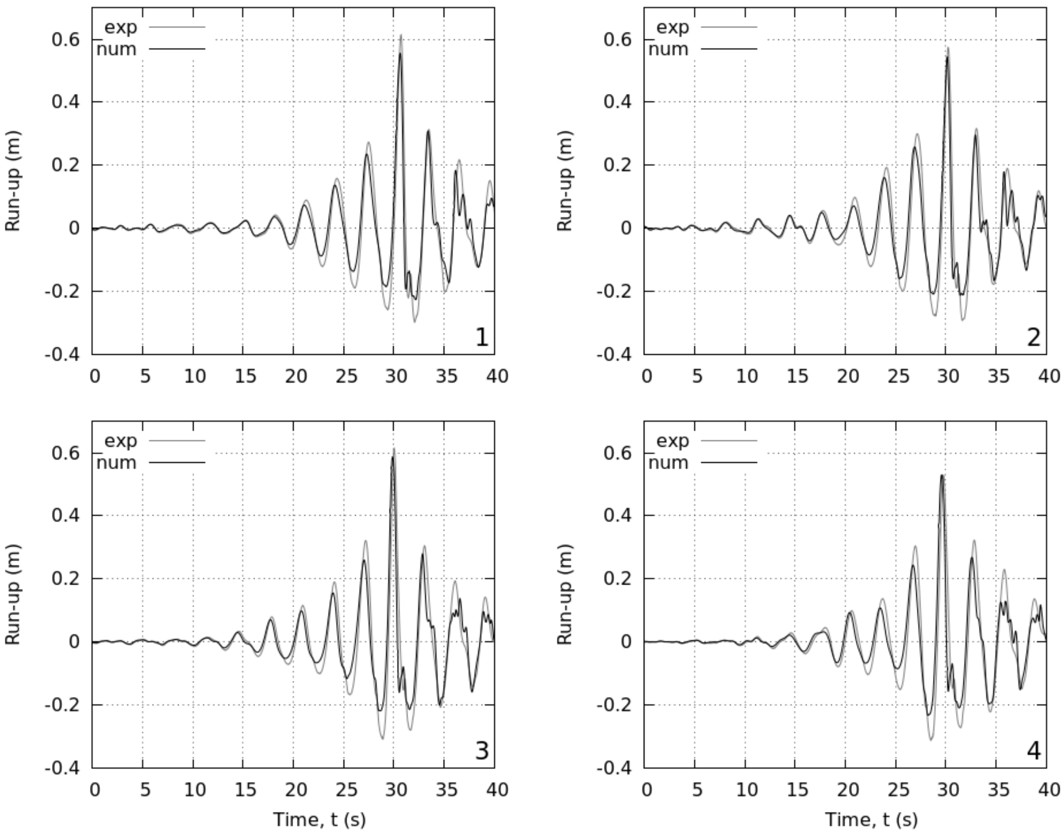

Figure 5.5: Run-up on the front of a cylinder when subject to four extreme waves with the target locations in Figure 5.2. Numerical (black); physical (grey).

Altogether the numerical simulation provides a very good approximation of the run-up and pressure on the front face of the cylinder. The comparison is particularly good during the low amplitude part of the wave packet and at the point of the maximum run-up which is reproduced to within a few percent of the physical result. This is a vast improvement on the run-up predicted by both linear and second-order diffraction theory when applied to steep nonlinear regular wave interactions with a bottom mounted cylinder (Kriebel 1992). As with the wave-only cases, the deep troughs (run-down) observed in the physical experiment have not been reproduced by the numerical simulation. Analysis of the accelerometer data does show a ± 0.01 m (2.5 % of the cylinder diameter) displacement at the base of the cylinder which may have caused some surface displacement but the majority of the differences between the numerical and physical results are likely to be due to the difference in the in-

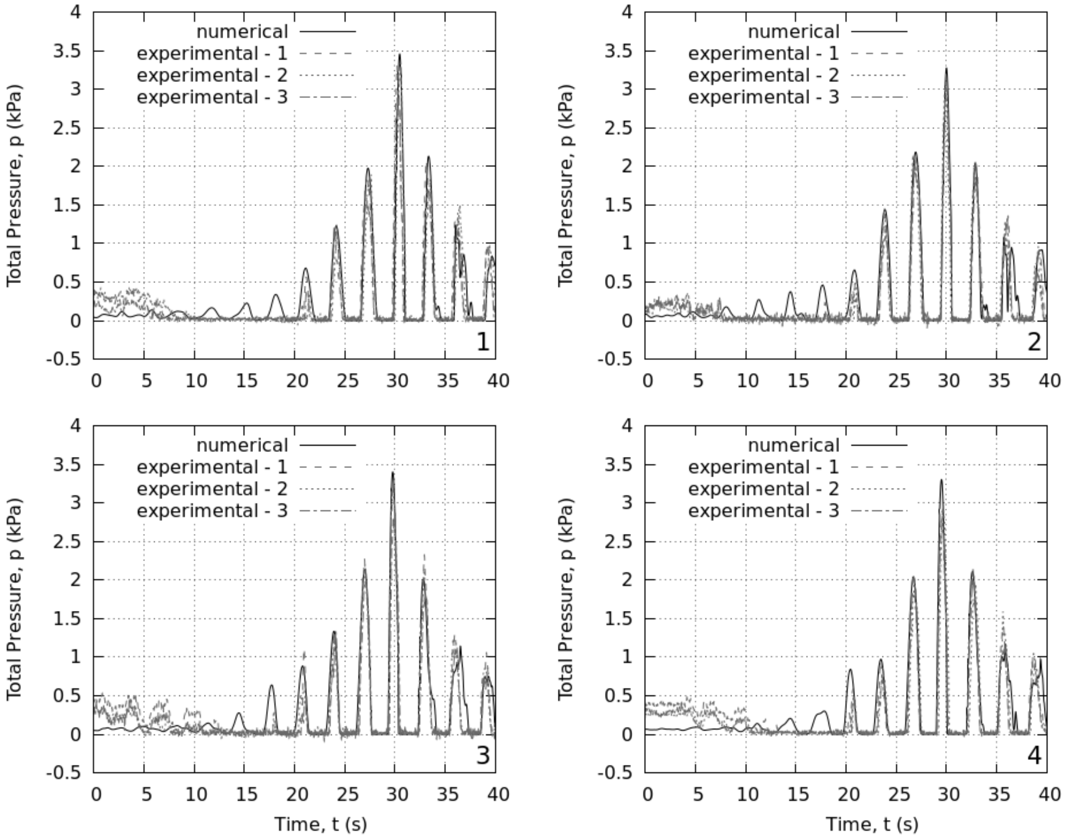

Figure 5.6: Pressure on the front of a cylinder, at the SWL, when subject to four extreme waves with the target locations in Figure 5.2. Numerical (black); three separate physical tests (grey).

cident wave as discussed in the wave-only case. Therefore, comparisons between the four cases will not be made here. However, there does not appear to be a significant difference in either pressure or run-up when the target location is moved relative to the cylinder axis.

One element worth further investigation is the additional peak on the trailing edge of the main crest. From observations made during the physical experiments a few interesting phenomena have been noted. Until the first of the three main crests, the water surface is undisturbed, no scattered waves are observed and the run-up is both comparable in amplitude and phase to the incident wave. As the larger crests arrive the difference in run-up around the cylinder's circumference increases significantly and some symmetrical wave scattering is observed in the lee of the cylinder. A deep trough is formed to the rear as

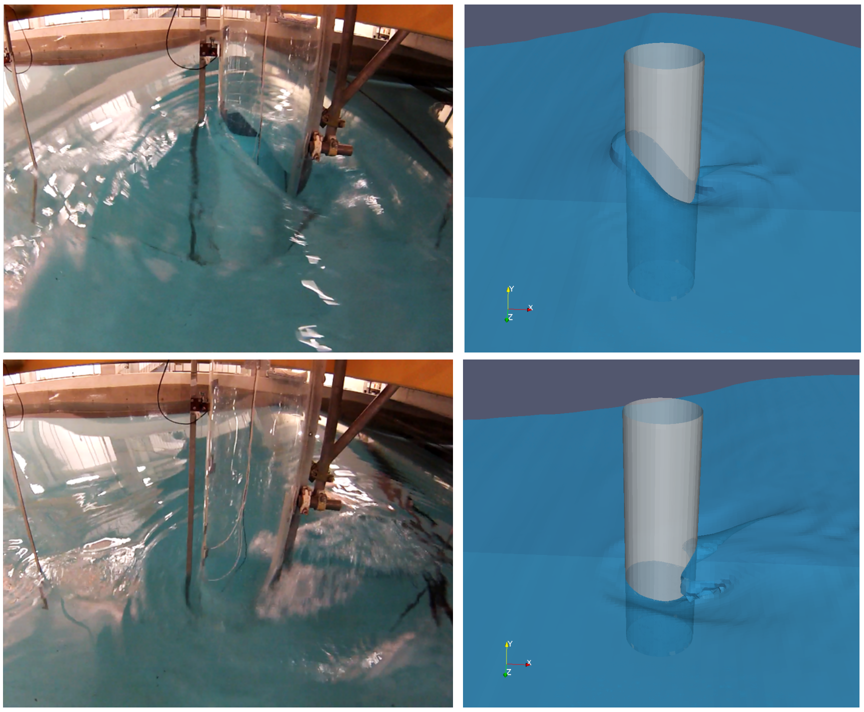

Figure 5.7: Snapshots at maximum run-up (top) and 0.4 s later (bottom) during the physical experiment (left) and the numerical simulation (right).

run-up considerably greater than the incident wave height is produced on the front of the cylinder. There is a thickening of the leading edge of the run-up jet when the wave crest is alongside the cylinder. There is then an upwelling on the back of the cylinder with pronounced depressions on either side. The free surface then collapses backwards at the rear of the cylinder producing a spilling broken wave which propagates upstream causing a dip and then a small additional peak in run-up on the front of the cylinder as it passes. Figure 5.7 shows snapshots at the point of maximum run-up (top) and 0.4 s later (bottom) during the physical experiments (left) and the numerical simulation (right). A wide-angle camera lens was used and so the numerical snapshot has been produced with Paraview's parallel projection function disabled. It can be seen that, qualitatively, the numerical solution reproduces the physical phenomena associated with run-up of a NewWave on a fixed truncated cylinder well. Despite the use of a truncated cylinder, the results from this investigation are very similar to the observations of Chaplin et al. (1997) when assessing the secondary loading cycle and ringing of a vertical cylinder in steep non-breaking waves.

5.1.4 Further numerical investigation and discussion - Fixed cylinder

Due to the differences in the incident wave shown in Figure 5.4a, the effect of changing the distance between the cylinder and the wave's target location is still unknown. However, as the numerical solutions for the run-up and pressure (Figures 5.5 and 5.6) appear to be reasonably accurate, the analysis has been continued using the NWT to generate the data.

In this investigation the incident wave was kept the same and the cylinder position, relative to the inlet boundary, was varied. This ensured the wave form was consistent in each case and allows the output results to be considered as a function of the distance between the target location and the cylinder axis. For this study, the wave in Case 1 was selected to be the incident wave as this was the one which best reproduced the experimental result at the target location in the wave-only cases (Figure 5.3). Perhaps controversially, however, it is insufficient to judge the quality of the numerical solution based on a single surface elevation time series. Even a perfect recreation of the surface elevation at a single point does not guarantee the other flow parameters, such as velocity, are also matched. At the very least, if the solution is accurate, the comparison of surface elevation time series at multiple locations should be equally good. This would suggest the propagation of the wave, and hence the solution for the fluid velocities, was adequate and provides greater confidence in the numerical result.

Figure 5.8 shows a comparison between the experimental and numerical surface elevation measured at three separate locations for the wave in Case 1 (target at $x = 5.8$ m). As can be seen, the numerical solution matches the experimental result very well at the target location (Figure 5.8a). However, the comparison worsens as the wave propagates down the basin (Figures 5.8b and 5.8c). It is possible that a difference in the reflections in both the physical and numerical tests are to blame. However, as discussed in the second extreme wave case in Section 4.4, it is suspected that the velocities specified on the numerical inlet boundary do not perfectly match those in the experiment leading to variations in the propagation of the wave throughout the wave tank. This is likely to have an effect on the run-up and pressures measured on the cylinder, which was centred at 8.2 m, and is also believed to be

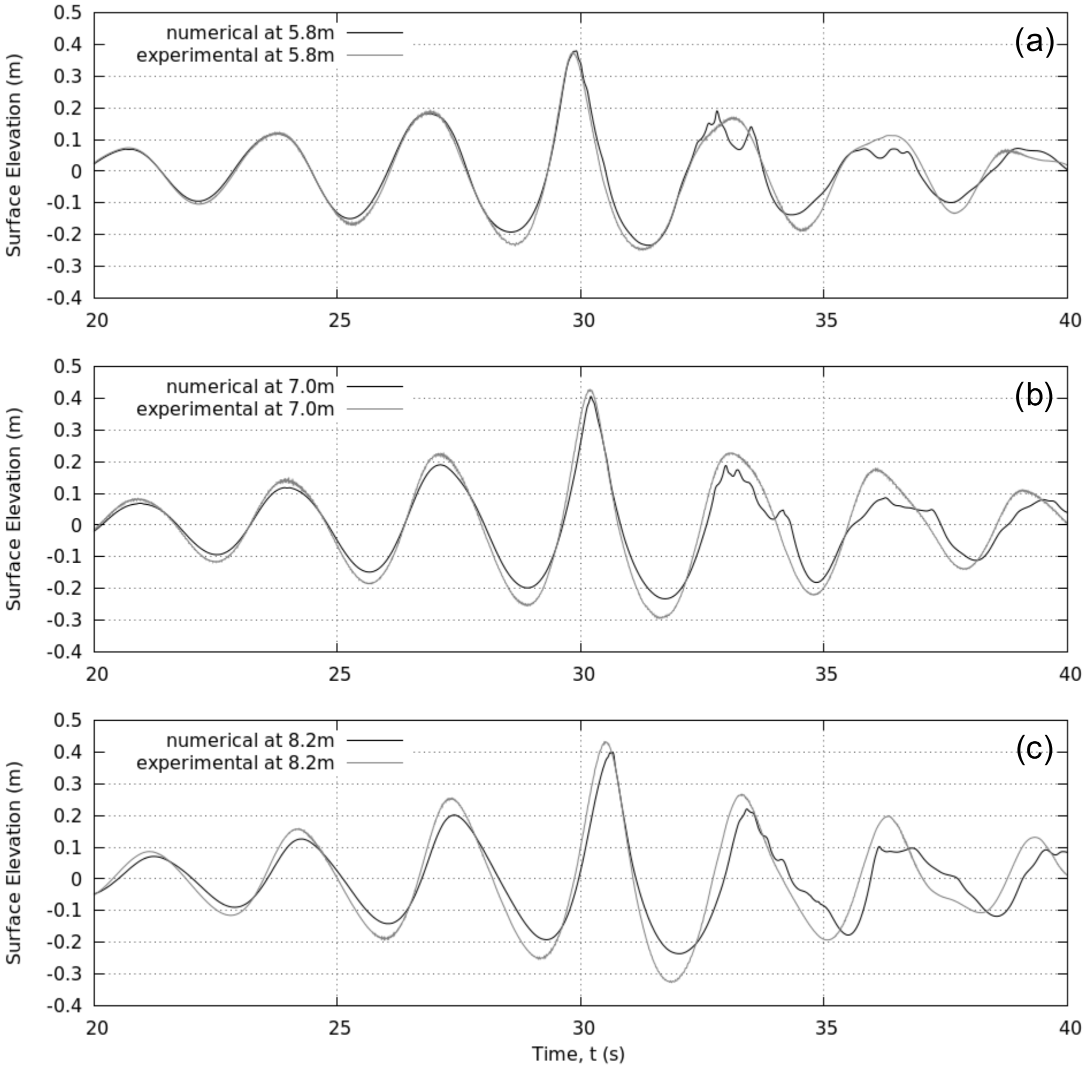

Figure 5.8: Comparisons between the experimental and numerical surface elevation of a NewWave with a target at 5.8 m measured at three separate places: the target position (5.8 m) (a), 7.0 m (b) and 8.2 m (c).

responsible for the free surface disturbances observed after the main crest (as mentioned earlier). In Figure 5.8, it can also be seen that although the wave is believed to be ‘focused’ at 5.8 m (because the wave form is symmetrical) it does not have the largest crest there. In fact, out of these three plots, it has the lowest crest height in both the numerical and the experimental results. According to linear theory, in particular linear superposition, this cannot be the case; if all wave components were in phase at focus the crest would have maximum amplitude. Either the components are not all in phase at the target location

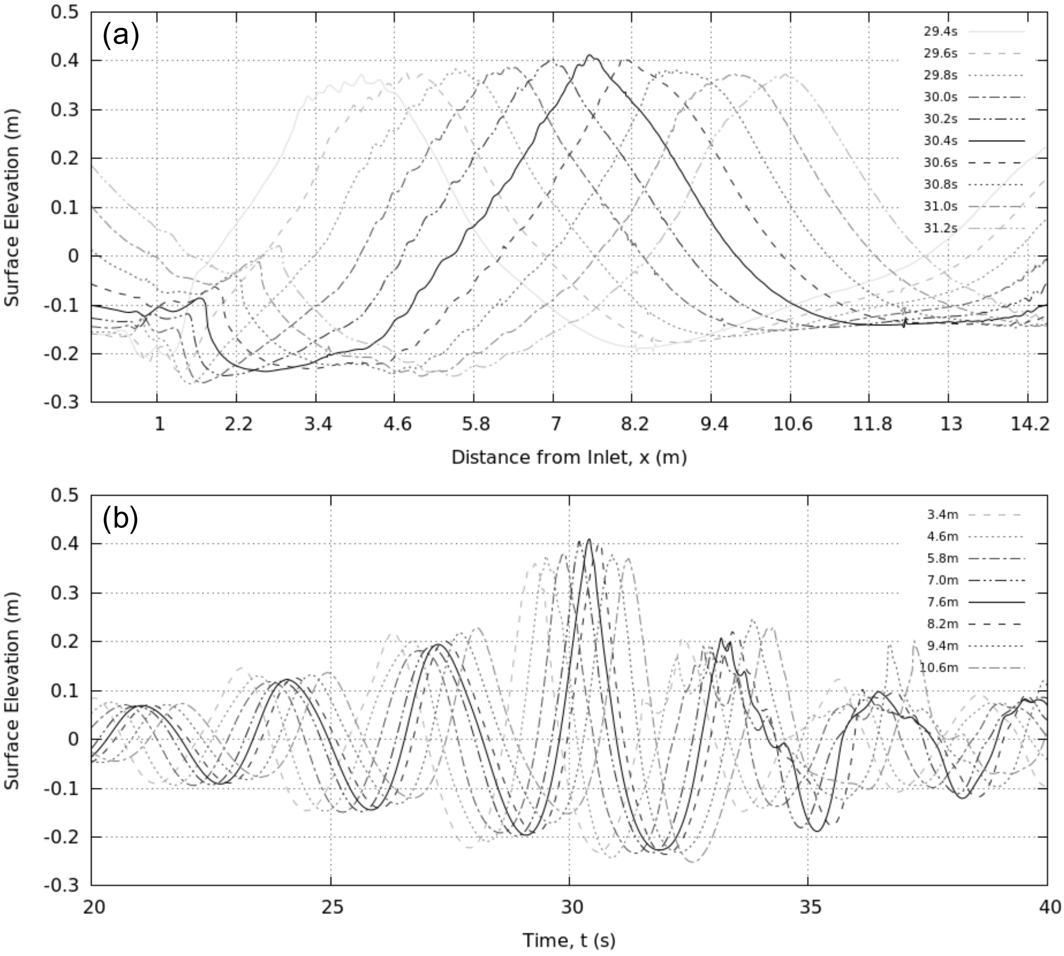

Figure 5.9: Numerical results for the surface elevation of an extreme wave with target location 5.8 m. (a) Snapshots of the free-surface as a function of distance from the inlet at a number of times close to the focus time. (b) Time series of the free-surface at the cylinder locations in the following work.

and it is coincidence that the time series is symmetrical, or more likely, using the linear superposition of sinusoids to describe the form and propagation of highly non-linear waves with significant 'wave-wave' interactions is not appropriate. Either way when it comes to the survivability of wave energy converters it is likely to be the largest wave which is of greatest concern to developers rather than the most symmetrical.

Figure 5.9a shows a series of free-surface snapshots from the numerical simulation looking perpendicular to the wave direction. The x-axis has been plotted in steps of 1.2 m as these are the cylinder positions in the following work. The focus location is believed to be at 5.8 m,

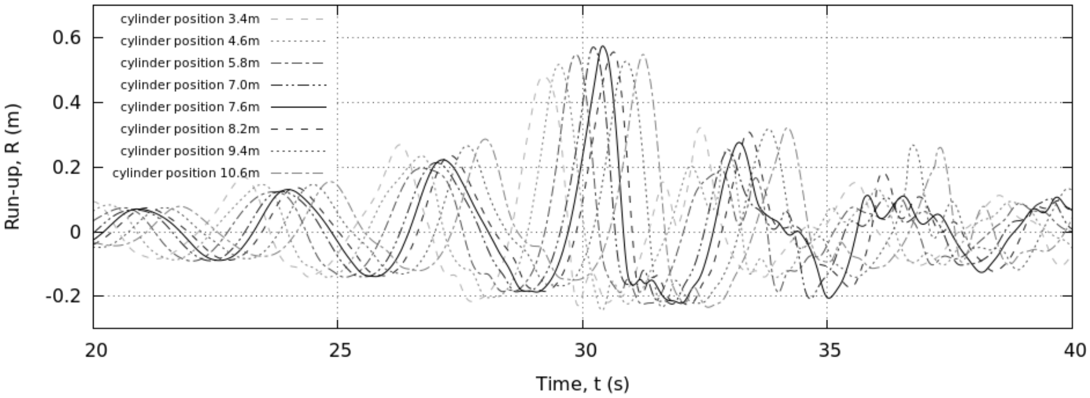

Figure 5.10: Run-up on a cylinder when positioned with its axis at 8 different locations relative to the target location of an extreme wave.

however, it can be seen that the greatest crest height is actually at 7.6 m at a time of 30.4 s. The is a commonly observed phenomenon in work involving large focused waves (Chaplin et al. 1997). Figure 5.9b shows the free-surface time series at each of the cylinder positions in the absence of the cylinder. Again the greatest crest height is recorded at 7.6 m and it reduces gradually away from there. The preceding crests have the opposite pattern and the preceding troughs are deeper closer to the inlet. If one still considers a symmetrical times series to be a sign of focusing then for this case the time series at 3.4 m is most symmetrical and has the lowest crest height. After the main crest has passed few conclusions can be drawn here due to the disturbed free-surface discussed earlier.

In order to find the load on a cylinder as a function of the wave's focus location, a series of numerical simulations were performed with the cylinder axis located at $x =$ 3.4 m, 4.6 m, 5.8 m, 7.0 m, 7.6 m, 8.2 m, 9.4 m and 10.6 m. The mesh was designed as described in Section 5.1.2 and the generic NWT decisions from Chapter 3 were applied in each case. Figure 5.10 shows the resulting run-up on the front face of the cylinder in these eight cases. The same trend as in the surface elevation of the wave only-case (Figure 5.9b) is observed. The greatest run-up is on the cylinder at 7.6 m and the maximum run-up decreases gradually as the cylinder moves away from this position. For all other peaks the opposite is true and the maximum 'run-down' (trough) appears to reduce with distance from the inlet boundary.

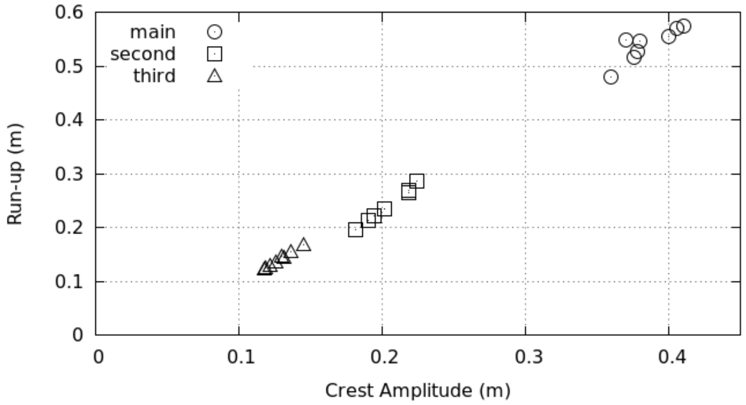

Figure 5.11: Run-up on a cylinder vs. the wave-only crest heights measured at the location of the cylinder's axis for an extreme wave event.

It is not surprising that the maximum run-up appears to be a direct function of the maximum incident surface elevation. Figure 5.11 shows a near linear relationship between the wave-only crest heights and the run-up on the front face of the cylinder whether considering the main crest or one of the smaller earlier crests. Clearly by comparing Figure 5.9b with Figure 5.10, this relationship is disrupted immediately after the main crest where, as discussed in the previous section, high-order diffraction effects have led to a secondary peak in the run-up without a corresponding peak in the incident surface elevation. Although present in all eight of the cases simulated, Figure 5.12 shows a magnification of the secondary peak in Figure 5.10 for four of the cases and the physical measurement with the cylinder positioned at 5.8 m. From Figure 5.12 it can be seen that the numerical solution predicts the magnitude of this secondary peak well, however, it predicts the peak slightly earlier than that seen in the experiment. Once again the deep trough following this additional peak has not been reproduced numerically due to differences in the incident waves. Finally, there does not seem to be a clear relationship between the characteristics of this secondary peak and the relative distance between focus location and cylinder position. It is possible, however, that this phenomenon is affected by turbulence; observations from the physical experiments show clear signs of wave breaking in the region behind the cylinder. Assessment of various turbulence closure models for wave-structure interaction will be considered in future work.

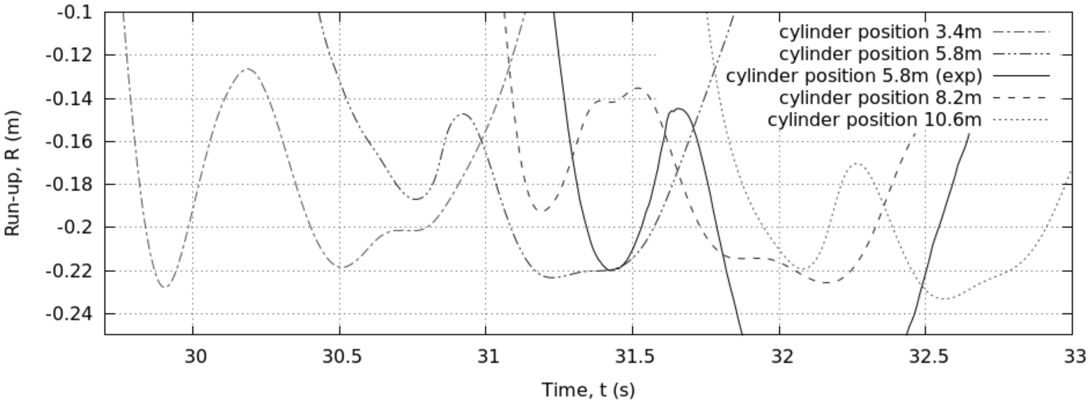

Figure 5.12: The secondary peak in run-up on the front face of a cylinder in 4 different positions relative to the focus location of an incident focused wave.

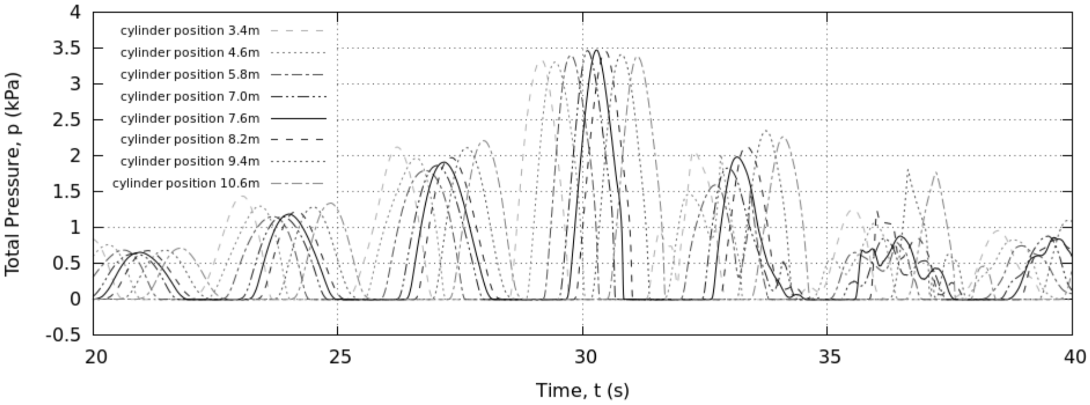

Figure 5.13: Pressure at the SWL on the front of a cylinder in 8 different positions relative to the target location of an extreme wave.

Figure 5.13 shows the pressure on the front of the cylinder at the SWL in each of the cases. As with the run-up, the pressure appears to be a direct function of the wave-only surface elevation in Figure 5.9b. This exemplifies the need to consider the highest crest height, instead of the most symmetrical case, when discussing run-up, possible green-water effects and pressure on the front face of a structure. The difference between the maximum run-up in the most symmetrical case (at 3.4 m) and that with the greatest run-up (at 7.6 m) is as much as 20 % which could be crucial for the design of offshore structures where water inundation or damage from vertical flows (Bredmose and Jacobsen 2011) are an issue.

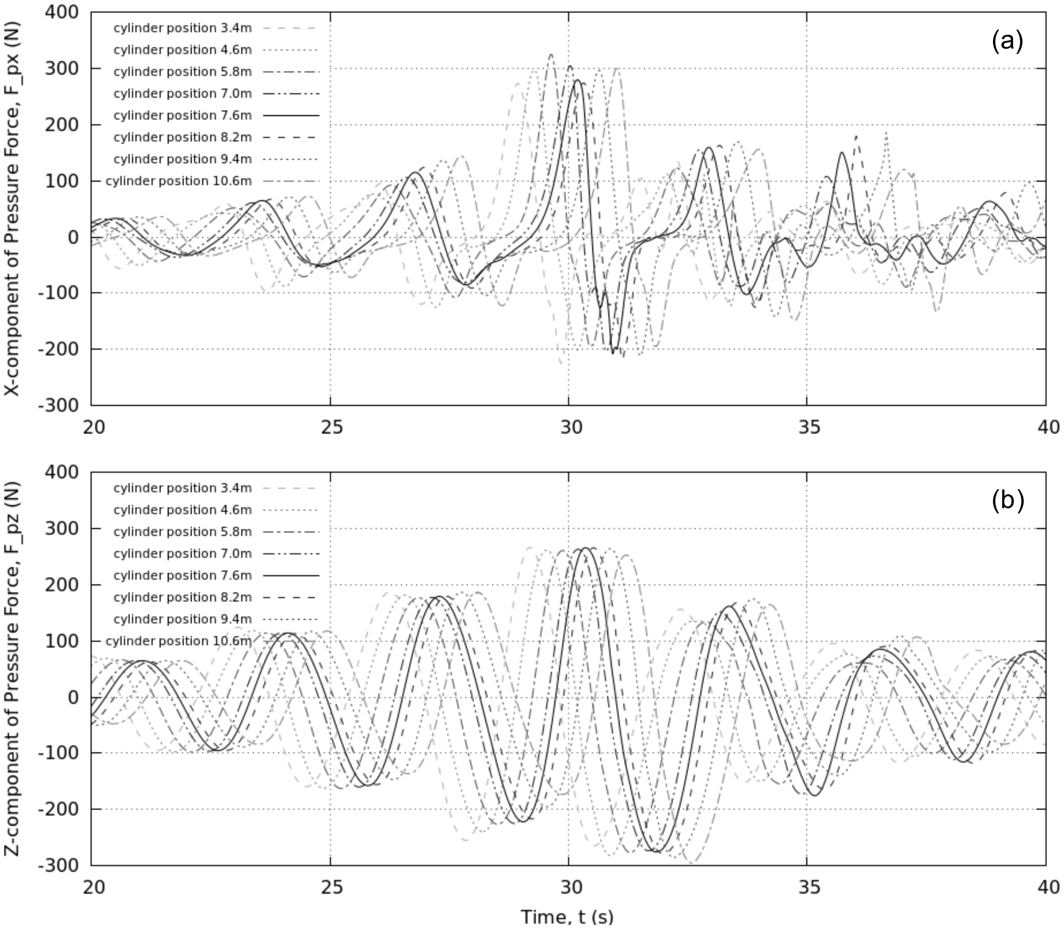

Figure 5.14: Horizontal (a) and vertical (b) force due to pressure on a cylinder at 8 different positions during the same extreme wave event.

In terms of forces on the cylinder, OpenFOAM® records both forces due to pressure and those due to viscous effects. In this case the viscous forces were negligible compared with the pressure forces and so only the latter have been presented here. Figure 5.14 shows a time series for both the horizontal (in the direction of wave propagation) and the vertical component of the pressure force. Surprisingly, the horizontal force does not follow the same pattern as the run-up and SWL pressure. In fact the case with the greatest run-up (7.6 m) has one of the lowest peak horizontal forces. The peak vertical forces appear to be completely independent of the cylinder's position whereas the rest of the time series appears to be proportional to the incident surface elevation. The only explanation for these unexpected trends is that the flow phenomena around the circumference of the cylinder

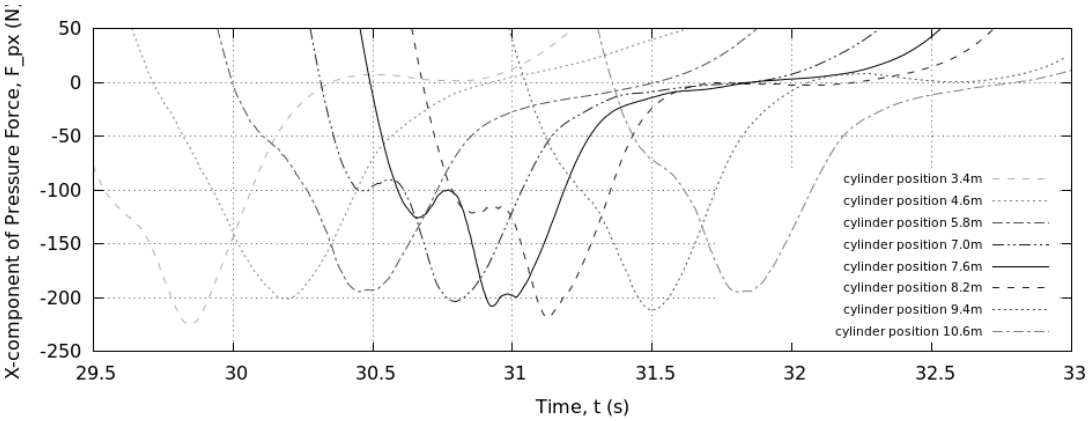

Figure 5.15: Secondary load cycle on a cylinder in 8 different positions relative to the target location of an extreme wave.

combine in some way to either counter or reinforce each other depending on the case. This is in line with the concept of 'ringing' of offshore structures in which the higher-order diffraction effects act to excite structures well above the corresponding peak frequency of the wave spectrum (Chaplin et al. 1997). This phenomena is particularly problematic for structures such as oil platforms which are typically designed to have high natural frequencies to avoid excitation; it is unclear as to how this may affect the behaviour of WECs which are designed to respond to wave excitation. Nevertheless, the numerical solution here has identified the secondary loading cycle seen in physical experiments (Chaplin et al. 1997), whereas simpler methods based on various adaptations of the Morison equation are not able to do so (Chaplin et al. 1997). A magnified view of the secondary loading cycle in Figure 5.14a can be seen, for all cylinder positions, in Figure 5.15. All of the results show a similar minimum and an extended period of zero horizontal force following the secondary load. Interestingly, it is the cylinder position at 7.6 m which has the highest magnitude secondary load. Moving the cylinder away from this position reduces the secondary load until there is no peak at all. There is then a hint of the peak returning as the cylinder is moved yet further. This pattern does not match that of the secondary run-up cycle but does correlate with the maximum run-up in Figure 5.10, *i.e.* the greater the run-up, the greater the magnitude of the secondary load. Furthermore, greater secondary loads correspond to smaller primary loads.

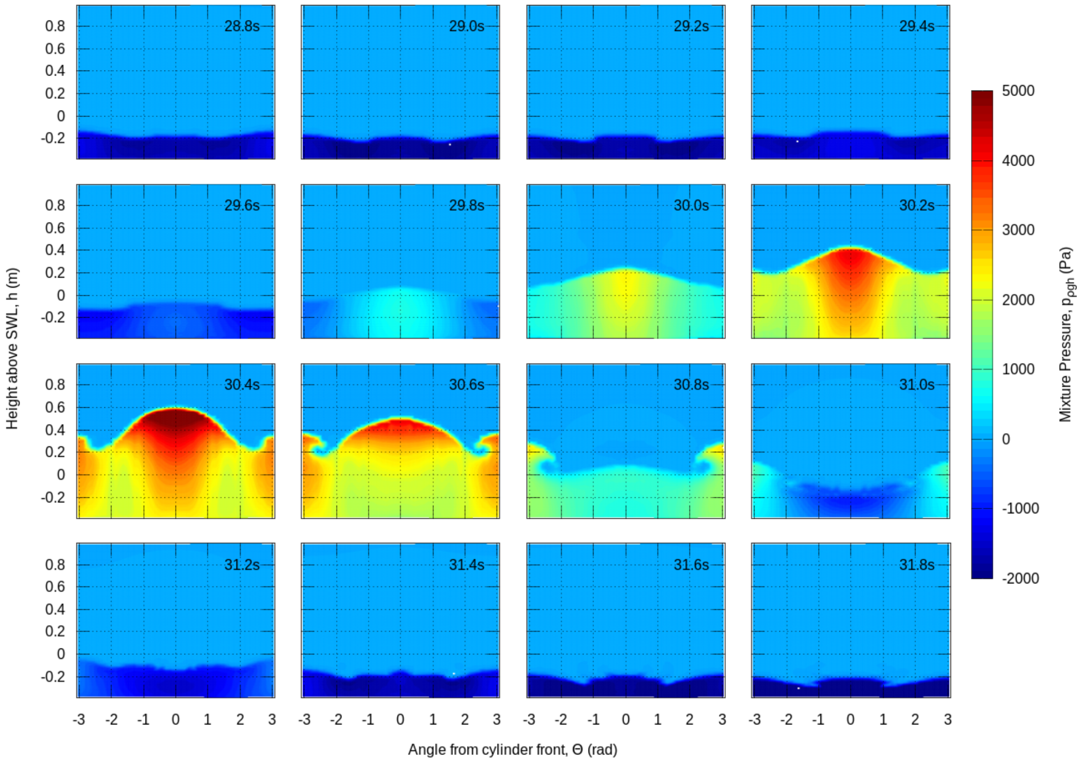

Figure 5.16: Pressure distributions around the cylinder at 7.6 m.

In an attempt to identify the processes responsible for the secondary loading cycle and the unexpected trend in the maximum horizontal force, the pressure distribution around the cylinder has been plotted at a number of times for two cylinder positions: at 7.6 m which has a low peak horizontal force despite having the greatest run-up (Figure 5.16), and; at 5.8 m which has the highest peak horizontal force (Figure 5.17). However, there does not appear to be any significant difference between these two results during the period of maximum horizontal force. Afterwards, it can be seen that at the moment of peak run-up there are high pressure regions on the front and back of the cylinder which would act against one another when it comes to the net horizontal force. Shortly after this, and in keeping with the measurements of Chaplin et al. (1997), there is higher pressure on the rear of the cylinder than on the front. The secondary loading cycle has been identified as corresponding to an interval over which the pressure on the rear of the cylinder reduces faster than that

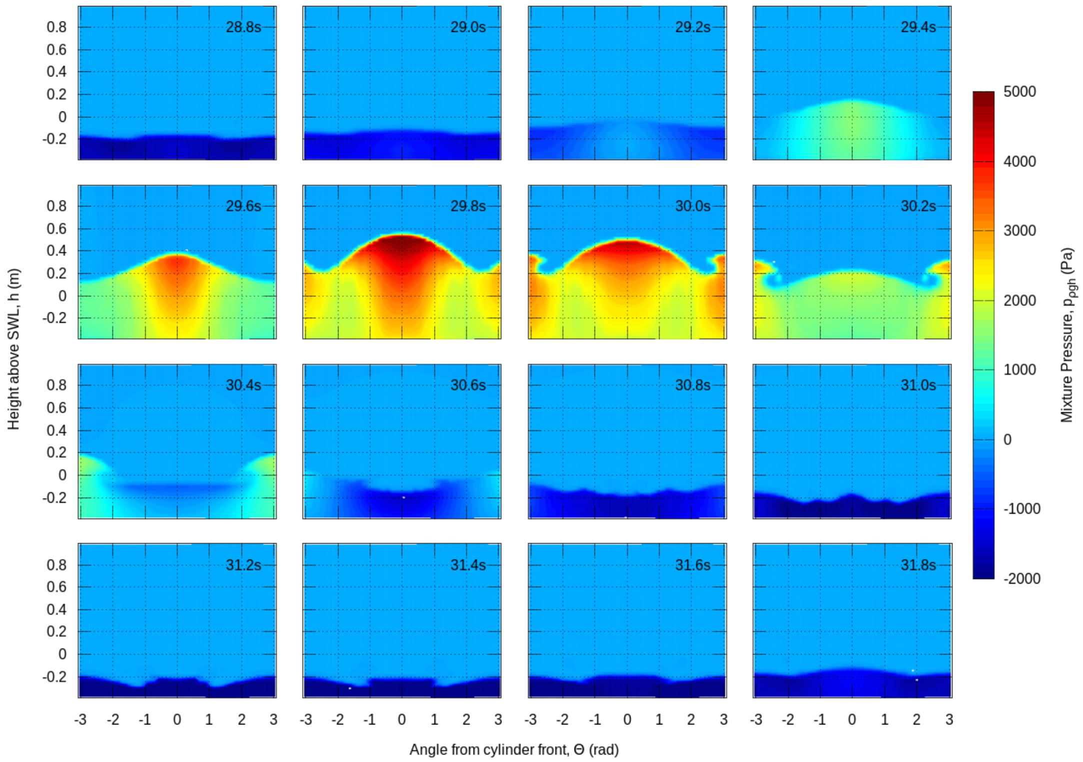

Figure 5.17: Pressure distributions around the cylinder at 5.8 m.

on the front (Chaplin et al. 1997). This is then followed by the reverse of this causing the load to reduce again. This behaviour and the infilling wave which is responsible for the high pressure on the rear of the cylinder are clearly sensitive to the incident wave as the secondary loading is present when the cylinder is positioned at 7.6 m but is not when the cylinder is positioned at 5.8 m. Furthermore, as shown by Chaplin et al. (1997) this phenomena is highly dependent on the diameter of the cylinder, but a full investigation of this aspect is outside the remit of this investigation.

5.1.5 Conclusions - Extreme wave interactions with a fixed cylinder

In conclusion, despite some concerns over the physical validation experiment, the NWT appears to reliably predict the pressure and run-up of an extreme wave on a fixed truncated circular cylinder. The addition of a fixed structure with simple geometry using the `snappyHexMesh` utility has been found to cause no issues and there are no obvious concerns over the solution strategy or numerical schemes used as part of the generic NWT setup.

There remains an issue with the wave maker boundary condition in that generation of the main crest of the waves considered here causes a localised ‘breaking’ phenomenon and subsequent disturbances to the free surface which persist throughout the simulation. It is suspected that this is a consequence of predicting the fluid properties using the superposition of linear wave components and the linear velocity potential which may have begun to break down at the high level of nonlinearity present in these cases. It would seem that an improved definition of the wave kinematics at the inlet boundary is required for very large waves. However, in this case the rapid change in water depth and the position of the forward wave gauge in the physical experiment may have caused issues which have not be accounted for in the numerical simulation.

In terms of extreme wave interactions with a truncated cylinder, there is a near-linear relationship between the incident surface elevation and both the run-up and pressure on the front of the cylinder. However, the total force on the cylinder displays an unexpected relationship when compared to the other variables. It appears the maximum vertical force is independent of the cylinder’s position, while the maximum horizontal force is a function of the incident wave’s target location and does not correspond to the maximum run-up. Higher order diffraction effects, unaccounted for by linear diffraction codes and poorly predicted by second-order methods (Kriebel 1992), have been reproduced in the NWT: the flow behaviour around the circumference of the cylinder has been captured well, as has the complex pressure distribution over the cylinder’s surface, matching the physical observations here and in the literature (Chaplin et al. 1997); the secondary loading cycle identified by Chaplin et al. (1997) which is not accounted for in Morison-type formulations has been reproduced and shows a distinct sensitivity to the incident wave’s target location. These processes are crucial in the design of offshore structures like oil platforms or wind turbines and may prove important when assessing the survivability of WECs. Therefore is it essential that the NWT tool is able to reproduce them. Having proven the capability of the NWT for a fixed truncated circular cylinder, more complex geometries and moving structures can now be considered with greater confidence.

5.2 The Wavestar machine

Building on the progress made in the previous application, wave interactions with the Wavestar machine have been reproduced numerically. As well as greatly increasing the complexity of the geometry, which makes analytical models of the device impossible; in this application the structure is allowed to move in response to wave loading. However, this particular device is only able to move in a single degree of freedom (pitch), providing a desirably gradual increase in complexity from fixed structures. Furthermore, the restriction on the degrees of freedom provides all of the required constraints on the body's motion without the need for additional restraints such as moorings.

In the case of nonlinear, time-domain simulations including multiphase flows and dynamic systems such as wave energy devices, it is common for the number of degrees of freedom to be restricted, even if this would not be the case in reality. This makes the application and analysis of their behaviour easier to interpret. Furthermore, in order to reduce the complexity of models further, it is common to 'drive' the motion of the structure and therefore remove any coupling between the pressure and viscous forces from the fluid and the movement of the structure. Qian et al. (2006) modelled the entry and total immersion of a wedge-shaped body driven with constant vertical velocity into initially calm water. In a separate simulation they also modelled the emergence of the wedge from beneath the water's surface. Their fully nonlinear NS method was based on the Cartesian cut cell technique for tracking moving solid boundaries and, despite having no experimental data for comparison, they showed it was capable of handling complex two-phase flows with moving bodies, interface break-up and recombination. Kleefsman et al. (2005) present results for constant velocity water entry of two 2D wedges and a 3D cone using the VOF based NS solver ComFLOW. They found that, with a fine grid, ComFLOW was able to resolve the jets on either side of the wedge and the results were good, based on visual comparisons. However, not all of the droplets and smaller details were captured by the model. In 3D, and with a coarser grid, the jets on the side of a 3D cone were less well resolved but the slamming coefficient found was in good agreement with theory. Kleefsman et al. (2005) also showed a comparison between numerical simulations and experimental results for the entry of a circular cylinder with constant velocity. They found that the free surface shape and the vertical hydrodynamic force computed compared well with experiments but the initial impact is slightly underestimated by ComFLOW. It was also concluded that a very fine mesh was required to resolve the free surface behaviour but this did not have a large effect on the total hydrodynamic force. Zhang et al. (2010) modelled both the entry and exit of a circular cylinder with constant velocity using their level set immersed boundary method and a full NS solver. They too found good visual agreement with experiments for the free surface and comparable values for the slamming coefficients. Westphalen et al. (2009) solved the fully nonlinear NS equations for a cone, but in their work the structure was driven in heave at the free surface using a Gaussian wave packet. They found their control-volume Finite Element (CV-FE) method predicted the high order force components on the structure well, although Westphalen (2010) found his model over-estimated the peak and under-estimated the minimum forces on the cone. He also found that the maximum and minimum surface elevations produced by the cone were over- and under-predicted respectively, particularly at high driving frequencies. Further-still, Westphalen (2010) found that, although the motion of the cone was not coupled with the fluid forcing, the inertia and drag forces on the structure appear to be much more complex than those for standard water entry problems *i.e.* there was a phase difference between the maximum flow velocities and the speed of the cone. Finally, Bangun and Utsunomiya (2008) investigated the viscous forces acting on a 2D barge with prescribed sinusoidal roll motion using a NS solver based on the FVM and using the SIMPLE algorithm. They found that viscosity plays an important role in problems involving floating bodies particularly in terms of the motion damping coefficients.

Simulations in which the motion of a moving object is calculated from the interaction between the object and the fluid dynamics are far more scarce. Kleefsman et al. (2005) modelled a wedge freely falling into initially still water using ComFLOW. When compared with experimental data they found that the force exerted on the wedge was over predicted and consequently the vertical velocity was under predicted. Zhang et al. (2010) also modelled the free falling wedge using their level set method. They too found that the force was over predicted leading to a greater deceleration and slower motion. Both Kleefsman et al. (2005) and Zhang et al. (2010) explain these discrepancies in terms of three-dimensional effects which were not accounted for in their 2D models. Agamloh et al. (2008) simulated regular wave excitation of a cylindrical WEC able to move in heave only using the commercial CFD package COMET. The RANS equations were solved using the VOF method and a HRIC technique for the free surface. Additional code was written to calculate the displacement of the buoy at each time step and instead of using mesh motion, their method required the mesh to be regenerated at every timestep. A second buoy was added to the domain in order to investigate interaction effects but no experimental results were provided to validate the model. Hu et al. (2011) modelled the interaction between an extreme wave and a hemispherical-bottomed cylindrical ‘Bobber’ which was constrained to motion in heave. They recorded the displacement, run-up, force and vertical velocity of the float using the CFD code AMAZON-SC but did not compare their results with corresponding physical measurements. Bhinder et al. (2009) modelled a pitching, flap-type WEC in linear regular waves using the commercial CFD code Flow-3D and a generalised moving object capability based on the FAVOR$^{\text{TM}}$ technique. They found that their model predicted the decay motion of the device well but under-predicted both the pitch motion and the torque on the device when subject to waves. Chen, Sun, Zang and Hillis (2014) compared results from a new solver based on the OpenFOAM® libraries with experiments of regular wave interactions with a 2D rectangular barge constrained to move in roll only. They found their model was able to predict the roll motion accurately but saw a large discrepancy in the damping coefficients due to the 2D flow assumptions used. Similarly to Bangun and Utsunomiya (2008), Chen, Sun, Zang and Hillis (2014) found that viscous effects play an important role in the rotational dynamics of floating bodies.

5.2.1 Background - The Wavestar concept

Started in 2000, by Niels and Keld Hansen, the Wavestar concept has become one of the leading wave energy technologies in the world (Kramer et al. 2011). The Wavestar machine is a point-absorber-type WEC which generates electricity through the oscillatory motion of

Figure 5.18: Photographs of the Wavestar prototype near Hanstholm, on the west coast of Denmark. Showing 2 point-absorbing floaters (b), the supporting platform and 4 monopile foundations (c). Photo Credit: E. Ransley (Sept. 2013).

hemispherical floats which drive hydraulic PTO systems (Figure 5.18b). Each float is connected to a static super-structure which is held stationary via a number of monopile-type foundations (Figure 5.18c). This constrains the motion of the floats to a single rotational degree of freedom about the hinge point between the support structure and the float arm. Over the previous decade, a range of scale experiments and real sea testing have been performed in order to investigate different aspects of the device design (Kramer et al. 2011; Ambühl et al. 2012; Vidal et al. 2012). The most recent set of experiments were performed in the COAST Laboratory Ocean basin at Plymouth University and were designed to assess the survivability of the device under extreme conditions in a controlled environment (Jakobsen et al. 2014). A 1:10 scale model of a single float and arm was mounted on the gantry in

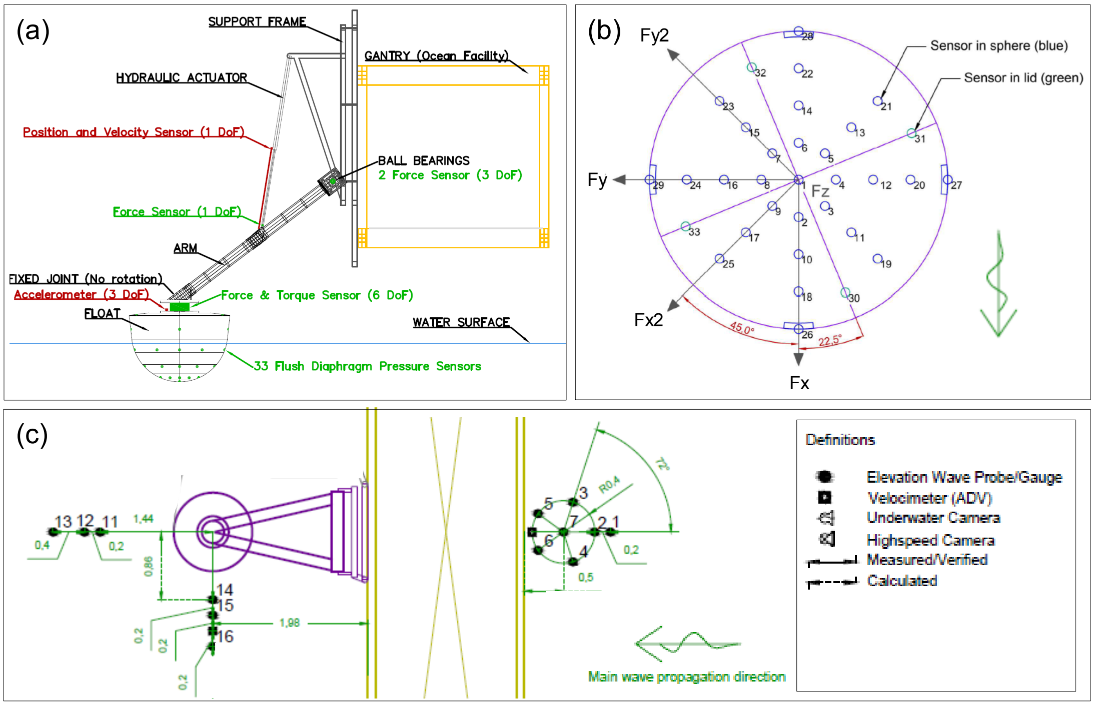

Figure 5.19: Schematics of the Wavestar experimental setup. (a) Profile of the model, frame and gantry-mounting showing the position of the force and torque sensors. (b) Plan view of the float showing the positions of the pressure sensors (Fx is the incident wave direction). (c) Plan view of the physical test area showing the positions of the wave gauges and velocimeters. Diagrams courtesy of M. M. Jakobsen.

the basin using a custom fitted frame and a set of ball-bearings to allow the system to pitch. A hydraulic piston, with variable damping and stiffness, was used to simulate the PTO of the full scale device but this will not be considered in this work. Figure 5.19 shows the experimental set-up and the array of sensors used to measure the force on the float, the pressure exerted on the surface of the float, the surface elevation in the vicinity of the float and the particle velocities near the float. A series of experiments were performed including regular wave tests of varied steepness with the float either fixed in place or allowed to move freely with the hydraulic system disabled. A subset of these regular wave experiments have been reproduced using the NWT developed in this project and compared with the experimental measurements. An assessment of the quality of the NWT as a function of incident wave steepness has then been made. A full description of the complete experimental program has been made by Jakobsen (2014).

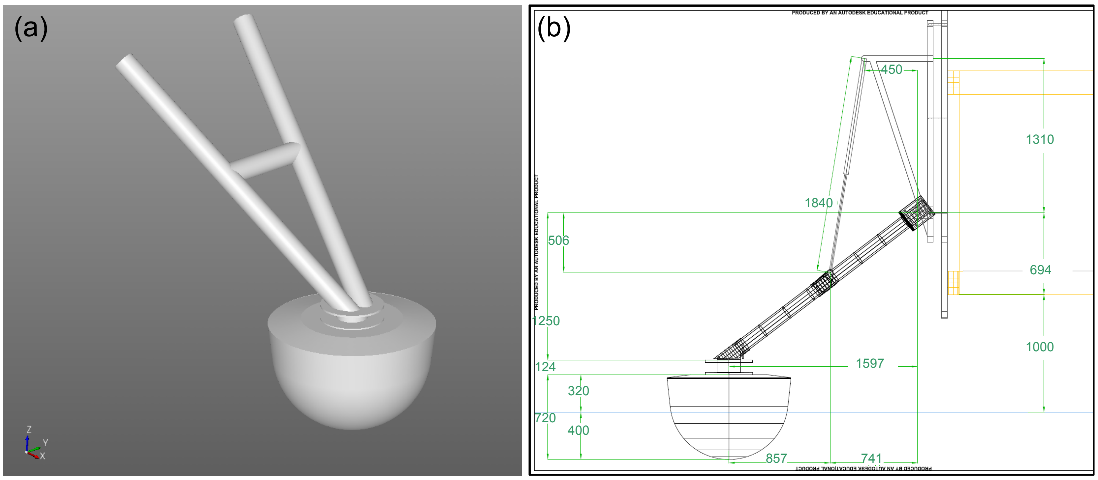

Figure 5.20: (a) Oblique view of the Wavestar CAD model, produced using Salome 7.2. (b) Dimensions of the 1:10 scale model of the Wavestar machine (diagram courtesy of M. M. Jakobsen)

5.2.2 Additions to the general NWT - Constrained rigid body motion

Although the geometry of the device is significantly more complicated than in the previous application, the same process was used to remove the region occupied by the structure from the computational domain; a CAD model with the same dimensions as the physical model was produced (Figure 5.20), exported in STL format and extracted from the domain using `snappyHexMesh`. The water depth in each of the experiments was 3 m and the height of the air phase was extended to 3.75 m to accommodate the device arm and allow space for the mesh to deform (which in some cases was excessive). The domain was made 16 m long and 6 m wide with the middle of the float positioned centrally 4.97 m from the inlet. Relaxation zones of 1 m and 6 m were positioned on the inlet and outlet boundaries respectively. The background mesh was made up of cubic cells with edge length 0.2 m. The region containing the free surface was then refined two levels giving cell edge length of 0.05 m. Based on the work in Section 3.1.2, this was considered to be sufficient for mesh independence, in the two wave cases here, with an RMS error of 2 %. The boundary of the structure was allowed a minimum refinement of level 2 or maximum of level 3 when the cell being refined had multiple intersections with the structure surface. A cross section of the mesh can be seen in Figure 5.21.

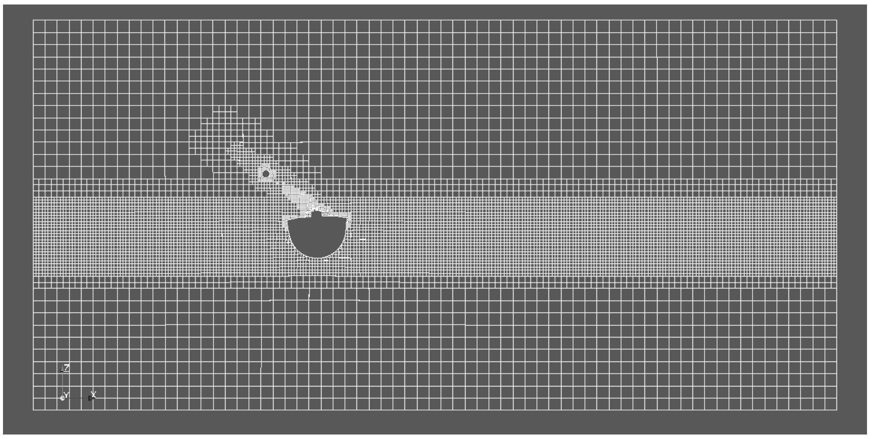

Figure 5.21: Cross-section of the mesh used in the Wavestar simulations at t=0s, produced using ParaView 4.1.0 64-bit.

The main addition to this case is the inclusion of coupled mesh motion. As mentioned in Section 3.1.2, OpenFOAM® is distributed with a range of dynamic mesh functionality including a 6DOF rigid body motion solver which is specified by a moving wall velocity condition on the patch describing the boundary of the body. Automatic mesh motion is then achieved via a force calculation on this patch and the mass properties of the structure. The position of grid nodes coinciding with the surface of the structure are then updated accordingly at every timestep. The mass properties, along with the mesh motion parameters, for all the moving structures in this work are tabulated in Appendix B. In this case, the mass of the scale model device was initially centred at (1.3954 0.0 -1.3305) m relative to the hinge point of the arm and had a magnitude of 220 kg; the moment of inertia for pitch motion was estimated as 124.26 kg m^2 using the parallel axis theorem and the mass distribution of the individual parts of the structure (this was later corroborated by results from free oscillatory tests). The motion in this case is unique and in order to model the behaviour of the Wavestar machine accurately, a pair of constraints were implemented using an explicit correction to the motion solution (OpenCFD 2014). Firstly, the device was constrained to rotate about an axis passing through the positions of the two bearings on the gantry end of the device arm. Then, a point constraint was added to this axis to remove any heave, surge or sway motion. In order to limit the degradation of mesh quality near the body and reduce the shearing of mesh cells, a region close to the structure can be set to remain static relative to the structure by means of a radial distance parameter. A further radial distance parameter can be used to limit the extent of the deforming region in which grid node positions are updated based on spherical linear interpolation with a cosine profile in the distancing function (OpenCFD 2014). Experience from analysing meshes deformed by rigid body motion suggests that mesh quality is best maintained by allowing the deformation region to be as large as possible. However, setting the limits of the deformation region outside of the computational domain forces cells on the domain boundary to absorb a greater share of the deformation and compromises the stability of the simulation. An example of this can be seen in Figure 5.22, where the cells at the top of the domain, to the right of the device, have been completely compressed whilst those on the top left and bottom of the domain have been significantly stretched. This deformation of the mesh caused the simulation to diverge. It would be desirable to be able to disable the outer distance function and allow the deformation region to be described by the limits of the domain instead. However, in OpenFOAM® 2.3.0 this functionality is not available in combination with other advantageous updates. This is why the height of the air phase has been increased in this case. The deformation region has been given an inner distance of 0.1 m and an outer distance of 3 m. Despite this, simulations with rigid body motion can easily become unstable when there are rapid changes in the velocity of the structure over a timestep. This is particularly problematic when the timestep becomes very small. In order to resolve this issue, the acceleration of the structure can be restricted between timesteps using the `accelerationRelaxation` factor in the rigid body solver, where a value of 1 corresponds to no relaxation of the acceleration and a value of 0 stops any change in velocity altogether. An `accelerationRelaxation` of 0.7 was found to be sufficient to stabilise the most extreme cases here and so was used throughout the Wavestar investigation. Assessment of any damping to the motion caused by excessive `accelerationRelaxation` remains a task for future studies. In this work the pressure and phase fraction boundary conditions on all moving structures were the `fixedFluxPressure` condition and a zero gradient condition respectively. The interpolation schemes and solution strategies used in this case were the same as those prescribed for the generic NWT tool in Chapter 3.

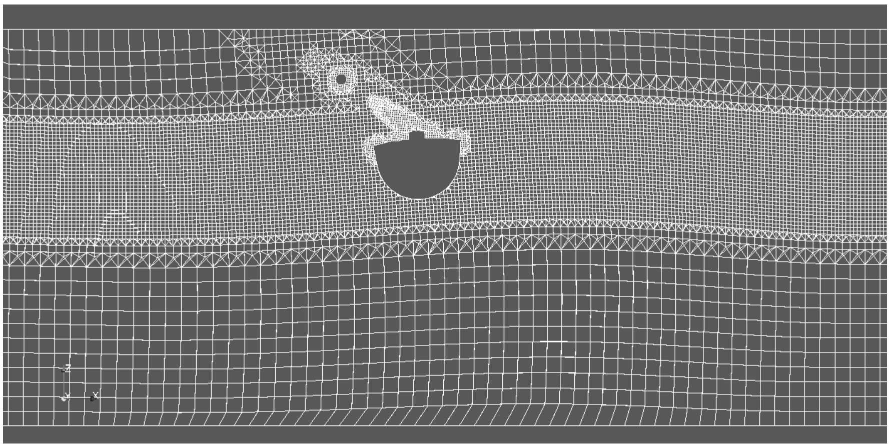

Figure 5.22: Cross section of the mesh during a freely moving Wavestar simulation with a poorly prescribed deformation region, showing unacceptable mesh degradation at the domain boundaries. Produced using ParaView 4.1.0 64-bit.

5.2.3 Results and discussion - The Wavestar machine

In this project a pair of regular wave cases have been considered with the device both fixed in place and able to freely pitch about the hinge point. The two waves are (retaining the names from Jakobsen et al. (2014)) RC02 and RA02 with heights of 0.25 m and 0.15 m, periods of 2.8 s and 1.4 s and steepnesses of 0.022 and 0.049 respectively. The surface elevation and velocities at the inlet were prescribed using waves2Foam's second-order Stokes theory expression-based boundary conditions. For the fixed cases, numerical wave gauges and pressure probes were positioned at locations corresponding to those in the physical experiments and the force and moment about the position of the force and torque sensor (just above the float) was also recorded at every timestep. Unfortunately, mesh motion causes the runtime function objects to malfunction and placing probes on a moving surface is not currently possible in OpenFOAM®. Therefore, only a coarse record of surface elevation and pressure is produced during the freely pitching cases. Despite this, the position of the device's Centre of Mass (CoM) can be recorded at every timestep and it is believed that this will give a sufficient indication of the quality of the numerical simulation.

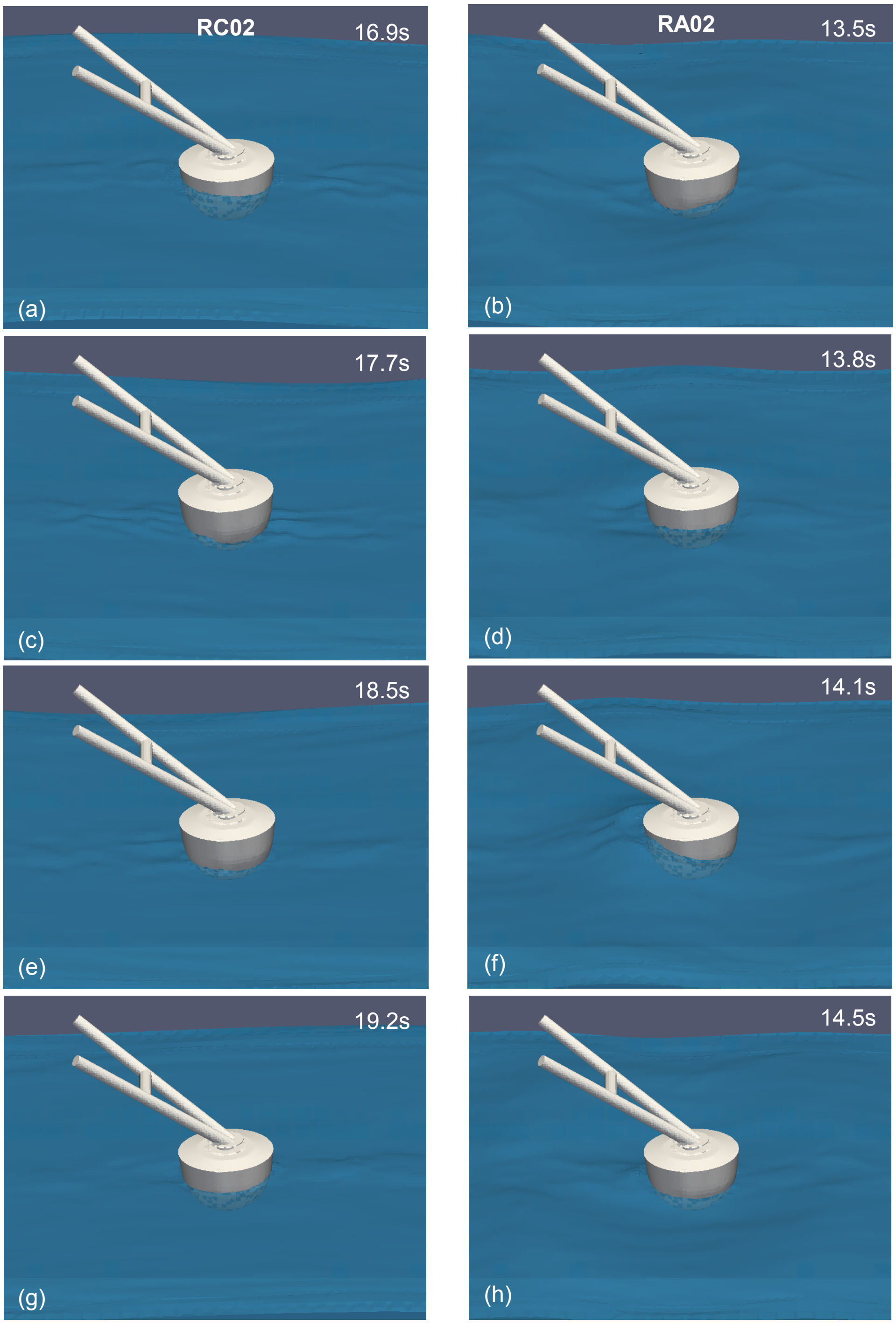

Figure 5.23: Snapshots from the fixed Wavestar simulations. Left column (a, c, e, g) are with regular incident wave RC02; right column (b, d, f, h) are with regular incident wave RA02.

Fixed cases

During the fixed cases, the device was locked in place in its neutrally buoyant position. Due to unforeseen issues with the float taking on water, the physical pressure probe measurements in undisturbed water were used to ensure the numerical model was positioned with the same orientation and draft as the device in the corresponding experiment.

Figure 5.23 shows a series of snapshots from the two numerical simulations with a fixed device. The direction of wave propagation is from left to right. The less steep, but greater amplitude, wave (RC02) is on the left with the steeper, but smaller, wave (RA02) on the right. Qualitatively these results appear similar to video footage taken during the experiments. For RC02 the most noticeable feature is the persistent wake structure behind the float which is of much higher frequency than the incident wave. There is also a high frequency disturbance to the free surface on the front of the float (left). For this case, there does not appear to be any enhanced run-up or signs of over-topping. On the contrary, there is a significant amplification of the run-up (Figure 5.23f) and run-down (Figure 5.23b) for the smaller, higher-frequency wave (RA02). One might expect this, as the wavelength of RA02 ($\lambda_{RA02} = 3.06\,\mathrm{m}$) is much closer to the diameter of the float (1 m) than that of RC02 ($\lambda_{RC02} = 11.39\,\mathrm{m}$) and so greater diffraction effects are likely. This also seems to be evident in the wake structure behind the float; in the case of RA02 the wake structure appears to be relatively stable (consistent with diffraction) whereas for RC02 the wake appears to be dominated by more complex structures. This too might be expected, as for the longer wave (RC02) the horizontal fluid velocity passing the structure is greater and so flow separation, vortex shedding and turbulence are more likely in the wake structure behind the float.

For a more quantitative assessment of these observations, Figures 5.24 and 5.25 show a sample of the surface elevation results from the numerical simulations compared to measurements taken in the two corresponding physical experiments. The line numbers correspond to the wave gauge labels in Figure 5.19c, *i.e.* running from (a)-(e): 2 is positioned close to the wave maker, 11 is just behind the float, 13 is further behind the float, 14 is inline with the float centre and slightly off to the left and 16 is further left of 14.

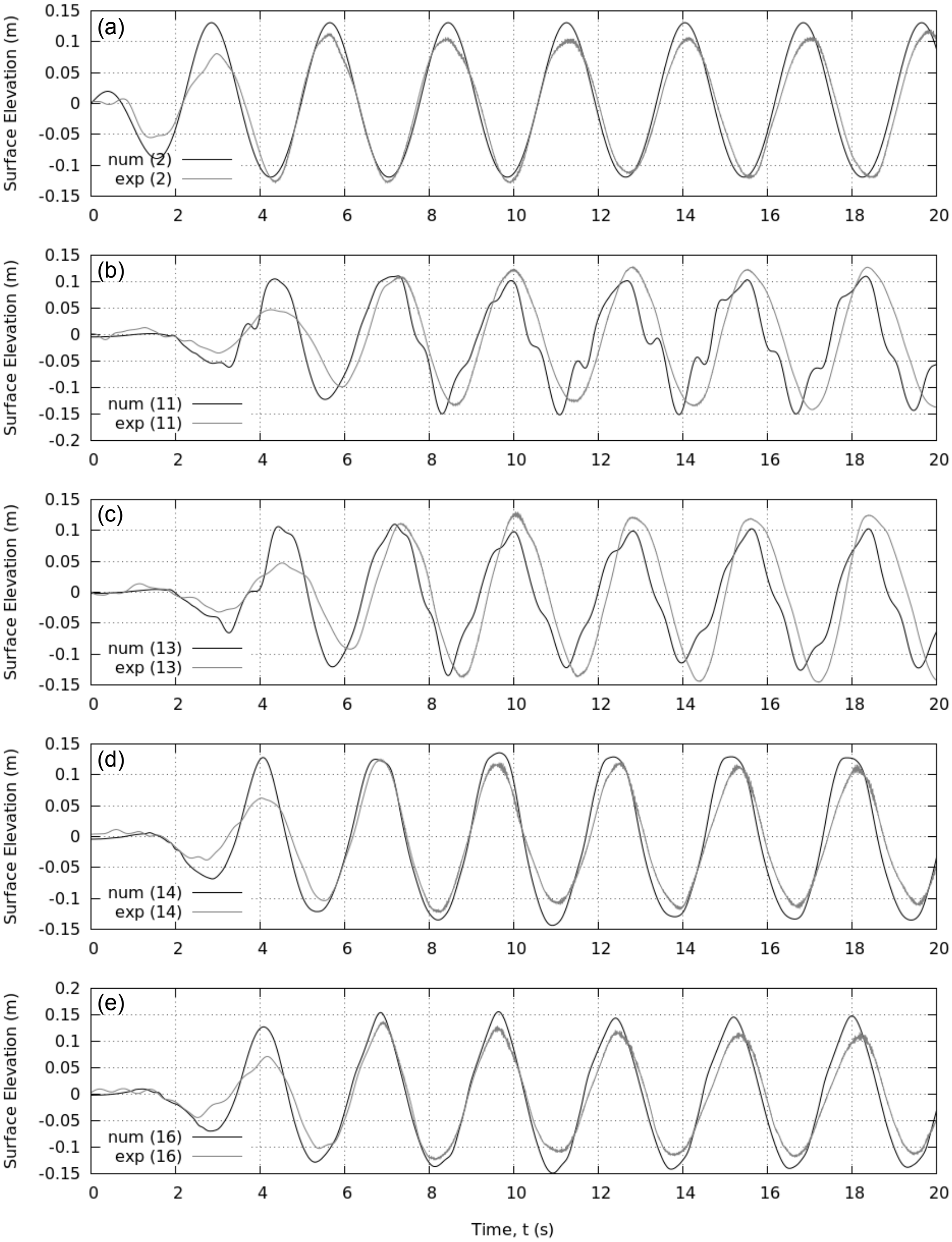

Figure 5.24: Surface elevation measurements for regular wave RC02 and a fixed Wavestar device. Physical (grey) and numerical (black) results at locations (a) upstream of the float centre (2), (b-c) downstream of the float centre (11) and (13) and (d-e) along-crest of the float centre (14) and (16). See Figure 5.19c for wave gauge locations.

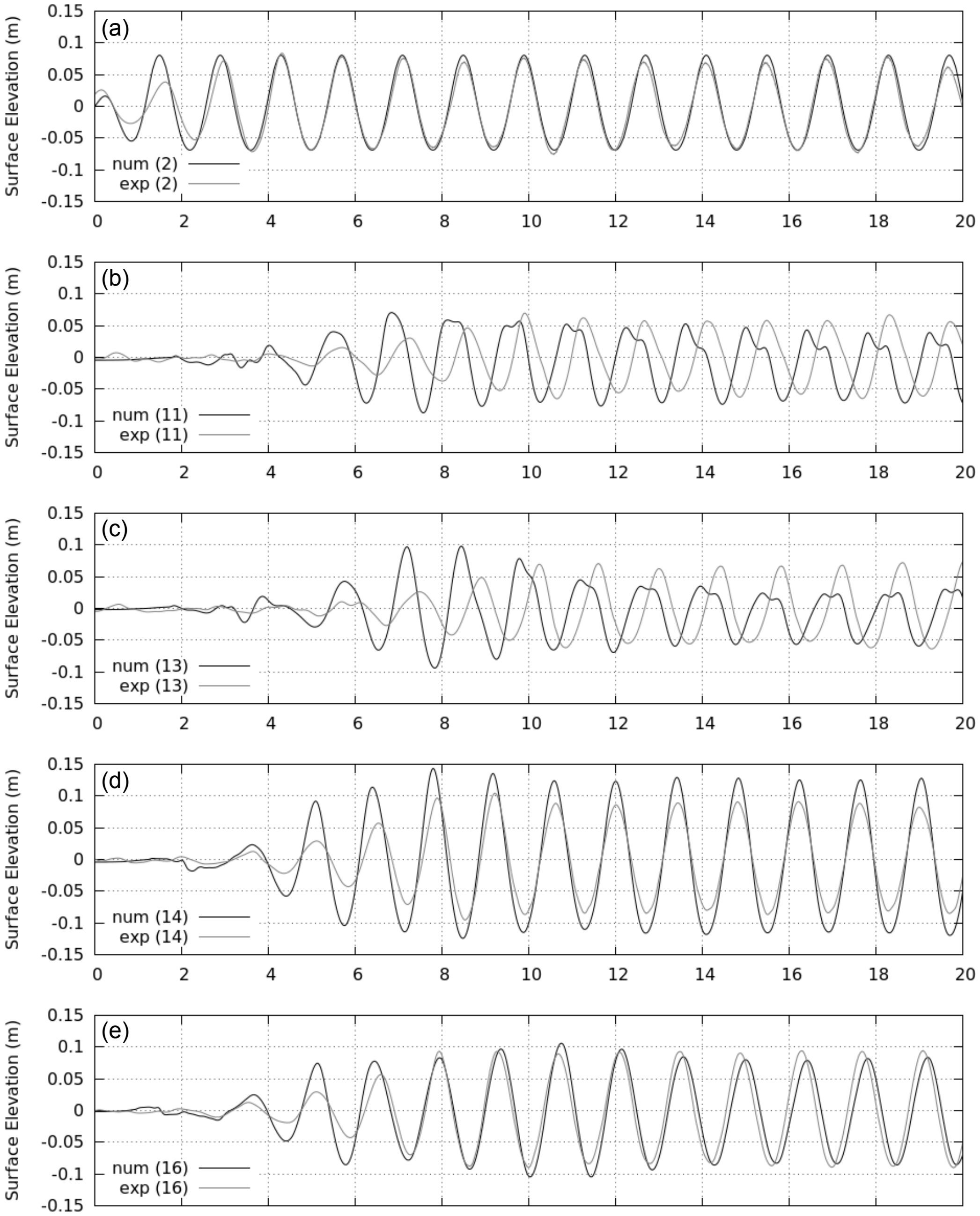

Figure 5.25: Surface elevation measurements for regular wave RA02 and a fixed Wavestar device. Physical (grey) and numerical (black) results at locations (a) upstream of the float centre (2), (b-c) downstream of the float centre (11) and (13) and (d-e) along-crest of the float centre (14) and (16). See Figure 5.19c for wave gauge locations.

Plot (a) in each figure shows how well the incident waves have been reproduced. Clearly in the second (steeper) case (RA02) (Figure 5.25) the incident wave has been reproduced very well with only some crest over-estimations. This provides confidence in the mesh design which in this case only has 3 mesh cells over the height of the wave. For the first case (RC02) (Figure 5.24) the numerical reproduction is not as good, the crest heights are consistently greater than in the physical case. It is possible that there has been some error in the zero offset of the physical records, although, the noise on the crests indicates some possible vibration of the physical wave gauge. This may be as a result of high crest velocities in the wave or excitation of the gantry and support structure for the wave gauges via wave loading on the fixed device. Furthermore, the change in water depth between the paddles and test area may have affected this longer wavelength wave more. Nevertheless, it is possible that a slightly smaller amplitude numerical wave input would better resemble the physical experiment.

Plots (b) and (c), in Figures 5.24 and 5.25, show the surface elevation in the wake region of the device. From the physical results, it is obvious in the higher frequency case (RA02) that the presence of the device disturbs the surface downstream. The wave height is greatly reduced immediately behind the float, suggesting significant diffraction effects consistent with the qualitative observations in Figure 5.23. In the lower frequency case there is less disturbance (again in keeping with Figure 5.23), the wave height actually appears to increase slightly and has a height closer to that expected in Figure 5.25a. However, the numerical results in the wake region are quantitatively quite poor. Although the reduction in wave height behind the device has been captured in RA02 (Figure 5.25), in both cases the numerical simulation predicts some higher frequency disturbances to the surface elevation and the phase of the resulting wave is incorrect. It would appear that the diffraction and scattering of waves has not been captured very well, similar to the timing of the secondary loading cycle in the cylinder case in Section 5.1. It is possible that the physical device was able to move slightly and produce radiated waves, which have damaged these records. However, video footage of the experiments does not show significant motion of the device. Perhaps the discrepancy at these locations is due to reflections from the tank walls, although there is no evidence of these propagating further upstream. As mentioned earlier, turbulence may play an important role in the wake region behind structures and so an investigation of various turbulence models is required. Alternatively, it is possible that an increased mesh resolution is needed around the structure as the one used here is only just sufficient for mesh independence in the wave-only case. A thorough grid convergence study, in order to parameterise the require mesh resolution in the vicinity of various shaped structure, is also planned as future work.

The final two plots ((d) and (e)), in Figures 5.24 and 5.25, show the surface elevation to the side of the float centre. At these locations we would expect to see the influence of any scattered (or radiated) waves from the float. The physical results show only a subtle influence from the scattered or radiated waves present (the time series almost matches the undisturbed incident time series). The only noticeable difference is a slight increase in the wave height to the side of the device in the shorter wave case (RA02) Figure 5.25. However, the numerical results show significantly more evidence of scattering; the longer wave case shows a strange flattening of the crests and troughs close to the float (Figure 5.24d) and a sharpening of the crests and troughs further from the float (Figure 5.24e); the shorter wave shows a much more exaggerated increase in wave height close to the float (Figure 5.25d) and a slight drift out of phase further from the float (Figure 5.25e). It is likely that any scattered waves would be re-reflected from the sides of the numerical domain (as there is no absorption there) and, due to concerns over CPU effort, the narrow domain may mean these reflected waves cause the observed discrepancies in the other time series.

In order to further investigate the discrepancies seen in the wake region, Figure 5.26 shows a spectral analysis of the free surface measurements taken directly behind the float at position 11 (plot b in Figures 5.24 and 5.25). Due to the relatively short length of time simulated in the numerical cases (20 s) the frequency resolution is fairly coarse. However, the numerical solution has accurately predicted the frequency of the main component in each case. The numerical solution has also predicted contributions at the higher harmonics of the main frequency in each case (up to the fourth harmonic in the low frequency case,

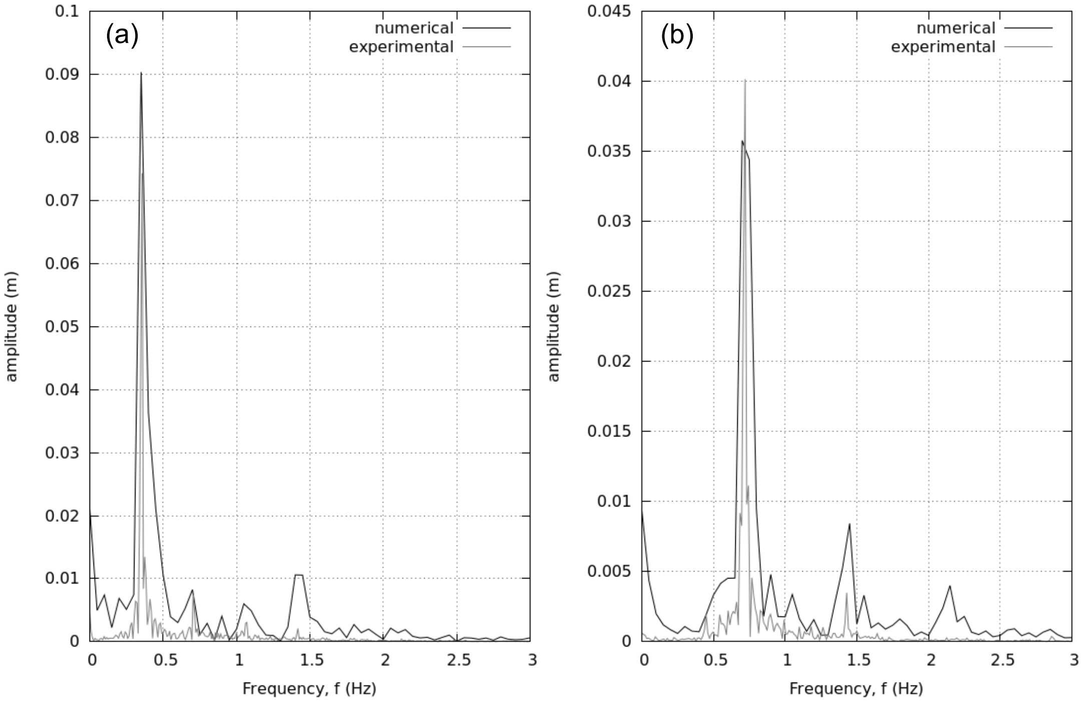

Figure 5.26: Frequency domain analysis of the surface elevation time series' measured directly downstream of the fixed Wavestar device at position 11, when subject to incident waves; (a) RC02 and (b) RA02.

RC02). These higher harmonic contributions are present in the experimental data but have significantly lower amplitudes compared to those predicted by the numerical simulation. As mentioned above, it is possible that the mesh resolution is insufficient to correctly simulate the higher harmonics in the diffraction field behind the float. However, the observed overestimation in amplitude at these frequencies might be expected if the physical model was able to move slightly during the experiment.

Figures 5.27 and 5.28 show samples of the pressure results on the surface of the float compared with those recorded in the two physical experiments. The line numbers correspond to the probe labels in Figure 5.19b, *i.e.* running from (a)-(g): 22, 14 and 6 are on the up-stream side of the float at progressively greater depth, 1 is at the bottom centre of the float and 2, 10 and 18 are on the downstream side of the float getting progressively shallower.

By considering the longer wave (RC02) results in Figure 5.27 first, we can see that the numerical solution is reasonably good. Bearing in mind that physical pressure transducers are

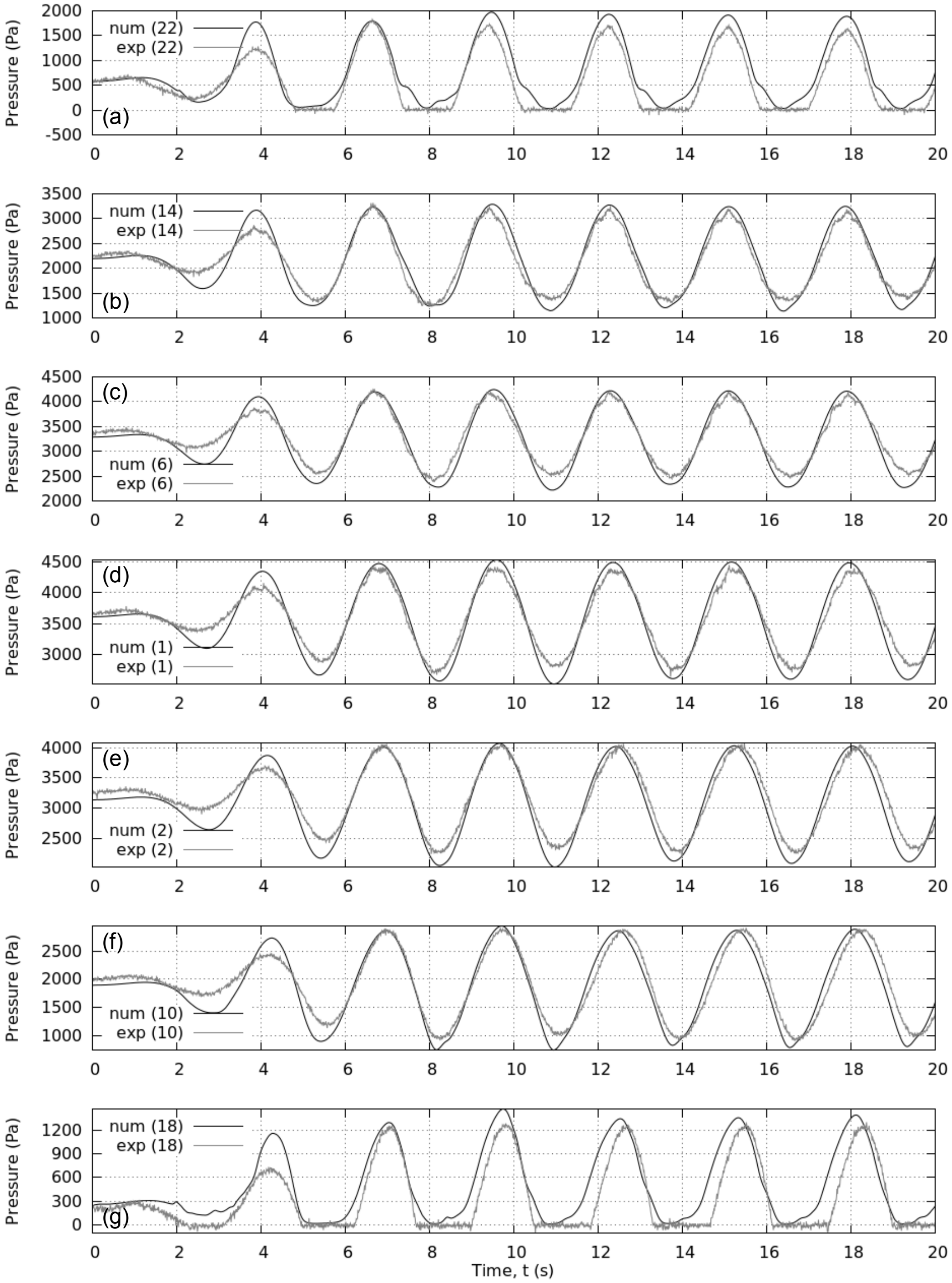

Figure 5.27: Pressure measurements for regular wave RC02 and a fixed Wavestar device. Physical (grey) and numerical (black) results at positions on the surface of the float along a line running from front to back parallel to the direction of wave propagation. See Figure 5.19b for probe locations.

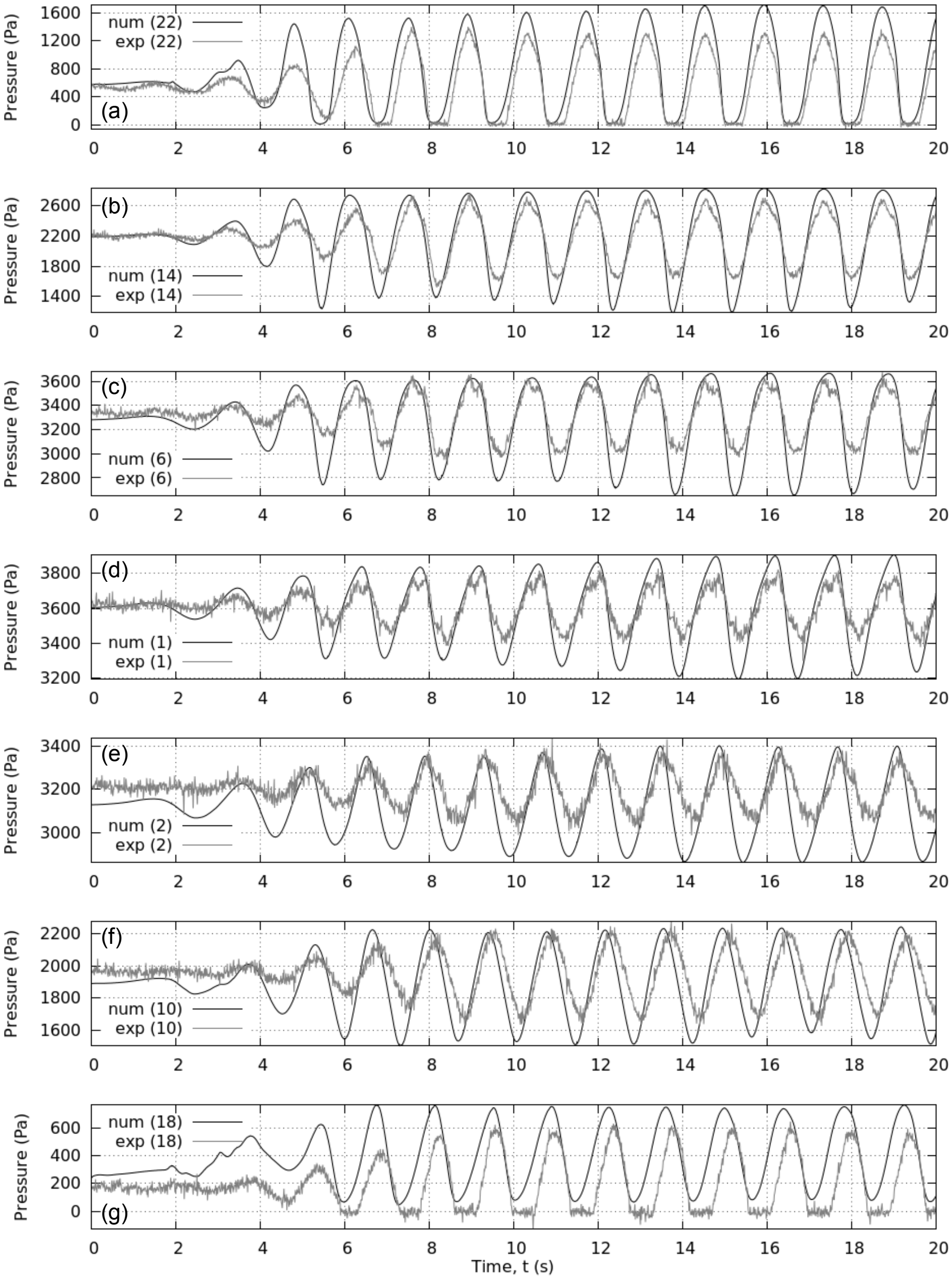

Figure 5.28: Pressure measurements for regular wave RA02 and a fixed Wavestar device. Physical (grey) and numerical (black) results at positions on the surface of the float along a line running from front to back parallel to the direction of wave propagation. See Figure 5.19b for probe locations.

notoriously temperamental, and the results plotted here are raw calibrated measurements, there are very few differences. Generally the numerical solution has a tendency to over estimate the depth of the troughs but the peaks are very good (except in Figure 5.27a). An explanation for the discrepancies in the Figure 5.27a could be that this position is very close to the free surface (evident by the flat troughs at 0 Pa showing the probe dried at these times) and so any complex behaviour in the interface region may have been lost due to the VOF treatment of the free surface. Furthermore, the surface elevation results hinted at the numerical simulation having a slightly greater incident wave height which may explain any over-estimations in the pressure. Despite this, the probe at position 18 (Figure 5.27g) shows the worst result. Although 18 is also near the free-surface there appears to be an additional phase shift relative to the experimental data. This position is on the downstream side of the float, in the wake region, and so this discrepancy is in keeping with phase shift observed in the surface elevation results. For the shorter wave (RA02), in Figure 5.28, the comparison between the numerical and physical results is far worse, however, the physical pressure measurements are very ‘noisy’ and so there is some doubt over their quality. The numerical simulation appears to capture the main behaviour but tends to overestimate the amplitude of the pressure fluctuations. Again, a phase shift relative to the experimental data is observed on the downstream side of the float. It is clear that, in this work, the numerical model has some difficulties reproducing the flow in the wake of the float.

Figures 5.29 and 5.30 show the velocity measurements, for the two wave cases, at the vectrino position in the along-crest direction from the float centre (between wave gauges 15 and 16 in Figure 5.19c). In both cases the numerical solution predicts the same behaviour as in the experiments. In general, however, the amplitude of the vertical velocity fluctuation (Figures 5.29a and 5.30a) is overestimated whilst the horizontal velocity in the direction of incident wave propagation, V_x, is underestimated in the longer wave case (Figure 5.29b) but a good match in the shorter wave case (Figure 5.30b). Of most interest, however, is the velocity perpendicular to the incident wave propagation, V_y, which, although much smaller in amplitude, displays a crucial difference between the numerical and physical results in the longer wave case (Figure 5.29c). In unidirectional waves V_y should be zero, therefore any

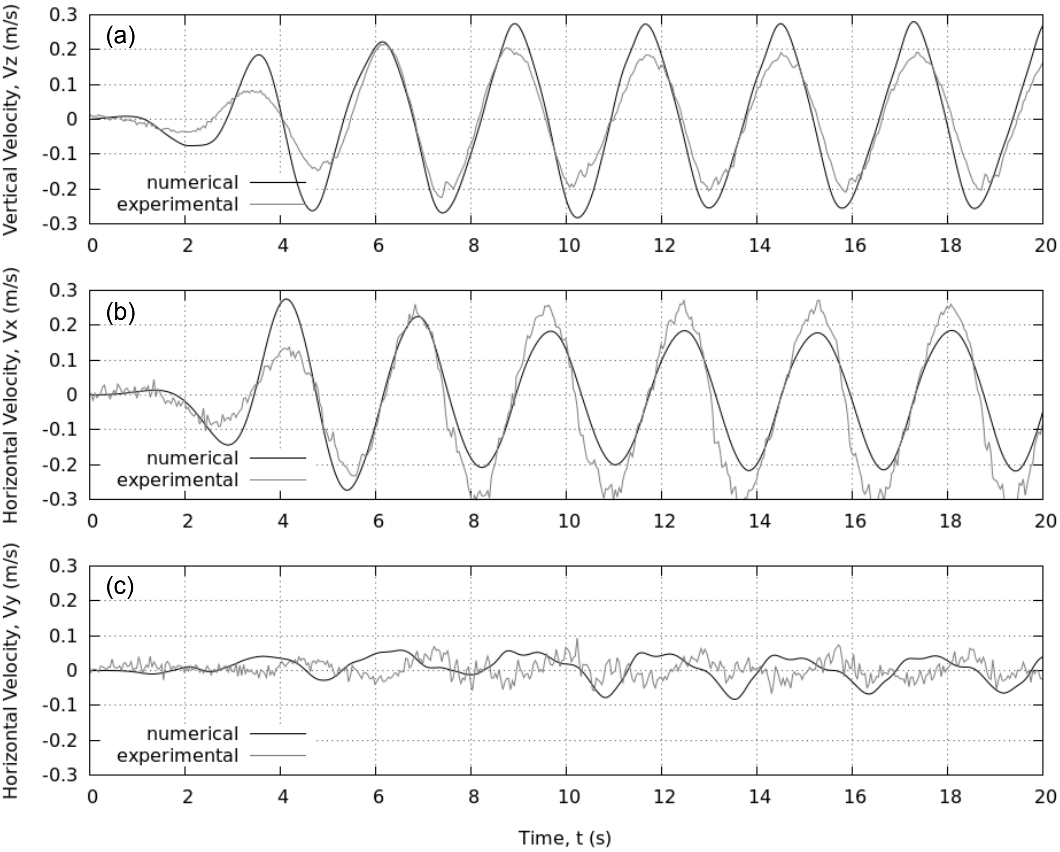

Figure 5.29: Velocity measurements for regular wave RC02 and a fixed Wavestar device. Physical (grey) and numerical (black) results at the along-crest Vectrino position (Figure 5.19c). (a) Vertical velocity, Vz; (b) horizontal velocity in direction of incident wave propagation, Vx; (c) horizontal velocity perpendicular to direction of incident wave propagation, Vy.

variation in V_y must be as a direct result of waves scattered (or radiated) from the device. In the shorter wave case (Figure 5.30c) the numerical solution predicts V_y, and the presence of the scattered wave, well with a slight overestimation of the amplitude; in the longer wave case (Figure 5.29c) the amplitude of V_y is correct but the scattered wave appears to arrive out of phase compared with the physical measurements. It is possible that the differences in the scattered wave could go some way to explain the difference in surface elevation and vertical velocity in the along crest direction from the float. For example, in the shorter wave case (Figure 5.30c) the numerical solution for V_y predicts a higher amplitude scattered wave than in the physical experiment and, arriving in phase at the Vectrino position, this

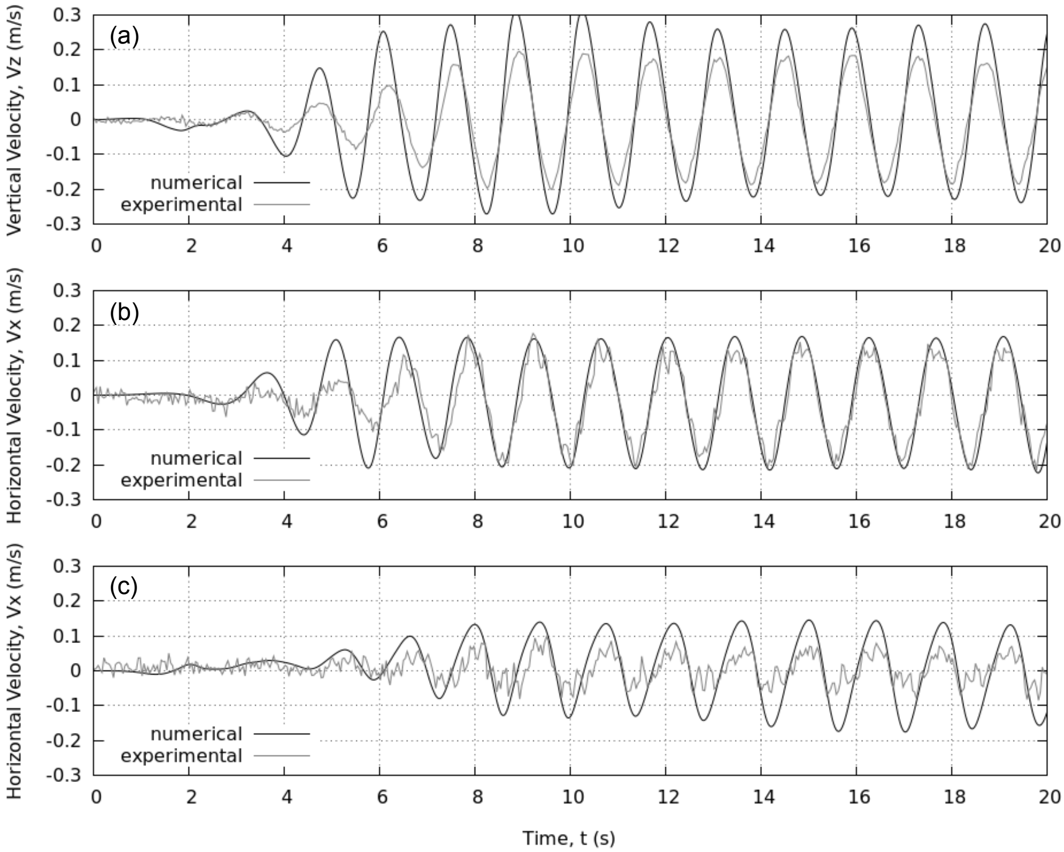

Figure 5.30: Velocity measurements for regular wave RA02 and a fixed Wavestar device. Physical (grey) and numerical (black) results at the along-crest Vectrino position (Figure 5.19c). (a) Vertical velocity, Vz; (b) horizontal velocity in direction of incident wave propagation, Vx; (c) horizontal velocity perpendicular to direction of incident wave propagation, Vy.

will constructively interfere with the incident wave to produce an overestimation of vertical velocity and surface elevation at this location. Furthermore, the differences in the scattered wave observed in the long wave case (Figure 5.29c) could explain the strange flattening and sharpening of the surface elevation results to the side of the float (Figure 5.24d-e). An additional concern is that, because there is no absorption on the side walls of the NWT, any scattered waves will be re-reflected and are likely to affect the results in the test area. This is also the case in the physical experiments, however, in the numerical case the side walls are much closer to the test area, in an attempt to improve the CPU efficiency, and so this effect is not only different but compounded in the numerical simulation.

Lastly, Figures 5.31 and 5.32 show the force and moment measurements for the two wave cases at the 6DOF force and torque sensor positioned just above the float (Figure 5.19a). In each figure, Plot (a) shows a time series of the vertical force on the float; Plot (b) shows the horizontal force in the direction of wave propagation, and; Plot (c) shows the moment about a horizontal axis perpendicular to the incident wave direction. In each case the experimental data has been transformed to the global coordinate system based on the orientation derived from the pressure measurements in still water. The zero offset has been applied based on the buoyancy force expected from Archimedes principle as a true zero offset measurement was not possible during the physical experiments.

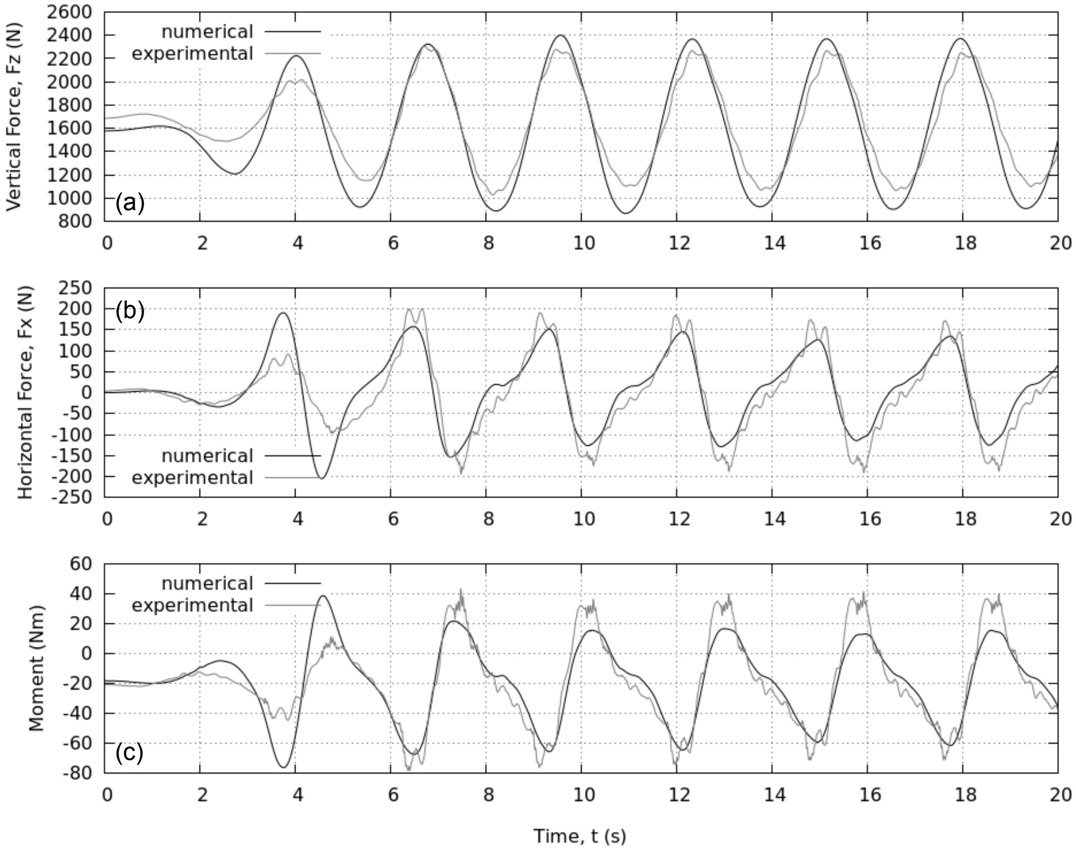

Figure 5.31: Force and moment on a fixed Wavestar device in regular wave RC02. Physical (grey) and numerical (black) results measured at the 6DOF force and torque just above the float (Figure 5.19a). (a) Vertical force, Fz; (b) horizontal force in direction of incident wave propagation, Fx; (c) moment about sensor location.

For the longer wave case considered (RC02) (Figure 5.31) the agreement between the numerical and experimental results is very good. The amplitude of the vertical force is overestimated but this is again in keeping for the slightly greater incident wave height observed in Figure 5.24. The physical results are unfiltered and if it was not for the noise in the these records the agreement for both horizontal force and moment would be excellent. One further observation is that the numerical solution has slightly underestimated the expected buoyancy force in still water (offset in vertical force at $t = 0$ s). It is possible that, as discussed when considering the pressure results, surface-piercing structures suffer from inaccuracies caused by the finite width of the interface region and this may have affected the buoyancy force.

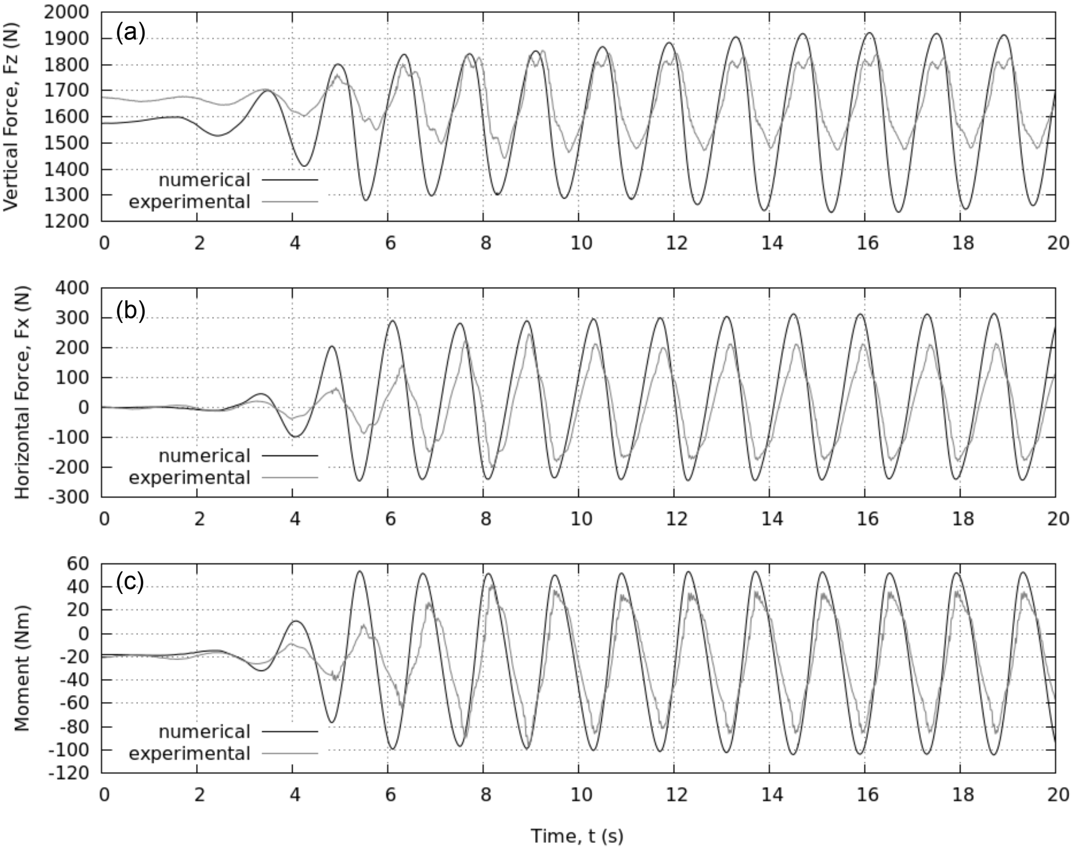

Figure 5.32: Force and moment on a fixed Wavestar device in regular wave RA02. Physical (grey) and numerical (black) results measured at the 6DOF force and torque just above the float (Figure 5.19a). (a) Vertical force, Fz; (b) horizontal force in direction of incident wave propagation, Fx; (c) moment about sensor location.

For the shorter wave case (RA02) shown in Figure 5.32 the agreement is not so good. As with the velocities and pressures, the numerical simulation tends to over-estimate the amplitude of the forces and moment. The correct frequency is observed and the slight asymmetry of the crests in both the horizontal force and moment time series is also reproduced, *i.e.* the horizontal force decreases more rapidly than it increases while the moment increases more rapidly than it decreases. In both the pressure and velocity measurements for this case, the experimental data has high frequency distortion throughout the time series. This could reduce confidence in the experimental results or be evidence of turbulence resulting from the wave-body interaction. Reviewing video footage of the experiments, the water was not completely still at the beginning of each experiment which may have contributed to the discrepancies observed in these comparisons, particularly in the smaller shorter wave case.

Despite the discrepancies discussed above, the NWT has performed very well, predicting the pressure and load on the float, as well as the surface elevation and velocity in the vicinity of the structure, to a good degree of accuracy. It is possible that the performance is slightly decreased for higher frequency incident waves and there is still some concern over the quality of the numerical result in the wake region behind the float. These discrepancies may be a result of an unconverged mesh and a thorough mesh convergence study is still required when including structures in the domain. However, for fixed structures, the NWT has been proven to produce reliable results for some relatively complex flow phenomena.

Lastly, the execution times for the two 20 s simulations were 23.75 and 26.77 hours for RC02 and RA02 respectively, each running on 2 Intel® Xeon(R) CPU E5630 @ 2.53 GHz processors. This may suggest, higher frequency waves require greater CPU effort, but, an execution time of 1 day is considered to be acceptable for such a complex CFD simulation.

Free cases

Progressing to moving structures, the same two wave cases have been simulated with the device able to move freely about the hinge point with the PTO system disabled. The computational domain and the device's starting position were identical to those used in the fixed cases. Figure 5.33 shows a series of snapshots from the two numerical simulations at the same times as those displayed in the fixed cases (Figure 5.23). These times were chosen to display the peak elevation of the device ((c) and (d)), the minimum elevation ((g) and (h)) and positions on the rise ((a) and (b)) and fall ((e) and (f)) of the device's motion cycle. Again the direction of wave propagation is from left to right. In contrast to the fixed case, the diffraction effects observed for the shorter wave (RA02) are no longer present. It seems that by allowing the device to be driven by the waves removes the wake structures behind the device as well as the free surface disturbances in front of the float. The same is true for the longer wave (RC02). However, in this case the motion of the device is far greater and produces a series of radiated waves as a consequence (most evident in Figure 5.33e as the device is on the way down). This same radiation pattern was observed in the physical experiments. Although the amplitude of the wave in the longer wave case (RC02) is greater, the motion is exaggerated compared with that observed in the shorter wave case (RA02). The device almost exits the water completely at peak elevation (Figure 5.33c) and is slightly over-topped at minimum elevation (Figure 5.33g). It is likely that this increased response is due to resonance effects caused by the incident wave frequency being similar to the natural frequency of the device. The motion observed in the physical experiment was not quite as extreme as that seen in the numerical simulation. However, it is known that the physical device was not completely free to move, *i.e.* the motion was slightly damped by frictional forces in the PTO cylinder, which would have affected the amplitude of oscillation and the natural frequency of the system. Despite this, the position of the device is deemed to be a good indicator of the quality of the numerical reproduction and so has been considered quantitatively in more detail below. Due to the constraints on the device's motion, its position can be transformed into a single linear displacement in the hydraulic cylinder, X_c.

Figure 5.34 shows both the experimental and numerical displacement in the cylinder during the longer wave case (RC02). Here a positive displacement corresponds to a lifting of the device, *i.e.* a crest. Clearly, according to the numerical results, the device was not initially set at its neutrally buoyant position. This has caused the device to oscillate at the beginning of the numerical simulation before the incident wave arrives to drive the motion. It is believed that, after a suitable amount of time, this discrepancy in the initial conditions will not affect

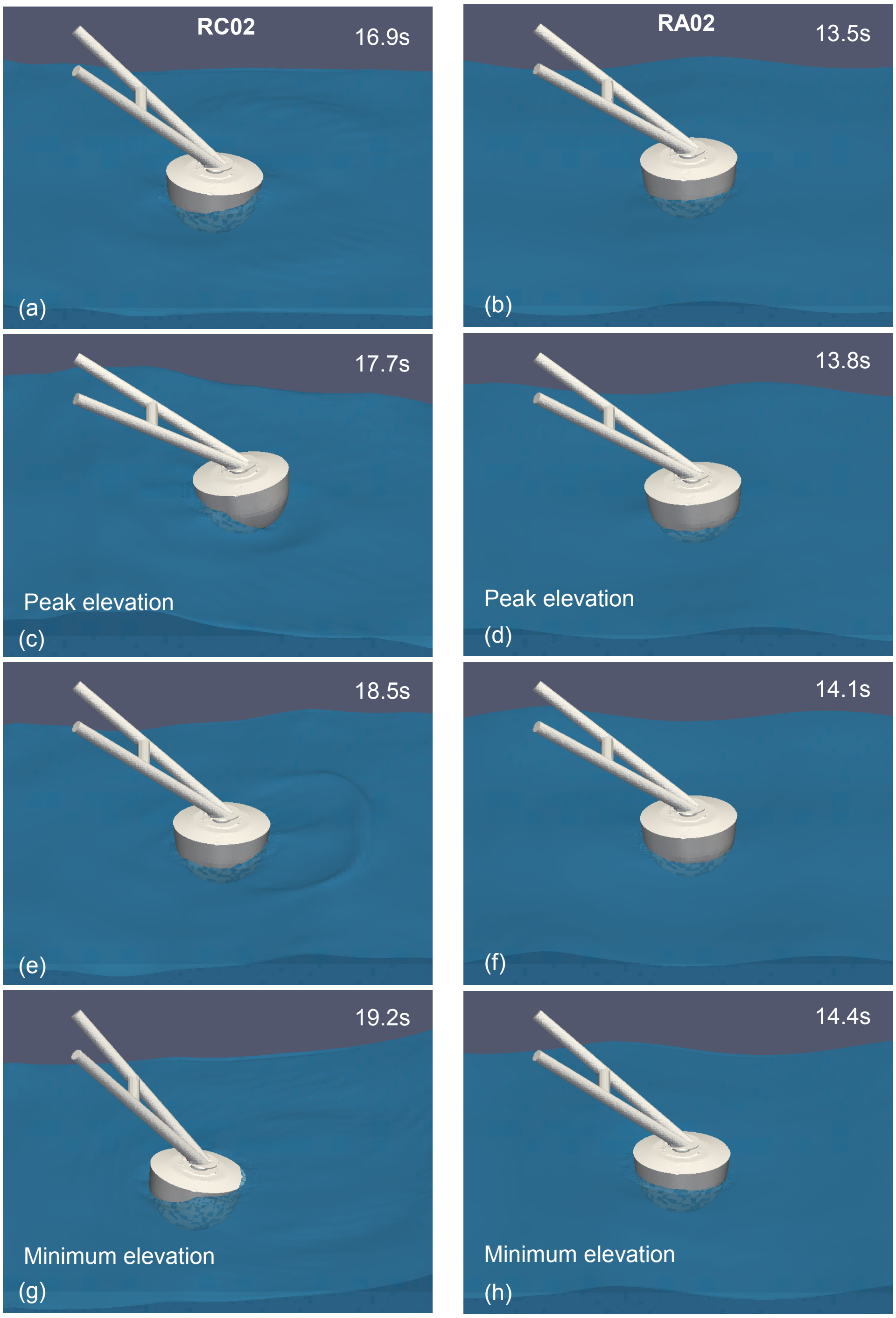

Figure 5.33: Snapshots from the freely moving Wavestar simulations. Left column (a, c, e, g) are with regular incident wave RC02; right column (b, d, f, h) are with regular incident wave RA02.

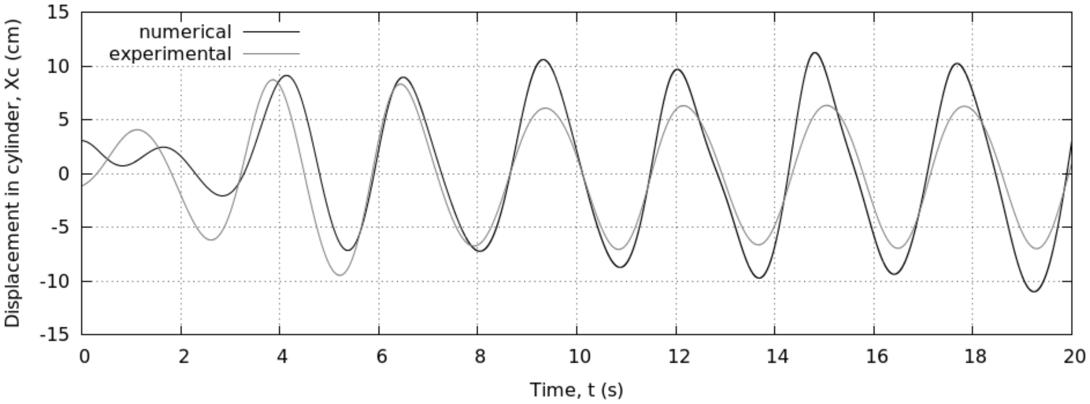

Figure 5.34: Comparison between experimental (grey) and numerical (black) results for the displacement in the cylinder of the Wavestar device with the PTO disabled and when subject to regular waves RC02.

the results and the system will reach some stable condition. This appears to be the case here as after approximately six seconds the numerical device begins to oscillate with the same frequency as that found in the physical case. However, as mentioned qualitatively above, the numerical simulation over-estimates the amplitude of the oscillation and also predicts a slight asymmetry in the motion which is not observed in the physical results. A possible alternative explanation to frictional damping in the cylinder, could be that, due to the increased proximity of the side walls in the NWT any scattered or radiated waves coming from the device will return to the test area with greater amplitude and interfere differently with the incident wave. Constructive interference between these reflected waves and the incident wave may lead to increased motion of the device. There does appear to be an unexpected increase in the amplitude of motion after the first stable cycles which may be evidence of the arrival of reflected waves once the device has started to oscillate. It is likely that this effect is dependent on the relationship between the radiated wave frequency (and wave speed) and the distance between the device and side walls of the NWT. In this case a radiated wave with the same frequency as the incident wave has a travel time of almost exactly half the incident wave period. Therefore a wave radiated out of phase with the incident wave would return in phase with the incident wave and cause constructive interference at the float location.

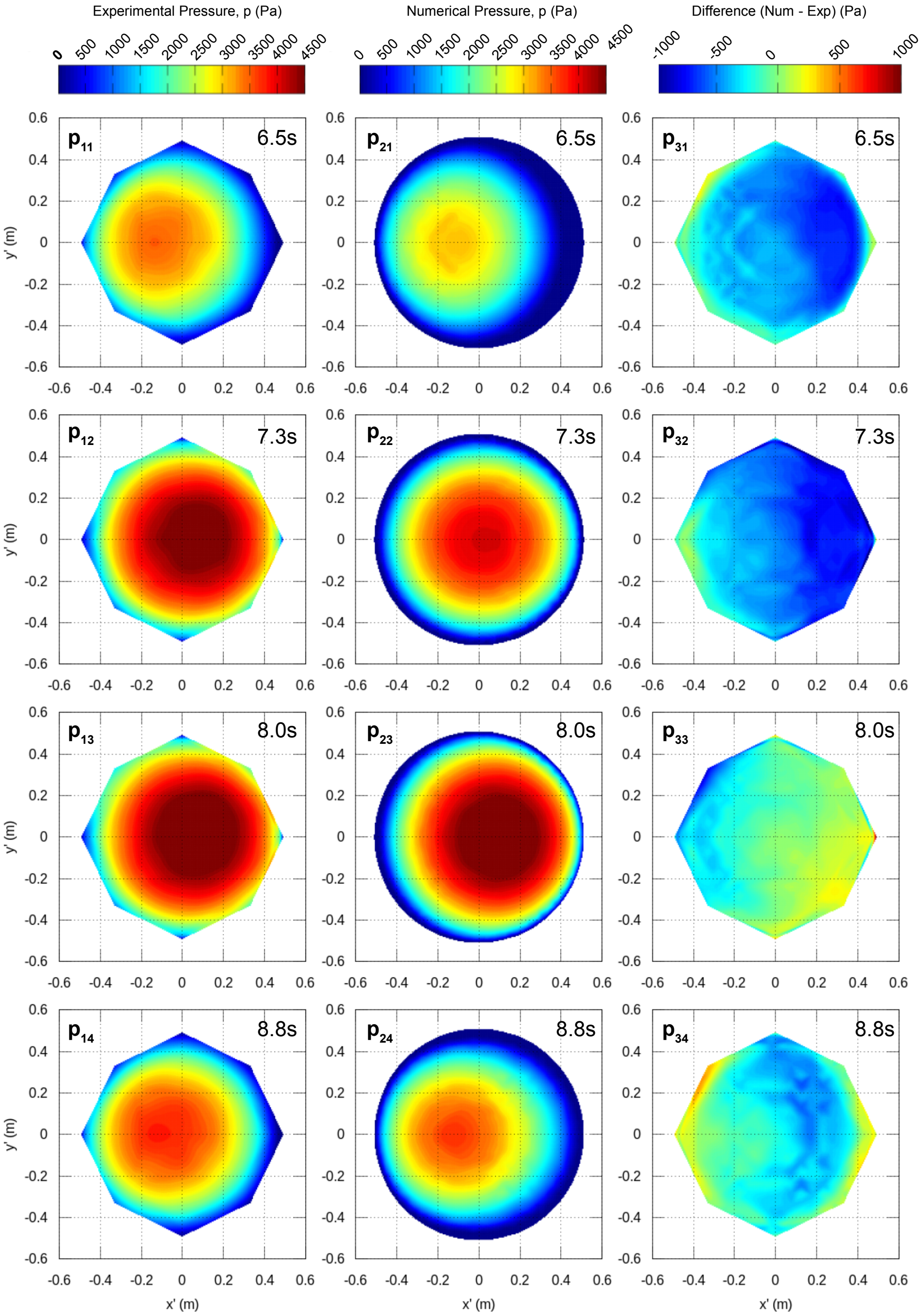

Figure 5.35: Distribution of pressure, projected onto a 2D Cartesian plane, in the frame of reference of the Wavestar float, during regular wave RC02. Experimental (column 1), numerical (column 2) and difference (column 3) at discrete times at a crest (row 1), falling (row 2), in a trough (row 3) and rising (row 4).

Figure 5.35 shows the distribution of pressure over a projection of the float surface at a number of discrete times during the experiment. The origin of the coordinate system (x',y') is the float centre and the coordinates x' and y' are the 2D Cartesian coordinates in the frame of reference of the float with y' running perpendicular to the direction of wave propagation. The plots in Figure 5.35 (and Figure 5.37) are labelled p_{ij} where the indices i and j indicate the column and row of the plot respectively. Column 1 ($i = 1$) shows the measurements from the physical experiment, interpolated over the float surface, using a cubic spline interpolation, based on the 29 pressure recordings on the bottom surface of the float. Column 2 ($i = 2$) shows the results from the numerical simulation and Column 3 ($i = 3$) shows the difference (numerical - physical) between the two. Row 1 ($j = 1$) is at a time close to a peak in the displacement, Row 2 ($j = 2$) is at a time on the falling side of a peak, Row 3 ($j = 3$) is at a time close to a trough in the displacement and Row 4 ($j = 4$) is at a time on the rising side of a peak. In general, the numerical result is good. It appears that there is an overestimation during a trough (p_{33}) and an underestimation during a peak (p_{31}). This is in keeping with the overestimated amplitude of motion response observed in Figure 5.34 and a number of discrepancies might be explained by the difference in motion. It might be speculated that the greatest differences occur on the positive x' side (the back) of the float which supports the observed inaccuracies in the wake region discussed in the fixed cases.

For the steeper wave case (RA02), the results for the displacement, X_c, are shown in Figure 5.36. Again, the numerical device does not begin in its neutrally buoyant position but after some time the motion is forced at the correct frequency by the incident wave. In this case the experimental results display some low frequency beating of the X_c displacement which can only be explained by reflected waves in the physical basin. The numerical result shows some similar behaviour but begins by over-estimating the amplitude of the motion and then under-estimates it after a period of comparable motion. If this behaviour is a result of reflections it is not surprising that there are differences between the numerical case and the physical case which has a much greater domain size. However, it is expected that the radiated, and so reflected, waves would have the same frequency as the incident wave and so the phase relationship, and hence the interference, should result in a constant modulation

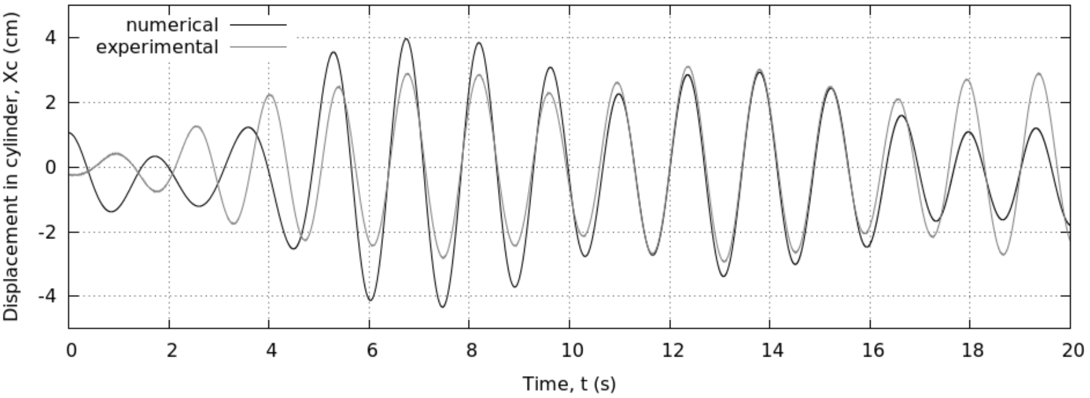

Figure 5.36: Comparison between experimental (grey) and numerical (black) results for the displacement in the cylinder of the Wavestar device with the PTO disabled and when subject to regular waves RA02

of the incident wave at the float position (assuming the float behaviour is a function of events at a point at its centre). The beating behaviour is typically associated with a combination of slightly differing frequencies the origin of which has not been identified in this case.

The equivalent pressure results for this steeper wave are shown in Figure 5.37. Again the numerical result is good. In this case the pressure is consistently under-estimated but it is likely that this can be explained by the difference in motion/position of the device (Figure 5.36) at the specific times plotted. Again, it seems as though the greatest discrepancies are present on the back of the float further highlighting that additional work is required to correctly simulate the fluid behaviour in the wake of the device.

Lastly, the execution times for the two 20 s simulations were 137.5 and 56.34 hours for RC02 and RA02 respectively, each running on 6 Intel® Xeon(R) CPU E5630 @ 2.53 GHz processors. This may suggest, that the amplitude of oscillation, and hence the mesh deformation, has a bigger affect on the CPU effort than the frequency does. Also, with the addition of mesh motion and the associated hydrodynamics, the execution time has increased dramatically compared to the fixed cases. For the larger wave case (RC02), the solution for a moving structure takes almost six times longer than that with the structure fixed, even with triple the processing power.

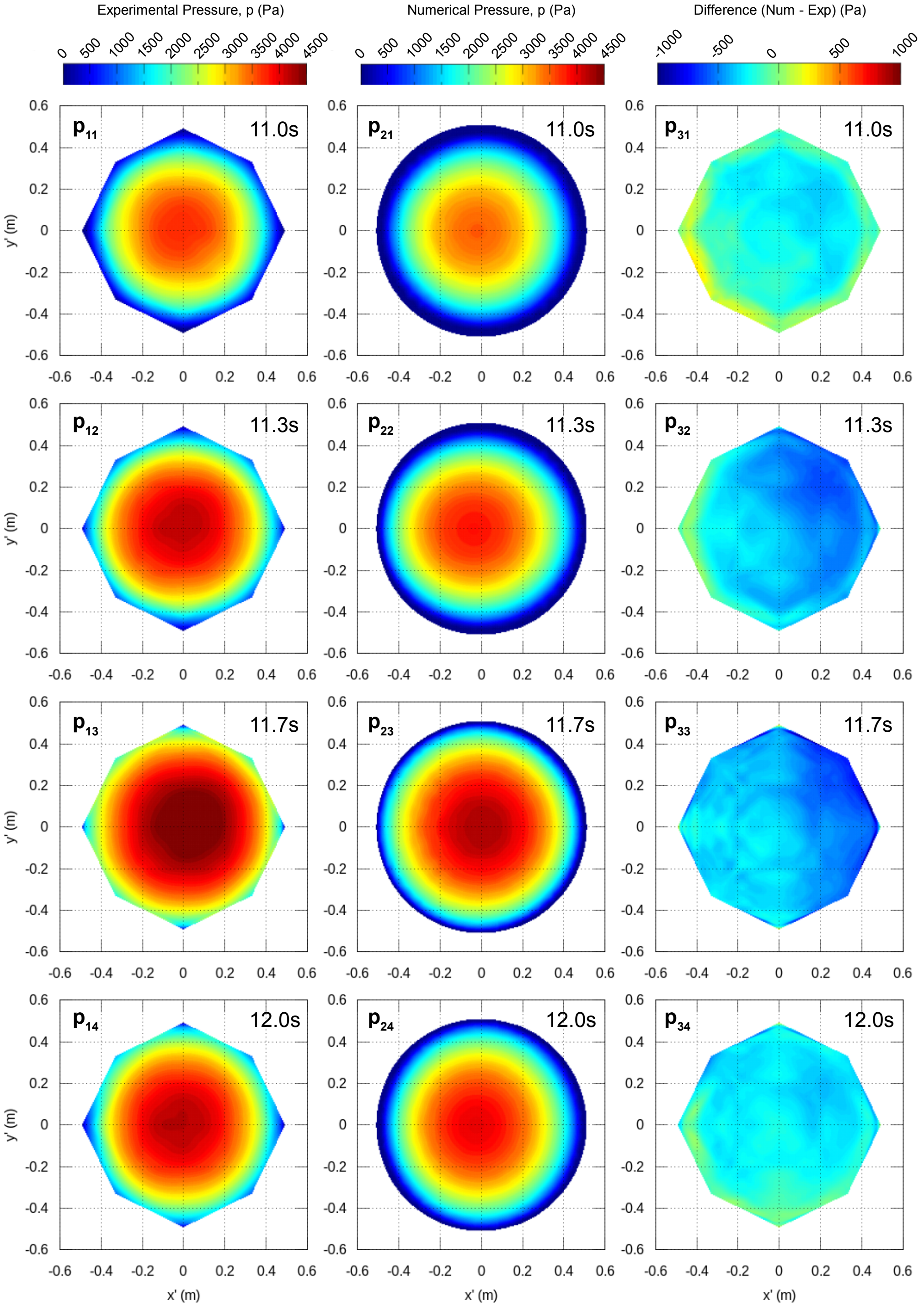

Figure 5.37: Distribution of pressure, projected onto a 2D Cartesian plane, in the frame of reference of the Wavestar float, during regular wave RA02. Experimental (column 1), numerical (column 2) and difference (column 3) at discrete times at a crest (row 1), falling (row 2), in a trough (row 3) and rising (row 4).

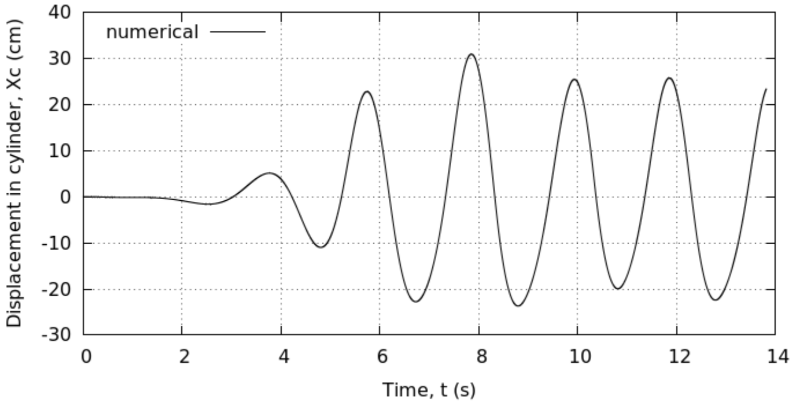

Figure 5.38: Numerical results for the displacement in the cylinder of the Wavestar device with the PTO disabled and when subject to extreme regular waves (RExt01)

5.2.4 Further numerical investigation - The Wavestar machine in extreme waves

In order to test the robustness of the NWT and 6DOF solver, an extreme regular wave was simulated with the device still able to move freely. The wave had a 2 s period, a height of 0.68 m and a steepness of 0.11. It was also part of the tests performed by Jakobsen et al. (2014) and had the label RExt01. However, due to fears over possible damage to the device due to excessive motion, physical test with this wave were only performed with the PTO system engaged. Therefore, there is no physical data for the freely oscillating device in this case. Despite this, a numerical simulation was performed using the same NWT design as for the other free cases and the resulting displacement in the cylinder, X_c, is shown in Figure 5.38. As can be seen, the motion of the device is extreme (more than double the displacement seen in the RC01 case). In addition to this, Figure 5.39 shows a series of snapshots from the simulation including the maximum elevation (b), the minimum elevation (d), and positions between these ((a) and (c)). It can be seen that, during a wave cycle the float goes from being completely submerged to almost leaving the water altogether. The fluid behaviour is correspondingly complex with high levels of free surface distortion, radiated waves, green water, spray and recombination. It is encouraging that the NWT has handled all of these without issue and that the end result appears to be qualitatively reasonable but physical validation is still required for cases with such extreme motion.

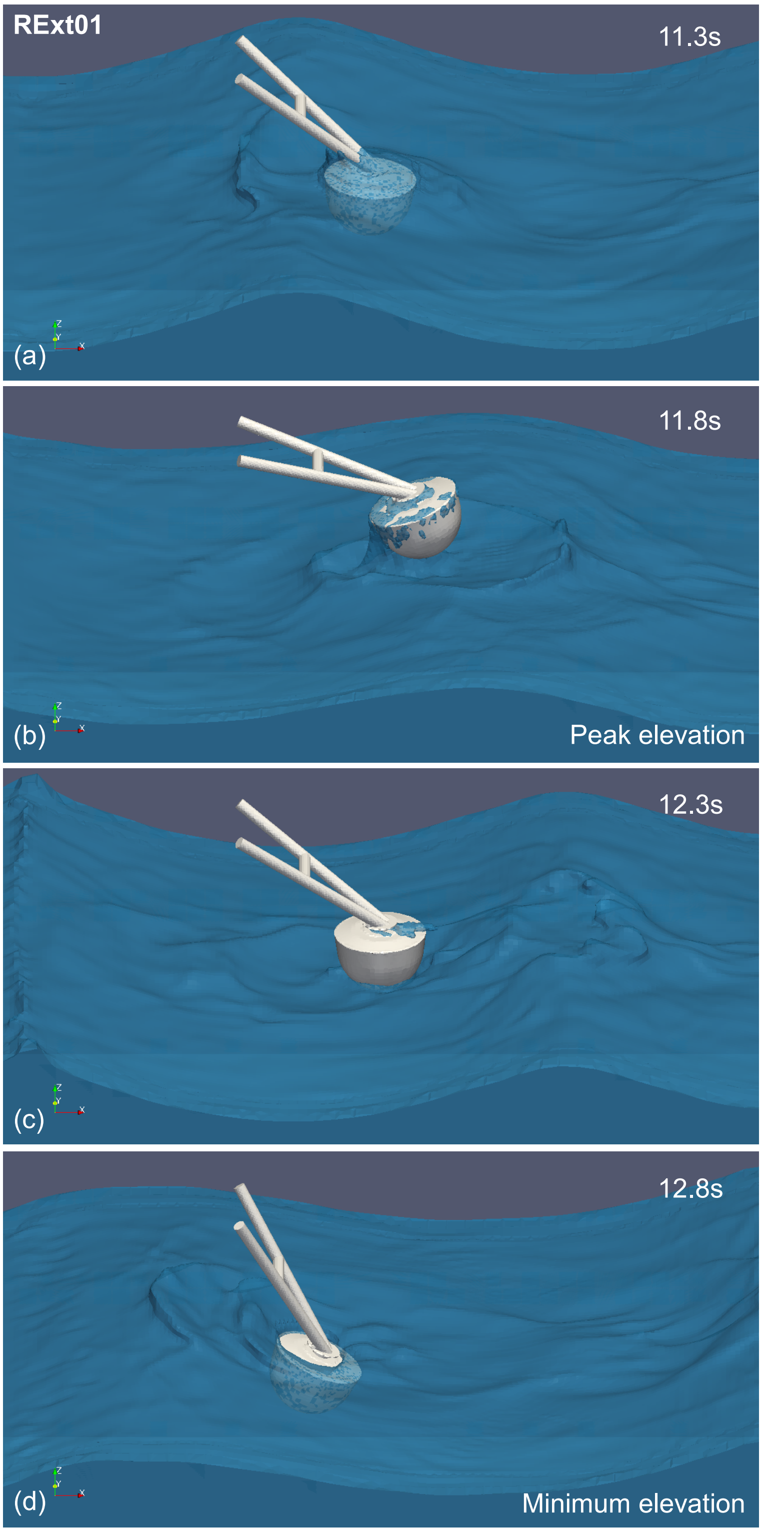

Figure 5.39: Snapshots of a freely moving Wavestar in extreme regular waves (REx t01).

Lastly, the execution times for the 13.82 s simulation was 185 hours, running on 6 Intel® Xeon(R) CPU E5630 @ 2.53 GHz processors. The large wave case above (RC02) took only 73 hours to reach the same time using the same hardware. This is further evidence, that the amplitude of oscillation and the associated complex hydrodynamics is critical in the CPU effort required to complete the simulation.

5.2.5 Conclusions - The Wavestar machine

In conclusion, with a significant increase in the complexity of the geometry, OpenFOAM® and the NWT continue to perform well for cases with a fixed structure. The pressure distribution and loading on the device is reproduced well but there appear to be some issues in the wake region behind the device; high frequency disturbances are present in the surface elevation behind the float and both the pressure and surface elevation results in this region exhibit a noticeable phase shift compared with the experiment. Furthermore, based on velocity measurements to the side of the float, the scattered waves are not reproduced correctly. However, this discrepancy may be a result of wave reflected from the side walls of the domain. The quality of the results does not appear to reduce with an increase in wave steepness although only two cases have been studied here and there is some concern over the quality of the experimental data in the steeper case.

For freely pitching cases, the comparison between the physical and numerical results is still promising. There are differences in the pressure distribution and the motion of the device but these can generally be attributed to issues with reflected waves and the assumption that the motion is undamped. Some unexplained ‘beating’ in the motion is observed for the higher frequency case but in general the behaviour of the device is captured well. As with the fixed case, the quality of the results does not appear to reduce with an increase in wave steepness.

Finally, the NWT has been shown to handle extreme motions including full submersion of the float, green water, break-up and recombination as well as slamming motions and strong radiation. All of which are likely to be important in the assessment of device survivability.

5.3 Moored buoy

Further increasing the complexity of the model, a floating, hemispherical-bottomed, cylindrical buoy with a linearly-elastic mooring has been simulated using the NWT. The buoy is part of the SuperGen UK Centre for Marine Energy Research (UKCMER) grand challenge project X-MED (eXtreme loading of Marine Energy Devices due to waves, currents, flotsam and mammal impact) which aims to identify and improve the understanding of extreme loading on tidal stream turbines and wave energy devices by modelling and experiments (SuperGen UKCMER 2015). The buoy is 0.5 m in diameter with a 0.25 m tall cylindrical section above its hemispherical bottom (Figure 5.40). It is constructed from 2 mm thick mild steel and has ballast weight secured within the hemispherical part. The total mass is 43.2 kg centred 0.181 m above the bottom mooring fixing. The moment of inertia of the buoy is (1.61 1.61 0.5) N m. Restrained only by a single-point mooring, which attaches at the bottom of the buoy where the symmetry axis intersects the surface of the hemisphere, the structure in this case is able to move in all six degrees of freedom (6DOF). The mooring has a stiffness of 67 N m^{-1} and a rest length of 2.18 m. Again, the mass properties and mesh motion parameters are tabulated in Appendix B.

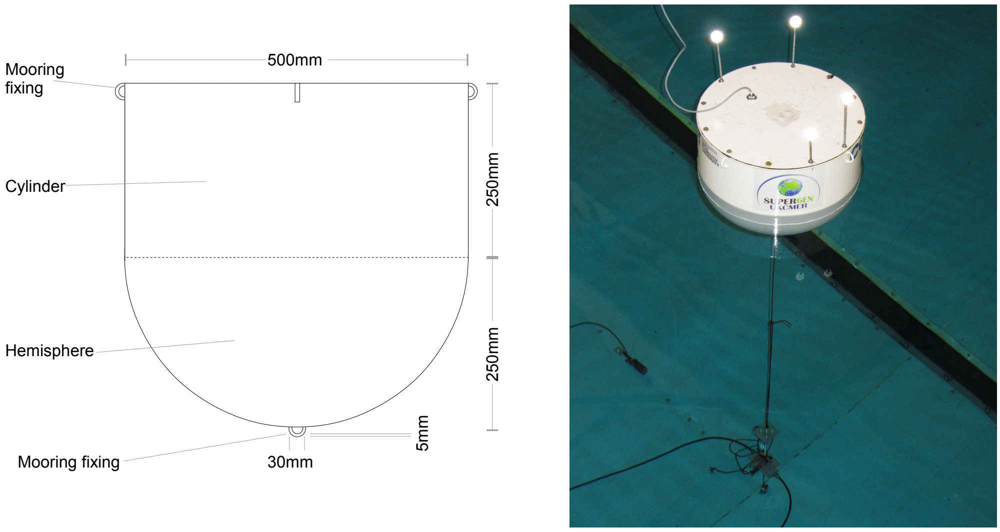

Figure 5.40: Dimensions of the hemispherical-bottomed, cylindrical buoy (left), and; a photograph from the COAST laboratory (right) showing the single-point, linear mooring and experimental setup.

5.3.1 Background - Modelling 6DOF rigid body motion

As mentioned before, full 6DOF motion is rarely considered when simplified dynamics can be assumed instead. For the majority of moored WECs, however, this is not an option as the behaviour of the body, due to wave excitation, is highly dependent on multiple coupled modes of motion. For example, in their summary of the water entry of a wedge using fully nonlinear potential theory, Wu et al. (2010) showed that asymmetry, horizontal velocity and rotational velocity all have significant effects on the flow and pressure and that there are strong couplings between these three degrees of freedom. Bai and Eatock-Taylor (2006) modelled the fully nonlinear radiated waves resulting from the forced oscillation of a truncated cylinder using a high order boundary element method. They found their model to be accurate, efficient and stable. However, of most interest was their discovery that strong nonlinear interactions exists between the heave and pitch motions. These cause a total run-up, in the combined case, that differs significantly from the linear superposition produced by the two motions independently.

The majority of nonlinear time-domain investigations into the motion of fully-coupled freely-floating bodies and mooring restraints are concerned with vessels like FPSOs and Liquid Natural Gas (LNG) carriers. Xing et al. (2001) obtained very good agreement between results from their NS solver and physical experiments of a 2D free-floating rectangular body in small regular waves. Yang et al. (2006) used a NS solver with a VOF treatment for the free surface to successfully model nonlinear wave interactions, green water and the motion of a freely-floating LNG carrier but provided no physical validation of their results. Lu (2009) modelled an FPSO able to move in heave and pitch in extreme regular waves using a NS solver and VOF method but found a number of differences in both the calculated motion and deck water height when compared to equivalent physical measurements. Despite this, Lu (2009) went on to investigate the effect of various mooring arrangements on both a single FPSO and for a pair of vessels. A linearly elastic mooring model was used with the force from compression set to zero. It was found that mooring restraints could be used to reduce the green water loads on the vessel but no validation for the moored cases was offered.

In addition, when it comes to dynamic systems, such as those including floating WECs and their moorings, it has been found that crucial design parameters, such as the load in the mooring line, can be highly dependent on the motion and position of the float when a wave arrives (Hann et al. 2015). The majority of theoretical and standard numerical models do not take into account the dynamics of the system and the consequences of past events on the orientation and positioning of the device. Hence, when estimating the loads, vital information is typically lost. Other than through physical modelling, fully coupled modelling of the system in the time-domain is the only way to ensure critical behaviour such as 'snatch-loading' is identified (Hann et al. 2015). Therefore, in order to identify the extreme values required for the design of these systems, a vast number of combinations of past wave histories and extreme wave events would be required. This is typically unfeasibly time-consuming and so it is desirable to extend the idea of a 'design wave' to a wave plus a 'design motion state' in which the device is at its most vulnerable. However, the precise situation in which these extremes in motion and mooring loads occur still remains unclear (Hann et al. 2015). Zhao et al. (2010) investigated the interactions between extreme waves and a floating body able to move freely in both heave and roll. Their NS solver with the Constrained Interpolation Profile (CIP) scheme based on a Cartesian grid method gave good comparisons with physical results for green water, impact pressures and motion response in regular, focused and combined waves. However, their model was not able to reproduce the peak pressure from a secondary loading cycle observed in the focused and combined wave experiments. Furthermore, their model tended to overestimate the amplitude of both heave and roll motions in the focused wave cases. Despite this, they found that the body showed significant nonlinear motion due to the suppressive effects of green water and that focused waves produced a large amplitude roll response. The maximum roll was found to be when the position of the body coincided with the focus location of the wave *i.e.* the crest, while the maximum heave corresponded to the trough.

5.3.2 Additions to the general NWT - 6DOF rigid body motion and restraint

Despite considerable differences between this and the previous case, the setup is very similar. The only difference is that all constraints on the motion have been removed and a restraint has been applied instead. Continuing the gradual progression towards a full WEC and mooring system, the restraint which corresponds to the mooring in this case is very simple. Assuming the mooring is linearly-elastic, massless and never becomes slack it can be modelled as a linear spring, which obeys Hooke's law,

$$F_{restraint} = k_{spring}e, \tag{5.1}$$

where $F_{restraint}$ is the force exerted in the direction of a vector from the mooring fixing on the buoy to the anchor position on the basin floor, k_{spring} is the spring constant or stiffness in $\mathrm{N\,m^{-1}}$ and e is the extension of the spring from its rest length. Clearly in Equation 5.1 a negative e (compression) is possible, producing a force that repels the buoy, however, this would not be the case in reality as the mooring line would become slack and produce no force at all. Furthermore, for a mooring with mass, the direction and magnitude of the restraint force will be altered by the sag in the line and the dynamics of its motion. These two effects have not been considered here, a more complicated restraint has been developed in the final application but the effect of mooring dynamics remains a task for the future.

5.3.3 Results and discussion - Moored buoy

In order to assess the 6DOF motion solver with the constraints removed, an initial test was conducted in which the buoy was released from an elevated position above still water and its heave displacement allowed to decay over time. This 'decay' test was performed with, and without, the mooring present in order to evaluate the accuracy of the motion prediction and the stability of the solver. Following this, the buoy was subjected to a focused wave event using the forward wave gauge method to reproduce a physical experiment in which the motion of the buoy and the load in the mooring were recorded.

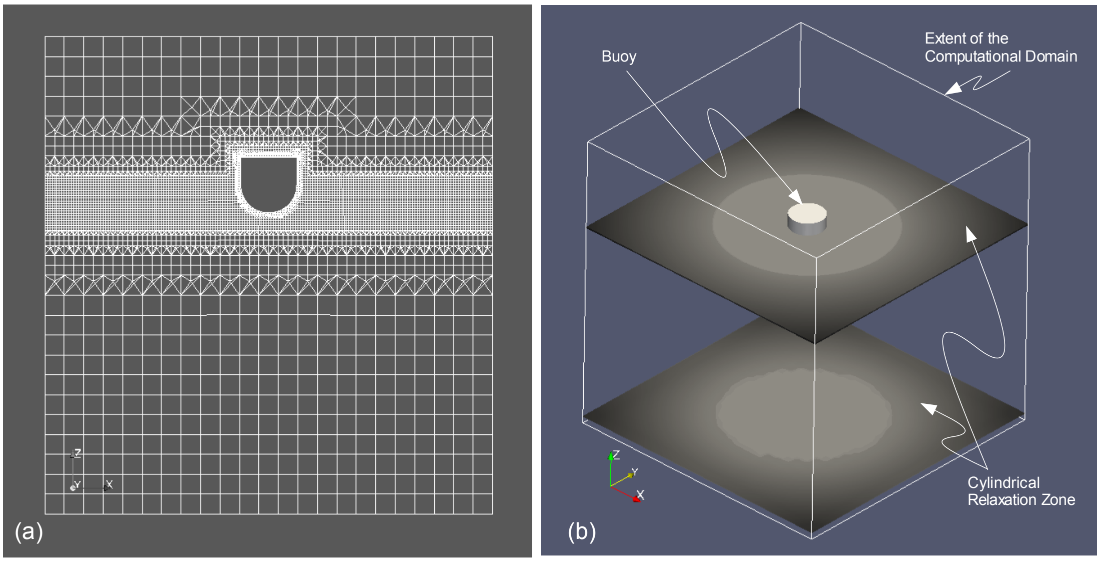

Figure 5.41: The computational domain set-up for the moored buoy decay tests. (a) a cross-section of the mesh; (b) the domain extents and cylindrical relaxation zone.

Decay tests

For the decay tests, the buoy was located, in an elevated position, in the centre of the domain, which had a square cross-section in the horizontal plane (Figure 5.41). The width of the domain was 4 m. The water depth was 2.8 m and the height of the air phase was 1.5 m. The mesh was constructed from cubic cells with a background mesh cell side-length of 0.17 m. The region containing the free-surface was refined to a quadtree level of 3 and the mesh close to the buoy was refined to level 4 (Figure 5.41a). A cylindrical RZ with an inner radius of 1m and an outer radius of 2.83 m was centred on the buoy in order to absorb any radiated waves that might affect the results (Figure 5.41b).

The results from the decay tests can be seen in Figure 5.42. It can be seen that the 6DOF solver in OpenFOAM® performs very well, particularly in the case with the mooring attached (Figure 5.42b). The unmoored case (Figure 5.42a) displays a slight inaccuracy in the frequency of oscillation and towards the end of the time series the solutions diverge from one another. This may be evidence of an issue with the force calculation or the pressure boundary condition on the surface of the buoy, however, this behaviour was not seen in

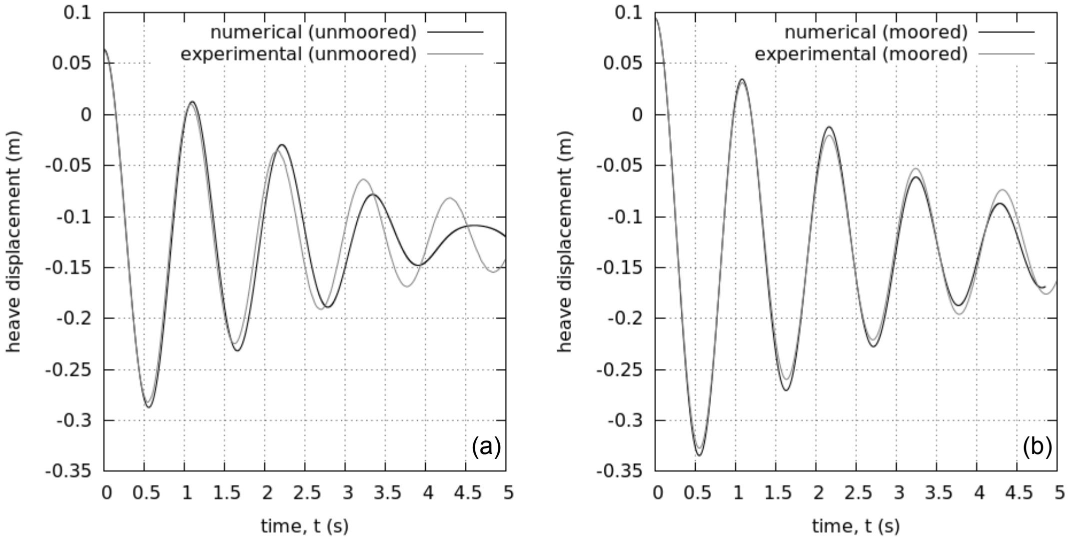

Figure 5.42: Comparisons between the heave displacement of a buoy in a physical (grey) and equivalent numerical (black) decay test with (right) and without (left) the mooring attached

the moored case. This may be a consequence of the additional driving force in the mooring dominating the motion and perhaps restricting additional degrees of freedom from becoming active. It is possible that the 'direction' of the interpolation scheme used could cause a slight asymmetry in the forcing which could excite other modes of motion but this does not seem to be the case here. It was found that the results were highly sensitive to the domain size and the amount of wave absorption, *i.e.* the influence of radiated waves reflecting from the domain boundaries, but no improvement on these results could be achieved by increasing the domain size or altering the RZ. A common concern with the dynamic mesh treatment in OpenFOAM® is that large motions cause the mesh to degrade and it has been speculated that artificial mesh 'stiffness' can result from this mesh deformation (OpenCFD 2014). In the case of this decay test, the buoy is released with the mesh undeformed and oscillates about its equilibrium state, which has a deformed mesh. This may cause issues that would not otherwise be a problem when the buoy begins in its equilibrium state. However, if this deformation were to be an issue, one might expect the associated error to increase with the displacement of the buoy, but of the two cases in Figure 5.42, the moored case has a greater displacement and a better result.

Focused wave test

To test the quality of the NWT and 6DOF motion solver in severe wave conditions, the buoy was subjected to a NewWave based on the 100 year event at the Wave Hub site. The forward wave gauge approach was used to reproduce a physical experiment in which the ~20 m high wave was produced at 1:50 scale using a PM spectrum with an f_p of 0.356 Hz instead of a JONSWAP (as used in the cylinder case in Section 5.1). The result is a more compact wave packet. As in the first wave-only validation case in Section 4.4, the depth of 2.8 m was not correctly scaled to the Wave Hub site as the small scale would require a dramatic depth change in the physical case between the wave paddles and the test area. Therefore, the conditions in this case represent a deep water (140 m) site instead of an intermediate one such as Wave Hub (~52 m).

Initially, in order to ensure the correct incident wave was being produced, the wave was generated in the absence of the buoy. A corresponding numerical simulation was run in a 2D domain, 18 m in length with an 11 m RZ on the outlet. The background mesh had a cell side length of 0.074 m and the region containing the free surface was refined one level. Based on the convergence work in Section 3.1.2 this was deemed sufficient for an RMS error of within 2 % based on a wave steepness of 0.04. Comparisons between the experimental and numerical results for the surface elevation at a number of distances from the inlet are shown in Figure 5.43. As can be seen, the NWT has performed exceptionally well in this 'wave-only' case. The main trough in Figure 5.43a is within 2 % of the experimental value and the main crest in 5.43c is within 6.5 %. Furthermore, unlike in the cylinder case, the comparative surface elevation results are equally good across a significant distance suggesting that the full range of flow variables have been captured correctly. This can only be attributed to the accuracy of the inlet wave definition. Perhaps in this case the reduced scale, more compact wave packet and increased depth have meant that linear superposition provides a better approximation to the actual wave than in the cylinder case. This may further suggest that the forward wave gauge in the cylinder case was positioned too close to the region of changing depth in the physical experiment.

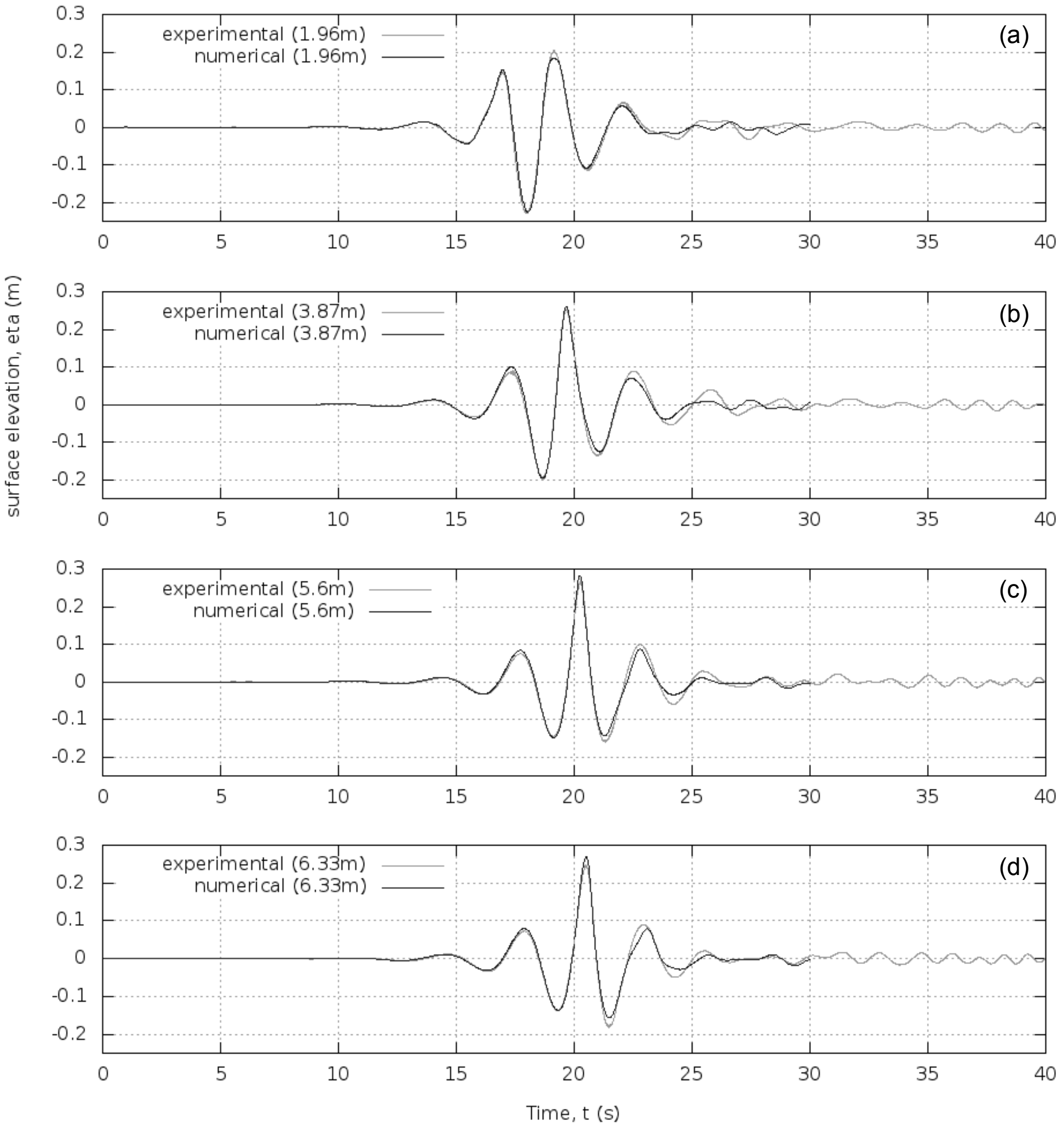

Figure 5.43: Comparison between the experimental (grey) and numerical (black) surface elevation of the extreme wave used in the moored buoy case measured at four separate distances relative to the numerical inlet: (a) 1.96 m, (b) 3.87 m, (c) 5.6 m and (d) 6.33 m.

The same wave was produced with the buoy positioned 5.49 m from the inlet and the computational domain expanded to have a width of 6 m. The mesh resolution was kept the same as in the wave-only case but expanded to have cubic cells. In addition, a cylindrical region of the mesh, with a radius of 2 m and a depth of 1.5 m, centred on the buoy was refined one level and the region in close proximity to the buoy was refined two levels.

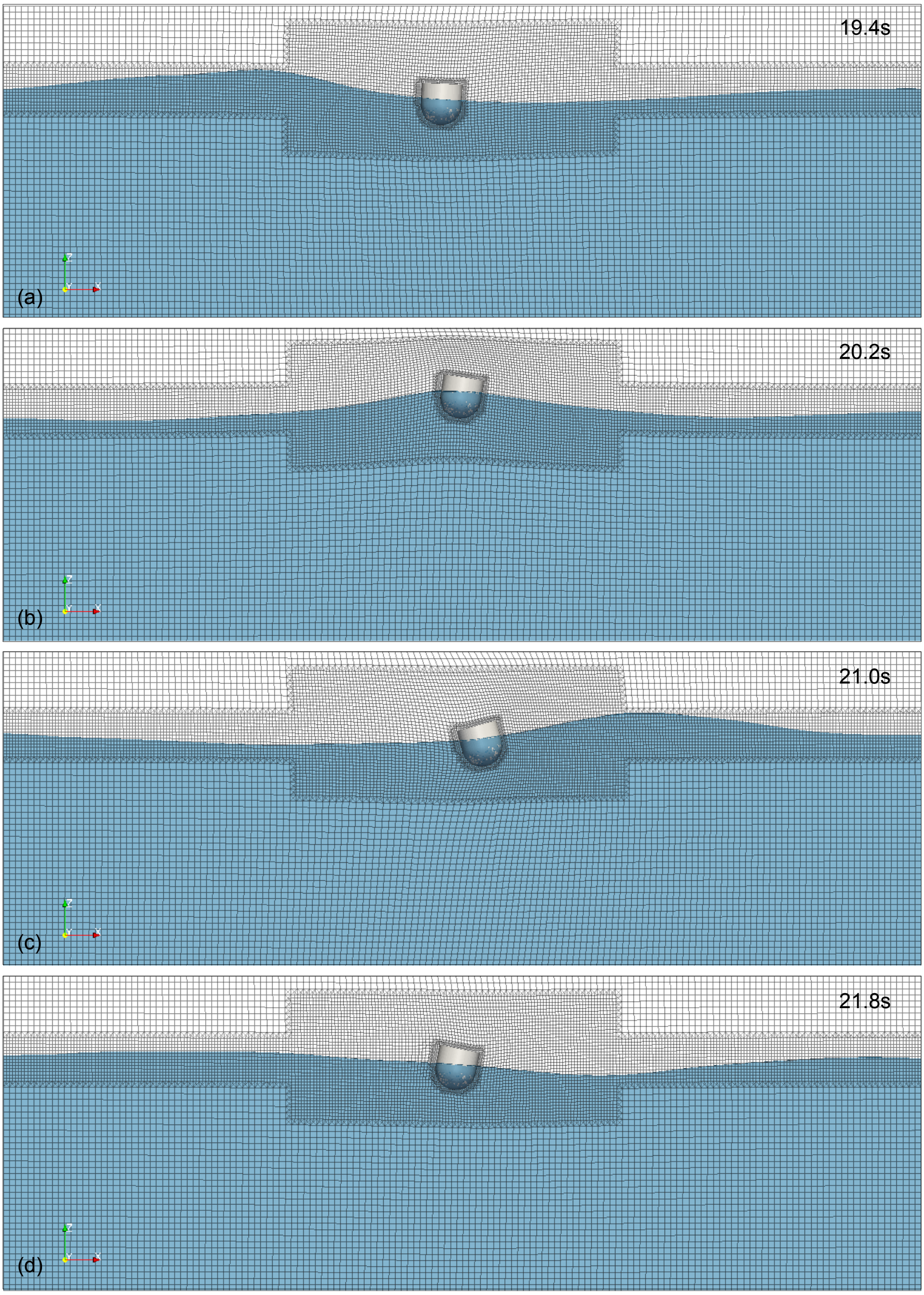

Figure 5.44: A series of vertical cross-sectional snapshots of a moored buoy simulation showing the mesh and free surface at times either side of the arrival of an extreme wave.

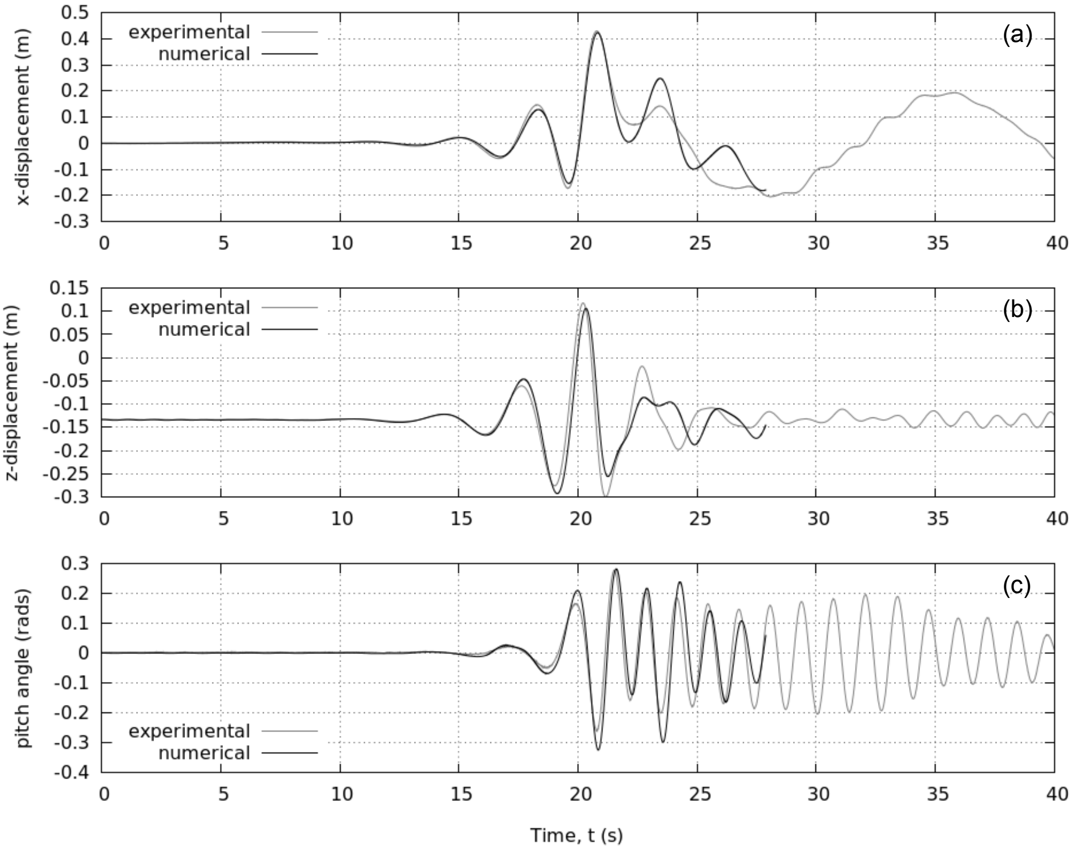

Figure 5.45: Numerical and experimental results for (a) the x-displacement, (b) z-displacement and (c) pitch angle of a buoy subject to an extreme wave event.

Figure 5.44 shows a series of vertical cross-sectional snapshots from the simulation at a number of times either side of the arrival of the main crest in the wave packet. The mesh design and the modest amount of mesh deformation caused by the buoy's motion can be seen as well as the free surface across ~10 m of the NWT. Clearly the buoy is displaced by the wave in heave, surge and pitch. The mooring has not been shown but its effect has been included in the simulation.

For a more quantitative analysis of the buoy's motion response, Figure 5.45 shows the resulting time series for the horizontal displacement of the centre of mass in the direction of wave propagation (Figure 5.45a), the vertical displacement (Figure 5.45b) and the pitch angle of the buoy (Figure 5.45c) compared with measurements taken in the physical experiment. As can be seen, the agreement is excellent until after the main wave crest has

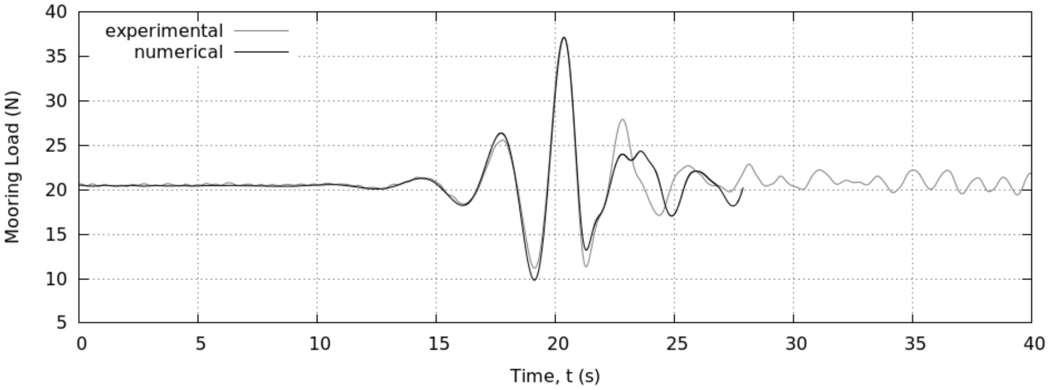

Figure 5.46: Numerical and experimental results for the load in the mooring of a buoy subject to an extreme wave event

passed, when the discrepancies are believed to be due to reflections from the end and side walls of the NWT. The motion of the buoy has been captured extremely well; the phase of the motion response matches that of the physical buoy, apart from a slight delay in the heave motion (Figure 5.45b), and both the peak heave and surge displacements are within 1 % of the physical values. The amplitude of the pitch motion is less accurate on some of the oscillations but in comparison with similar work in the literature (Lu 2009; Westphalen 2010), this is an exceptional reproduction of the buoy's motion. After the passing of the main wave crest, reflections begin to damage the numerical result due to the NWT being relatively short and narrow in order to reduce CPU effort. However, features like the long period surge oscillation (Figure 5.45a) appear to have been captured. The excellent agreement between the numerical and physical results here is a clear consequence of a high quality reproduction of the wave only case (Figure 5.43), but also evidence that the 6DOF rigid-body solver performs very well even for reasonably large displacements.

Finally, the load in the mooring, prescribed by Equation 5.1 and based on the position of the float in the numerical simulation, is shown in Figure 5.46 along with the measurements made during the physical experiment. Again the agreement is excellent until after the main crest where reflections have altered the motion of the buoy in the numerical case. Although the troughs either side show some differences, the peak load has been reproduce to within 0.2 % of the physical result.

Unfortunately, the 28 s simulation took almost 500 hours of CPU time running on 6 Intel® Xeon(R) CPU E5630 @ 2.53 GHz processors. This is excessive and part of the reason why full NS solvers are seen as unwieldy for use in device design. It is possible that the execution time can be greatly reduced by decomposing the domain across many more processors, but, the parallel efficiency of individual cores has been seen to reduce as the number of processes increases. Furthermore, the scalability of simulations, particularly in 3D, can quickly become restricted by the available hardware. The amount of RAM and the quality of connectivity between chips can be a defining factor in the execution time of simulations. The most effective way to reduce the execution time is to optimise the mesh by reducing the mesh resolution in regions of the domain where the flow conditions allow, *i.e.* where there are low gradients. However, this is generally case specific and without a thorough parametric study this can only be achieved through a series of time-consuming convergence tests.

5.3.4 Conclusions - Moored buoy

In conclusion, with the extension to 6DOF motion, the NWT has been shown to perform exceptionally well, arguably better than in the constrained case in Section 5.2. Even when subject to a large focused wave, the motion of the buoy and load in the mooring has been reproduced well. There are still some issues with reflected waves from the side walls of the computational domain but in the case of focused waves these typically only affect the results after the point of interest. The CPU effort required is, however, excessive and significant work is still required if NWTs based on full NS solvers are to be used regularly as part of the device development framework.

5.4 Seabased wave energy generator

The final application considered in this project is the Seabased wave energy generator developed at Uppsala University, Sweden. At full scale the device consists of a surface float connected via a single mooring line to a linear generator with limited stroke-length located on the sea floor (Figure 5.47a). Reaching the main goal of this project, in this application the fully coupled, 6DOF motion of an existing WEC, including complex float geometry, mooring restraint and PTO mechanism, is numerically simulated and compared with physical measurements. Furthermore, in this case, the float becomes fully submerged as a consequence of the limited stroke length, adding additional complexity which may be important in the assessment of a device's survivability.

To the author's knowledge, complete models such as this have rarely been attempted. Typically, simplifications to the behaviour are enforced or the PTO system is omitted (as described in the previous applications). Agamloh et al. (2008) did add a damper to the motion of their cylindrical WEC in order to represent the PTO system, but the float was only able to move in heave and no experimental validation was presented. Westphalen (2010) added the effect of a counterweight and its inertia into his model of the Manchester Bobber using a number of strategies. With the inertia of the counterweight correctly specified *i.e.* including its instantaneous acceleration, Westphalen et al. (2014) showed their FVM predicted the vertical motion of the Bobber reasonably well, with some overestimation of the response, during an extreme wave event. However, the float was, again, only able to move in heave, whereas the experiments showed large surge and pitch motions. Westphalen et al. (2014) went on to apply the SPH model, SPHysics, to a flat-based version of the Bobber with the same counterweight system. With a fine resolution and 6DOF they showed good agreement between the SPH result and physical measurements of the device response. However, they did not present results for individual degrees of freedom. In this application a novel PTO system including a translator mass and its inertia, limited stroke length and an endstop spring has been coupled with the 6DOF rigid body motion solver that was used in the previous application.

5.4.1 Background - The Seabased concept

The Seabased wave energy generator is the product of experiments completed at the Swedish wave energy research site located near Lysekil on the west coast of Sweden. Run by the Swedish Centre for Renewable Electric Energy Conversion at Uppsala University, the Lysekil project has involved a range of sea trails with the purpose of evaluating the device concept owned by Seabased AB (Svensson and Leijon 2014). Founded by Mats Leijon and Hans Bernhoff in 2001, Seabased AB has become a world leader in generator design and boasts an unmatched number of patents for their submerged linear PTO system (Figure 5.47a). The design specifically addresses concerns over the survivability of WECs by ensuring the units are safeguarded against high forces with minimal maintenance required (Seabased AB 2014).

The company, which works closely with academics at Uppsala University, is continually engaged in research and development and the project history extensively covers the full range of multidisciplinary issues surrounding the development of wave energy. During a recent set of physical experiments undertaken in the COAST laboratory Ocean basin at Plymouth University, UK, the resulting forces on a 1:20 scale model of the device due to high, steep but non-breaking waves were recorded (Göteman et al. 2015; Engström et al. 2015). In these tests, the PTO system was located on the gantry in the COAST laboratory, above the water level, and connected to the float via a single, inelastic mooring line and pulley system. In the model, the PTO damping, which at full scale is achieved electrically, was approximated by friction damping exerted via a pair of Teflon blocks. Included in the extensive testing program were a range of regular and extreme wave tests, based on conditions at the Wave Hub site, with a return period of 80 years. In these tests the load in the mooring line was measured using a miniature, low-profile load cell attached to the top of the translator and the 6DOF motion of the float was recorded using the Qualysis 3D optical tracking system. Figure 5.47b shows a photograph of the float and PTO system used in the experiments.

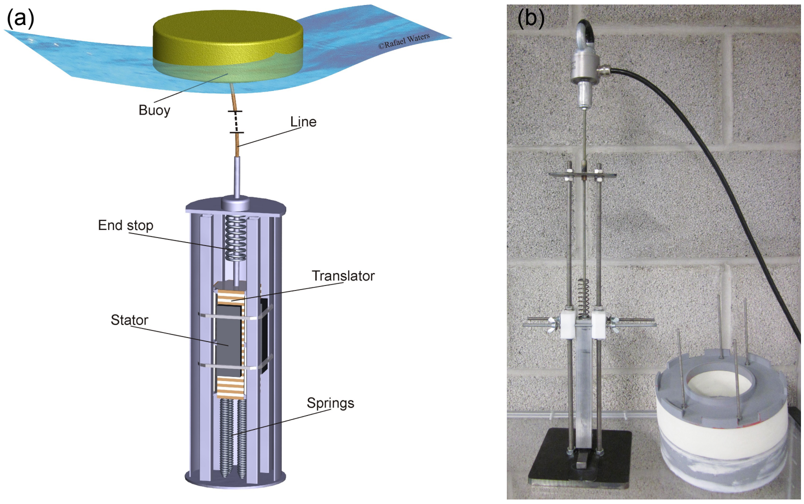

Figure 5.47: The Seabased wave energy generator: (a) an artist's impression of the full scale device and PTO system; (b) a photograph of the model PTO system and float used in the physical experiments (images courtesy of M. Göteman).

5.4.2 Additions to the general NWT - PTO systems and turbulence modelling

In addition to a more complicated float geometry, this application requires a restraint on the float motion that provides a restoring force corresponding to the translator, limited stroke and endstop of the PTO system shown in Figure 5.47b. Therefore a bespoke restraint was created where the tension in the mooring is given as a function of the distance and acceleration between the restraint attachment point, $\mathbf{R}$, and the anchor position, $\mathbf{A}$. The original computer code for this restraint can be found in Appendix C. Figure 5.48 shows a schematic diagram of the restraint conditions. In this case, no PTO damping was applied. The force exerted by the restraint is then

$$F_{restraint} = \begin{cases} 0, & \text{if } |\mathbf{r}| < (r_0 - s_b) \\ m(g+a_r), & \text{if } (r_0 - s_b) \leq |\mathbf{r}| < (r_0 + s_t) \\ m(g+a_r) + k_{es}[r - (r_0 + s_t)], & \text{if } (r_0 + s_t) \leq |\mathbf{r}| \end{cases} \tag{5.2}$$

where $\mathbf{r}$ is the vector between $\mathbf{R}$ and $\mathbf{A}$ with magnitude $|\mathbf{r}| = r$, r_0 is the distance between $\mathbf{R}$ and $\mathbf{A}$ when the float is at rest in still water, m is the translator mass, k_{es} is the endstop spring constant, l_{es} is the endstop spring rest length, s_t is the distance between the translator and the endstop at rest and s_b is the distance between the translator and the floor at rest. $\mathbf{g}$ is the acceleration due to gravity and $\mathbf{a}$ is the acceleration of the float. a_r is the acceleration of the float in the direction of $\mathbf{r}$ which is also the acceleration of the translator. Due to the inclusion of the acceleration in the restraint force *i.e.* the inertia of the translator mass, and because the acceleration of the body is notoriously unstable, an additional constraint was imposed on the value of a_r.

$$|a_r| \leq g. \tag{5.3}$$

This ensures the translator cannot accelerate downwards faster than free-fall, which would suggest a negative tension in the mooring line, and removes abnormally large inertial forces from high accelerations, which can occur when the time-step reduces to very small values. However, it was found that in order to stabilise the simulations an `accelerationRelaxation` of 0.2 was required which meant this condition rarely had to be enforced.

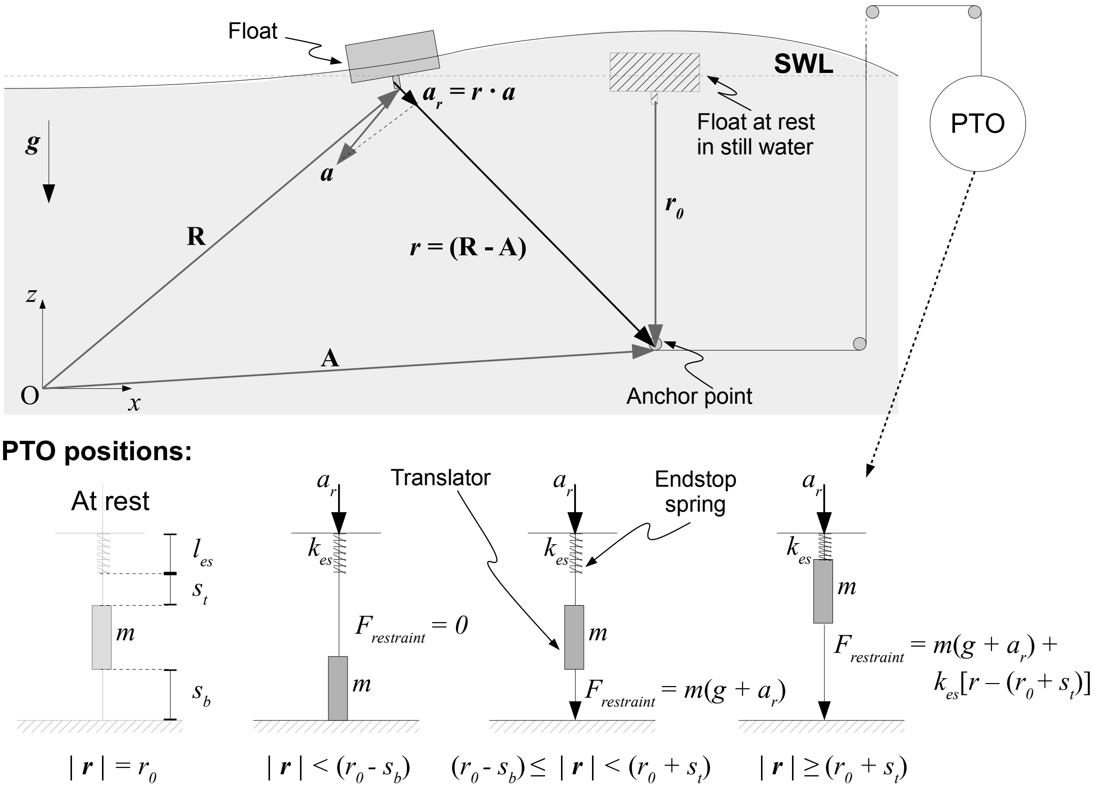

Figure 5.48: Schematic representation of the Seabased PTO restraint conditions.

In addition to the PTO model (Figure 5.48 and Equation 5.2), it was suspected that turbulence might play an important role in this case. From observations of the physical experiments, the motion of the float was relatively violent at times, particularly when being pulled under the water by the limited stroke length. This resulted in spray, vorticity and over-turning of the water flooding over the irregular-shaped float and being forced through the centre. For this reason a number of turbulence models have been implemented in an attempt to incorporate an approximation of these effects into the NWT.

As mentioned in Section 3.1.6, there are many different turbulence-closure models developed for the RANS equations. In this work only two of the most common have been considered; the standard $k-\varepsilon$ model and the Renormalised Group (RNG) $k-\varepsilon$ model. Both of these require a set of boundary conditions for the turbulent kinetic energy, k, and its rate of dissipation, ε. On the inlet and top boundaries of the domain an `inletOutlet` condition is used for both values, which applies a zero-gradient condition for positive flux (out of the domain) and a user-defined value (of 0.1 in this case) for negative flux. On the remaining boundaries, including the structure, a wall function is applied based on the log-law described in Section 3.1.6. As with the previous applications, the complete set of boundary conditions used in the Seabased simulations are tabulated in Appendix A.

Finally, the geometry of the Seabased float is significantly more complicated than that of the X-MED buoy used in the previous section. The 0.2 m diameter, cylindrical float has a 0.1 m diameter, cylindrical hole through its centre (a ‘moon-pool’) with a supporting frame for a central mooring attachment. Furthermore, there are turrets on the top of the device designed to trap green water and increase the effect of hydraulic damping (Engström et al. 2015). A transparent view of the Seabased CAD geometry used can be seen in Figure 5.49a. The float has a mass of 0.962kg and a moment of inertia of (0.0053 0.0053 0.006) N m. The mass and mesh motion properties, including the PTO restraint values are given in Appendix B.

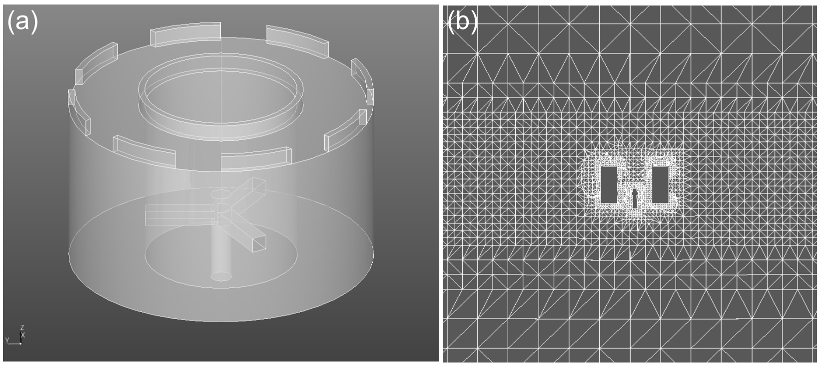

Figure 5.49: (a) Transparent view of the Seabased CAD model. (b) Cross-section of the mesh used in the Seabased simulations at t=0 s.

5.4.3 Results and discussion - The Seabased wave energy generator

As in the previous application, an initial decay test was undertaken to ensure the float and translator arrangement was behaving as expected. Following this, the Seabased device was simulated in steep regular waves. In both cases the results from the numerical solution have been compared to those measured in an equivalent physical experiment.

Decay tests

For the decay tests, the float was initially submerged slightly below its equilibrium position in the centre a domain with a square plan of edge length 4 m. The water depth was 2.8 m and the height of the air phase was 1.5 m. The mesh was constructed from cubic cells with a background mesh cell side-length of 0.174 m. The region containing the free-surface was refined to a octree level of 3 and the mesh close to the buoy was refined to a minimum of level 4 and a maximum of level 5. The inner and outer radial distance parameters for the dynamic mesh were set at 0.1 m and 2 m respectively. As in the case of the buoy in Section 5.3, a cylindrical RZ with an inner radius of 1 m and an outer radius of 2.83 m was centred on the float in order to absorb any radiated waves that might affect the results. A cross-section of the mesh used is shown in Figure 5.49b. The float was then released and ascended under its own buoyancy before a decaying oscillation in heave about the free surface. In the decay tests, the displacement was not sufficient enough to activate the endstop or limited stroke in the PTO, but the effect of the translator mass was necessary.

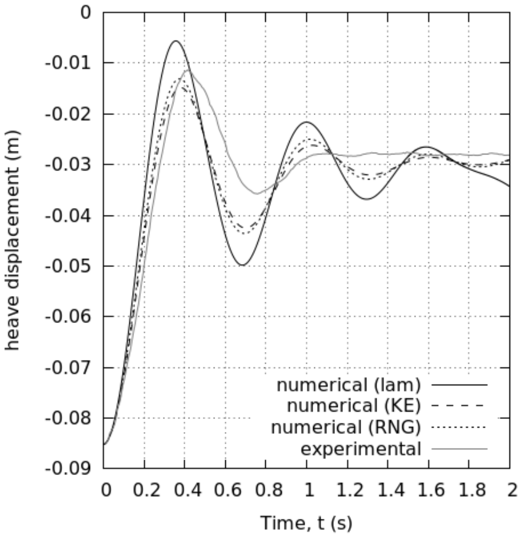

Figure 5.50: Comparisons between the heave displacement of the Seabased float in a physical and equivalent numerical decay test with either a k-ε, RNG k-ε or no turbulence (laminar) model implemented

The results from the decay test when using the k-ε and RNG k-ε turbulence models are plotted alongside the laminar case and the physical measurements in Figure 5.50. Despite good results for a similar simulation in the case of the moored buoy in Section 5.3, it can be seen here that the case without a turbulence model (laminar) over-predicts the amplitude of oscillations. The frequency of oscillation is also over-predicted. The k-ε model acts to reduce the amplitude of the oscillations but the frequency remains higher than that seen in the physical experiment. The RNG k-ε model reduces the amplitude slightly less than the k-ε model but also shows no improvement, compared to the laminar case, in terms of over-estimating the frequency of oscillation. However, it is believed that the discrepancy seen here is a result of unwanted friction in the PTO system and pulley arrangement that will have damped the motion of the float in the physical case. This would tend to reduce the amplitude of the oscillation as well as the natural frequency of the system and has not been accounted for in the numerical simulations. In the following section, it is hoped that with the float's motion being driven by waves, the amplitude of the oscillation will be greater and the influence of this damping will be reduced. Assessment of the effect of damping in the PTO system is planned as further work.

Regular wave test

Finally, in order to validate the combination of NWT and PTO model developed here, the physical interaction of the Seabased device with a regular wave of height 0.3 m, period 2.4 s and steepness 0.035 has been reproduced numerically. To place this application in the context of survival testing, the wave height and period were based on the significant wave height and peak period of storm conditions at the Wave Hub Site with a return period of 80 years (Göteman et al. 2015; Engström et al. 2015). The centre of the float was located in its neutrally buoyant position, 5.937 m from the inlet of a 14 m long and 4 m wide NWT. As in the decay tests, the mesh was constructed from cubic cells with a background mesh cell side-length of 0.174 m. The region containing the free-surface was refined to a octree level of 3 and the mesh close to the buoy was refined to a minimum of level 4 and a maximum of level 5. A 6 m RZ was place on the outlet. During the experiment, the 6DOF motion of the float was recorded along with the tension in the mooring cable.

Figure 5.51 shows a comparison between the physical results and the numerical results assuming laminar flow conditions. As can be seen, the comparison is reasonably good considering the complexity of the system under investigation. The main features in the time series of mooring load (Figure 5.51a) have been reproduced; the pair of peaks in load, corresponding to the translator being restrained by the endstop spring, have approximately the correct magnitude; the drop to zero load, when the translator is at rest on the bottom of the PTO, is present; and the variation in loading due to the translator's inertia has also been captured, even though the experimental data is far noisier than the numerical result. Both the surge and heave displacement of the float (Figure 5.51b and c) show similar periodic motion to the experimental measurements and the heave motion has the same characteristic higher frequency oscillations on the peaks and troughs due to the limited stroke length of the PTO. However, with all three of these results the underlying periodicity of the oscillations is predicted at a lower frequency by the numerical simulation when compared to the experiment. The proposed explanation for this is that there are some inconsistencies between the PTO dimensions used in the physical case and those supplied for the

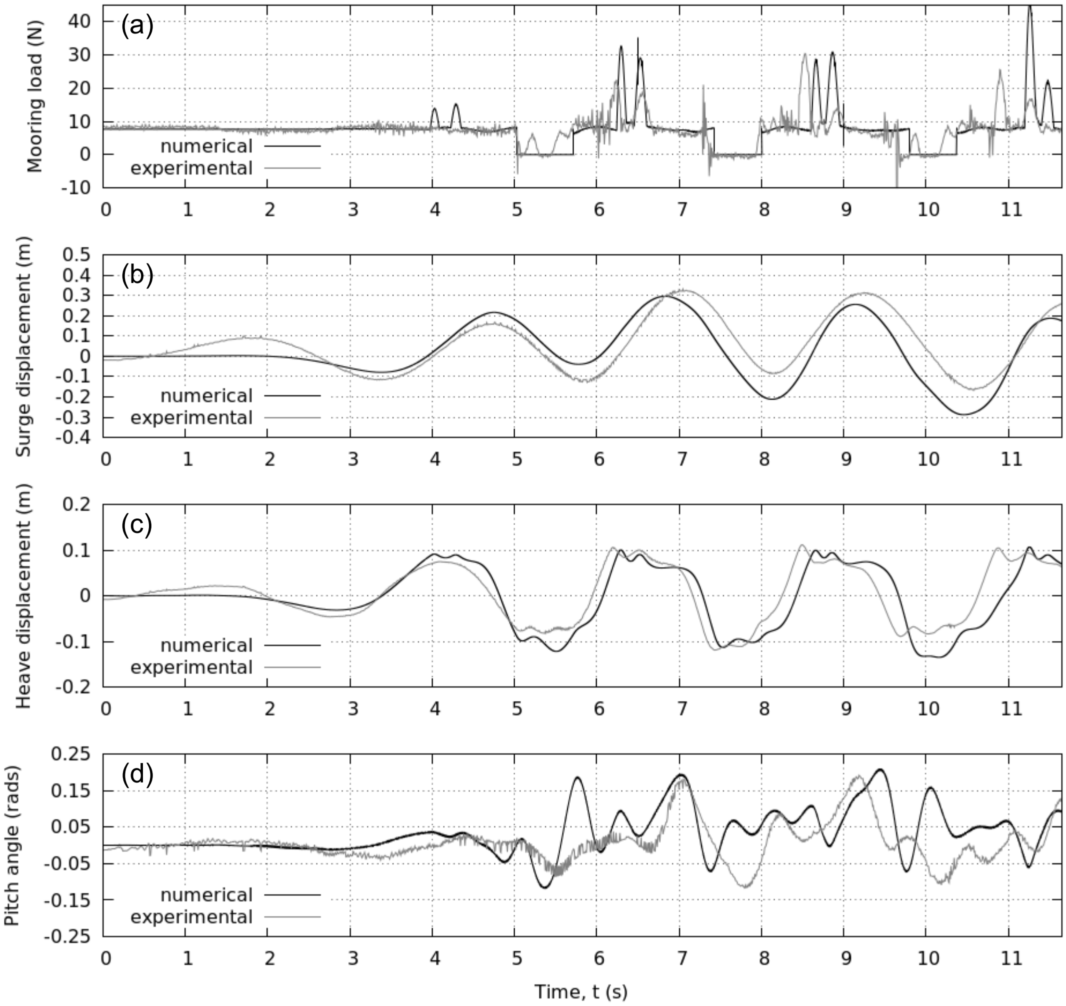

Figure 5.51: Physical (grey) and laminar numerical (black) results from simulation of the Seabased wave energy generator when subject to regular waves. (a) mooring load, (b) surge displacement, (c) heave displacement, and (d) pitch angle.

numerical simulation. Additional simulations show that the precise behaviour of the device is highly sensitive to these dimensions, however, reflected waves or artificial stiffness in the mesh may also be an issue. Furthermore, the weight of the Qualysis targets have not been accounted for in the mass and moment of inertia of the float and for such a small float these may have had a significant effect on the dynamics. This may be particularly evident in the pitch result in Figure 5.51d where the numerical simulation has not managed to capture the pitch motion as well as in the previous application. Further, it is also possible that the prescribed `accelerationRelaxation` of 0.2 is too severe and has resulted in

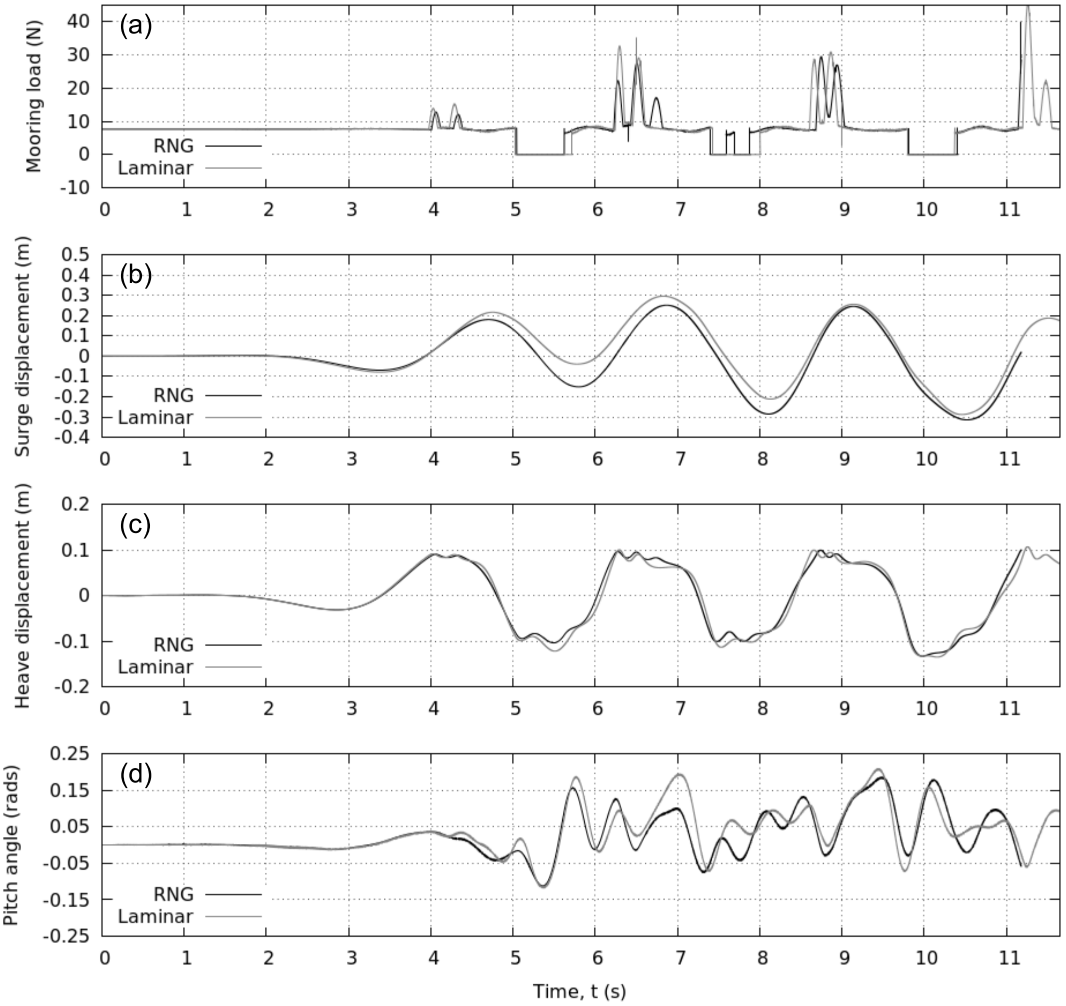

Figure 5.52: Results from numerical simulation of the Seabased wave energy generator in regular waves with the RNG k-ε model (black) or laminar flow (grey). (a) mooring load, (b) surge displacement, (c) heave displacement, and (d) pitch angle.

an artificial damping to the float's motion. However, simulations with greater values of the `accelerationRelaxation` tend to become unstable as very small time steps produce divergent results for the body's acceleration. By inspecting the full domain results, it is believed that spurious high velocity air flow causes the length of the adjustable time step to be reduced excessively. Not only is this air flow physically incorrect but, it greatly reduces the efficiency of the simulation and compromises the stability without the use of a considerable `accelerationRelaxation`.

As mentioned earlier, it is possible that this case is greatly affected by turbulence. However, Figure 5.52 shows the laminar results from Figure 5.51 compared against those from the same simulation with the RNG k-ε model used to model the turbulence. As can be seen, the addition of this turbulence model has not made a big difference to the results and certainly has not resolved the inaccuracies in the pitch motion or the underlying frequency of the oscillations. Assessment of turbulence models for cases involving structures like the Seabased device is outside the scope of this work and should be revisited in future studies. Lastly, as in the previous application, the execution is still excessive. The first 11 s of simulated time in the laminar case took approximately 21 days of CPU time running on 15 Intel® Xeon(R) CPU E5630 @ 2.53 GHz processors. Interestingly, with the RNG k-ε model applied the same 11 s took only 18 days. It is thought that the turbulence model suppresses some of the more extreme flow conditions allowing the Courant condition to be satisfied for a longer timestep.

5.4.4 Conclusions - The Seabased wave energy generator

In this application, the unique case of the Seabased wave energy generator has been successfully simulated using the NWT developed thoughout this project, including 6DOF motion of a float with complex geometry, mooring restraint and PTO system with limited stroke length and endstop spring. As a result, this application represents a level of complexity that has not been seen in CFD applications before now and, despite being highly sensitive to the precise details of the validation experiment, the numerical solution given here compares well with physical measurements of mooring load and float dynamics. Furthermore, qualitative observations of surface elevation snapshots in the vicinity of the float show that the NWT is capable of simulating extremely complicated over-topping and green-water effects (Figure 5.53), which are crucial in understanding the behaviour and survivability of the device. However, quantitative analysis of these effects is still required and further work is needed to resolve stability issues caused by anomalous air flow in the domain. To account for possible turbulence effects, a pair of k-ε models have been applied, but no conclusions regarding their effectiveness can be drawn as any improvement resulting from their use has likely been obscured by inconsistencies between the complicated physical and numerical setups. Finally, the execution time is still regarded as excessive, even for this complex case. Nevertheless, in this application it has been shown that the NWT developed here is capable of reliably predicting the bevaiour of WEC and mooring systems in extreme conditions.

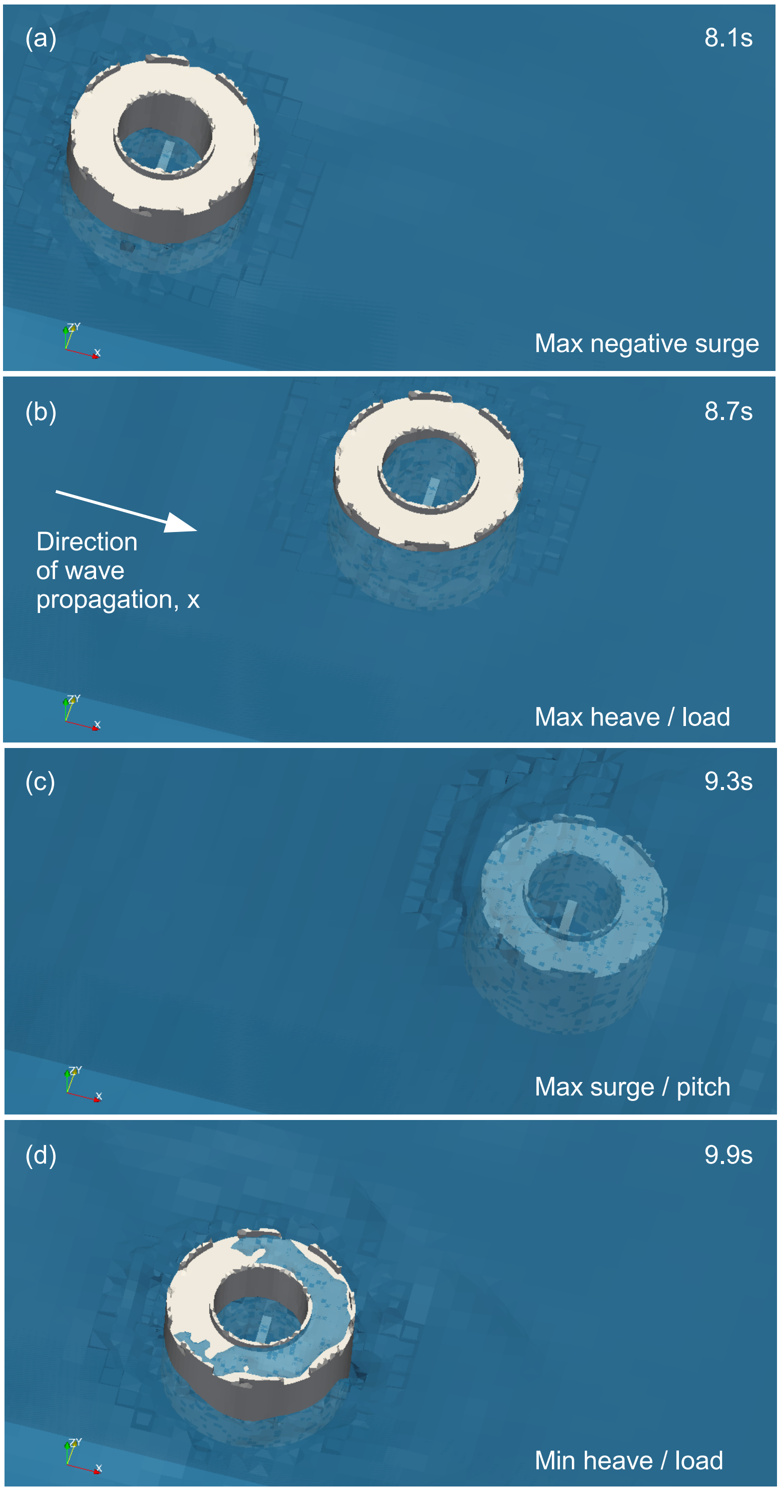

Figure 5.53: A series of snapshots from the laminar simulation of the Seabased device when subject to regular waves.

Chapter 6

Final Remarks

> *"A conclusion is the place where you got tired thinking"* - Martin H. Fischer as quoted in Smith (1945)

With growing concerns over the ‘energy trilemma’ *i.e.* sustainability, security and cost of energy, exploitation of renewable energy sources has become a priority among many of the World’s governments. For countries with significant resource, it is hoped that wave energy will make up at least part of the energy mix. However, presently, the conversion of ocean wave energy into electricity is far from commercially viable. The technology remains significantly more expensive than many of the alternatives and a history of device failure has meant that the required investment has become increasingly difficult to secure. Furthermore, the number of device concepts is still excessive and the industry has yet to converge on a successful design solution. In order to de-risk and encourage investment in wave energy technologies, a narrower band of cost-effective design solutions is required along with greater confidence in the devices’ abilities to survive at sea.

When assessing the survivability of a particular device there are a number of things to consider, including: fatigue failure, component reliability and mechanical failure, due to salt ingress. In this work, however, the focus has been on the single maximum loading event resulting from an extreme wave interaction with the device. Many lessons can be learned from other maritime activities, such as oil and gas or offshore wind, and present guidelines for WECs rely heavily on the existing design standards. However, in contrast with traditional offshore structures, point-absorber-type WECs are typically designed to respond to wave motion in order to generate power and this response is normally dictated by a complex set of interactions between the structure, mooring and an array of environmental factors, including wind, waves and currents. Therefore, in the case of a point-absorber, the behaviour of the structure and the survival considerations differ greatly from those for which the design standards were intended, *i.e.* for FPSO platforms. Consequently, in order to ensure a device is ready for deployment at sea, a series of stepwise development processes are typically performed in accordance with the commonly used Technology Readiness Level (TRL) metric. An important component of this process is numerical modelling and with the continued increase in the performance-to-cost ratio of modern computers, sophisticated numerical models are being used more and more, with physical modelling reserved for proof of concept and validation purposes only. However, in the context of survivability, there is a lack of confidence in the ability of numerical models to capture the physics of the most extreme loading events. Developers have, therefore, been limited to scale model experiments in a physical wave tank where scale effects remain an issue and the cost of suitable laboratory time can be very high. Furthermore, the precise conditions responsible for the maximum load on a WEC are not known, meaning long-term simulations, which are not feasible when using complex numerical models, are typically required to give a statistical representation of the extreme loading events.

In this project, these issues have been addressed and a computational tool has been developed that can provide a reliable understanding of the behaviour of WEC systems under extreme wave loading.

Based on assessment of existing numerical methods for wave-structure interaction problems, a fully nonlinear CFD approach was selected. A FVM discretisation and a VOF interface capturing method have been used to solve the RANS equations for two incompressible, isothermal, immiscible fluids. This allowed for simulation of multiphase, viscous flow and the ability to handle large deformations of the free surface, including wave breaking and green water effects, which were deemed essential for assessing WEC survivability.

The open-source CFD platform, OpenFOAM®, was selected and many of the crucial elements involved in the development of a NWT have been assessed.

Mesh design has been found to be extremely important, although very few guidelines are available regarding good meshing practice in NWTs. Unique to this project, a parametric study of the required mesh resolution, as a function of wave steepness, has been performed and it is clear that for steeper waves a greater mesh resolution is needed to ensure mesh independence. However, it has been proposed here that the required mesh resolution is strongly influenced by the magnitude of the surface compression applied. Optimal mesh design should, therefore, consider both mesh resolution and surface compression to be a function of the wave steepness. Square (cubic) mesh cells have been shown to be superior in both convergence and CPU efficiency when compared to other quadrilateral (hexahedral) cell shapes and selective mesh refinement at the free surface can improve the efficiency of simulations greatly but a parametric study of this is required to ensure mesh independence is retained. `snappyHexMesh` has been shown to allow for the addition of complex structure geometries and the resulting mesh performs better than the most basic meshing tool. However, a thorough mesh dependency study is required when including structures and alternative meshing tools and different cell shapes are still to be considered. Furthermore, generation of spurious air flow in the vicinity of structures, and as a result of poor mesh design, poses a problem and can result in significant losses in efficiency.

For moving structures, the rigid body motion solver and the deforming mesh functionality of OpenFOAM® has been used extensively and has been shown to be capable of accommodating the large motions necessary for survival testing, provided the mesh and dynamic mesh parameters are defined correctly.

Both wave generation and wave absorption has been achieved using the additional toolbox `wave2Foam`. The expression-based boundary conditions used have been shown to successfully generate waves based on analytical wave theories. When reproducing a physical experiment, a forward wave gauge measurement has been used as the numerical input, greatly reducing the computation domain size and improving the simulation efficiency by removing the region close to the wave paddles. However, there is a problem when trying to reproduce a wave climate that cannot be described analytically *i.e.* a highly nonlinear focused wave event. Crucially for survival testing, once the incident wave exceeds a critical size/steepness, an improved definition of the fluid properties is likely to be required in order to ensure a smooth transition between the boundary conditions and the internal domain. Wave absorption on both the inlet and outlet boundaries of the domain has been achieved with varied success using the passive absorption method known as a Relaxation Zone. Reflected waves are still a problem in the NWT simulations and the required increase in the domain size is undesirable. Furthermore, absorption on the side walls has yet to be implemented, causing issues in simulations where waves are radiating from a central structure.

In terms of the solver control, the numerical schemes and solver types have not been optimised, however, it has been found that a fixed time step shows divergent behaviour and so the adjustable time step function based on the CFL condition is considered to be essential.

Another contribution made here is the implementation of the dispersively focused design wave, NewWave, into CFD simulations. This provides a deterministic method for recreating extreme wave events, which is more realistic than large regular wave tests and removes the need for long term simulations. Using this method, ‘the most probable’ extreme wave event at a particular site can be generated at a desired position and time allowing for relatively short simulations, making the use of computationally expensive CFD models feasible. The NWT developed in this project has been used to successfully reproduce physical experiments involving NewWaves, however, for the most extreme case, the expression-based boundary condition, used to generate the waves, requires improvement. Furthermore, the precise conditions under which the maximum loads occur have not yet been established. Therefore, in order to test the survivability of a dynamically responding body such as a WEC, a design wave on its own is insufficient. The position and velocity of the body when the wave arrives has a significant effect on the resultant load in the mooring (Hann et al. 2015) and so in order to deterministically replicate the highest loads, the arrival of a design wave must be combined with a designed motion state for the particular body. Unfortunately, this motion state is likely to be highly case specific requiring an extensive test program to be identified. This is not currently possible with the present execution time of CFD models.

As well as wave-only cases, a number of physical experiments, including both stationary and moving structures, have been reproduced using the NWT developed in this project. Comparisons between the experimental measurements and numerical results documented here show a marked improvement in convergence over the limited examples in the literature, particularly for 6DOF motion. The performance of the NWT is particularly good when the incident wave has been reproduced correctly. However, when the incident wave is very steep or strong nonlinear diffraction occurs or an excessive amount of green water is present, the quality of the numerical reproduction appears to be reduced slightly. This is likely to be an issue for survivability assessment although, at the level of detail under investigation here, it is possible that inaccuracies in the physical validation cases are at least partly responsible for the observed discrepancies. In this project it has been shown that, with careful specification of a number of parameters, state-of-the-art NWT tools can perform very well at each of the increasing levels of complexity investigated: Extreme waves can be reproduced well as can their interaction with fixed and floating structures; complex geometries can be handled without issue; coupled motion of both constrained devices and those able to move in all 6DOF can be predicted correctly, and; the load in mooring lines, both with and without complex nonlinear PTO systems, can be calculated accurately.

Among the applications in this project, a number of unique test cases have been performed and, crucially, validated against physical measurements. A scale model of the Wavestar device has been simulated and, with the novel addition of a full PTO model, the unique behaviour of the Seabased wave energy generator, including a geometrically complex float, mooring and limited stroke PTO, has been reproduced successfully. This shows that entire, existing WEC systems can be simulated and the coupled behaviour of the float, mooring and PTO system can be captured accurately using the computational tool developed in this project. In addition to this, the 6DOF motion and mooring load of a simple buoy and restraint system has been reproduced with exceptional accuracy during an extreme wave event. These results provide supporting evidence that state-of-the-art numerical methods can be used to assess the response and loading on WECs in extreme sea states and could be included in the design guidance when considering device survivability.

Despite this, as with physical modelling, in order to ensure quantitatively robust and trustworthy results, a series of quality control checks and standardisation of the methodological practices is needed. Before this can happen and generic guidelines for the numerical testing of WEC survivability can be produced, a number of specific elements of the technique described here require further investigation:

1. **Mesh** - A considerable amount of work has gone into the meshing methodology used in this project. However, the required mesh resolution has been shown to increase rapidly with wave steepness leading to excessive execution times particularly in cases with moving structures. Further work is required to optimise the mesh and reduce the CPU demand. Square cells have been found to have the most desirable convergence behaviour of any quadrilateral, but, the requirements of the mesh in the vicinity of structures and the effect of mesh deformation are still unknown. Furthermore, potential savings from reducing the mesh resolution in some regions of the domain need to be realised. Future work will involve further parametric studies to optimise the mesh used in NWT simulations and understand the balance between accuracy and CPU demand. These studies will be based on case specific properties, such as the wave steepness, to provide standardised mesh design guidelines and ensure the mesh independence of simulations with the minimum possible execution time.

2. **Wave generation** - An expression-based inlet boundary condition has been shown to accurately produce both regular and focused waves and a forward wave gauge method has been developed to reproduce physical experiments with a greatly reduced domain size. However, the wave generation is limited by the accuracy of the imposed boundary conditions and it has been shown that an improved definition of the kinematics of irregular waves, particularly highly nonlinear focused waves, is needed to provide for extreme wave generation. Future work will include investigation into focused wave kinematics including optimisation of the forward wave gauge method and a parametric study of the required order of boundary conditions as a function of incident wave nonlinearity.

3. **Wave absorption** - A passive wave absorption method known as ‘relaxation zones’ has been implemented with varied success. Reflected waves remain a significant issue in the NWT developed here, particularly at the wave maker boundary and on the side walls of three dimensional domains. Furthermore, implementation of relaxation zones leads to an increase in both the domain size and the CPU demand. Future work will include a parametric study of the performance of relaxation zones in order to reduce the effect of reflected waves whilst minimising losses in efficiency. Alternative wave absorption methods will also be considered.

4. **Stability** - Spurious air flow, when using the VOF method, has been seen to compromise the stability and efficiency of NWT simulations, as has dramatic mesh deformation when including moving structures. Further investigation is required to understand and reduce the effect of unphysical momentum transfer and mesh deformation and ultimately ensure the robustness of NWT simulations.

5. **Solution strategy** - Many numerical schemes and solution strategies exist that have not been considered here. In future work, each of these requires assessment, in the context of a NWT, to optimise the accuracy-to-stability ratio and computational efficiency of simulations.

6. **Scalability** - The NWT tool developed in this project has been shown to accurately predict the behaviour of WEC and mooring coupled systems. However, for simulations including 6DOF rigid body motion, mooring restraints and complex free surface flow, the execution time remains excessive. Optimisation of the mesh and both the wave generation and absorption is required, as well as resolution of any stability issues. In addition to this, future work will investigate the scalability of NWT simulations, including assessment of alternative decomposition methods and analysis of parallel efficiency on High Powered Computing (HPC) facilities.

List of References

Adcock, T., Taylor, P., Yan, S., Ma, Q. and Janssen, P. (2011), 'Did the Draupner wave occur in a crossing sea', *Proceedings of the Royal Society A: Mathematical, Physical and Engineering Science* **467**(2134), 3004–3021.

Agamloh, E. B., Wallace, A. K. and von Jouanne, A. (2008), 'Application of fluid-structure interaction simulation of an ocean wave energy extraction device', *Renewable Energy* **433**, 748–757.

Ambühl, S., Kramer, M., Kofoed, J. P. and Sørensen, J. D. (2012), Reliability assessment of wave energy devices, *in* 'Proceedings of the 4th International Conference on Ocean Energy (ICOE)', Dublin, Ireland.

Anderson, J. J. D. (1995), *Computational Fluid Dynamics: The Basics with Applications*, McGraw-Hill International Editions.

ANSYS, Inc. (2015), 'Ansys aqwa', website. `http://www.ansys.com/Products/Other+Products/ANSYS+AQWA` accessed 7th January 2015.

Bai, W. and Eatock-Taylor, R. (2006), 'Higher-order boundary element simulation of fully nonlinear wave radiation by oscillating vertical cylinders', *Applied Ocean Research* **28**, 247–265.

Bangun, E. P. and Utsunomiya, T. (2008), Evaluation of viscous forces acting on a moving body by navier-stokes solver, *in* 'Proceedings of OCEANS 2008', Kobe, Japan, pp. 1–8.

Barth, T. J. and Jespersen, D. C. (1989), The design and application of upwind schemes on unstructured meshes, *in* '27th Aerospace Meeting. AIAA '89', Reno, Nevada.

Bateman, W. J. D., Katsardi, V. and Swan, C. (2012), 'Extreme ocean waves. part 1. the practical application of fully nonlinear wave modelling', *Applied Ocean Research* **34**, 209–224.

Beam, R. M. and Warming, R. F. (1976), 'An implicit finite-difference algorithm for hyperbolic systems in conservation-law form', *Journal of Computational Physics* **22**(1), 87–110.

Beam, R. M. and Warming, R. F. (1978), 'An implicit factored scheme for the compressible Navier-Stokes equations', *AIAA Journal* **16**(4), 393–402.

Berberović, E., van Hinsberg, N. P., Jakirlić, S., Roisman, I. V. and Tropea, C. (2009), 'Drop impact onto a liquid layer of finite thickness: Dynamics of the cavity evolution', *Physical Review E* **79**. 036306.

Bhinder, M. A., Mingham, C. G., Causon, D. M., Rahmati, M. T., Aggidis, G. A. and Chaplin, R. V. (2009), Numerical and experimental study of a surging point absorber wave energy converter, *in* 'Proceedings of the 8th European Wave and Tidal Energy Conference', Uppsala, Sweden.

BMT Fluid Mechanics Ltd (2001), *Review of model testing requirements for FPSO's*, Health and Safety Executive.

Bodony, D. J. (2006), 'Analysis of sponge zones for computational fluid mechanics', *Journal of Computational Physics* **212**(2), 681–702.

Boris, J. P. and Book, D. L. (1973), 'Flux-corrected transport. I. SHASTA, a fluid transport algorithm that works', *Journal of Computational Physics* **1**(1), 38–69.

Bos, F. (2009), Numerical simulation of flapping foil and wind aerodynamics: Mesh deformation using radial basis functions, PhD thesis, Technical University Delft.

Box, G. E. P. and Draper, N. R. (1987), *Empirical Model Building and Response Surfaces*, John Wiley & Sons, New York.

Bredmose, H. and Jacobsen, N. G. (2010), Breaking wave impacts on offshore wind turbine foundations: focused wave groups and CFD, *in* 'Proceedings of the ASME 29th International Conference on Ocean, Offshore and Arctic Engineering (OMAE)', Shanghai, China.

Bredmose, H. and Jacobsen, N. G. (2011), Vertical wave impacts on offshore wind turbine inspection platforms, *in* 'Proceedings of the ASME 30th International Conference on Ocean, Offshore and Arctic Engineering (OMAE)', Rotterdam, The Netherlands.

Bredmose, H., Skourup, J., Hansen, E. A., Christensen, E. D., Pedersen, L. M. and Mitzlaff, A. (2006), Numerical reproduction of extreme wave loads on a gravity wind turbine foundation, *in* 'Proceedings of the 25th International Conference on Offshore Mechanics and Arctic Engineering (OMAE)', Hamburg, Germany.

Brown, S. A., Magar, V., Greaves, D. M. and Conley, D. C. (2014), An evaluation of RANS turbulence closure models for spilling breakers., *in* 'Proceedings of the 34th International Conference on Coastal Engineering', Seoul, Korea.

Budar, K. and Falnes, J. (1975), 'A resonant point absorber of ocean-wave power', *Nature* **256**, 478–479.

Burroughs, J. (1916), *Under the apple-trees*, Boston, New York, Houghton Mifflin company, p. 308.

Cao, H., Zha, J. and Wan, D. (2011), Numerical simulation of wave run-up around a vertical cylinder, *in* ‘Proceedings of the 21st International Offshore and Polar Engineering Conference’, Maui, Hawaii, USA.

Chan, R. K. and Street, R. L. (1970), ‘A computer study of finite amplitude water waves’, *Journal of Computational Physics* **6**, 68–94.

Chaplin, J. R., Rainey, R. C. T. and Yemm, R. W. (1997), ‘Ringing of a vertical cylinder in waves’, *Journal of Fluid Mechanics* **350**, 119–147.

Chen, L. F., Sun, L., Zang, J. and Hillis, A. (2014), Numerical simulation of wave-induced roll of a 2-D rectangular barge using OpenFOAM, *in* ‘Proceedings of the 29th International Workshop on Water Waves and Floating Bodies’, Osaka, Japan.

Chen, L. F., Zang, J., Hillis, A. J., Morgan, G. C. J. and Plummer, A. R. (2014), ‘Numerical investigation of wave-structure interaction using OpenFOAM’, *Ocean Engineering* **88**, 91–109.

Clauss, G. F. (2010), Freak waves and their interaction with ships and offshore structures, *in* Q. Ma, ed., ‘Advances in Numerical Simulation of Nonlinear Water Waves’, World Scientific Publishing Co. Pte. Ltd, pp. 641–690.

Craik, A. D. D. (1985), *Wave Interactions and Fluid Flows.*, Cambridge University Press.

Cruz, J. (2008), *Ocean Wave Energy. Current Status and Furture Perspectives*, Springer.

Daly, B. J. (1969), ‘A technique for including surface tension effects in hydrodynamic calculations’, *Journal of Computational Physics* **4**(1), 97–117.

Dawish, M. and Moukalled, F. (2006), ‘Convection schemes for capturing interfaces of free-surface flows on unstructured grids’, *Numerical Heat Transfer, Part B: Fundamentals: An International Journal of Computation and Methodology* **49**(1), 19–42.

Dean, R. G. (1965), ‘Stream function representation of nonlinear water waves’, *Journal of Geophysical Research* **70**(18), 4561–4572.

Dean, R. G. and Dalrymple, R. A. (1991), *Water wave mechanics for engineers and scientists*, Vol. 2 of *Advanced Series on Ocean Engineering*, World Scientific.

DeBar, R. (1974), Fundamentals of the KRAKEN code, Technical report, Lawrence Livermore Laboratory. Report UCIR-760.

Demirdžić, I. and Perić, M. (1990), ‘Finite volume method for prediction of fluid flow in arbitrarily shaped domains with moving boundaries’, *International Journal for Numerical Methods in Fluids* **10**, 771–790.

Det Norske Veritas (2010), *Position Mooring. Offshore Standard DNV-OS-E301*.

Dingemans, M. W. (1997), *Water wave propogation over uneven bottoms.*, World Scientific Publishing Co.

Drew, B., Plummer, A. R. and Sahinkaya, M. N. (2009), A review of wave energy converter technology, *in* ‘Proceedings of the Institution of Mechanical Engineers, Part A: Journal of Power and Energy’, Vol. 223. no. 8.

Dullweber, A., Leimkuhler, B. and McLachlan, R. (1997), ‘Symplectic splitting methods for rigid body molecular dynamics’, *The Journal of Chemical Physics* **107**(14), 5840–5851.

Dysthe, K., Krogstad, H. E. and Müller, P. (2009), Rogue waves, *in* J. H. Steele, K. K. Turekian and S. A. Thorpe, eds, ‘Encyclopedia of Ocean Sciences’, 2 edn, Academic Press, Oxford, pp. 770–780.

EMEC (2009*a*), *Guidelines for Reliability, Maintainability and Survivability of Marine Energy Conversion Systems*, The European Marine Energy Centre Ltd.

EMEC (2009*b*), *Tank Testing of Wave Energy Conversion Systems*, The European Marine Energy Centre Ltd.

Engsig-Karup, A. P. (2006), VUnstructured Nodel DG-FEM Solution of High-order Boussinesq-type Equations, PhD thesis, Technical University of Denmark.

Engström, J., Göteman, M., Eriksson, M., Hann, M., Ransley, E., Greaves, D. and Leijon, M. (2015), ‘Scale tests on the survivability of point-absorbing wave energy converters - part ii’, *Renewable Energy* . awaiting review.

EU (2010), *Energy 2020 - A strategy for competitive, sustainable and secure energy.*, European Union.

Falcão, A. F. O. (2010), ‘Wave energy utilization: A review of the technologies’, *Renewable and Sustainable Energy Reviews* **14**, 899–918.

Faltinsen, O. M., Greco, M. and Landrini, M. (2002), ‘Green water loading on a FPSO’, *Journal of Offshore Mechanical and Artic engineering* **124**(2), 97–103.

Faulkner, D. (2000), Rogue waves - defining their characteristics for marine design, *in* ‘Rogue Waves 2000’, Brest, France.

Fenton, J. D. (1990), Nonlinear wave theories, *in* B. Le Méhauté and D. M. Hanes, eds, 'The Sea, Volume 9: Ocean Engineering Science', Wiley, New York.

Ferrant, P., Malencia, Š. and Molin, B. (1999), Nonlinear wave loads and runup on a vertical cylinder, *in* O. Mahrenholtz and M. Markiewicz, eds, 'Nonlinear Water Wave Interaction', WIT Press, p. 252.

Ferziger, J. H. and Perić, M. (2002), *Computational Methods for Fluid Dynamics*, 3 edn, Springer.

Fochesato, C., Grilli, S. and Dias, F. (2007), 'Numerical modeling of extreme rogue waves generated by directional energy focusing', *Wave Motion* **44**, 395–416.

Fuhrman, D. R., Madsen, P. A. and Bingham, H. B. (2006), 'Numerical simulation of lowest-order short-crested wave instabilities', *Journal of Fluid Mechanics* **563**, 415–441.

Gao, F., Ingram, D. M., Causon, D. M. and Mingham, C. G. (2007), 'The development of a cartesian cut cell method for incompressible viscous flows', *International Journal for Numerical Methods in Fluids* **54**, 1033–1053.

Göteman, M., Engström, J., Eriksson, M., Hann, M., Ransley, E., Greaves, D. and Leijon, M. (2015), 'Scale tests on the survivability of point-absorbing wave energy converters - part i', *Renewable Energy* . awaiting review.

Greaves, D. M. (2004), 'A quadtree adaptive method for simulating fluid flows with moving interfaces', *Journal of Computational Physics* **194**, 35–56.

Greenwood, C. (2014), 'Mesh of the west coast of Lewis and Harris'. Private communication 11/09/2014.

Gschaider, B. (2014), 'swak4Foam', online at `http://openfoamwiki.net/index.php/Contrib/swak4Foam` accessed 03/09/2014.

Hafsia, Z., Haj, M. B. and Maalel, K. (2009), 'Comparison between moving paddle and mass source methods for solitary wave generation and propagation over a steep sloping beach', *Engineering Applications of Computational Fluid Mechanics* **3**(3), 355–368.

Hagen, O. (2002), Statistics for the Draupner January 1995 freak wave event, *in* 'Proceedings of the 21st International Conference on Offshore Mechanics and Arctic Engineering (OMAE '02)', Oslo.

Hann, M., Greaves, D. and Raby, A. (2015), 'Snatch loading of a single taut moored floating wave energy converter due to focussed wave groups', *Ocean Engineering* **96**, 258–271.

Harlow, F. H. and Welch, J. E. (1965), ‘Numerical calculation of time-dependent viscous incompressible flow of fluid with free surface’, *The Physics of Fluids* **8**(12), 2182–2189.

Hasselmann, K., Barnett, T. P., Bouws, E., Carlson, H., Cartwright, D. E., Enke, K., Ewing, J. A., Gienapp, H., Hasselmann, D. E., Kruseman, P., Meerburg, A., Müller, P., Olbers, D. J., Richter, K., Sell, W. and Walden, H. (1973), Measurements of wind-wave growth and swell decay during the Joint North Sea Wave Project (JONSWAP), *in* ‘Erägnzungsheft zur Deutschen Hydrographischen Zeitschrift Reihe’. A(8), Nr. 12.

Haver, S. (2004), A possible freak wave event measured at the draupner jacket january 1, 1995, *in* ‘Rogue Waves 2004: Proceedings of a Workshop Organized by Ifremer’, Brest, France.

Haver, S. and Anderson, O. J. (2000), Freak waves: Rare realization of a typical population or typical realization of a rare population?, *in* ‘Proceedings of the 10th International Offshore and Polar Engineering Conference (ISOPE)’, Seattle, USA.

Henfridsson, U., Neimane, V., Strand, K., Kapper, R., Bernhoff, H., Danielsson, O., Leijon, M., Sundberg, J., Thorburn, K., Ericsson, E. and Bergman, K. (2007), ‘Wave energy potential in the baltic sea and the danish part of the north sea, with reflections on the skagerrak.’, *Renewable Energy* **32**(12), 2069–2084.

Higuera, P., Lara, J. L. and Losada, I. J. (2013), ‘Realistic wave generation and active wave absorption for Navier-Stokes models aplication to OpenFOAM®’, *Coastal Engineering* **71**, 102–118.

Hirt, C. W. and Nichols, B. D. (1981), ‘Volume of fluid (VOF) method for the dynamics of free boundaries’, *Journal of Computational Physics* **39**, 201–225.

Holthuijsen, L. (2007), *Waves in Oceanic and Coastal Waters*, Cambridge University Press.

Horizon (2002), ‘Freak wave’, BBC Two television program. Transcript available at `http://www.bbc.co.uk/science/horizon/2002/freakwavetrans.shtm` accessed June 2014.

Hu, Z. Z., Causon, D. M., Mingham, C. G. and Qian, L. (2011), ‘Numerical simulation of floating bodies in extreme free surface waves’, *Natural Hazards and Earth System Sciences* **11**, 519–527.

Hughes, S. A. (1993), *Physical Models and Laboratory Techniques in Coastal Engineering*, Vol. 7 of *Advanced Series on Ocean Engineering*, World Scientific.

Hunt, A. (2003), Extreme Waves, Overtopping and Flooding at Sea Defences, PhD thesis, Oxford University.

Hunt-Raby, A. C., Borthwick, A. G. L., Stansby, P. K. and Taylor, R. H. (2011), ‘Experimental measurements of focused wave group and solitary wave overtopping’, *Journal of Hydraulic Research* **49**(4), 450–464.

IPCC (2007), *Climate Change 2007 Synopsis Report: Summary for Policymakers.*, Intergovernmental Panel on Climate Change.

Irschik, K., Sparboom, U. and Oumeraci, H. (2004), Breaking wave loads on a slender pile in shallow water, *in* ‘Proceedings of the 29th International Conferencein Coastal Engineering (ICCE)’, Lisbon.

Issa, R. I. (1986), ‘Solution of the implicitly discretised fluid flow equations by operator-splitting’, *Journal of Computational Physics* **62**(1), 40–65.

Jacobsen, N. G. (2014), ‘Contrib/waves2Foam’, website. `http://openfoamwiki.net/index.php/Contrib/waves2Foam` accessed 15th September 2014.

Jacobsen, N. G., Fuhrman, D. R. and Fredsøe, J. (2012), ‘A wave generation toolbox for the open-source CFD library: OpenFOAM®’, *International Journal for Numerical Methods in Fluids* **70**, 1073–1088.

Jakobsen, M. M. (2014), Wave-structure interactions on point absorber, Technical report, Aalborg University, Denmark.

Jakobsen, M. M., Iglesias, G., Kramer, M. and Vidal, E. (2014), Experimental study of forces on point absorber, *in* ‘Proceedings of the 5th International Conference Coastlab 14’, Varna, Bulgaria.

Jang, D. S., Jetli, R. and Acharya, S. (1986), ‘Comparison of the PISO, SIMPLER, and SIMPLEC algorithms for the treatment of pressure-velocity coupling in steady flow problems’, *Numerical Heat Transfer* **10**, 209–228.

Jasak, H. (1996), Error Analysis and Estimation for the Finite Volume Method with Applications to Fluid Flows, PhD thesis, Imperial College of Science, Technology and Medicine.

Jasak, H. (2009), Dynamic mesh handling in OpenFOAM, *in* ‘Proceedings of the 48th AIAA Aerospace Sciences Meeting’, Orlando, Florida. AIAA 2009-341.

Jasak, H. and Tuković, Ž. (2010), Dynamic mesh handling in OpenFOAM applied to fluid-structure interation simulations, *in* ‘Proceedings of the V European conference on computational fluid dynamics ECCOMAS CFD’, Lisbon, Portugal.

Jeffery, H. and Sedgwick, J. (2011), *ORECCA European Offshore Renewable Energy Roadmap*, The University of Edinburgh.

Jonathon, P. and Taylor, P. H. (1997), 'On irregular, nonlinear waves in a spread sea', *Journal of Offshore Mechanics and Artic Engineering* **119**(37).

Keulegan, G. H. and Carpenter, L. H. (1958), 'Forces on cylinders and plates in an oscillating', *Journal of Research of the National Bureau of Standards* **60**(5), 423–440.

Khalil, M. and Wesseling, P. (1992), 'Vertex-centered and cell-centered multigrid for interface problems', *Journal of Computational Physics* **98**, 1–10.

Kim, C. H., Xu, Y. and Zou, J. (1997), 'Impact and nonimpact on vertical truncated cylinder due to strong and weak asymmetric wave', *International Journal of Offshore and Polar Engineering* **7**(3), 161–167.

Kleefsman, K. M. T. (2005), Water Impact Loading on Offshore Structures - A Numerical Study, PhD thesis, Rijksuniversiteit Groningen.

Kleefsman, K. M. T., Fekken, G., Veldman, A. E. P., Iwanowski, B. and Buchner, B. (2005), 'A Volume-of-Fluid based simulation method for wave impact problems', *Journal of Computational Physics* **206**, 363–393.

Kraemer, S. (2010), 'Massive offshore waves sink Australia's OceanLinx wavepower pilot', online. `http://cleantechnica.com/2010/05/22/massive-offshore-waves-sink-australias-oceanlinx-wavepower-pilot/` accessed 3rd January 2015.

Kramer, M., Marquis, L. and Frigaard, P. (2011), Performance evaluation of the wavestar prototype, *in* 'Proceedings of the 9th European Wave and Tidal Conference (EWTEC)', Southamption, UK.

Kriebel, D. L. (1992), 'Nonlinear wave interaction with a vertical circular cylinder. Part II: Wave run-up', *Ocean Engineering* **19**(1), 75–99.

Lafaurie, B., Nardone, C., Scardovelli, R., Zaleski, S. and Zanetti, G. (1994), 'Modelling merging and fragmentation in multiphase flows with SURFER', *Journal of Computational Physics* **113**(1), 134–147.

Lara, J. L., Garcia, N. and Losada, I. J. (2006), 'RANS modelling applied to random wave interaction with submerged permeable structures', *Coastal Engineering* **53**, 395–417.

Lara, J. L., Losada, I. J. and Guanche, R. (2008), 'Wave interaction with low-mound breakwaters using a RANS model', *Ocean Engineering* **35**(13), 1388–1400.

Le Méhauté, B. (1976), *Introduction to Hydrodynamics and Wave Waves*, Spring-Verlag, New York.

Leijon, M., Bernhoff, H., Berg, M. and Ågren, O. (2003), 'Economical considerations of renewable electric energy production - especially development of wave energy.', *Renewable Energy* **28**(8), 1201–1209.

Leijon, M., Danielsson, O., Eriksson, M., Thorburn, K., Bernhoff, H., Isberg, J., Sundberg, J., Ivanova, I., SjÃűstedt, E., Ågren, O., Karlsson, K. E. and Wolfbrandt, A. (2006), 'An electrical approach to wave energy conversion.', *Renewable Energy* **31**(9), 1309–1319.

Leonard, B. P. (1988), 'Simple high-accuracy resolution program for convective modelling of discontinuities', *International Journal for Numerical Methods in Fluids* **8**(10), 1291–1318.

Levitt, T. (1983), *The marketing imagination*, New York: The Free Press.

Lighthill, J. (1978), *Waves in fluids.*, Cambridge University Press.

Lin, C. L., Lee, H., Lee, T. and Weber, L. (2005), 'A level set characteristic galerkin finite element method for free surface flows', *International Journal for Numerical Methods in Fluids* **49**, 521–547.

Lin, P. (2008), *Numerical Modeling of Water Waves*, 1 edn, New York: Taylor and Francis.

Lin, P. and Liu, P. L. (1999), 'Internal wave-maker for Navier-Stokes equations models', *Journal of Waterway, Port, Coastal, and Ocean Engineering (ASCE)* **1259**.

Liu, M. and Liu, G. (2010), 'Smoothed particle hydrodynamics (SPH): an overview and recent developments', *Archives of Computational Methods in Engineering* **17**(1), 25–76.

Lu, H. (2009), On the simulation of ship motions induced by extreme waves, PhD thesis, George Mason University.

MacCormack, R. W. (1969), The effect of viscosity in hypervelocity impact cratering, *in* 'AIAA Hypervelocity Impact Conference', Cincinnati, Ohio. Paper 69-354.

MacCormack, R. W. (1982), 'A numerical method for solving the equations of compressible viscous flow', *AIAA Journal* **20**(9), 1275–1281.

Mallory, J. K. (1974), 'Abnormal waves on the southeast coast of South Africa', *International hydrographic review* **51**, 99–129.

Massel, S. R. (2013), *Ocean Surface Waves - Their Physics and Prediction*, Vol. 36 of *Advanced Series on Ocean Engineering*, World Scientific.

Massey, B. and Ward-Smith, J. (1998), *Mechanics of Fluids*, 7 edn, Stanley Thornes Ltd.

Mendez, F. J., Losada, I. J. and Losada, M. A. (2001), 'Wave-induced mean magnitudes in permeable submerged breakwaters', *Journal of Waterway, Port, Coastal, and Ocean Engineering* **127**, 7–15.

Monaghan, J. J. (2005), 'Smoothed particle hydrodynamics', *Reports on Progress in Physics* **68**(8), 1703–1759.

Mooney, K., Menon, S. and Schmidt, D. (2010), A computational study of viscoelastic droplet collisions, *in* 'Proceedings of the 22nd Annual Conference on Liquid Atomization and Spray Systems, ILASS-Americas', Cincinnati, OH, USA.

Morison, J., O'Brien, M. P., Johnson, J. W. and Schaaf, S. A. (1950), 'The forces exerted by surface waves on piles', *Journal of Petroleum Technology* **2**(5), 149–154.

Moroney, T. J. (2006), An Investigation of a Finite Volume Method Incorporating Radial Basis Functions for Simulating Nonlinear Transport, PhD thesis, Queensland University of Technology, Australia.

Muzaferija, S. and Perić, M. (1997), 'Computation of free-surface flows using the finite-volume method and moving grids', *Numerical Heat Transfer, Part B: Fundamentals: An International Journal of Computation and Methodology,* **32**(4), 369–384.

Muzaferija, S. and Perić, M. (1999), Computation of free-surface flows using interface-tracking and interface-capturing methods, *in* O. Mahrenholtz and M. Markiewicz, eds, 'Nonlinear Water Wave Interaction', WIT Press, p. 252.

Naulin, J. N. and Nielsen, A. H. (2003), 'Accuracy of spectral and finite difference schemes in 2d advection problem.', *SIAM Journal on Scientific Computing* **25**, 104–126.

Newman, J. N. and Lee, C. H. (2002), 'Boundary-element methods in offshore structural analysis.', *Journal of Offshore Mechanics and Arctic Engineering Transactions of the ASME* **142**, 81–89.

Noh, W. F. and Woodward, P. (1976), 'SLIC (simple line interface calculation)', *Lecture notes in physics* **59**, 330–340.

OpenCFD (2014), 'OpenFOAM®', website. `http://www.openfoam.org/` accessed 29th May 2014.

OpenFOAM Foundation (2012), *OpenFOAM User Guide*.

Orcina Ltd. (2015), 'Orcina ... home of orcaflex', website. `http://www.orcina.com/index.php` accessed 7th January 2015.

Parkinson, G. (2014), 'CETO wave energy machine swept away in cyclone, report says', online. `http://reneweconomy.com.au/2014/ceto-wave-energy-machine-destroyed-cyclone-reports-say` accessed 3rd January 2015.

Patankar, S. V. (1980), *Numerical Heat Transfer and Fluid Flow*, Hemisphere Publishing Corporation, Taylor & Francis Group, New York.

Patankar, S. V. and Spalding, D. B. (1972), 'A calculation procedure for heat, mass and momentum transfer in three-dimensional parabolic flows', *International Journal of Heat and Mass Transfer* **15**, 1787–1806.

Pierson, W. J. and Moskowitz, L. (1964), 'A proposed spectral form for fully developed wind seas based on the similarity theory of S. A. Kitaigorodskii', *Journal of Geophysical Research* **69**(24), 5181–5190.

Pizer, D. J., Retzler, C., Henderson, R. M., Cowieson, F. L., Shaw, M. G., Dickens, B. and Hart, R. (2005), Pelamis wec - recent advances in the numerical and experimental modelling programme, *in* 'Proceedings of the 6th European Wave and Tidal Energy Conference', Glasgow, UK.

Qian, L., Causon, D. M., Mingham, C. G. and Ingram, D. M. (2006), 'A free-surface capturing method for two fluid flows with moving bodies', *Proceedings of the Royal Society A* pp. 21–42.

Qiu, L.-C. (2008), 'Two-dimensional SPH simulations of landslide-generated water waves', *Journal of Hydraulic Engineering* **134**(5), 668–671.

Ransley, E., Hann, M., Greaves, D., Raby, A. and Simmonds, D. (2013*a*), 'Numerical and physical modeling of extreme waves at Wave Hub', *Journal of Coastal Research Special Issue No. 65* pp. 1645–1650.

Ransley, E., Hann, M., Greaves, D., Raby, A. and Simmonds, D. (2013*b*), Numerical and physical modelling of extreme wave impacts on a fixed truncated circular cylinder, *in* 'Proceedings of the 10th European Wave and Tidal Energy Conference (EWTEC)', Aalborg, Denmark.

Renardy, Y. and Renardy, M. (2002), 'PROST: a parabolic reconstruction of surface tension for the volume-of-fluid method', *Journal of Computational Physics* **183**, 400–421.

Retzler, C., Pizer, D. J., Henderson, R. M., Ahlqvist, J., Cowieson, F. L. and Shaw, M. G. (2003), Pelamis: Advances in the numerical and experimental modelling programme, *in* 'Proceedings of the 5th European Wave Energy Conference', Cork, Ireland.

Rhee, S. H., Makarov, B. P., Krishinan, H. and Ivanov, V. (2005), 'Assessment of the volume of fluid method for free-surface wave flow', *Journal of Marine Science and Technology* **10**, 173–180.

Rhie, C. M. and Chow, W. L. (1983), ‘Numerical study of the turbulent flow past an airfoil with trailing edge separation’, *AIAA Journal* **21**(11), 1525–1532.

Rienecker, M. and Fenton, J. D. (1981), ‘Numerical solution of the exact equations of water waves’, *Journal of Fluid Mechanics* **104**, 119–137.

Rosenthal, W. and Lehner, S. (2008), ‘Rogue waves: Results of the MaxWave project’, *Journal of Offshore Mechanics and Arctic Engineering* **130**(2), 21006–21013.

Rozario, J. B., Tromans, P. S., Taylor, P. H. and Efthymiou, M. (1993), Comparison of loads predicted using "NewWave" and other wave models with measurements on the Tern structure, *in* ‘Wave Kinematics and Environmental Forces’, Vol. 29 of *Advances in Underwater Technology, Ocean Science and Offshore Engineering*, Springer Netherlands, pp. 143–159.

Ruehl, K. and Bull, D. (2012), Wave energy development roadmap: Design to commercialization, *in* ‘Harnessing the Power of the Ocean, proceedings of OCEANS ’12’, Hampton Road, VA, pp. 1–10.

Rusche, H. (2002), Computational fluid dynamics of dispersed two-phase flows at high phase fractions, PhD thesis, Imperial College of Science, Technology & Medicine.

Santo, H., Taylor, P. H., Eatock Taylor, R. and Choo, Y. S. (2013), ‘Average properties of the largest waves in hurricane camille’, *Journal of Offshore Mechanics and Arctic Engineering* **135**.

Schäffer, H. A. (1996), ‘Second-order wavemaker theory for irregular waves’, *Ocean Engineering* **23**(1), 47–88.

Schreck, E., Perić, M. and Snyder, D. (2012), ‘Overset grids technology in STAR-CCM+: Methodology and applications’, online at `http://2012.oversetgridsymposium.org/assets/pdf/presentations/2_3/Overset_Schreck_Peric_Snyder.pdf` accessed 03/09/2014.

Schwartz, A. (2009), ‘Portugal’s Pelamis wave power project killed’, online. `http://cleantechnica.com/2009/03/17/portugals-pelamis-wave-power-project-killed/` accessed 3rd January 2015.

Seabased AB (2014), ‘Seabased’, website. `http://www.seabased.com/en/` accessed 29th October 2014.

Seng, S., Jensen, J. J. and Pedersen, P. T. (2012), ‘Numerical prediction of slamming loads’, *Proceedings of the Institution of Mechanical Engineers, Part M: Journal of Engineering for the Maritime Environment* **226**(2), 120–134.

Smith, D., ed. (1945), *Encore : A Continuing Anthology (March 1945)*, Encore Press, chapter "Fischerisms", p. 309.

Stansberg, C. T. and Karlsen, S. I. (2001), Green sea and water impact on FPSO in steep random waves, *in* ‘Practical Design of Ships and Other Floating Structures. Proceedings of the Eighth International Symposium on Practical Design of Ships and Other Floating Structures’, Shanghai, China, pp. 593–601.

Stansby, P. K., Xu, R., Rogers, B., Hunt, A., Borthwick, A. and Taylor, P. (2008), Modelling tsunami overtopping of a sea defence by shallow-water boussinesq, vof and sph methods, *in* ‘Proceedings of the European Conference on Flood Risk management: Research and Practice (FLOODRISK 2008)’, Oxford.

SuperGen Marine (2011), SuperGen Marine energy Research - Full Report, Technical report, University of Edinburgh.

SuperGen UKCMER (2015), ‘SuperGen UK Centre for Marine Energy Research (UKCMER) website’, online. `http://www.supergen-marine.org.uk/drupal/` accessed 8th February 2015.

Sussman, M., Smereka, P. and Osher, S. (1994), ‘A level-set approach for computing solutions to incompressible two-phase flow’, *Journal of Computational Physics* **183**, 83–116.

Svendsen, I. A. (2006), *Introduction to nearshore hydrodynamics*, Vol. 24 of *Advanced Series on Ocean Engineering*, World Scientific.

Svensson, O. and Leijon, M. (2014), ‘Peak force measurements on a cylindrical buoy with limited elastic mooring’, *IEEE Journal of Oceanic Engineering* **39**(2), 398–403.

Tanizawa, K. (2000), The state of the art on numerical wave tank, *in* ‘Proceedings of the 4th Colloquium on Seakeeping Performance of Ships’, Osaka, Japan, pp. 95–114.

Taylor, P. H. and Williams, B. A. (2004), ‘Wave statistics for intermediate depth water - NewWaves and symmetry’, *Journal of Offshore Mechanics and Artic Engineering* **126**(55), 629–634.

The Carbon Trust (2005), *Guidelines on design and operation of wave energy converters*.

Thies, P. R., Flinn, J. and Smith, G. H. (2009), Reliability assessment and criticality analysis for wave energy converters, *in* ‘Proceedings of the 8th European Wave and Tidal Energy Conference’, Uppsala, Sweden.

Thorpe, T. W. (1999), ‘A brief review of wave energy’. A report produced for the UK Department of Energy. Report No ETSU-120, available at `http://www.mech.ed.ac.uk/research/wavepower/Tom%20Thorpe/Tom%20Thorpe%20report.pdf`.

Toffoli, A. and Bitner-Gregerson, E. M. (2011), ‘Extreme and rogue waves in directional wave fields’, *The Open Ocean Engineering Journal* **4**, 24–33.

Torres-Freyermuth, A., Lara, J. L. and Losada, I. J. (2010), ‘Numerical modelling of short- and long-wave transformation on a barred beach’, *Coastal Engineeringl* **57**(3), 317–330.

Tromans, P. S., Anaturk, A. R. and Hagemeijer, P. (1991), A new model for the kinematics of large ocean waves - application as a design wave, *in* ‘Proceedings of the 1st International Offshore and Polar Engineering Conference’, Edinburgh, UK, pp. 64–71.

Ubbink, O. (1997), Numerical prediction of two fluid systems with sharp interfaces, PhD thesis, Imperial College of Science, Technology and Medicine.

UK Energy Research Centre (2008), UKERC Marine (Wave and Tidal Current) Renewable Energy Technology Roadmap - Summary Report, Technical report, University of Edinburgh.

U.S. Army Corps of Engineers (2006), *Coastal Engineering Manual. Engineering Manual 1110-2-1100*, U.S. Army Corps of Engineers, Washington, D.C.

Van Doormaal, J. P. and Raithby, G. D. (1984), ‘Enhancements of the simple method for predicting incompressible fluid flows’, *Numerical Heat Transfer* **7**(2), 147–163.

van Leer, B. (1973), Towards the ultimate conservative difference scheme I. the quest of monotonicity, *in* ‘Proceedings of the Third International Conference on Numerical Methods in Fluid Mechanics Lecture Notes in Physics’, Vol. 18, Reno, Nevada, pp. 163–168.

van Leer, B. (1976), ‘Towards the ultimate conservative difference scheme V. a second order sequel to Godunov’s method’, *Journal of Computational Physics* **32**, 101–136.

Versteeg, H. K. and Malalasekera, W. (2007), *An Introduction to Computational Fluid Dynamics: The Finite Volume Method*, 2 edn, Pearson Education Ltd.

Vidal, E., Hansen, R. H. and Kramer, M. (2012), Early performance assessment of the electrical output of wavestars prototype, *in* ‘Proceedings of the 4th International Conference on Ocean Energy (ICOE)’, Dublin, Ireland.

Vyzikas, T., Ransley, E., Hann, M., Magagna, D., Greaves, D., Simmonds, D., Magar, V. and Conley, D. (2013), Integrated numerical modelling system for extreme wave events at the Wave Hub site, *in* ‘Proceedings of Institute of Civil Engineers (ICE) Coasts, Marine Structures and Breakwaters 2013: From Sea to Shore - Meeting the Challenges of the Sea’, Edinburgh, UK.

Wacławczyk, T. and Koronowicz, T. (2008), ‘Comparison of CICSAM and HRIC high-resolution schemes for interface capturing’, *Journal of theoretical and applied mechanics* **46**, 325–345.

Walker, D. A. G., Taylor, P. H. and Eatock Taylor, R. (2005), ‘The shape of large surface waves on the open sea and the draupner new year wave’, *Applied Ocean Research* **26**(3), 73–83.

WAMIT Inc. (2015), ‘WAMIT Inc. The state of the art in wave interaction analysis’, website. `http://www.wamit.com/` accessed 7th January 2015.

Wave Hub Ltd. (2015), ‘Wave Hub’, website. `http://www.wavehub.co.uk/` accessed 9th January 2015.

Westphalen, J. (2010), Extreme Wave Loading on Offshore Wave Energy Devices using CFD, PhD thesis, Plymouth University.

Westphalen, J., Greaves, D. M., Raby, A., Hu, Z. Z., Causon, D. M., Mingham, C. G., Omidvar, P., Stansby, P. K. and Rogers, B. D. (2014), ‘Investigation of wave-structure interaction using state of the art cfd techniques’, *Open Journal of Fluid Dynamics* **4**, 18–43.

Westphalen, J., Greaves, D., Williams, C., Drake, K. and Taylor, P. (2009), Numerical simulation of an oscillating cone at the water surface using computational fluid dynamics, *in* ‘Proceedings of International Workshop on water waves and floating bodies’, Zelegnorsk, Russia.

White, B. S. and Fornberg, B. (1998), ‘On the chance of freak waves at sea’, *Journal of Fluid Mechanics* **355**, 113–138.

Widman, M. (2007), ‘While Finavera’s buoy sinks, hopes of harnessing ocean energy survive’, online. `http://www.renewableenergyworld.com/rea/news/article/2007/11/while-finaveras-buoy-sinks-hopes-of-harnessing-ocean-energy-survive-50510` accessed 3rd January 2015.

Wienke, J. and Oumeraci, H. (2005), ‘Breaking wave impact force on a vertical and inclined slender pile - theoretical and large-scale model investigations’, *Coastal Engineering* **52**, 435–462.

Wu, G. X., Xu, G. D. and Duan, W. Y. (2010), A summary of water entry problem of a wedge based on the fully nonlinear velocity potential theory, *in* ‘The Proceedings of the 9th International Conference on Hydrodynamics’, Shanghai, China.

Xing, Y., Hadzic, I., Muzaferija, S. and Peric, M. (2001), CFD simulation of flow-induced floating-body motions, *in* 'The Proceedings of the 16th International Workshop on Water Waves and Floating Bodies', Hiroshima, Japan.

Yang, C., Löhner, R. and Lu, H. (2006), 'An unstructured-grid based volume-of-fluid method for extreme wave and freely-floating structure interactions', *Journal of Hydrodynamics, Ser. B* **18**(3), 415–422.

Yang, G., Causon, D. M., Ingram, D. M., Saunders, R. and Batten, P. (1997), 'A cartesian cut cell method for compressible flows part b: moving body problems', *Aeronautical Journal* **101**(1002), 57–65.

Yang, J. and Stern, F. (2007), Large-eddy simulation of breaking waves using embedded-boundary/level-set method, *in* '45th AIAA Aerospace Sciences Meeting and Exhibit', Reno, Nevada.

Yemm, R. W., Henderson, R. M. and Taylor, C. A. E. (2000), *The OPD Pelamis WEC: Current Status and Onward Programme.*, Ocean Power Delivery Ltd., Edinburgh, UK.

Zhang, Y., Zou, Q. and Greaves, D. M. (2009), 'Numerical simulation of free-surface flow using the level-set method with global mass correction', *International Journal for Numerical Methods in Fluids* **63**, 651–680.

Zhang, Y., Zou, Q., Greaves, D. M., Reeve, D., Hunt-Raby, A., Graham, D., James, P. and Lv, X. (2010), 'A level set immersed boundary method for water entry and exit', *Communications in Computational Physics* **8**(2), 265–288.

Zhao, Q., Armfield, S. and Tanimoto, K. (2004), 'Numerical simulation of breaking waves by a multi-scale turbulence model', *Coastal Engineering* **51**, 53–80.

Zhao, X. and Hu, C. (2012), 'Numerical and experimental study on a 2-D floating body under extreme wave conditions', *Applied Ocean Research* **35**, 1–13.

Zhao, X., Hu, C. and Sun, Z. (2010), 'Numerical simulation of extreme wave generation using VOF method', *Journal of Hydrodynamics* **22**(4), 466–477.

Zwart, P. J., Raithby, G. D. and Raw, M. J. (1999), 'The integrated space-time finite volume method and its application to moving-boundary problems', *Journal of Computational Physics* **154**, 497–519.

Appendix A

Generalised NWT Decisions

A.1 Pre-processing decisions

Table A.1: Fluid properties

Property	Value	Units
Density of air	1.2	kg m$^{-}3$
Density of water	1000	kg m$^{-}3$
Kinematic viscosity of air	1.36×10$^{-}5$	m^{2}s^{-1}
Kinematic viscosity of air	1×10$^{-}6$	m^{2}s^{-1}

Table A.2: Mesh design

Property	Decision
Mesh cell shape	Square (2D), cubic (3D)
Refinement strategy	Quadtree (2D), octree (3D)
Mesh resolution at free surface for RMS error 2%	10 cells per H (0.01$<$ H/λ $<$0.1)
Mesh resolution at free surface for RMS error 1%	1 cell per H (H/λ $<$0.01)
Including structures	Use `snappyHexMesh` without layers

Table A.3: Boundary conditions

Property	**Boundary condition**	**Value**
front / back / bottom / outlet		
Phase fraction (`alpha1`)	`zeroGradient`	
Velocity (`U`)	`FixedValue`	0
Mixture pressure (`p_rgh`)	`fixedFluxPressure`	
Turbulent KE (k)	`kqRWallFunction`	`uniform` 0.1
Dissipation (ε)	`epsilonWallFunction`	`uniform` 0.1
top		
Phase fraction (`alpha1`)	`inletOutlet`	0
Velocity (`U`)	`pressureInletOutletVelocity`	
Mixture pressure (`p_rgh`)	`totalPressure`	`uniform` 0
Turbulent KE (k)	`inletOutlet`	`uniform` 0.1
Dissipation (ε)	`inletOutlet`	`uniform` 0.1
inlet		
Phase fraction (`alpha1`)	`waveAlpha` (expression-based)	
Velocity (`U`)	`waveVelocity` (expression-based)	
Mixture pressure (`p_rgh`)	`zeroGradient`	
Turbulent KE (k)	`inletOutlet`	`uniform` 0.1
Dissipation (ε)	`inletOutlet`	`uniform` 0.1
structure		
Phase fraction (`alpha1`)	`zeroGradient`	
Velocity (`U`)	`movingWallVelocity`	0
Mixture pressure (`p_rgh`)	`fixedFluxPressure`	
Turbulent KE (k)	`kqRWallFunction`	`uniform` 0.1
Dissipation (ε)	`epsilonWallFunction`	`uniform` 0.1

A.2 Solver decisions

Table A.4: Fundamental solver decisions

Property	**Decision**
Equations	Reynolds-Averaged Navier-Stokes (RANS)
Discretisation	Finite Volume Method (FVM)
Interface treatment	Volume Of Fluid (VOF)
Pressure-velocity coupling	Pressure Implicit with Splitting of Operators (PISO)

Table A.5: Numerical schemes (`fvSchemes`)

Property	**Decision**
Integration method	`Gauss` (1-point Gaussian quadrature)
Gradient terms (default)	`linear` (second-order unbounded)
Gradient terms (bounded)	`van Leer` or `MUSCL` (first/second-order bounded)
Diffusion coefficient (Laplacian terms)	`linear`
Surface normal gradient (Laplacian terms)	`corrected` (second-order unbounded)

Table A.6: Time discretisation and time-step control

Property	**Decision**
Time discretisation	`Euler`
Time step	`adjustableTimeStep`
Maximum Co (`maxCo`)	0.25
Maximum Alpha Co (`maxAlphaCo`)	0.25
Maximum time-step (`maxDeltaT`)	1 s

Table A.7: Solver types

Property	**Solver type**	**Preconditioner**	**Smoother**
Pressure option 1	Geometric-Algebraic Multi-Grid (GAMG)		Diagonal Incomplete-Cholesky (DIC)
Pressure option 2	Preconditioned Conjugate Gradient (PCG)	GAMG	DIC or Gauss-Seidel
Velocity/ alpha option 1	`smoothSolver`		Gauss-Seidel
Velocity/ alpha option 2	Preconditioned Bi-Conjugate Gradient (PBiCG)	Diagonal Incomplete-LU (DILU)	

Table A.8: Solver tolerances

Property	**Value**
Relative tolerance (`relTol`)	0
Tolerance (`tolerance`)	1×10^{-8}
Maximum iterations (`maxIter`)	100
Under-relaxation (`relaxationFactors`)	1 (none)

Appendix B

Mesh Motion and Mass Properties

B.1 The Wavestar machine

Table B.1: Mass properties for the WaveStar application in Section 5.2.

Property	**OpenFOAM® name**	**Value**	**Units**
Mass	`mass`	220	kg
Centre of Mass	`centreOfMass`	(4.6814 0.0 0.3245)	m
Centre of Rotation	`centreOfRotation`	(3.286 0.0 1.655)	m
Moment of Inertia	`momentOfInertia`	(124.26 124.26 124.26)	N m

Table B.2: Dynamic mesh properties for the WaveStar application in Section 5.2.

Property	**OpenFOAM® name**	**Value**	**Units**
Inner extent of deforming region	`innerDistance`	0.1	m
Outer extent of deforming region	`outerDistance`	2.95	m
Relaxation of the acceleration	`accelerationRelaxation`	0.7	

Table B.3: Motion constraints used in the WaveStar application in Section 5.2.

Property	**OpenFOAM® name**	**Value**	**Units**
Constraint 1			
Constraint type	`axis`	(0 1 0)	
Centre of Rotation	`centreOfRotation`	(3.286 0.0 1.655)	m
Relaxation	`relaxationFactor`	0.7	
Tolerance	`tolerance`	0.001	
Constraint 2			
Constraint type	`point`	(3.286 0.0 1.655)	m
Centre of Rotation	`centreOfRotation`	(3.286 0.0 1.655)	m
Relaxation	`relaxationFactor`	0.7	
Tolerance	`tolerance`	0.001	

B.2 Moored buoy

Table B.4: Mass properties for the moored buoy application in Section 5.3.

Property	OpenFOAM® name	Value	Units
Mass	`mass`	43.2	kg
Centre of Mass	`centreOfMass`	(5.49 0.0 -0.133)	m
Moment of Inertia	`momentOfInertia`	(1.61 1.61 0.5)	N m

Table B.5: Dynamic mesh properties for the moored buoy application in Section 5.3.

Property	OpenFOAM® name	Value	Units
Inner extent of deforming region	`innerDistance`	0.1	m
Outer extent of deforming region	`outerDistance`	2.95	m
Relaxation of the acceleration	`accelerationRelaxation`	0.7	

Table B.6: Motion restraint used in the moored buoy application in Section 5.3.

Property	OpenFOAM® name	Value	Units
Restraint type	`linearSpring`		
Anchor position	`anchor`	(5.49 0 -2.8)	m
Attachment point	`refAttachmentPt`	(5.49 0 -0.314)	m
Spring stiffness	`stiffness`	67	N/m
Spring rest length	`restLength`	2.18	m

B.3 Seabased wave energy generator

Table B.7: Mass properties for the Seabased application in Section 5.4.

Property	OpenFOAM® name	Value	Units
Mass	`mass`	0.962	kg
Centre of Mass	`centreOfMass`	(5.937 0.0 -0.02777)	m
Moment of Inertia	`momentOfInertia`	(0.0053 0.0053 0.006)	N m

Table B.8: Dynamic mesh properties for the Seabased application in Section 5.4.

Property	**OpenFOAM® name**	**Value**	**Units**
Inner extent of deforming region	`innerDistance`	0.1	m
Outer extent of deforming region	`outerDistance`	2	m
Relaxation of the acceleration	`accelerationRelaxation`	0.2	

Table B.9: Motion restraint used in the Seabased application in Section 5.4.

Property	**OpenFOAM® name**	**Value**	**Units**
Restraint type	`SBPTOacc`		
Anchor position	`anchor`	(5.937 0 -2.5)	m
Attachment point	`refAttachmentPt`	(5.937 0 -0.0726)	m
Distance above translator	`topStrokeLength`	0.142	m
Distance below translator	`bottomStrokeLength`	0.083	m
Endstop length	`topSpringLength`	0.0547	m
Endstop stiffness	`topSpringK`	1920	N/m
Translator mass	`translatorMass`	0.78	kg

Appendix C

Original Computer Code

C.1 The Seabased PTO system

/OpenFOAM-2.3.0/src/sixDoFRigidBodyMotion/restraints/SBPTOacc/SBPTOacc.C

```
/*---------------------------------------------------------------------------*\
  =========                 |
  \\      /  F ield         | OpenFOAM: The Open Source CFD Toolbox
   \\    /   O peration     |
    \\  /    A nd           | Copyright held by original author
     \\/     M anipulation  |
-------------------------------------------------------------------------------
License
    This file is part of OpenFOAM.

    OpenFOAM is free software: you can redistribute it and/or modify it
    under the terms of the GNU General Public License as published by
    the Free Software Foundation, either version 3 of the License, or
    (at your option) any later version.

    OpenFOAM is distributed in the hope that it will be useful, but WITHOUT
    ANY WARRANTY; without even the implied warranty of MERCHANTABILITY or
    FITNESS FOR A PARTICULAR PURPOSE.  See the GNU General Public License
    for more details.

    You should have received a copy of the GNU General Public License
    along with OpenFOAM.  If not, see <http://www.gnu.org/licenses/>.

\*---------------------------------------------------------------------------*/

#include "SBPTOacc.H"
#include "addToRunTimeSelectionTable.H"
#include "sixDoFRigidBodyMotion.H"

// * * * * * * * * * * * * * * Static Data Members * * * * * * * * * * * * * //

namespace Foam
{
namespace sixDoFRigidBodyMotionRestraints
{
    defineTypeNameAndDebug(SBPTOacc, 0);

    addToRunTimeSelectionTable
    (
```

```
        sixDoFRigidBodyMotionRestraint,
        SBPTOacc,
        dictionary
    );
}
}

// * * * * * * * * * * * * * * * * Constructors  * * * * * * * * * * * * * * //

Foam::sixDoFRigidBodyMotionRestraints::SBPTOacc::SBPTOacc
(
    const word& name,
    const dictionary& sDoFRBMRDict
)
:
    sixDoFRigidBodyMotionRestraint(name, sDoFRBMRDict),
    anchor_(),
    refAttachmentPt_(),
    topStrokeLength_(),
    topSpringK_(),
    topSpringLength_(),
    bottomStrokeLength_(),
    translatorMass_(),
    topSpringFullyCompressedLength_()
{
    read(sDoFRBMRDict);
}

// * * * * * * * * * * * * * * * * Destructors * * * * * * * * * * * * * * * //

Foam::sixDoFRigidBodyMotionRestraints::SBPTOacc::~SBPTOacc()
{}

// * * * * * * * * * * * * * * Member Functions  * * * * * * * * * * * * * * //

void Foam::sixDoFRigidBodyMotionRestraints::SBPTOacc::restrain
(
    const sixDoFRigidBodyMotion& motion,
    vector& restraintPosition,
    vector& restraintForce,
    vector& restraintMoment,
    scalar deltaT
) const
{
//initial seperation from attachment to anchor
    vector i = refAttachmentPt_ - anchor_;
    scalar magI = mag(i);

    restraintPosition = motion.currentPosition(refAttachmentPt_);
    vector r = restraintPosition - anchor_;
    scalar magR = mag(r);
    r /= (magR + VSMALL); //normalises the vector

//active when translator hits top endstop
    scalar a = pos(magR-magI-topStrokeLength_+topSpringLength_);
```

```
//deactive when translator hits bottom of PTO
    scalar b = pos(magR+bottomStrokeLength_-magI);
//active when translator fully depresses endstop
    scalar c = pos(magR-magI-topStrokeLength_+topSpringFullyCompressedLength_);

    scalar grav = 9.81; //gravity

    vector v = motion.currentVelocity(restraintPosition);
    vector vp = motion.previousVelocity(restraintPosition);
    vector acc = (v-vp)/deltaT;
    scalar accInline = acc & r;
    if (accInline < -grav)
    {
        accInline = -grav;
    }
    if (accInline > grav)
    {
        accInline = grav;
    }
    restraintForce = -(a*topSpringK_*(magR-magI-topStrokeLength_+topSpringLength_) +
b*translatorMass_*(grav+accInline) +
c*100*topSpringK_*(magR-magI-topStrokeLength_+topSpringFullyCompressedLength_))*r;

    restraintMoment = vector::zero;

    if (motion.report())
    {
        Info<< " attachmentPt - anchor " << r*magR
            << " line length " << magR
            << " force " << restraintForce
            << " translator acceleration " << accInline
            << endl;
    }
}

bool Foam::sixDoFRigidBodyMotionRestraints::SBPTOacc::read
(
    const dictionary& sDoFRBMRDict
)
{
    sixDoFRigidBodyMotionRestraint::read(sDoFRBMRDict);

    sDoFRBMRCoeffs_.lookup("anchor") >> anchor_;
    sDoFRBMRCoeffs_.lookup("refAttachmentPt") >> refAttachmentPt_;
    sDoFRBMRCoeffs_.lookup("topStrokeLength") >> topStrokeLength_;
    sDoFRBMRCoeffs_.lookup("topSpringK") >> topSpringK_;
    sDoFRBMRCoeffs_.lookup("topSpringLength") >> topSpringLength_;
    sDoFRBMRCoeffs_.lookup("bottomStrokeLength") >> bottomStrokeLength_;
    sDoFRBMRCoeffs_.lookup("translatorMass") >> translatorMass_;
    sDoFRBMRCoeffs_.lookup("topSpringFullyCompressedLength")
>> topSpringFullyCompressedLength_;


    return true;
}
```

```
void Foam::sixDoFRigidBodyMotionRestraints::SBPTOacc::write
(
    Ostream& os
) const
{
    os.writeKeyword("anchor")
        << anchor_ << token::END_STATEMENT << nl;

    os.writeKeyword("refAttachmentPt")
        << refAttachmentPt_ << token::END_STATEMENT << nl;

    os.writeKeyword("topStrokeLength")
        << topStrokeLength_ << token::END_STATEMENT << nl;

    os.writeKeyword("topSpringK")
        << topSpringK_ << token::END_STATEMENT << nl;

    os.writeKeyword("topSpringLength")
        << topSpringLength_ << token::END_STATEMENT << nl;

    os.writeKeyword("bottomStrokelength")
        << bottomStrokeLength_ << token::END_STATEMENT << nl;

    os.writeKeyword("translatorMass")
        << translatorMass_ << token::END_STATEMENT << nl;

    os.writeKeyword("topSpringFullyCompressedLength")
        << topSpringFullyCompressedLength_ << token::END_STATEMENT << nl;

    //os.writeKeyword("damping")
        //<< damping_ << token::END_STATEMENT << nl;
}

// ************************************************************************* //
```

/OpenFOAM-2.3.0/src/sixDoFRigidBodyMotion/restraints/SBPTOacc/SBPTOacc.H

```
/*---------------------------------------------------------------------------*\
  =========                 |
  \\      /  F ield         | OpenFOAM: The Open Source CFD Toolbox
   \\    /   O peration     |
    \\  /    A nd           | Copyright held by original author
     \\/     M anipulation  |
-------------------------------------------------------------------------------
License
    This file is part of OpenFOAM.

    OpenFOAM is free software: you can redistribute it and/or modify it
    under the terms of the GNU General Public License as published by
    the Free Software Foundation, either version 3 of the License, or
    (at your option) any later version.
```

```
    OpenFOAM is distributed in the hope that it will be useful, but WITHOUT
    ANY WARRANTY; without even the implied warranty of MERCHANTABILITY or
    FITNESS FOR A PARTICULAR PURPOSE.  See the GNU General Public License
    for more details.

    You should have received a copy of the GNU General Public License
    along with OpenFOAM.  If not, see <http://www.gnu.org/licenses/>.

Class
    Foam::sixDoFRigidBodyMotionRestraints::SBPTOacc

Description
    sixDoFRigidBodyMotionRestraints model.  Linear spring.

SourceFiles
    SBPTOacc.C

\*---------------------------------------------------------------------------*/

#ifndef SBPTOacc_H
#define SBPTOacc_H

#include "sixDoFRigidBodyMotionRestraint.H"
#include "point.H"

// * * * * * * * * * * * * * * * * * * * * * * * * * * * * * * * * * * * * * //

namespace Foam
{

namespace sixDoFRigidBodyMotionRestraints
{

/*---------------------------------------------------------------------------*\
                          Class SBPTOacc Declaration
\*---------------------------------------------------------------------------*/

class SBPTOacc
:
    public sixDoFRigidBodyMotionRestraint
{
    // Private data

        //- Anchor point, where the spring is attached to an immovable
        //  object
        point anchor_;

        //- Reference point of attachment to the solid body
        point refAttachmentPt_;

        //- Gap between translator and top of PTO when at rest (m)
        scalar topStrokeLength_;

        //- Top spring stiffness coefficient (N/m)
        scalar topSpringK_;
```

```
        //- Rest length of top spring - when no forces are applied to it (m)
        scalar topSpringLength_;

        //- Gap between translator and base of PTO when at rest (m)
        scalar bottomStrokeLength_;

//- Translator mass (kg)
scalar translatorMass_;

//- Fully compressed length of the top spring (m)
scalar topSpringFullyCompressedLength_;

        //- Damping coefficient (Ns/m)
        //scalar damping_;

public:

    //- Runtime type information
    TypeName("SBPTOacc");


    // Constructors

        //- Construct from components
        SBPTOacc
        (
            const word& name,
            const dictionary& sDoFRBMRDict
        );

        //- Construct and return a clone
        virtual autoPtr<sixDoFRigidBodyMotionRestraint> clone() const
        {
            return autoPtr<sixDoFRigidBodyMotionRestraint>
            (
                new SBPTOacc(*this)
            );
        }


    //- Destructor
    virtual ~SBPTOacc();


    // Member Functions

        //- Calculate the restraint position, force and moment.
        //  Global reference frame vectors.
        virtual void restrain
        (
            const sixDoFRigidBodyMotion& motion,
            vector& restraintPosition,
            vector& restraintForce,
            vector& restraintMoment,
```

```
            scalar deltaT
        ) const;

        //- Update properties from given dictionary
        virtual bool read(const dictionary& sDoFRBMRCoeff);

        //- Write
        virtual void write(Ostream&) const;
};


// * * * * * * * * * * * * * * * * * * * * * * * * * * * * * * * * * * * * * //

} // End namespace solidBodyMotionFunctions
} // End namespace Foam

// * * * * * * * * * * * * * * * * * * * * * * * * * * * * * * * * * * * * * //

#endif

// ************************************************************************* //
```